EDITORIAL OFFICE

EDITOR-IN-CHIEF
Malcolm J. Crocker

MANAGING EDITOR
Marek Pawelczyk

ASSOCIATE EDITORS
Dariusz Bismor
Nickolay Ivanov
Zhuang Li

ASSISTANT EDITORS
Teresa Glowka
Sebastian Kurczyk
Karol Jablonski

EDITORIAL ASSISTANT
Macie Franklin
Neha Patel

EDITORIAL BOARD

Jorge P. Arenas
Valdivia, Chile

Jonathan D. Blotter
Provo, USA

Leonid Gelman
Cranfield, UK

Samir Gerges
Florianópolis, Brazil

Colin H. Hansen
Adelaide, Australia

Hugh Hunt
Cambridge, England

Dan Marghitu
Auburn, USA

Manohar Lal Munjal
Bangalore, India

Kazuhide Ohta
Fukuoka, Japan

Goran Pavic
Villeurbanne, France

Subhash Sinha
Auburn, USA

International Journal of Acoustics and Vibration

A quarterly publication of the International Institute of Acoustics and Vibration

Volume 21, Number 3, September 2016

EDITORIAL

What I Don't Know Part 2 of 2
Richard J. Peppin 238

ARTICLES

Investigation on a High-Frequency Controller for Rotor BVI Noise Alleviation
Alessandro Anobile, Giovanni Bernardini and Massimo Gennaretti 239

Reliability-Based Optimization of the Coupled Structural-Acoustic System with Random Parameters
Xiaojun Wang, Yunlong Li, Zhiliang Ma and Zhiping Qiu 249

Frequency Identification of Flexible Hub-Beam System Using Control Data
Xie Yong, Liu Pan and Cai Guo-Ping 257

Exact Solution for a Free Vibration of Thermoelastic Hollow Cylinder Under GNIII Model
Ibrahim A. Abbas 266

The Effect of Crack Geometry on the Nondestructive Fault Detection in a Composite Beam
Sadettin Orhan, Murat Lüy, M. Hüsnü Dirikolu and Gazi Mustafa Zorlu . . . 271

Fault Diagnosis For Exhaust Fan Using Experimental Predictive Maintenance Method
Hamdi Taplak, Emrah Kurt and Mehmet Parlak 274

Dynamic Analysis of Draft Gear and Draft Pad of Freight Wagon due to Localized Defects using FEM
Sachin S. Harak, Satish C. Sharma and S. P. Harsha 281

Effects of Young's Modulus on Disc Brake Squeal using Finite Element Analysis
Ali Belhocine and Nouby M. Ghazaly 292

Acoustic Characteristic Analysis of Prestressed Cylindrical Shells in Local Areas
Lu-yun Chen and Yong Liu 301

Nonlinear Vibrations and Chaos in Rectangular Functionally Graded Plates with Thermo-mechanical Coupling
Seyedeh Elnaz Naghibi and Mojtaba Mahzoon 308

Response of a Cylindrical Shell with Finite Length Ring Stiffeners
Andrew J. Hull and Geoffrey R. Moss 317

Aeroelastic Analysis of Unrestrained Aircraft Wing with External Stores Under Roll Maneuver
Seyed Ahmad Fazelzadeh, Amir Hosein Ghasemi and Abbas Mazidi 327

Research on Fault Feature Extraction of Rubbing Rotor Based on Vector-bispectrum Energy
Zhang Chao 334

Performance of Sound Insulation in Buildings — A Case Study
Marcus Vinícius Manfrin de Oliveira Filho and Paulo Henrique Trombetta Zannin 339

Dynamic Feature Extraction for Speech Signal Based On MUSIC and Modulation Spectrum
Han Zhiyan and Wang Jian 346

About the Authors 352

Editor's Space

What I Don't Know Part 2 of 2

The U.S. Occupational Safety and Health Administration (OSHA) 90 dBA Exposure Limit. This OSHA limit purports to protect workers' hearing. No one ever accused me of knowing too much about the health effects of noise. If asked, I quote the OSHA limits. I wonder how much "good science" was used to develop the criteria. Consider the available technology back then: no integrating sound level meters, many noisy industries, no standard measuring methodology, and strong politics to encourage or kill a regulation's development. So I ask, what data were used to determine whether hearing damage may ensue if someone is exposed to A-weighted sound pressure levels of 90 dB for 8 hours/day for his or her lifetime? I do not question the intense-noise relationship with hearing loss, I just wonder how the data were considered sufficient enough to be so precise in the wording of 29CFR1910.95. Without sophisticated instrumentation (like dosimeters or integrating-averaging meters), and measurement methodology, I suspect there was not such strong epidemiological evidence between a particular noise level and the expected hearing loss.

Correcting' for Ambient Noise. To correct for ambient noise, we normally use an equation that is in the form of a table: $L_p(\text{source}) = f[L_p(\text{source+ambient}) - L_p(\text{ambient})]$. The equation and table require that $L_p(\text{source+ambient})$ be greater that $L_p(\text{ambient})$. From this table, if the difference between the source with only the ambient is 10 dB, then the correction is about –0.5 dB; if the difference is 5 dB, then the correction is about –1.5 dB, and if the difference is 3 dB, then the correction is –3 dB. If we continue using the equation and the difference is only 1 dB, then the correction is –6.8 dB. However, the conventional rule of thumb is if the source with the ambient is within 3 dB of the ambient alone, then the measurement of the source can't be made. Why the restraint? Keep in mind that community noise, especially ambient noise, is often not steady, which complicates the situation (little guidance is given to defining ambient noise, especially compared to a maximum fast, A-weighted sound pressure level). I suspect this is because of the uncertainty in the instrumentation specifications. Perhaps, with old analog meters, accurately reading a fast moving needle, or averaging it, gave an uncertainty of 3 dB. Also, the 3 dB limit could arise from the uncertainties allowed in the sound level meter standards with different "classes" of instruments. I am suggesting we are currently putting too much time and effort into the measurements and instrumentation than is necessary for the appropriate application of the results.

Transmission Loss (TL). This is a measure of the noise insulation of a partition. I want to discuss what the measured results mean. A flat panel is placed at the opening between two reverberation rooms. Noise is produced in one and the sound pressure level on both sides is measured. The panel area and the receiving room absorption are used to get a TL value. But what is being measured? The specimen's size, shape, and boundary conditions have a large effect on the TL measured. Leaving aside the specimen's internal construction, the TL frequency response will be a function of the aspect ratio, the boundary conditions, and the size. Imagine that a very large specimen would have a very low, low-frequency loss and vice versa for a very small specimen. What confidence can we have with the TL test results?

Uncertainty. Every measurement has an associated uncertainty. It arises from instrumentation imprecision, lack of known bias, operator variability, and procedure variations. Every test method, test report, and piece of test data should have an associated uncertainty so readers know the data is imprecise. This should also go for every algorithm. Since an algorithm is an approximation of a physical process, some uncertainty, determined when the algorithm was developed, should be part of it. The user of the algorithms, consultant or customer, should know that the prediction is no better than the uncertainty. Of course, this complicates reports and explanations and makes our jobs harder.

Field Transmission Loss. If laboratory transmission loss TL results are not well understood, then the field versions are even worse. A realistic comparison between the field and laboratory values of TL is fraught because variability of room diffusion and volume, flanking, measurement method, and specimen area are often impossible to reproduce in the laboratory. My recommendation is to abolish the concept of Field TL and use Noise Reduction (NR) which, in my opinion, is the only realistic measure of isolation of partitions. We should forget trying to compare laboratory tests with field tests.

Richard J. Peppin
Director, IIAV

Investigation on a High-Frequency Controller for Rotor BVI Noise Alleviation

Alessandro Anobile, Giovanni Bernardini and Massimo Gennaretti

Department of Engineering, Roma Tre University, Via della Vasca Navale 79, 00146, Rome, Italy

(Received 26 November 2013; acepted 12 November 2014)

Among the several sources of acoustic annoyance produced by rotorcraft in operating conditions, blade-vortex interactions (BVIs) capture the interest of much of the current research. This paper deals with the reduction of BVI noise from helicopter main rotors by application of the active twist rotor concept (ATR), exploiting smart materials for twisting blades through higher-harmonic torque loads. An optimal, multi-cyclic, control approach is applied to identify the control law driving the ATR actuation during the occurrence of severe BVI events. Numerical predictions are obtained through a computational tool that is able to predict the aeroelastic response of the rotor blades and the emitted noise in arbitrary steady flight conditions. The approach for the control law identification is described and numerical results concerning aeroelastic and aeroacoustic performance of the controlled rotor are presented to assess the proposed methodology.

NOMENCLATURE

$\mathbf{f}_{aer}, \mathbf{f}_{str}^{nl}$	Forcing terms of linear structural dynamics
$\mathbf{m}$	Generalized ATR torque moments
p'_T, p'_L	Thickness and loading noise
$\mathbf{q}$	Vector of the Lagrangian coordinates
$\mathbf{r}$	Distance between source and observer positions
$\mathbf{u}, \mathbf{z}$	Vectors of control and output variables
$\mathbf{v}$	Flow velocity
$\mathbf{x}, \mathbf{y}$	Observer and source position
G	Unit-source solution of the Laplace equation
$\mathbf{G}_u, \mathbf{G}_z$	Gain matrices
J	Cost function
$\mathbf{M}, \mathbf{C}, \mathbf{K}$	Mass, damping and stiffness matrices
S_B, S_W^N, S_W^F	Body, near wake and far wake surfaces
$\mathbf{T}$	Input-output control transfer matrix
$\mathbf{W}_u, \mathbf{W}_z$	Optimal control weighting matrices
c_0, p_0, ρ_0	Speed of sound, pressure and density of undisturbed medium
τ	Emission time
φ_S, φ_I	Scattered and incident velocity potential
u_n, v_n	Flow and body normal velocity components

1. INTRODUCTION

The acoustic annoyance is one of the critical issues concerning the flight of helicopters. The main rotor plays a crucial role in noise generation, through several aerodynamic phenomena that affect its performance. Among these, blade-vortex interactions (BVIs) are relevant sources of noise. Indeed, BVI noise has an impulsive nature, which is particularly annoying for the human ear and typically occurs when the helicopter is in descent or in slow advancing flight[1,2] (i.e., when it operates near the ground and the community). As a consequence, prediction and control of BVI noise (in terms of magnitude and directivity pattern) are important issues for rotorcraft designers both for civil applications and for improving stealthiness in military missions.

Identification of optimal rotor blade shapes and active controls, as well as a definition of optimal minimum noise descent trajectories are strategies extensively investigated by researchers to reduce the acoustic impact of helicopters on communities. Active control systems are particularly suitable for BVI alleviation, in that severe BVIs occur during low speed flight when more power is available to actuators, as compared to high speed forward flight. Approaches based on higher harmonic blade control have been investigated in detail, both numerically and experimentally in the past literature.[2–5] Specifically, the attention has focused mainly on two types of control systems: the individual blade control (IBC), for which each blade is controlled in the rotating frame through pitch links or flaps, and the so-called higher harmonic control (HHC), which acts on all the blades simultaneously by driving the non-rotating component of the swashplate. The benefits of HHC and IBC in reducing both vibrations and acoustic annoyance have been widely discussed, although some drawbacks emerged. Besides problems related to the increase of weight and complexity of the actuation devices, the way these controllers act for BVI noise reduction often corresponds to an increase in low-frequency noise content and in rotor vibration levels.[2,6] Furthermore, the actuators that are typically used for the conventional active control are characterized by limited frequency bandwidth and high vulnerability of the hydraulic systems. Active materials help to overcome most of these limitations, since they operate through the direct conversion from the electrical signal to the mechanical deformation of the material. This allows low-mass and high-bandwidth actuators thus increasing the ability to control the aeroelastic behavior of the individual blades for cancelling the unsteady high-frequency aerodynamic loads, which are the main cause of rotor noise and vibrations. Indeed, in recent years increasing attention to the application of the smart materials to rotorcraft systems has been paid by the research community.[7–12]

This paper presents an IBC controller relying on active twist rotor (ATR) actuation that is aimed at reducing high-frequency rotor noise aerodynamically generated by BVIs. It is an extended version of the work recently presented by the authors,[13] where the conceptual idea of this active twist BVI-controller has been introduced.

The proposed control strategy relies on high-frequency actuation to generate loads aimed at direct suppression/alleviation of those due to BVI. This approach is different from the more

commonly used ones that apply low-frequency (2 to 6/rev) actuators to alter key factors of BVI phenomena, such as miss-distance and blade-vortex interaction angle.[14] It operates in bounded time slots during blade rotation through small, localized blade torsional moments. This allows the system to evolve unaffected by the controller in the rest of the revolution. In this way, BVI phenomena (and related emitted noise) are altered where they occur, which minimizes the onset of negative by-products effects like, for instance, vibratory hub loads increase. The actuation is driven by a control law identified by an optimal, multi-cyclic control method based on main rotor aeroelastic/aeroacoustic numerical simulations. The control law is synthesized by using as control variables the blade torsional deformations, that are suited for suppressing high-frequency BVI loads. The corresponding ATR actuation torques are determined by the application of a simplified linear blade-torsion aeroelastic differential formulation. A high-frequency, BVI-effects alleviation approach is presented also by Modini et al.,[15] where the control law is determined through numerically efficient two-dimensional parallel-BVI simulations, although not accounting for influence of aeroelastic phenomena. Note that the technological feasibility of the proposed high-frequency controller is still an open issue, although much research is under development in this field.[6] Thus, the goal of this paper is to explore its potential performance, as well as to provide an efficient procedure for synthesis and application of control law.

In the following section, the theoretical formulations implemented in the simulation numerical tools applied for control synthesis and verification are briefly outlined. Section 3 provides a detailed description of the control methodology proposed, and finally Section 4 presents and discusses numerical applications aimed at assessing its capability to reduce BVI-induced blade loads and noise.

2. ROTOR BVI NOISE PREDICTION

The simulation of the acoustic disturbance generated by rotors in BVI conditions is a multidisciplinary task; accurate modelling of blade aeroelasticity and aerodynamics is required to yield the blade surface pressure distribution that, in turn, is the input to an aeroacoustic tool providing the radiated noise. Indeed, blade and wake deformations strongly affect BVI phenomena through the corresponding blade-wake miss distance. However, the prediction of the aeroelastic behavior is of paramount importance for the proposed controller, in that it is based on blades aeroelastic twist response to actuation torques.

The following sections provide a brief outline of the methodologies applied in this work to obtain BVI noise predictions used for synthesis and verification of the proposed controller (an extensive validation of them is available, for instance, in Gennaretti et al.[16] or Bernardini et al.[17]).

2.1. Rotor Aeroelastic Modeling

Aeroelastic responses are obtained by combining a blade structural dynamics model with aerodynamic loads given by a quasi-steady sectional formulation corrected with wake inflow.

Blade structural dynamics is described through a beam-like model. It derives from a nonlinear, bending-torsion formulation valid for slender, homogeneous, isotropic, nonuniform, and twisted blades, undergoing moderate displacements.[18] The radial displacement is eliminated from the set of equations by solving it in terms of local tension, and thus the resulting structural operator consists of a set of coupled nonlinear differential equations governing the bending of the elastic axis and the blade torsion.[19] If present, the effects of blade pre-cone angle, hinge offset, torque offset, and mass offset are included in the model.[20]

The aerodynamic loads are evaluated through the quasi-steady approximation of the Greenberg sectional theory.[21] Three-dimensional, unsteady effects deriving from the wake vorticity are taken into account through the influence of the corresponding wake inflow on the downwash at the blade cross sections. The evaluation of the wake inflow is obtained by the boundary element method (BEM) for the solution of a boundary integral equation approach, suited for the analysis of potential flows around helicopter rotors in arbitrary flight condition.[16]

Coupling blade structural dynamics with aerodynamic loads yields an aeroelastic integro-partial differential system of equations. These are spatially integrated through the Galerkin approach with the description of elastic axis deformation and cross-section torsion as linear combinations of shape functions satisfying the homogeneous boundary conditions. This yields a set of nonlinear, ordinary differential equations of the type

$$\mathbf{M}(t)\,\ddot{\mathbf{q}} + \mathbf{C}(t)\,\dot{\mathbf{q}} + \mathbf{K}(t)\,\mathbf{q} = \mathbf{f}_{str}^{nl}(t,\mathbf{q}) + \mathbf{f}_{aer}(t,\mathbf{q}) + \mathbf{m}(t); \quad (1)$$

where $\mathbf{q}$ denotes the vector of the Lagrangian coordinates, $\mathbf{M}$, $\mathbf{C}$, and $\mathbf{K}$ are time-periodic, mass, damping, and stiffness structural matrices that represent the linear structural terms, while $\mathbf{m}$ denotes the generalized torque moments driving the ATR actuation. Nonlinear structural contributions are collected in the forcing vector $\mathbf{f}_{str}^{nl}(t,\mathbf{q})$, whereas vector $\mathbf{f}_{aer}(t,\mathbf{q})$ collects the generalized aerodynamic forces. Since the aim here is to predict the aeroelastic periodic response during steady flight, the aeroelastic system in Eq. (1) is solved by using the harmonic balance approach.[20,22] It is a methodology suitable for the analysis of the asymptotic solution (as time goes to infinity) of differential equations forced by periodic terms, as in the present case. Because of the presence of nonlinear contributions deriving both from structural terms and from the free-wake aerodynamic loads prediction, the final system has to be solved using an iterative approach. To this aim, the Newton-Raphson procedure is applied. In the iterative loop, BEM boundary conditions and corresponding wake inflow are continuously updated accordingly to actual blade aeroelastic response.

2.1.1. Linearized Blade Torsion Dynamic Response

As mentioned in Section 1, in the control feedback process a simplified aeroelastic model is used to identify the ATR actuation torque moments, as those yielding (rapidly, but with a satisfactory degree of accuracy) the optimal blade torsion deformation indicated by the control law (see Section 3). Specifically, for the aeroelastic inverse problem used in the feedback process to determine the actuation torque moments, a reduced version of Eq. (1) describing only the linear torsion behavior is applied. The resulting simplified aeroelastic formulation for the torsional degrees of freedom, $\mathbf{q}_T$, reads:

$$\mathbf{M}_T(t)\,\ddot{\mathbf{q}}_T + \mathbf{C}_T(t)\,\dot{\mathbf{q}}_T + \mathbf{K}_T(t)\,\mathbf{q}_T = \mathbf{f}_{aer,T}(t) + \mathbf{m}(t); \quad (2)$$

where $\mathbf{M}_T$, $\mathbf{C}_T$, and $\mathbf{K}_T$ represent linear structural and aerodynamic contributions, and $\mathbf{f}_{aer,T}(t)$ denotes generalized aerodynamic torque moments independent on blade deformation.

2.2. Rotor Aerodynamic Solver

As already mentioned, the aerodynamic loads collected in $\mathbf{f}_{aer}$ and $\mathbf{f}_{aer,T}$ are obtained by the spanwise integration of loads from the Greenberg sectional theory.[21] In order to be able to predict BVI occurrence and corresponding aeroelastic effects, a three-dimensional, free-wake inflow correction is used. This wake inflow is evaluated by a boundary integral formulation for potential flows suited for the prediction of strong aerodynamic body-wake interaction phenomena,[16] which is also used to determine the blades pressure distribution to be applied for the prediction of BVI acoustic effects radiation (see Section 2.3).

Considering a potential velocity field such that the velocity is given by $\mathbf{v} = \nabla\varphi$, this formulation assumes the potential field, φ, to be given by the superposition of an incident field, φ_I, and a scattered field, φ_S (i.e., $\varphi = \varphi_I + \varphi_S$). The scattered potential is generated by sources and doublets over the surfaces of the blades, S_B, and by doublets over the wake portion that is very close to the trailing edge from which it is emanated (near wake, S_W^N). The incident potential is due to doublets distributed over the complementary wake region that compose the far wake S_W^F.[16] The wake surface partition is such that the far wake is the only wake portion that may come in contact with blades and generate BVI effects. The incident potential is discontinuous across S_W^F, whereas the scattered potential is discontinuous across S_W^N and is represented by[16]

$$\varphi_S(\mathbf{x},t) = \int_{S_B}\left[G\left(v_n - u_n\right) - \varphi_S\frac{\partial G}{\partial n}\right]\mathrm{d}S(\mathbf{y}) - \int_{S_W^N}\Delta\varphi_S\,\frac{\partial G}{\partial n}\,\mathrm{d}S(\mathbf{y}); \quad (3)$$

where $G = -1/4\pi\, r$ is the unit-source solution of the three-dimensional Laplace equation, with $r = \|\mathbf{y} - \mathbf{x}\|$, while $\Delta\varphi_S$ is the potential jump across the wake surface, known from past history of potential discontinuity at the blade trailing edge through the Kutta-Joukowski condition.[23] In addition, $v_n = \mathbf{v}_B \cdot \mathbf{n}$, with $\mathbf{v}_B$ representing the blade velocity (with inclusion of aeroelastic deformation effects), and $\mathbf{n}$ being its outward unit normal, whereas $u_n = \mathbf{u}_I \cdot \mathbf{n}$, with $\mathbf{u}_I$ denoting the velocity induced by the far wake.

Considering the far wake discretized into M panels, assuming the potential jump to be constant over each panel, and recalling the equivalence between surface distribution of doublets and vortices, the incident velocity field is evaluated through the Biot-Savart law applied to the vortices that have the shape of the panel contours. In order to assure a regular distribution of the induced velocity within the vortex core, and thus a stable and regular solution even in blade-vortex impact conditions, a Rankine finite-thickness vortex model is introduced in the Biot-Savart law.[16] The wake-induced velocity field is applied to evaluate the term u_n in Eq. (3) (and the wake inflow correction for the sectional loads theory), as well as the velocity field from which the wake shape evolution is determined in a free-wake analysis. Note that for an accurate prediction of BVI phenomena, the accurate evaluation of the wake distorted shape is essential, meaning that a crucial role is played by the relative positions between the body and the wake.

In this formulation, the incident potential affects the scattered potential through the induced-velocity, while the scattered potential affects the incident potential by its trailing-edge discontinuity that is convected along the wake and yields the intensity of the vortices of the far wake.[16] Once the potential field is known, the Bernoulli theorem yields the pressure distribution to be provided to the aeroacoustic solver.[24]

2.3. Rotor Noise Radiation

In the aeroacoustic simulation presented here, the noise radiated by rotor blades is evaluated through solution of the well-known Ffowcs Williams and Hawkings (FW-H) equation,[25] which governs the propagation of acoustic disturbances generated aerodynamically by moving bodies.

The boundary integral formulation developed by Farassat known as Formulation 1A[26,27] is a widely-used and computationally efficient way to determine the acoustic field as solution of the FW-H equation, and is particularly suited for the problems examined in this paper. When the velocity of the rotor blades is far from the transonic/supersonic range, it yields the aeroacoustic field as a superposition of a term, p'_T, depending on blade geometry and kinematics (thickness noise), and of a term, p'_L, which is related to the blade airloads (loading noise). These two noise contributions are given by the following integrals evaluated over the actual blade surface, S_B.[26,27]

$$4\pi p'_T(\mathbf{x},t) = \int_{S_B}\left[\frac{\rho_0\dot{v}_n}{r|1-M_r|^2}\right]_\tau \mathrm{d}S(\mathbf{y}) + \int_{S_B}\left[\frac{\rho_0 v_n\left(r\dot{\mathbf{M}}\cdot\hat{\mathbf{r}} + c_0M_r - c_0M^2\right)}{r^2|1-M_r|^3}\right]_\tau \mathrm{d}S(\mathbf{y}); \quad (4)$$

$$4\pi p'_L(\mathbf{x},t) = \frac{1}{c_0}\int_{S_B}\left[\frac{\dot{\tilde{p}}\,\mathbf{n}\cdot\hat{\mathbf{r}} + \tilde{p}\,\dot{\mathbf{n}}\cdot\hat{\mathbf{r}}}{r|1-M_r|^2}\right]_\tau \mathrm{d}S(\mathbf{y}) + \int_{S_B}\left[\frac{\tilde{p}\,\mathbf{n}\cdot\hat{\mathbf{r}} - \tilde{p}\,\mathbf{M}\cdot\mathbf{n}}{r^2|1-M_r|^2}\right]_\tau \mathrm{d}S(\mathbf{y}) + \frac{1}{c_0}\int_{S_B}\left[\frac{\tilde{p}\,\mathbf{n}\cdot\hat{\mathbf{r}}}{r^2|1-M_r|^3}\left(r\dot{\mathbf{M}}\cdot\hat{\mathbf{r}} + c_0M_r - c_0M^2\right)\right]_\tau \mathrm{d}S(\mathbf{y}); \quad (5)$$

where c_0 and ρ_0 are, respectively, the speed of sound and the density in the undisturbed medium, whereas $\tilde{p} = (p - p_0)$, with p_0 representing the undisturbed medium pressure, $\mathbf{M} = \mathbf{v}_B/c_0$, $M = \|\mathbf{M}\|$, and $M_r = \mathbf{M}\cdot\hat{\mathbf{r}}$ with $\hat{\mathbf{r}} = \mathbf{r}/\|\mathbf{r}\|$. In addition, $\dot{\mathbf{n}}$ and $\dot{\mathbf{M}}$ denote time derivatives, respectively, of the outward blade surface unit normal vector and of the local blade velocity Mach vector, as observed in a frame of reference fixed with the undisturbed medium, whereas the notation $[...]_\tau$ indicates that these quantities must be evaluated at the emission time, τ, i.e., the time at which the signal arriving in $\mathbf{x}$ at time t started from $\mathbf{y} \in S_B$.[26,27]

In problems dealing with weakly loaded rotors, the thickness and loading noise are comparable. However, when strongly loaded rotors are examined, the thickness noise contribution tends to be negligible and the acoustic disturbance is dominated by the loading noise. Rotors in BVI conditions fall within this category of acoustic phenomena.

3. CONTROL PROCEDURE FOR BVI NOISE ALLEVIATION

In this section, the optimal control method adopted to identify an ATR control law aimed at reducing BVI noise generated by helicopter main rotors is described.

3.1. Definition of the Control Approach

As already pointed out, the proposed controller relies on higher harmonic blade twist deformations to reduce rotor BVI noise as much as possible. Blade torsion deformations suited for noise alleviation are determined by a closed-loop, multicyclic, and optimal control algorithm, in which the corresponding actuation torques to be applied to the blades are provided by a simplified inverse, aeroelastic problem (see Fig.(1) for a scheme of the controller action).

Prior to control law synthesis, preliminary considerations are useful to identify suitable sets of control (input) variables, $\mathbf{u}$, and of (output) variables, $\mathbf{z}$, to be monitored and controlled. Within helicopter configurations in descent flight, several interactions between blades and wake vortices occur in specific regions of both advancing and retreating sides of the rotor disk.[1] For the work presented here, the control action is focused within a time interval during the retreating blade motion defined through the application of the Hann window, and specific harmonics of the blade torsion deformation in that windowed period are chosen as control variables, $\mathbf{u}$. Furthermore, the output variables, $\mathbf{z}$, which are considered in the controller, are noise harmonics decibels predicted at a microphone suitably located. Specifically, the microphone is positioned at the rear edge of the left skid of the helicopter, which is just below the retreating side region of the disk rotor affected by strong BVI, where the controller is actuated. Akin to the approach followed in a previous work on this subject,[2] the noise harmonics considered in the output vector, $\mathbf{z}$, are those between the 6^{th} and the 17^{th} blade passage frequency that represent the BVI contribution to the noise. Note that, differently to the present analysis, in Patt et al.2 the feedback microphone is located on the right skid, since controller action is mainly focused on advancing side BVI.

3.2. Optimal Control Algorithm

Following an approach already used in the past by several authors[2,28,29] that have dealt with the problem of helicopter noise and/or vibration control, the identification of the control law is achieved through a multi-cyclic optimal procedure that consists of minimizing the cost function, $J = \mathbf{z}^{\mathrm{T}}\,\mathbf{W}_z\,\mathbf{z} + \mathbf{u}^{\mathrm{T}}\,\mathbf{W}_u\,\mathbf{u}$, where $\mathbf{W}_z$ and $\mathbf{W}_u$ are weighting matrices defined to get the best compromise between high control effectiveness and low control effort. Because of the inherently time-periodic nature of the problem, in this control approach $\mathbf{u}$ and $\mathbf{z}$ collect sine and cosine harmonic components of variables, thus disregarding transient evolution effects.

Akin to the standard optimal LQR control method (of which the present approach may be interpreted as the natural extension for application to steady-periodic systems), the minimization of the cost function is obtained under the constraint of satisfying the governing equation of the controlled system. The constraint is given by a simplified linear relationship between control variables and system response, $\mathbf{z}_n = \mathbf{z}_{n-1} + \mathbf{T}_{n-1}\,(\mathbf{u}_n - \mathbf{u}_{n-1})$, where $\mathbf{T}_{n-1}$ is the (gradient) transfer matrix for $\mathbf{u} = \mathbf{u}_{n-1}$, which provides the system response perturbation corresponding to a control input perturbation. It describes the aerodynamic/aeroacoustic behavior of the rotor system, and may be obtained by a set of suited numerical simulations. Then, combining the cost function with the constraint equation and minimizing the resulting cost function yield the following optimal control input:

$$\mathbf{u}_n = \mathbf{G}_u\,\mathbf{u}_{n-1} - \mathbf{G}_z\,\mathbf{z}_{n-1}; \tag{6}$$

where the gain matrices are given by $\mathbf{G}_u = \mathbf{D}\,\mathbf{T}_{n-1}^{\mathrm{T}}\,\mathbf{W}_z\mathbf{T}_{n-1}$ and $\mathbf{G}_z = \mathbf{D}\,\mathbf{T}_{n-1}^{\mathrm{T}}\,\mathbf{W}_z$, with $\mathbf{D} = (\mathbf{T}_{n-1}^{\mathrm{T}}\mathbf{W}_z\mathbf{T}_{n-1} + \mathbf{W}_u)^{-1}$.

Equation (6) has to be used in a recursive way: starting from a given control input and corresponding output, the law of the optimal controller is updated until convergence. This provides a closed-loop controller applicable both in a validation process based on simulations given by the complete aerodynamic/aeroelastic/aeroacoustic model and in real helicopter configurations.

3.3. Efficient ATR Control Synthesis

A drawback in using this local controller lies in the significant computational cost of the gradient matrix evaluation that, in principle, is required at each step of the iterative control process about different values of the control variables (it is worth recalling that, evaluating the gradient matrix means determining sensitivities of the noise emitted with respect to each twist deformation harmonic considered in the control actuation).

To obtain an efficient determination of the matrix $\mathbf{T}_n$, the following procedure is applied: (i) starting from undeformed rotor blades, a set of output vectors, $\mathbf{z}$, is evaluated as open-loop responses to a set of small blade twist deformations (input vector, $\mathbf{u}$); (ii) from this database, a least squares polynomial approximation of the functions relating each output variable to each input variable is determined; (iii) at each step of the iterative control process, each element of the gradient matrix, $T_{ij} = \partial z_i/\partial u_j$, is analytically derived from the identified polynomial forms. Thanks to the least squares approximation applied, the application of the optimal local controller is as fast as that of a global controller (i.e., considering a constant gradient matrix), in that it avoids the numerical evaluation of the gradient matrix at each step of the control process. The final step of the identification of the ATR controller consists of determining the torque moments to be applied to the blade, to get the twist deformations required by the optimal control algorithm. For the sake of numerical efficiency (and feasibility of real-time controller), these are derived from the simplified aeroelastic model presented in Eq. (2). Indeed, for a steady-periodic rotor response, expressing the system matrices, the twist Lagrangian coordinates, and the forcing vector in terms of their Fourier coefficients, and then applying a harmonic-balance approach, it yields an algebraic relation between harmonics of the forcing terms (actuation torque moments, in particular) and the harmonics of the twist variables. Thus, letting the harmonics of the twist variables coincide with the elements of the control variables vector, $\mathbf{u}$, from the Fourier representation of Eq. (2) it is possible to derive the harmonic components of the actuation torque moments. This completes the control feedback that, starting from noise measurements at the rear edge of the left skid provides the ATR actuation moments, as synthetically described in the scheme of Fig. (1), where steps of the control process, as well as data exchanged among them, are illustrated.

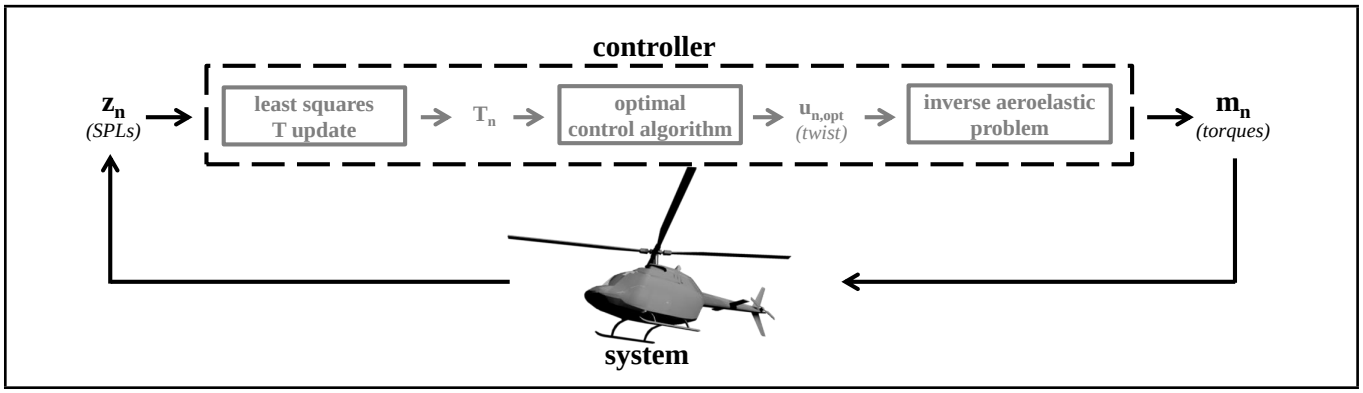

Figure 1. Controller block diagram.

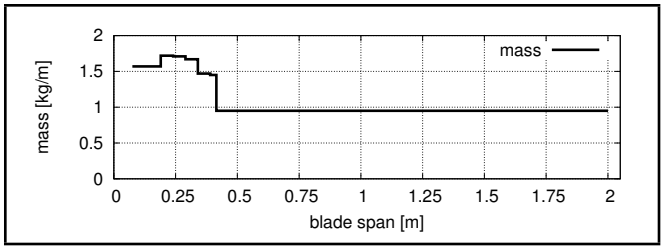

Figure 2. Blade mass distribution.

mode	frequency [Hz]
lag	13.54
flap	20.80
torsion	89.15

Table 1. Blade flap, lag and torsional first natural frequencies of vibration.

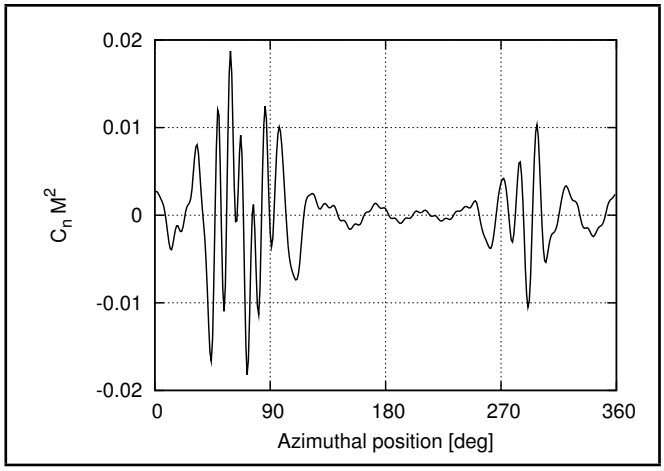

Figure 3. Time history of C_nM^2 high-frequency content ($\geq$ 7/rev), at $r/R = 0.87$.

4. NUMERICAL RESULTS

For validation purposes, the noise control methodology proposed has been applied to a fully hingeless model rotor with a radius $R = 2$ m, that has four blades of constant chord $c = 0.121$ m, a linear twist angle of $-8°$, NACA 23012 section profiles, and a rotational speed $\Omega = 190.12$ rad/s. Blade mass distribution is given in Fig. (2) and blade structural properties are reported in Table 1 in terms of natural frequencies of vibration. The operating condition examined is typically affected by strong BVI events, and consists of a $6°$ descent flight at advance ratio $\mu = 0.15$, with shaft angle $\alpha_S = -5.4°$ (i.e., tilted backwards). The rotor is trimmed with constraints of providing 3300N thrust and null in-plane moments. Free-wake aerodynamic calculations are performed discretizing each blade surface through 15 (upper and lower) chordwise panels and 18 spanwise panels, using 180 azimuth discretization steps, and a 2-spiral wake length.

In the following paragraphs, preliminary studies of the baseline (uncontrolled) case are shown, which allow characterization of the blade's operating conditions and the identification of suited control variables. Then, results concerning two numerical applications of the closed-loop noise control approach are presented, which differ in the aeroelastic tool that provides the rotor feedback to the controller: in the first one, the rotor blades are assumed to have bending stiffness tending to infinity (rigid bending), whereas in the second case the complete, and more realistic, aeroelastic modeling of the rotor blades is considered. From these results, it is possible to assess the effectiveness of the control methodology that was investigated, as well as to estimate the influence of the approximations introduced in the blade aeroelastic modeling applied for control synthesis.

4.1. Preliminary Analysis

Here, investigations aimed at identifying sets of variables $\mathbf{u}$ and $\mathbf{z}$ that are suitable for the control process are presented. Since the purpose of this work is the assessment of the ATR ability to alleviate BVI noise through control of blades high-frequency aeroelastic behavior, an analysis of the blade sectional loads is useful to derive guidelines for the definition of the most appropriate actuation process. In this regard, Fig. (3) presents the time history of the high-frequency content of the C_nM^2 coefficient at the cross section located at $r = 0.87R$ (the frequency content $\geq$ 7/rev has been selected, in that it is strongly affected by BVI events). The figure shows two different blade-vortex interaction occurrences: the most severe in the advancing region, the other appearing in the retreating side.

Hereafter, the ATR control application is focused on the alleviation of the retreating side BVI occurrence. Indeed, it generates effects that are clearly bounded with respect to those due to advancing BVI, and thus provides a well-suited test case for proposed control verification.

The Hann windowing function is applied to the high-frequency content of Fig. 3, in order to highlight the retreating side BVI effects. Figure 4(a) depicts the signal extracted in the azimuth range $\Psi_{ret} = [260°, 320°]$, while Fig. (4(b)) shows the corresponding spectrum related to the windowing period considered, which demonstrates that the dominant BVI

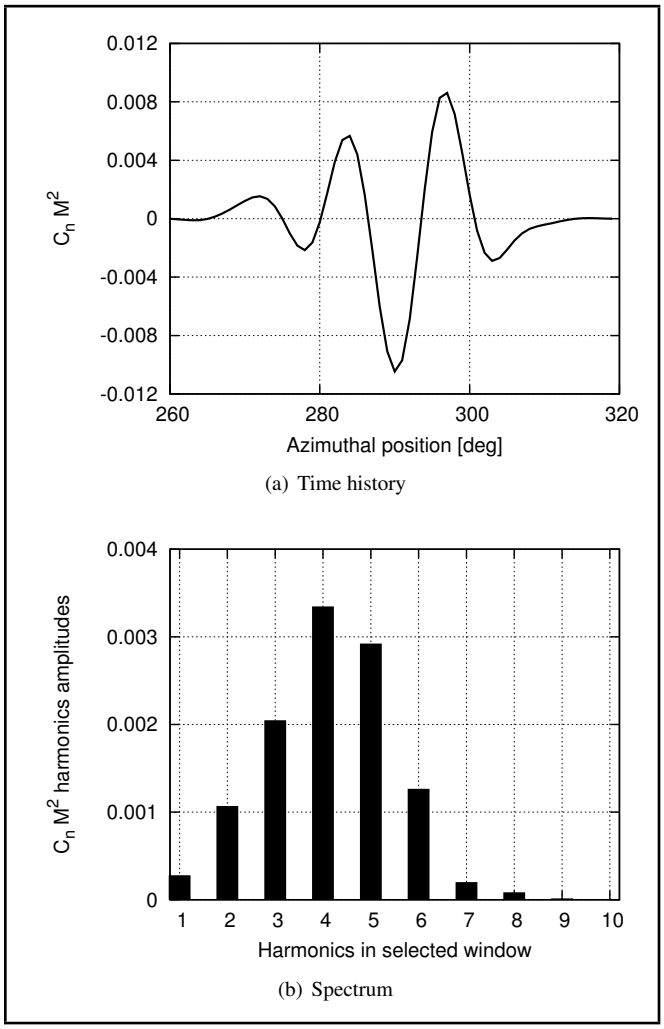

Figure 4. Windowed $C_n M^2$ high-frequency content.

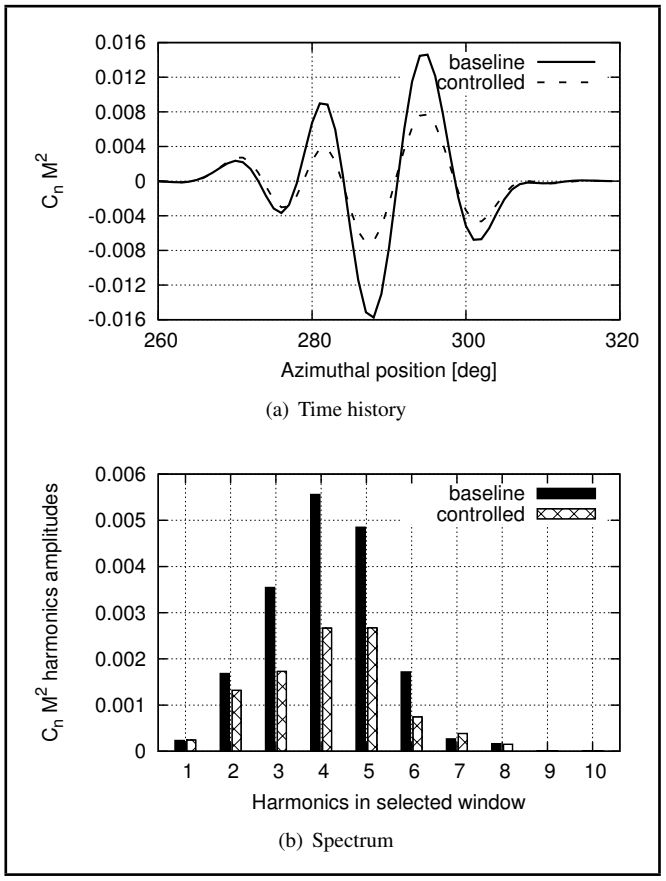

Figure 5. $C_n M^2$ high-frequency, windowed signal from only-torsion aeroelastic model.

signal harmonics are the 4^{th} and 5^{th} ones (i.e., the 24/rev and the 30/rev, respectively). Considering these results, the sine and cosine components of the 4^{th} and 5^{th} harmonics in $\psi \in \Psi_{ret}$ of the first two blade torsional Lagrangian degrees of freedom, ϕ^I, ϕ^{II}, are assumed as control inputs, $\mathbf{u}$. As mentioned above, the ATR actuation is related to these control inputs through the linearized aeroelastic system in Eq. (2), which yields the torque moment to be applied to the blade in order to get the twist deformations indicated by the optimal control algorithm. In this work, ATR actuation consists of two concentrated torques located at $r_1 = 0.75R$ and $r_2 = 0.90R$, through which it is possible to control the first two blade torsional modes (indeed, their nodes are far from torque locations).

Further, SPLs of the noise signature evaluated/measured at the rear edge of the left skid of the helicopter have been selected as output variables.. Specifically, these are the SPLs of the noise harmonics between the 6^{th} and 17^{th} blade passage frequency, which are strongly affected by BVI; the position of the monitoring microphone has been chosen to be approximately underneath the retreating side of the rotor disk where the controller is actuated.

4.2. Noise Control of Only-Torsion Blades Rotor

First, the closed-loop control is applied to alleviate the noise emitted by the rotor assumed to be composed of blades undergoing only-torsion deformations (i.e., governed by Eq. (2), like for the evaluation of the actuation torque moments). The results from this control application provide highlights on the nominal performance of the controller synthesized, while the effect of a more realistic rotor aeroelastic response to the ATR actuation will be discussed later.

Figure 5 shows an uncontrolled (baseline) and controlled high-frequency content ($>$ 7/rev) of coefficient $C_n M^2$ evaluated at the blade cross section $r = 0.87R$. Time history and spectrum regard the selected azimuth window, Ψ_{ret}, and the controlled signal is that obtained when the control algorithm convergence is reached. This figure demonstrates that a significant reduction of BVI-induced loads is achieved. The corresponding actuated control variables are given in Table 2 in terms of their sine and cosine components. Further, Fig. (6) depicts the effects of control action on blade tip torsion, showing a maximum peak-to-peak difference between controlled and uncontrolled responses of 0.6°, and negligible transient oscillations due to actuation windowing.

Regarding the acoustic effects of control action, the noise emitted on a horizontal plane located 2.3 m below the rotor hub is examined similarly to the analysis presented by Patt et al.[2] Figure 7 shows the noise contour plots predicted from baseline and controlled configurations. The two plots concern the so-called BVISPL, which is evaluated as the Overall Sound Pressure Level (OASPL), but is limited to the noise spectrum between the 6^{th} and the 40^{th} blade passage frequency (i.e., those most affected by BVI events). These figures demonstrate the evident effectiveness of the controller in alleviating the noise generated by the retreating-side BVI occurrence, particularly in the region behind the rotorcraft.

Table 2. Control variables from only-torsion aeroelastic simulation.

variables	ϕ^I_{4C}	ϕ^I_{4S}	ϕ^{II}_{4C}	ϕ^{II}_{4S}	ϕ^I_{5C}	ϕ^I_{5S}	ϕ^{II}_{5C}	ϕ^{II}_{5S}
values [deg]	-0.229	+0.001	+0.024	+0.035	+0.144	-0.048	+0.042	-0.002

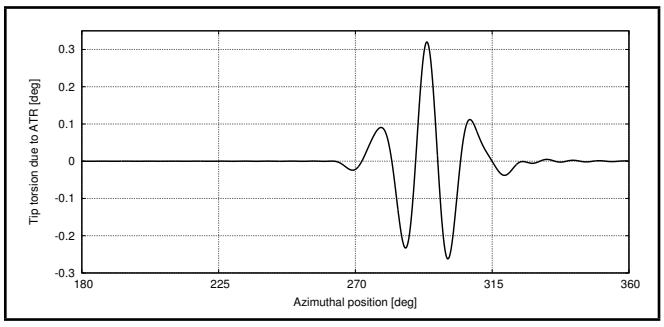

Figure 6. Difference between controlled and uncontrolled blade tip torsion.

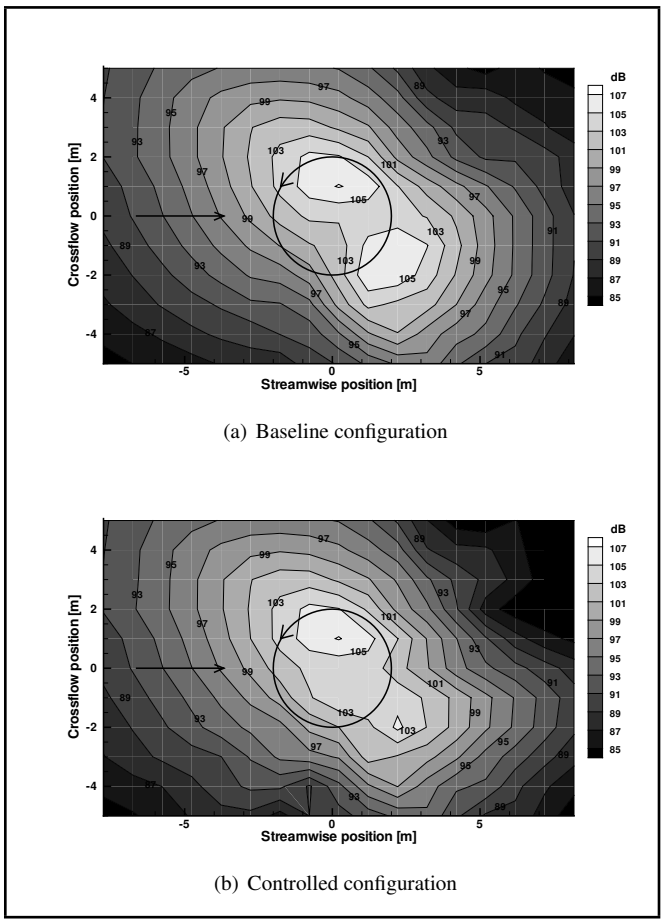

(a) Baseline configuration

(b) Controlled configuration

Figure 7. BVISPL contour plot predicted by only-torsion aeroelastic rotor simulation.

The differences between controlled and uncontrolled noise are presented in Fig. 8(a), where it is evident the presence of a quite large region of noise reduction in the rotor rear side (up to -7dB), whereas noise increase (up to 2.5dB) appears in a limited area close to the rotor retreating side.

Further, Fig. 8(b) shows the difference between controlled and uncontrolled noise in terms of the OASPL, i.e., including also the low-frequency harmonics. In this case, controller effects are smoother than those observed in Fig. 8(a). The noise is generally alleviated with a maximum reduction of about 2dB, while the peak of noise increment (limited to a small region) is equal to 1dB.

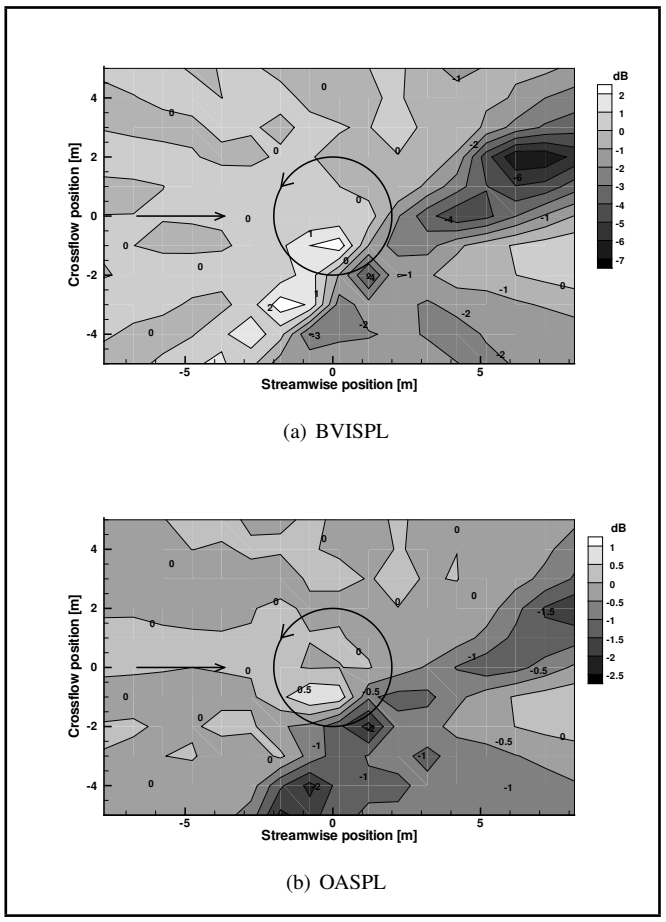

(a) BVISPL

(b) OASPL

Figure 8. Effect of controller on (a) BVISPL and (b) OASPL predicted by only-torsion model.

The effects of the proposed control law on the emitted noise can be considered to be satisfactory by producing reductions of noise levels in most of the examined region. They present a remarkable directivity. Further, it is worth noting that the corresponding aeroelastic response has demonstrated no influence of control actuation on vibratory hub loads transmitted to the airframe, which confirms the advantage of high-frequency controllers in terms of drawbacks onset.

4.3. Noise Control with Complete Rotor Aeroelastic Response

Now, the noise control procedure is applied to a rotor simulated by a complete nonlinear, bending-torsional aeroelastic formulation (see Section 2.1). Unlike the analysis discussed in the section above, here the aeroelastic tool yields a response that may significantly differ from the one that was predicted by the transfer matrix, $\mathbf{T}$, which was used in the controller synthesis. Hence, the following results are a test of proposed control robustness, namely, an assessment of its capability in providing good performance when applied to a system more complex than that used for its synthesis.

Figure 9 shows the high-frequency content of the $C_n M^2$ coefficient for the same blade section and azimuth windowing considered in Section 4.2. Similarly, the controlled signal is

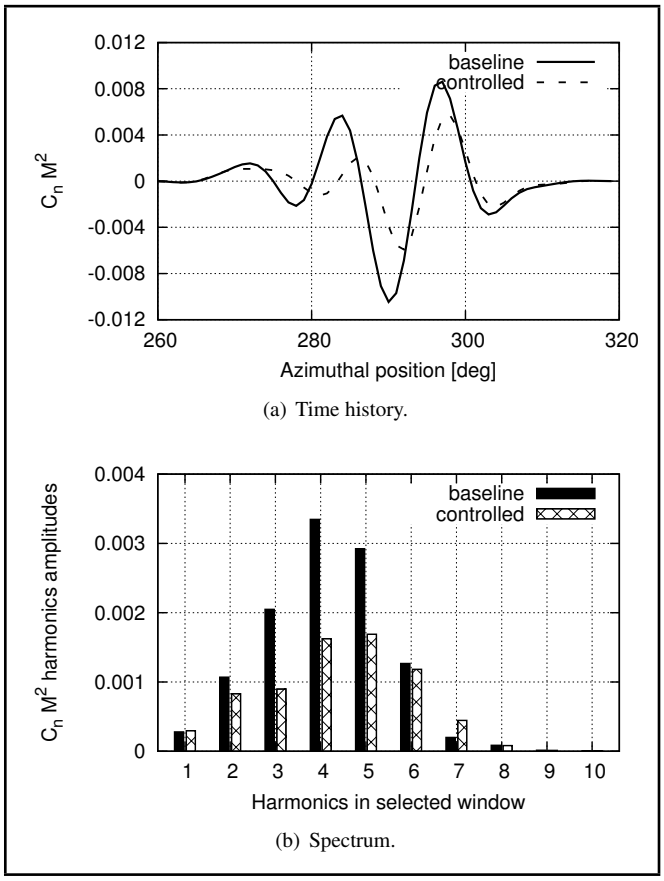

(a) Time history.

(b) Spectrum.

Figure 9. $C_n M^2$ high-frequency, windowed signal from complete aeroelastic model.

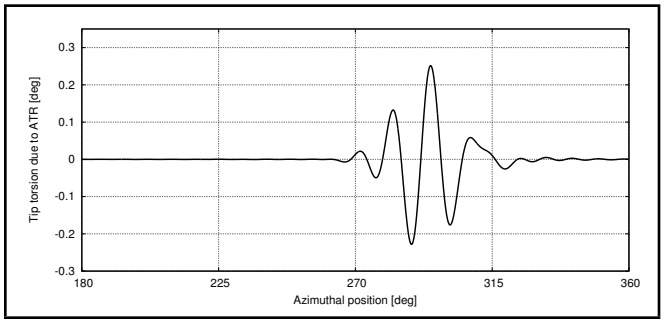

Figure 10. Difference between controlled and uncontrolled tip torsion.

provided at the final step of the iterative control procedure. Then, Fig. 9(b) shows that, for the 4^{th} and 5^{th} windowed load harmonics, alleviations similar to those obtained by the only-torsion aeroelastic model are achieved, although the rest of the harmonics examined are subjected to a smaller reduction. Nonetheless, the overall control effect is still very satisfactory.

In Table 3, the values of the corresponding control variables are given. In this case, the combination of these coefficients gives a maximum peak-to-peak blade tip twist of $0.45°$, showing that good results can also be reached with a smaller control effort. The difference between controlled and uncontrolled blade tip torsion responses is presented in Fig. 10, which shows that also in this case, transient effests due to actuation windowing are negligible.

Next, the effect of the controller on noise alleviation is analyzed in terms of BVISPL contour plots, on the same plane considered in Section 4.2. Figures 11(a) and 11(b) show, re-

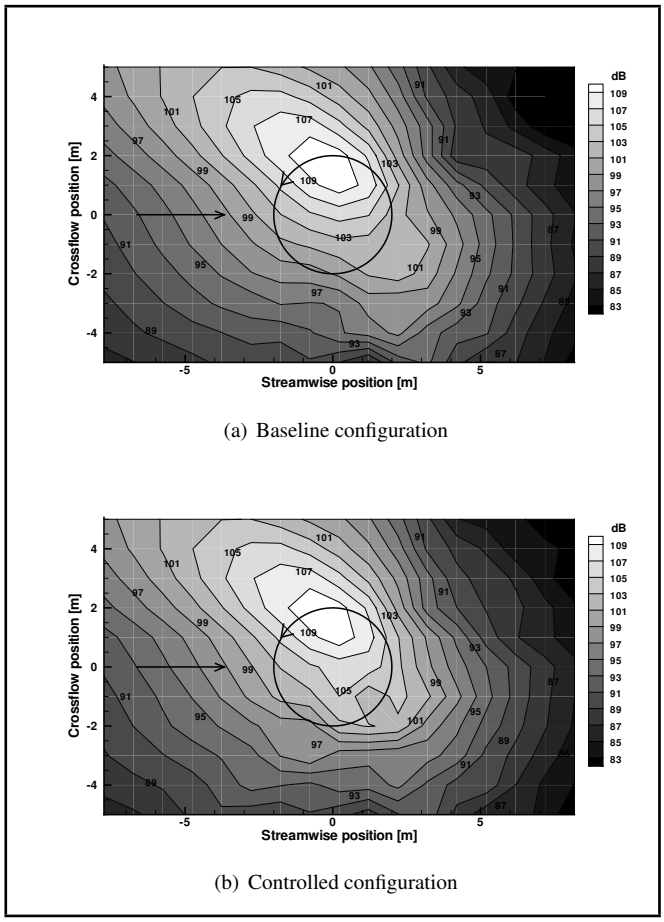

(a) Baseline configuration

(b) Controlled configuration

Figure 11. BVISPL contour plot predicted by complete aeroelastic rotor simulation.

spectively, the acoustic disturbance from uncontrolled and controlled rotor configurations. Compared to the results achieved by the only-torsion aeroelastic model, these figures reveal a lower influence of the controller on the emitted sound, both in terms of noise peaks and directivity modification. This appears more clearly in Fig. 12(a), which highlights the differences between the BVISPL distribution emitted by controlled and uncontrolled configurations. In this case, the maximum reduction of the BVISPL is about 2.7dB, whereas the BVISPL increase is greater than the one from the only-torsion model, which reached 3dB in a limited portion of the observed region. Further, Fig. 12(b) shows the control effectiveness in terms of differences between the OASPL distributions. This plot reveals that the inclusion of low-frequency acoustics tends to reduce peaks and the extent of the region where noise is increased; in this case, peaks of both augmented and alleviated noise are close to about 1.5dB. In terms of vibration levels, also in this case, no differences have been found between the baseline and controlled configurations, which confirms the results obtained for the only-torsion blades rotor.

The outcomes presented in this section show that the efficiency of the control process proposed decreases when noise simulation is based on the complete rotor aeroelastic behavior. Despite this, blade loads are still considerably alleviated, and a wide area in the vicinity of the rotor disk presents a satisfactory reduction in noise levels.

Finally, note that the computational cost required for implementing the control process (see dashed rectangle of Fig. (1) is less than a tenth of a second for each iterative step, by using a single 1.7GHz AMD core. Observing that in real applica-

Table 3. Control variables from complete aeroelastic simulation.

variables	ϕ^{I}_{4C}	ϕ^{I}_{4S}	ϕ^{II}_{4C}	ϕ^{II}_{4S}	ϕ^{I}_{5C}	ϕ^{I}_{5S}	ϕ^{II}_{5C}	ϕ^{II}_{5S}
values [deg]	-0.092	-0.019	-0.047	+0.068	+0.040	+0.002	+0.018	+0.008

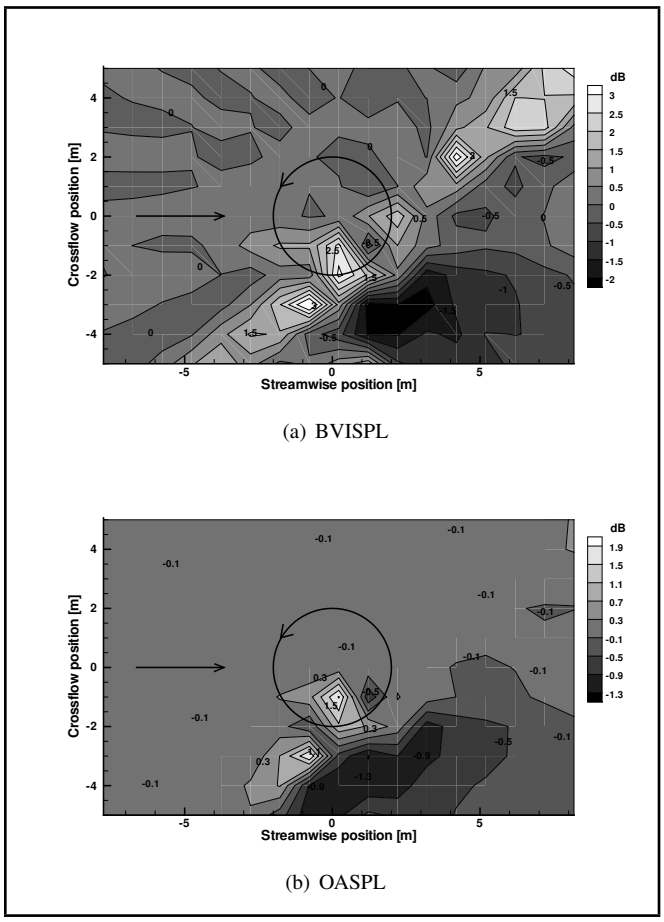

Figure 12. Effect of controller on (a) BVISPL and (b) OASPL predicted by complete model.

tions, several rotor revolutions would be taken by rotor systems to reach steady state condition after each step of the iterative control actuation process, and that real scale helicopter rotor revolution periods are significantly longer than that of the examined model, this means that the real time applications of the proposed controller are potentially feasible.

5. CONCLUSIONS

An efficient procedure based on an optimal, multi-cyclic, control algorithm has been proposed and applied for the synthesis of an ATR control law aimed at reducing helicopter rotor BVI noise. Rotor blades have been actuated through localized torque moments in order to drive their twist motion in specific intervals of the blade azimuth location, where the strongest interactions between blades and wake vortices occur. To ensure numerical efficiency and feasibility of a real-time controller, a simplified aeroelastic operator has been applied in the closed-loop actuation process, and the least squares approximation method for identification of the input-output gradient matrix of the local controller has been applied. The main outcomes of the numerical investigation performed are: (1) a preliminary analysis has shown the high-frequency nature of the aerodynamic loads occurring in presence of BVI, thus confirming the need for high-bandwidth actuators (like those relying on smart materials) for providing a direct action to alleviate them; (2) two different closed-loop control actuations have been performed: first, evaluating the rotor aeroelastic response through the simplified only-torsion model, then introducing the complete aeroelastic solver (controlled maximum peak-to-peak blade tip twist of $0.6°$ and $0.45°$ have been obtained, respectively); (3) for both closed-loop control applications, significant reductions of the higher-harmonic loads, as well as noise decrease (up to 7dB for the only-torsion response and 2.7dB for the complete aeroelastic response) in some areas of the acoustic field examined have been obtained; in both cases, increase of the controlled acoustic disturbance ears in a small area located below the rotor retreating side (more than 3dB in the worst case); (4) more relevant BVI noise reductions and directivity pattern changes have been obtained when the simplified response feedback is used; when the complete aeroelastic formulation is used, the increase of the acoustic disturbance below the retreating rotor side becomes higher; (5) both positive and negative effects of the controller on the acoustic field appear mitigated (more than halved) if it is examined in terms of the OASPL, rather than in terms of the high-frequency acoustic content (BVISPL); (6) vibratory levels are observed to be unaffected by control actuation, confirming the advantage of high-frequency controllers in terms of drawbacks onset. (7) the proposed controller is potentially feasible for real-time applications. The findings mentioned above have proven the potentiality of the proposed approach for alleviation of the unsteady aerodynamic loads due to BVIs occurrence, and provide an assessment of its capability in reducing the corresponding emitted noise. They confirm the attractiveness of smart materials for rotorcraft control applications, where low-mass and high-bandwidth actuators are of strong interest. Finally, future development of the proposed control methodology will include its application in reducing advancing side BVI effects, implementing an adaptive control procedure for the high-performance gradient matrix update, and enhancement of control-low synthesis process through application of more efficient blade aeroelastic solvers based on semi-analytic formulations.

REFERENCES

[1] Yu, Y. Rotor Blade-Vortex Interaction Noise. *Progress in Aerospace Sciences*, **36**(2), 97–115, February (2000). http://dx.doi.org/10.1016/S0376-0421(99)00012-3.

[2] Patt, D., Liu, L., and Friedmann, P. P. Simultaneous Vibration and Noise Reduction in Rotorcraft Using Aeroelastic Simulation. *Journal of the American Helicopter Society*, **51**(2), 127–140, (2006). http://dx.doi.org/10.4050/JAHS.51.127.

[3] Yu, Y., Gmelin, B., Splettstoesser, W., Philippe, J., Prieur, J., and Brooks, T. Reduction of Helicopter Blade-Vortex Interaction Noise by Active Rotor Control Technology. *Progress in Aerospace Sciences*, **33**(9-10), 647–687, (1997).

[4] JanakiRam, R. D., Sim, B. W., Kitaplioglu, C., and Straub, F. K. Blade-Vortex Interaction Noise Characteristics of a Full-Scale Active Flap Rotor. *Proc. American Helicopter Society 65th Annual Forum*. Grapevine, Texas, (2009).

[5] Chia, M. H., Padthe, A. K., and Friedmann, P. P. A Parametric Study of On-Blade Control Device Performance for Helicopter Vibration and Noise Reduction. *Proc. 70th Annual Forum of the American Helicopter Society*. Montreal, Quebec, Canada, (2014).

[6] Chen, P. C., Baeder, J. D., Evans, R. a. D., and Niemczuk, J. Blade-Vortex Interaction Noise Reduction with Active Twist Smart Rotor Technology. *Smart Materials and Structures*, **10**(1), 77–85, February (2001). http://dx.doi.org/10.1088/0964-1726/10/1/307.

[7] Chopra, I. Status of Application of Smart Structures Technology to Rotorcraft Systems. *Journal of the American Helicopter Society*, **45**(4), 228–252, (2000). http://dx.doi.org/10.4050/JAHS.45.228.

[8] Chopra, I. Review of State of Art of Smart Structures and Integrated Systems. *AIAA Journal*, **40**, 2145–2187, (2002). http://dx.doi.org/10.2514/2.1561.

[9] Riemenschneider, J. and Keye, S. Overview of the Common DLR/ONERA Project Active Twist Blade (ATB). *Proc. 30th European Rotorcraft Forum*, , (2004).

[10] Thakkar, D. and Ganguli, R. Active Twist Control of Smart Helicopter Rotor - A Survey. *Journal of Aerospace Sciences and Technologies*, , (2005).

[11] Monner, H., Riemenschneider, J., Opitz, S., and Schulz, M. Development of Active Twist Rotors at the German Aerospace Center (DLR). *Proc. 52nd AIAA/ASME/ASCE/AHS/ASC Structures, Structural Dynamics and Materials Conference*, number April, pages 1–10, (2011).

[12] Brillante, C., Morandini, M., and Mantegazza, P. H2 Periodic Control on Active Twist Rotor for Vibration Reduction. *Proc. 70th Annual Forum of the American Helicopter Society*. Montreal, Quebec, Canada, (2014).

[13] Anobile, A., Bernardini, G., and Gennaretti, M. Active Twist Rotor Controller Identification for Blade-Vortex Interaction Noise Alleviation. *Proc. 19th AIAA/CEAS Aeroacoustics Conference*. Berlin, Germany, May (2013). http://dx.doi.org/10.2514/6.2013-2290.

[14] Anobile, A., Bernardini, G., Testa, C., and Gennaretti, M. Synthesis of Rotor BVI Noise Active Controller Through Efficient Aerodynamics/Aeroacoustics Solver. *Proc. 20th AIAA/CEAS Aeroacoustics Conference*. Atlanta, USA, (2014).

[15] Modini, S., Graziani, G., Bernardini, G., and Gennaretti, M. Parallel Blade-Vortex Interaction Analyses and Rotor Noise Control Synthesis. *Proc. 19th AIAA/CEAS Aeroacoustics Conference*. Berlin, Germany, (2013).

[16] Gennaretti, M. and Bernardini, G. Novel Boundary Integral Formulation for Blade-Vortex Interaction Aerodynamics of Helicopter Rotors. *AIAA Journal*, **45**(6), 1169–1176, June (2007). http://dx.doi.org/10.2514/1.18383.

[17] Bernardini, G., Serafini, J., Ianniello, S., and Gennaretti, M. Assessment of Computational Models for the Effect of Aeroelasticity on BVI Noise Prediction. *International Journal of Aeroacoustics*, **6**(3), 199–222, September (2007). http://dx.doi.org/10.1260/147547207782419570.

[18] Hodges, D. and Dowell, E. Nonlinear Equations of Motion for the Elastic Bending and Torsion of Twisted Nonuniform Rotor Blades. *NASA TN D-7818*, , (1974).

[19] Hodges, D. H. and Ormiston, R. A. Stability of Elastic Bending and Torsion of Uniform Cantilever Rotor Blades in Hover with Variable Structural Coupling. *NASA TN D-8192*, , (1976).

[20] Gennaretti, M., Molica Colella, M., and Bernardini, G. Prediction of Tiltrotor Vibratory Loads with Inclusion of Wing-Proprotor Aerodynamic Interaction. *Journal of Aircraft*, **47**(1), 71–79, January (2010). http://dx.doi.org/10.2514/1.41825.

[21] Greenberg, J. M. Airfoil in Sinusoidal Motion in a Pulsating Stream. *NACA TN-1326*, , (1947).

[22] Gennaretti, M. and Bernardini, G. Aeroelastic Response of Helicopter Rotors Using a 3D Unsteady Aerodynamic Solver. *The Aeronautical Journal*, **110**(1114), 793–802, (2006).

[23] Gennaretti, M., Luceri, L., and Morino, L. A Unified Boundary Integral Methodology for Aerodynamics and Aeroacoustics of Rotors. *Journal of Sound and Vibration*, **200**, 467–489, (1997).

[24] Bernardini, G., Serafini, J., Molica Colella, M., and Gennaretti, M. Analysis of a Structural-Aerodynamic Fully-Coupled Formulation for Aeroelastic Response of Rotorcraft. *Aerospace Science and Technology*, **29**(1), 175–184, August (2013). http://dx.doi.org/10.1016/j.ast.2013.03.002.

[25] Ffowcs Williams, J. E. and Hawkings, D. L. Sound Generation by Turbulence and Surfaces in Arbitrary Motion. *Philosophical Transactions of the Royal Society of London*, **264**(1151), 321–342, (1969).

[26] Brentner, K. Prediction of Helicopter Rotor Discrete Frequency Noise - A Computer Program Incorporating Realistic Blade Motions and Advanced Acoustic Formulation. *NASA - TM 87721*, , (1986).

[27] Farassat, F. Derivation of Formulations 1 and 1A of Farassat. *NASA TM 214853*, , (2007).

[28] Zhang, J., Smith, E., and Wang, K. *Active-Passive Hybrid Optimization of Rotor Blades with Trailing Edge Flaps*. PhD thesis, (2001).

[29] Gennaretti, M., Colella, M. M., and Bernardini, G. Analysis of Helicopter Vibratory Hub Loads Alleviation by Cyclic Trailing-Edge Blade Flap Actuation. *The Aeronautical Journal*, **113**, 549–556, (2009).

Reliability-Based Optimization of the Coupled Structural-Acoustic System with Random Parameters

Xiaojun Wang, Yunlong Li, Zhiliang Ma and Zhiping Qiu

Institute of Solid Mechanics, Beihang University, Beijing,100191, China

(Received 18 February 2014; accepted: 19 April 2016)

Structural noise is an important factor that endangers aircraft fatigue life and flight safety. It also has a negative effect on aircraft stealth performance and noise navigability. An optimal design of a structure-acoustic coupled system is an effective way to reduce noise and vibration. Due to the uncertainties that exist in the structural and acoustical parameters, the traditional deterministic optimization method may be unfeasible when the parameters are subject to fluctuations. This means that when the parameters are uncertain, the results obtained from the deterministic optimization method may be beyond their constraints. This paper proposes to apply the stochastic reliability-based optimization method to the design optimization of the coupled structural-acoustic system with random parameters. A comparison between the results of the stochastic reliability-based method, the safety factor-based method, and the deterministic method show that the first two methods can effectively consider the dispersion of the parameters.

1. INTRODUCTION

Due to the modern industry's rapid development, traffic, city construction, and noise pollution have all attracted attention because they are harmful to structural performance and the general populace's health. Aircraft noise affects both the comfort and work efficacy of the pilot as well as the normal use of instruments inside the aircraft. Uncertainty widely exists in the objective world: it is inevitably subjected to the impact of the uncertainty of a load, structural size, material properties, the influence of various sudden external factors in production, design and use of aircrafts, spacecrafts, etc. These will all have an effect on the working characteristics and normal use of structures and could even lead to failure.

Since the 1970's, some scholars have begun to pay close attention to uncertain structure vibrations and acoustic radiation and have obtained some research results. Shuku and Ishihara[1] investigated the analysis of the acoustic field in irregularly-shaped rooms using the finite element method. Craggs[2] proposed an acoustic finite element approach for studying boundary flexibility and sound transmission between irregular enclosures. Chen and Chertock[3,4] computed sound radiation by using the boundary element method. Marburg[5] studied an optimization problem of the acoustic radiation of finite element beam structures, and analyzed the influence of variables on the objective function where the variables were density, thickness, and young's modulus. Bös[6] studied the optimization problem of three-dimensional structural acoustic performance. Mullen and Muhanna[7] considered the static structure problem with uncertain structural loads based on the fuzzy set theory and interval analysis. Zheng-Dong Ma[8–11] studied the sensitivity of response sound pressure, eigenvalue, and eigenvector to structural parameters based on the modal method, the iterative method, and the direct method. Papadopoulos[12] constructed a finite element model of a room sound field and improved the sound quality of a room by redistributing the low frequency sound modal. Denli[13] studied the structural vibration and acoustic radiation optimization by optimizing the boundary condition. Christensen[14,15] studied the coupled structural-acoustic sensitivity analysis and optimization problem.

The Stochastic reliability-based optimization method is a rather classical approach in the field of optimization, but it has never been used for acoustic optimization. Besides, the previous optimization of the coupled structural-acoustic system were still limited to the deterministic method, and did not take the system parameter uncertainties into account. Deterministic structural optimization design often fails to consider the influence on structural performance by the randomness of material parameters, geometric dimensions, and loading. The optimal solution is usually located at the boundary of the constraint condition because if the randomness of the parameters is considered, the optimal solution may be in violation of the constraint condition and lead to an optimization failure.

The contribution of this paper is to overcome the shortcomings of the structural-acoustic deterministic optimization method by using two different methods: the interference theory of stress- intensity[16–18] and the stochastic reliability-based optimization method, which are both applied to the coupled structural-acoustic system with established random parameters.

2. THE FINITE ELEMENT METHOD OF COUPLED STRUCTURAL-ACOUSTICSYSTEM

2.1. The Finite Element Equation of the Coupled Structural-Acoustic System

The finite element equation of the coupled structural-acoustic system under frequency domain is as follows:

$$-\omega^2\mathbf{MU} + j\omega\mathbf{CU} + \mathbf{KU} = \mathbf{F}; \tag{1}$$

where $\mathbf{M} = \begin{bmatrix} \mathbf{M}^s & \mathbf{0} \\ \mathbf{M}^{couple} & \mathbf{M}^a \end{bmatrix}$; $\mathbf{C} = \begin{bmatrix} \mathbf{C}^s & \mathbf{0} \\ \mathbf{0} & \mathbf{C}^a \end{bmatrix}$; $\mathbf{K} = \begin{bmatrix} \mathbf{K}^s & \mathbf{K}^{couple} \\ \mathbf{0} & \mathbf{K}^a \end{bmatrix}$; $\mathbf{U} = \begin{Bmatrix} \mathbf{U}^s \\ \mathbf{P} \end{Bmatrix}$; $\mathbf{F} = \begin{Bmatrix} \mathbf{F}^s \\ 0 \end{Bmatrix}$; $\mathbf{M}^{couple} = -(\mathbf{K}^{couple}) = \mathbf{S}^T$.

$\mathbf{M}^{couple}$ and $\mathbf{K}^{couple}$ represent the coupled stiffness matrix and coupled mass matrix, respectively; $\mathbf{K}^s$ and $\mathbf{K}^a$ represent the total stiffness matrix of structure and sound field, respectively; $\mathbf{M}^s$ and $\mathbf{M}^a$ represent the total mass matrix of structure and sound field, respectively; $\mathbf{F}^s$ is the external forces vector applied to the structure; $\mathbf{U}^s$ is the node displacement amplitude vector of the structure; ω is the excitation natural frequency; $\mathbf{C}^s$ and $\mathbf{C}^a$ represent the damping matrix of structure and sound field respectively; $\mathbf{P}$ is the unknown sound pressure.

2.2. The Finite Element Method for Frequency Response Analysis for the Coupled Structural-Acoustic System with Random Parameters

A parameter vector $\boldsymbol{\alpha} = (a_1, a_2, ...a_m)^T$ is used to denote all the physical parameters of the structural-acoustic system, m is the structural parameter number. The matrix and vector of the coupling finite element equation could be expressed as the function of the parameter vector $\boldsymbol{\alpha}$. Thus, Eq. (1) can be represented in the following form:

$$-\omega^2\mathbf{M}(\boldsymbol{\alpha})\mathbf{U}(\boldsymbol{\alpha}) + j\omega\mathbf{C}(\boldsymbol{\alpha})\mathbf{U}(\boldsymbol{\alpha}) + \mathbf{K}(\boldsymbol{\alpha})\mathbf{U}(\boldsymbol{\alpha}) = \mathbf{F}(\boldsymbol{\alpha}). \tag{2}$$

It is assumed that the uncertain parameter vector has a normal distribution and the random variables are independent of each other, namely:

$$\boldsymbol{\alpha} \sim N(\boldsymbol{\alpha}^c, \boldsymbol{\sigma}_a). \tag{3}$$

The solution to the coupled structural-acoustic system with random parameters is converted to find all of the solutions that satisfy Eq. (2), namely:

$$\boldsymbol{\Omega} = \{\mathbf{U}(\boldsymbol{\alpha})| -\omega^2\mathbf{M}(\boldsymbol{\alpha})\mathbf{U}(\boldsymbol{\alpha}) + j\omega\mathbf{C}(\boldsymbol{\alpha})\mathbf{U}(\boldsymbol{\alpha}) + \mathbf{K}(\boldsymbol{\alpha})\mathbf{U}(\boldsymbol{\alpha}) = \mathbf{F}(\boldsymbol{\alpha})\}. \tag{4}$$

3. STOCHASTIC RELIABILITY-BASED OPTIMIZATION METHOD

3.1. Model of Stochastic Reliability-Based Optimization

A class of important problems in structural stochastic reliability-based optimization design minimizes the structural weight by selecting a reasonable distribution of the structural section size in a given reliability. Obviously, this kind of structural design is economical and reliable. Usually, structural weight is expressed as a linear function of the component's cross section dimensions (the design variables). One model of the stochastic reliability-based optimization is as follows:

$$\begin{cases} \text{Find } \mathbf{x}(x_1, x_2, \ldots, x_n \in R^n) \\ \min W(\mathbf{x}) = \sum_{j=1}^{n} w_j(x_j) \\ \text{s.t. } g(\mathbf{x}) = \beta_s(\mathbf{x}) - \beta_s^{\alpha} \geq 0 \\ \mathbf{x}^l \leq \mathbf{x} \leq \mathbf{x}^u \end{cases}; \tag{5}$$

Among them, $\mathbf{x}$ is the design variable of the structure; W is the mass of the structure; β_s is the index reliability of a constraint; β_s^{α} is the lower limit value of the reliability constraints.

3.2. The Mean Value First Order and Second Moment (MVFOSM) Reliability Method

The basic idea of the MVFOSM reliability method is to expand the nonlinear limit state functions at midpoints of random variables, ignore the higher order terms rather than second order, and then approximately calculate the mean and standard deviation of the limit state functions. The reliability index can be expressed as functions of the mean and standard deviation.

In stochastic reliability-based optimization of the coupled structural-acoustic system with random parameters, if the response $\mathbf{U}(\boldsymbol{\alpha}, \omega)$ satisfies the constraint that has a normal distribution $\mathbf{U}_{\boldsymbol{\delta}} \sim N(\mu_\delta, \sigma_\delta)$, the limit state functions about the response amplitude and the constraint can be represented as:

$$\mathbf{Z} = \mathbf{U}_{\boldsymbol{\delta}} - \mathbf{U}(\boldsymbol{\alpha}, \omega). \tag{6}$$

A Taylor series expansion about the limit state functions Eq. (6) at the midpoints of uncertain parameters $\boldsymbol{\alpha}^c$ is then implemented:

$$\mathbf{Z} = \mathbf{U}_\delta - \mathbf{U}(\boldsymbol{\alpha}^c, \omega) + \sum_{i=1}^{m} \frac{\partial \mathbf{U}(\boldsymbol{\alpha}^c, \omega)}{\partial \alpha_i}\delta\alpha_i + \sum_{i,j=1}^{m} \frac{\partial \mathbf{U}^2(\boldsymbol{\alpha}^c, \omega)}{\partial \alpha_i \partial \alpha_j}\delta\alpha_i\delta\alpha_j + \cdots. \tag{7}$$

According to the MVFOSM reliability method, the mean μ_z and the variance $\boldsymbol{\sigma}_z^2$ of the limit state functions are expressed as follows:

$$\boldsymbol{\mu}_{\mathbf{z}} = \boldsymbol{\mu}_{\boldsymbol{\delta}} - \mathbf{U}(\boldsymbol{\alpha}^c, \omega) + \sum_{i=1}^{m} \frac{\partial \mathbf{U}(\boldsymbol{\alpha}^c, \omega)}{\partial \alpha_i}\delta\alpha_i; \tag{8}$$

$$\boldsymbol{\sigma}_{\mathbf{z}}^2 = \boldsymbol{\sigma}_{\boldsymbol{\delta}}^2 + \sum_{i=1}^{m} \left[\frac{\partial \mathbf{U}(\boldsymbol{\alpha}^c, \omega)}{\partial \alpha_i}\right]_{\mu_{\alpha^c}}^2 \sigma_{\alpha_i}^2. \tag{9}$$

The central difference method is applied to approximate the derivative of the above matrices or vectors about $\boldsymbol{\alpha}$:

$$\frac{\partial \mathbf{U}(\boldsymbol{\alpha}^c, \omega)}{\partial \boldsymbol{\alpha}} \approx \frac{\mathbf{U}(\boldsymbol{\alpha}^c + \delta\boldsymbol{\alpha}, \omega) - \mathbf{U}(\boldsymbol{\alpha}^c - \delta\boldsymbol{\alpha}, \omega)}{2\delta\boldsymbol{\alpha}}; \tag{10}$$

$$\delta\boldsymbol{\alpha} = \boldsymbol{\alpha} - \boldsymbol{\alpha}^c. \tag{11}$$

By substituting Eqs. (10) and (11) into Eqs. (8) and (9), the mean and variance of the limit state functions can be obtained.

The reliability index $\boldsymbol{\beta}$ and failure probability $\mathbf{P}_f$ can be evaluated using Eqs. (12) and (13):

$$\boldsymbol{\beta} = \frac{\boldsymbol{\mu}_{\mathbf{z}}}{\boldsymbol{\sigma}_{\mathbf{z}}}; \tag{12}$$

$$\mathbf{P}_{\mathbf{f}} = \Phi(-\boldsymbol{\beta}). \tag{13}$$

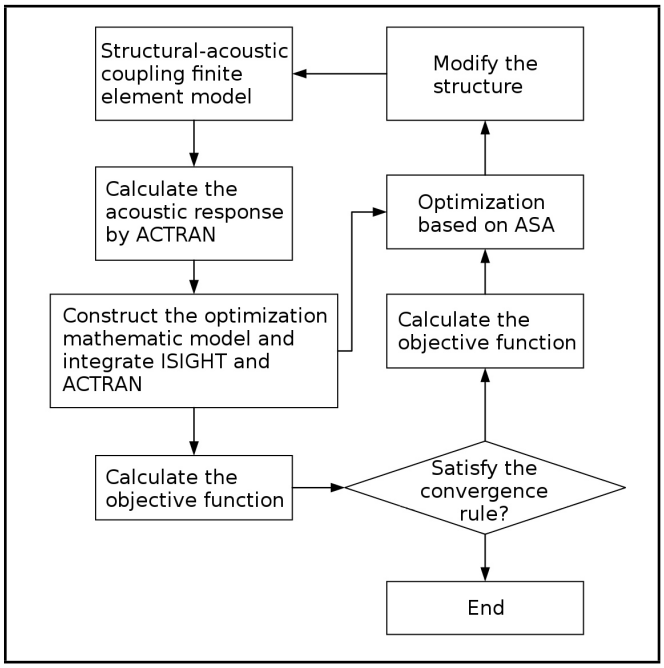

Figure 1. The flow chart of integration optimization for both ISIGHT and ACTRAN.

4. SAFETY FACTOR METHOD BASED ON RELIABILITY

In conventional mechanical design, strength calculation is carried out according to the principle of $s \leq r/n$, where s is the load stress, r is material strength, and n is the safety factor. The safety factor includes uncertain factors such as the difference in calculation methods, the manufacturing allowable deviation, and the difference between actual stress and theoretical stress. As a result, conventional mechanical design is bound to result in a lot of unreasonable designs. The main reason is that $s \leq r/n$ can't reflect the changing law of stress and strength. In fact, even though the component is made from the same material and subjected to the same loading, if the changing law of strength and load is different, the failure probability may be different. In short, conventional design doesn't consider the consequences of failure.

Due to all of these reasons and the lack of any suitable theories or sufficient experimental data, our country's current given safety factor in the specifications and standards are usually too conservative. It may not be economical and may even cause the design to be unreliable. Therefore,in recent years, people have associated the safety factor with stress and strength, and have put it forward based on reliability so it can improve the design's reliability.

The mean safety factor is defined as the ratio of the mean of parts intensity to stress in the dangerous section parts:

$$n = \frac{\mu_\delta}{\mu_s}. \tag{14}$$

When the stress and intensity obey normal distribution, the mean safety factor is associated with the reliability of the parts, so we have the equation:

$$\beta = \frac{\mu_\delta - \mu_s}{\sqrt{\sigma_\delta^2 + \sigma_s^2}}; \tag{15}$$

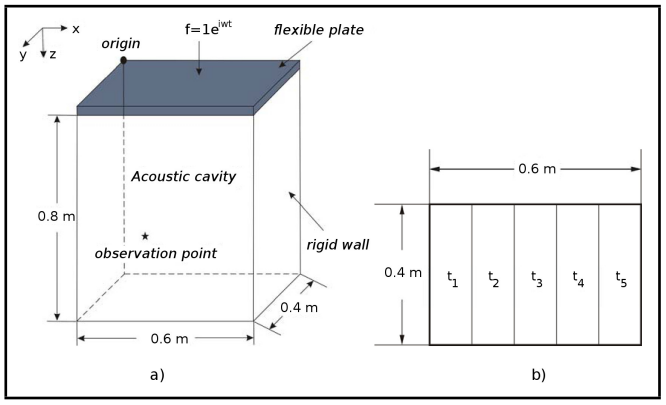

Figure 2. The coupled structural-acoustic system: a) a cuboid cavity and b) the distribution of design variables about plate thickness.

β is the reliability index. According to Eqs. (14) and (15), the mean safety factor n can be rewritten as:

$$n = \frac{\mu_\delta}{\mu_\delta - \beta\sqrt{\sigma_\delta^2 + \sigma_s^2}}. \tag{16}$$

This paper introduces the stress-intensity interference theory to the coupled structural-acoustic system. When a stochastic reliability-based optimization of the structural-acoustic system is implemented, we make the value of the mean and variance of the acoustic response and its constraints correspond to the mean and variance of stress and strength in Eq. (16), respectively. We can obtain the safety factor corresponding to each iterative step of stochastic reliability-based optimization (as can be seen from Fig. 3c). If we implement the safety factor based optimization, we should choose the maximum safety factor obtained from stochastic reliability- based optimization as the safety factor.

5. THE IMPLEMENTATION METHOD OF THE STRUCTURAL-ACOUSTIC OPTIMIZATION

TThe structural-acoustic finite model and the optimization mathematic model should be established before optimization. And the proper mathematical method should be selected to implement the optimization. In the process of acoustic optimization, each iteration process needs to compute the acoustic response of the system. In this paper, the acoustic responses are obtained by ACTRAN software. The optimization processes are based on the integration of ACTRAN and ISIGHT. Response values calculated by ACTRAN can be transformed into the objective function value through multidisciplinary design language within the ISIGHT. The adaptive simulated annealing algorithm (ASA) is used to find the optimization solution. The integrated block diagram is shown in Fig. 1. ASA is a variant of the simulated annealing (SA) algorithm in which the algorithm parameters that control temperature schedule and random step selection are automatically adjusted according to algorithm progress. This makes the algorithm more efficient and less sensitive to user defined parameters than canonical SA. These are in the standard variant often selected on the basis of experience and experimentation (since optimal values are problem dependent), which represents a significant deficiency in practice. Certainly, the optimization procedure based on deterministic analysis is also able to reduce the value of acoustic responses of structures[19–22] significantly.

6. NUMERICAL EXAMPLE

A 3D acoustic cuboid model with length (0.6 m), width (0.4 m) and height (0.8 m) is shown in Fig. 2a. A flexible aluminum plate with the thickness of 6mm is imposed on one surface of the cuboid cavity $z = 0$, which composes a coupled structural-acoustic system. The remaining surfaces are perfectly rigid and the outer environment is a vacuum. The density, elastic modulus, damping coefficient, and Poisson ratio of the aluminum plate are 2700 kg·m^{-3}, 70 GPa, 0.01, and 0.3, respectively. The cuboid cavity is surrounded by air with density 1.225 kg·m^{-3} and sound speed 340 m·s^{-1}.

A harmonic excitation with the amplitude of 1 N is imposed at the central point of the flexible plate along the vertical direction. The frequency step is selected as 2 Hz to analyze the deterministic coupled system in the frequency domain of 1-300 Hz. From the results on field point 0.1, 0.1, and 0.6, we know that the first two characteristic frequencies are located in the values of 108 Hz and 214 Hz, respectively. Here, we select the thicknesses of the sub-block regions in the aluminum plate as design variables $\mathbf{t} = (t_1, \cdots, t_5)^T$ as shown in Fig. 2. Supposing that the mean square sound pressure amplitude at ten special frequencies, such as 104 Hz, 106 Hz, 108 Hz, 110 Hz, 112 Hz, 210 Hz, 212 Hz, 214 Hz, 216 Hz, and 218 Hz, MSP_{10} is less than 40 Pa (Stochastic reliability-based optimization requires its reliability not less than 0.99). The objective function is to find the optimal solution to make the total mass as small as possible. The initial value of the design variable is 0.006 m, with a range of 0.003 m to 0.007 m. All of the random variables have a normal distribution and are independent of each other. The stochastic reliability- based optimization design and safety factor-based optimization design (with the aid of ACTRAN and ISIGHT software) when the variation coefficient of random variables is 0.02, 0.05, and 0.1 respectively, was implemented.

6.1. Deterministic Optimization of the Structural-Acoustic System

The mathematical model of deterministic optimization about this example is:

$$\begin{cases} \min W \\ \text{s.t. } MSP_{10} \le 40 \text{ Pa} \\ 3 \text{ mm} \le t_1, t_2, t_3, t_4, t_5 \le 7 \text{ mm} \end{cases};$$

The deterministic optimization results are show in Table 1 to Table 3.

6.2. Optimization When the Variation Coefficient of Random Variables Is 0.02

1) *The stochastic reliability-based optimization method*

The mathematical model of stochastic reliability-based optimization in this example is:

$$\begin{cases} \min W \\ \text{s.t. } \beta \ge 2.3263^* \\ 3 \text{ mm} \le \mathbf{t_1}, \mathbf{t_2}, \mathbf{t_3}, \mathbf{t_4}, \mathbf{t_5} \le 7 \text{ mm} \end{cases}$$

*(corresponding to the reliability not less than 0.99); (17)

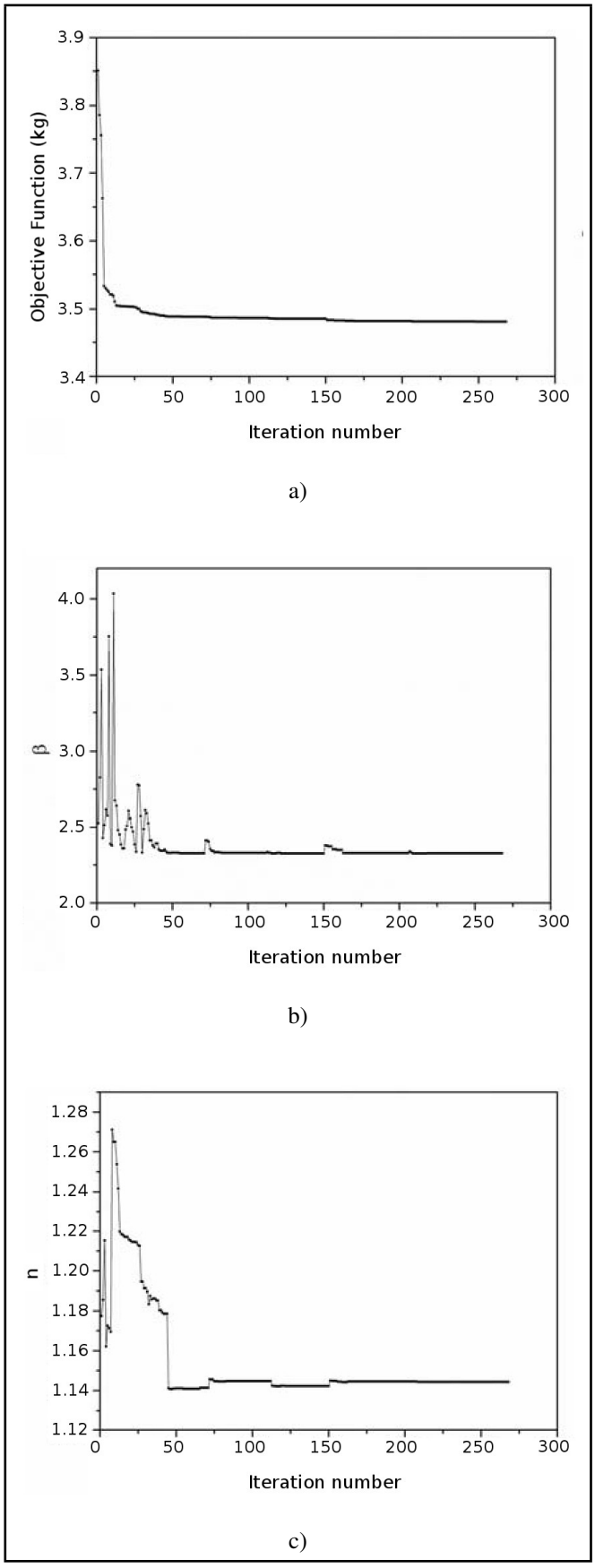

Figure 3. Iterative curves of reliability based optimization (the variation coefficient of random variables is 0.02): a) objective function, b) reliability index, and c) safety factor.

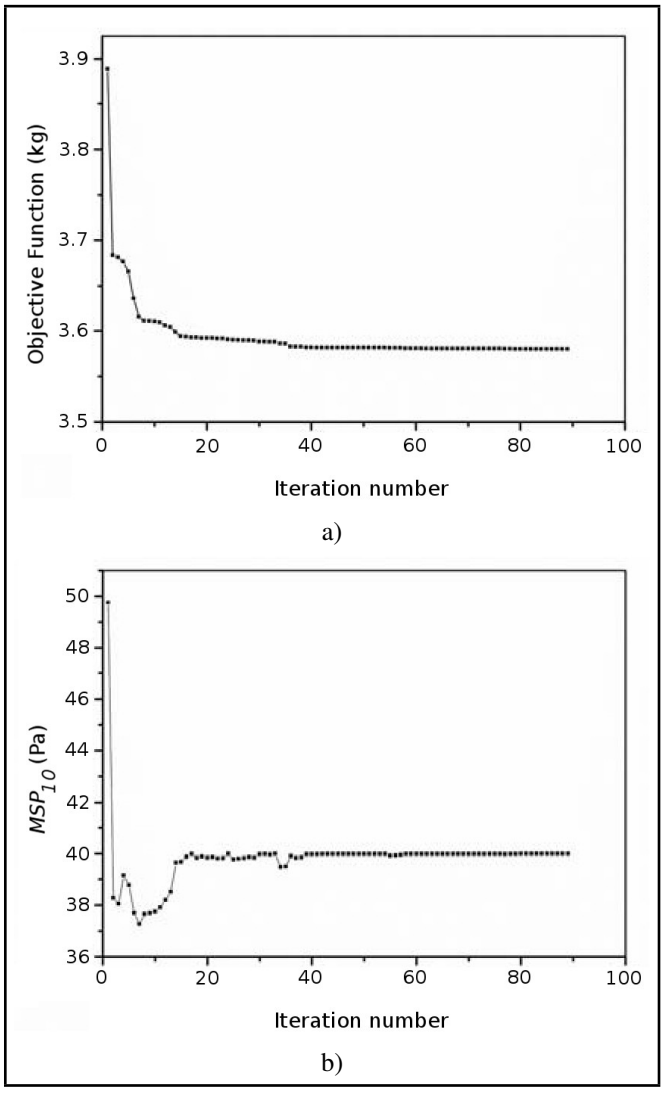

Figure 4. Iterative curves of the safety factor-based optimization ($n = 1.144$): a) objective function and b) MSP.

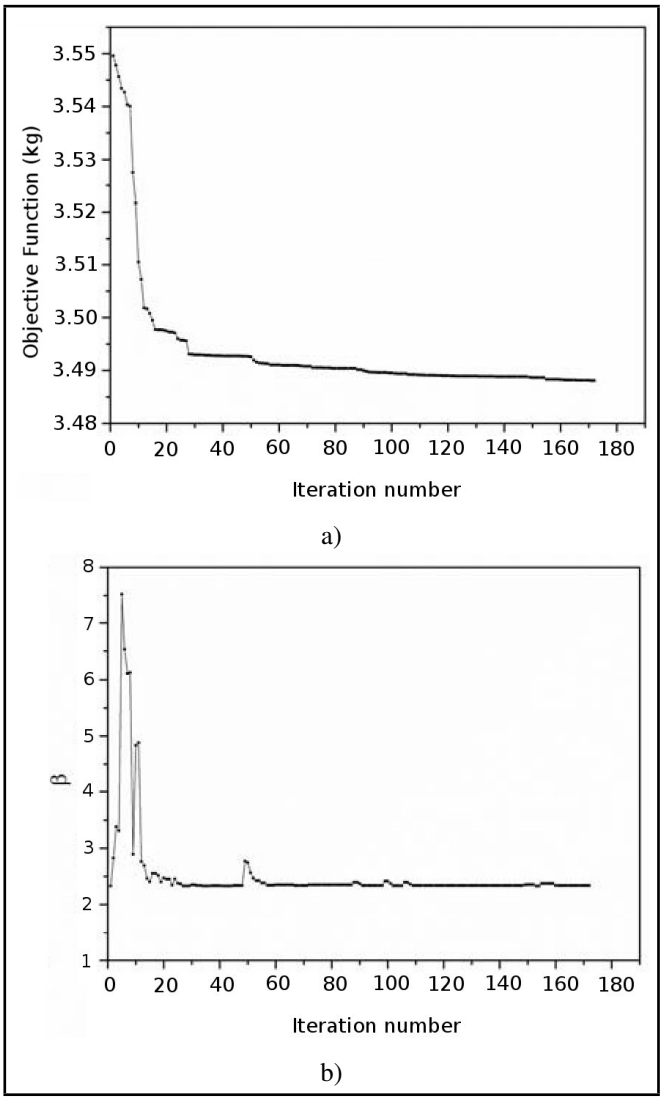

Figure 5. Iterative curves of the reliability-based optimization with random parameters (The variation coefficient of random variables is 0.05): a) objective function and b) reliability index.

The iterative curves of the reliability-based optimization method are shown as Fig. 3 and the safety factor n is obtained from reliability index β according to Eq. (16).

2) *The safety factor-based optimization method*

In this example, the mean square sound pressure amplitude and the mean square sound pressure constraint value in stochastic reliability-based optimization corresponds to the stress μ_s and strength μ_δ in the stress-strength interference theory, and σ_δ is 0. According to Eq. (16), we can calculate the safety factor corresponding to the optimal solution $n = 1.144$, which satisfies the requirement of reliability: n is the mean safety factor obtained from the optimal solutions by stochastic reliability-based optimization (reliability is not less than 0.99). The mathematical model of the safety factor-based optimization method is

$$\begin{cases} \min W \\ \text{s.t. } MSP_{10} \le 40/n \\ 3 \text{ mm} \le \mathbf{t_1}, \mathbf{t_2}, \mathbf{t_3}, \mathbf{t_4}, \mathbf{t_5} \le 7 \text{ mm} \end{cases} . \qquad (18)$$

6.3. Optimization When the Variation Coefficient of Random Variables Is 0.05

1) *The stochastic reliability-based optimization method*

2) *The safety factor-based optimization method*

According to Eq. (16), we can calculate the safety factor corresponding to the optimal solution and n is 1.085.

7. OPTIMIZATION WHEN THE VARIATION COEFFICIENT OF RANDOM VARIABLES IS 0.1

1) *The stochastic reliability-based optimization method*

2) *The safety factor-based optimization method*

According to Eq. (16), we can calculate the safety factor corresponding to the optimal solution and n is 1.352.

The results of the different optimization methods are shown in Table 1 to Table 3. The objective function (structural

Table 1. Comparison between the stochastic reliability-based optimization method and the safety factor-based method (the variation coefficient of random variables is 0.02).

Optimization type	Design variables (mm)					MSP_{10} (Pa)	Objective function (Kg)
	t_1	t_2	t_3	t_4	t_5		
Initial values	6.0000	6.0000	6.0000	6.0000	6.0000	49.7358	3.8880
The deterministic optimization method	5.1848	5.6531	4.9841	3.0000	3.0004	39.9982	2.8282
The stochastic reliability-based optimization method	3.6495	6.3726	6.5625	5.4085	4.8695	34.9550	3.4814
The safety factor-based method	5.2485	5.2700	6.7173	6.4458	3.2036	39.9989	3.4843

Table 2. Comparison between the stochastic reliability-based optimization method and the safety factor-based method (the variation coefficient of random variables is 0.05).

Optimization type	Design variables (mm)					MSP_{10} (Pa)	Objective function (Kg)
	t_1	t_2	t_3	t_4	t_5		
Initial values	6.0000	6.0000	6.0000	6.0000	6.0000	49.7358	3.8880
The deterministic optimization method	5.1848	5.6531	4.9841	3.0000	3.0004	39.9982	2.8282
The stochastic reliability-based optimization method	6.9406	3.6815	5.8479	6.3075	4.1366	36.8664	3.4881
The safety factor-based method	5.5517	5.0535	6.8061	5.7098	3.5169	39.9996	3.4523

Table 3. Comparison between the stochastic reliability-based optimization method and the safety factor-based method (the variation coefficient of random variables is 0.1).

Optimization type	Design variables (mm)					MSP_{10} (Pa)	Objective function (Kg)
	t_1	t_2	t_3	t_4	t_5		
Initial values	6.0000	6.0000	6.0000	6.0000	6.0000	49.7358	3.8880
The deterministic optimization method	5.1848	5.6531	4.9841	3.0000	3.0004	39.9982	2.8282
The stochastic reliability-based optimization method	5.7675	5.0835	6.8865	6.5635	3.2975	29.5858	3.5768
The safety factor-based method	6.7060	4.5992	6.6061	6.2562	3.3688	39.6467	3.5687

weight) of the safety factor optimization method and stochastic reliability-based optimization method is greater than the deterministic optimization method because the latter does not consider the influence of the random parameters on the response andits constraint value is larger than the other two methods. In addition, as seen on Table 1, the optimal value of the deterministic optimization method of t_4 and t_5 is close to the lower limit of design variables (3 mm). If the uncertainties of the system parameter are considered, the design variables may be beyond the constraint scope (3 mm), which is why the reliability of the deterministic optimization method does not have strong robustness.

8. CONCLUSIONS

Compared with the deterministic optimization design method, the reliability-based method and the safety factor method based on reliability can consider the effect of structural parameter randomness on the structural performance, so the optimization results are more reasonable than that of the deterministic optimization method. In this paper, the safety factor is obtained from the reliability index (mean and standard deviation) of the mean square acoustic pressure. Using this method to determine the safety factor and to implement the optimization design can help overcome the deficiency of the deterministic optimization method. Compared to the conventional design, the data processing and calculation process is simpler and the calculation precision is higher and closer to the actual. For example, when the variation coefficient of the random parameters is 0.02, 0.05, and 0.1 respectively, the difference of the two methods is about 1%, which shows that the safety factor method can effectively consider the dispersion of parameters. The main advantage in using this method is that it can save materials and ensure reliability.

ACKNOWLEDGEMENT

This project is supported by the National Natural Science Foundation of China (Grant No.11002013; Grant No.11372025), Defense Industrial Technology Development Program (Grant No. A2120110001; Grant No. B2120110011) and the Aeronautical Science Foundation of China (Grant No. A2012ZA51010).

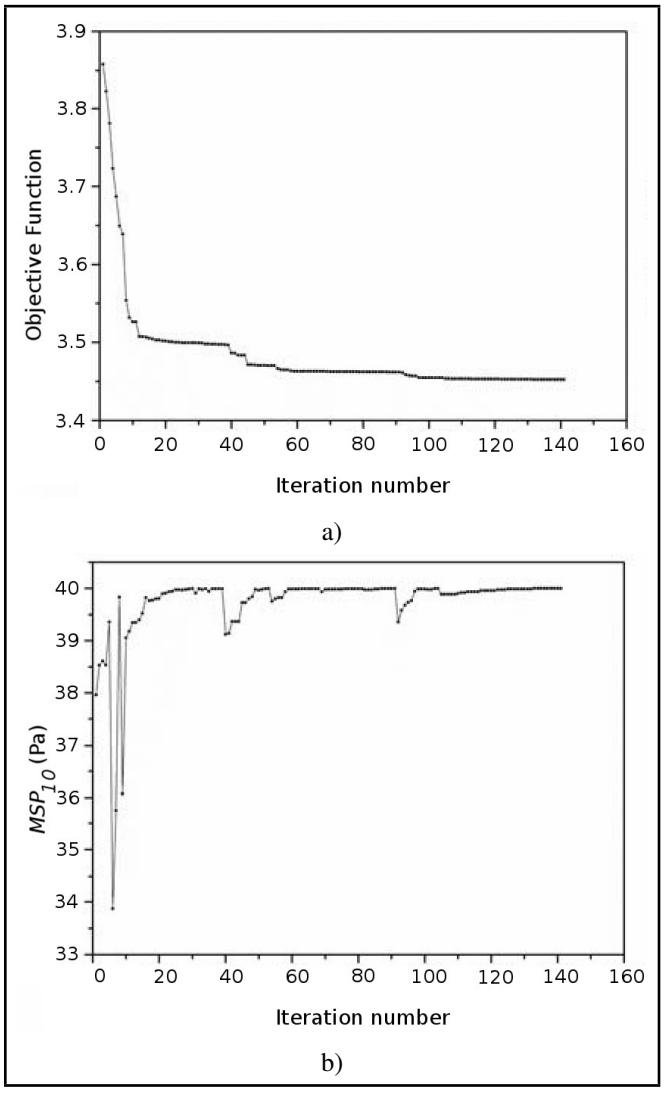

Figure 6. Iterative curves of the traditional safety factor-based optimization (n=1.085): a) objective function and b) MSP.

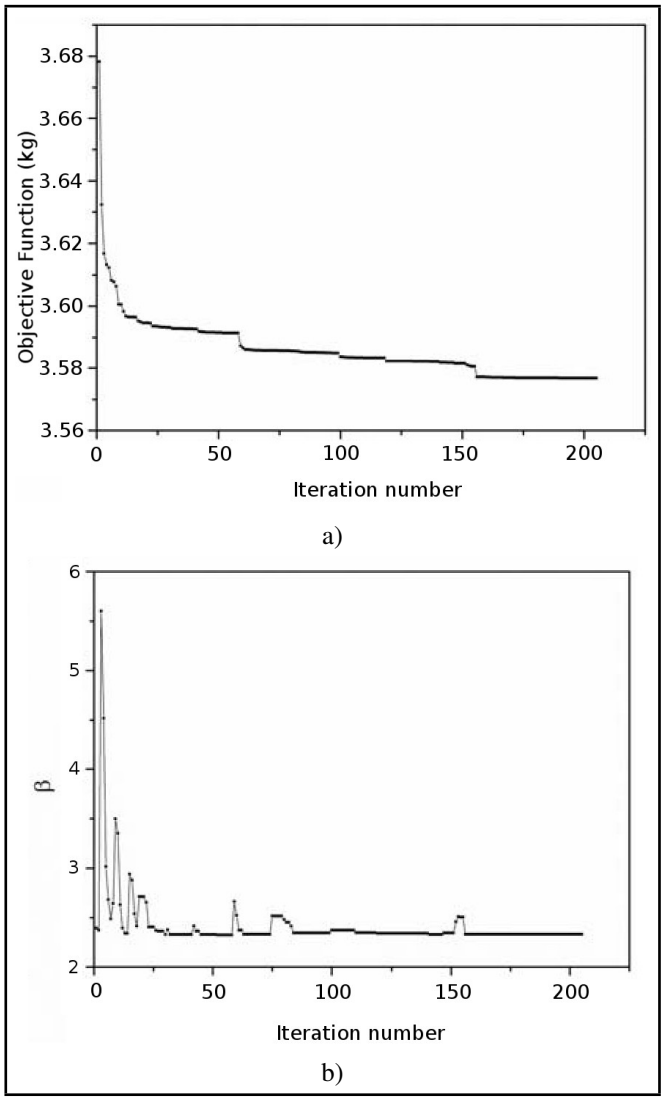

Figure 7. Iterative curves of the reliability-based optimization with random parameters (The variation coefficient of random variables is 0.1): a) objective function and b) reliability index..

REFERENCES

[1] Shuku, T. and Ishihara, K. The analysis of the Acoustic Field in Irregularly Shaped Rooms by the Finite Element Method, *Journal of Sound and Vibration*, **29** (1), 67–68, (1973). http://dx.doi.org/10.1016/s0022-460x(73)80126-9

[2] Craggs, A. An Acoustic Finite Element Approach for Studying Boundary Flexibility and Sound Transmission between Irregular Enclosures, *Journal of Sound and Vibration*, **30** (3), 343–357, (1973). http://dx.doi.org/10.1016/s0022-460x(73)80243-3

[3] Chen, L. and Schweikert, D. Sound Radiation from an Arbitrary Body, *The Journal of the Acoustical society of America*, **35** (10), 1626, (1963). http://dx.doi.org/10.1121/1.1918770

[4] Chertock, G. Sound Radiation from Vibrating Surfaces, *The Journal of the Acoustical Society of America*, **36** (7), 1305–1313, (1964). http://dx.doi.org/10.1121/1.1919203

[5] Marburg, S., Dienerowitz, F., Fritze, D., and Hardtke, H. J. Case Studies on Structural-acoustic Optimization of a Finite beam, *Acta Acustica United with Acustica*, **92** (3), 427–439, (2006).

[6] Bös, J. Numerical Optimization of the Thickness Distribution of Three-dimensional Structures with Respect to Their Structural Acoustic Properties, *Structural and Multidisciplinary Optimization*, **32** (1), 12–30, (2006). http://dx.doi.org/10.1007/s00158-005-0560-y

[7] Mullen, R. and Muhanna, R. Bounds of Structural Response for All Possible Loading Combinations, *Journal of Structural Engineering*, **125** (1), 98–106, (1999). http://dx.doi.org/10.1061/(asce)0733-9445(1999)125:1(98)

[8] Ma, Z. D. and Hagiwara, I. Sensitivity Analysis Methods for Coupled Acoustic-structural Systems Part I: Modal Sensitivities, *AIAA Journal*, **29** (11), 1787–1795, (1991). http://dx.doi.org/10.2514/3.61525

[9] Ma, Z. D. and Hagiwara, I. Sensitivity Analysis Methods for Coupled Acoustic-structural Systems Part ii: Direct Frequency Response and Its Sensitivities, *AIAA Journal*, **29** (11), 1796–1801, (1991). http://dx.doi.org/10.2514/3.61526

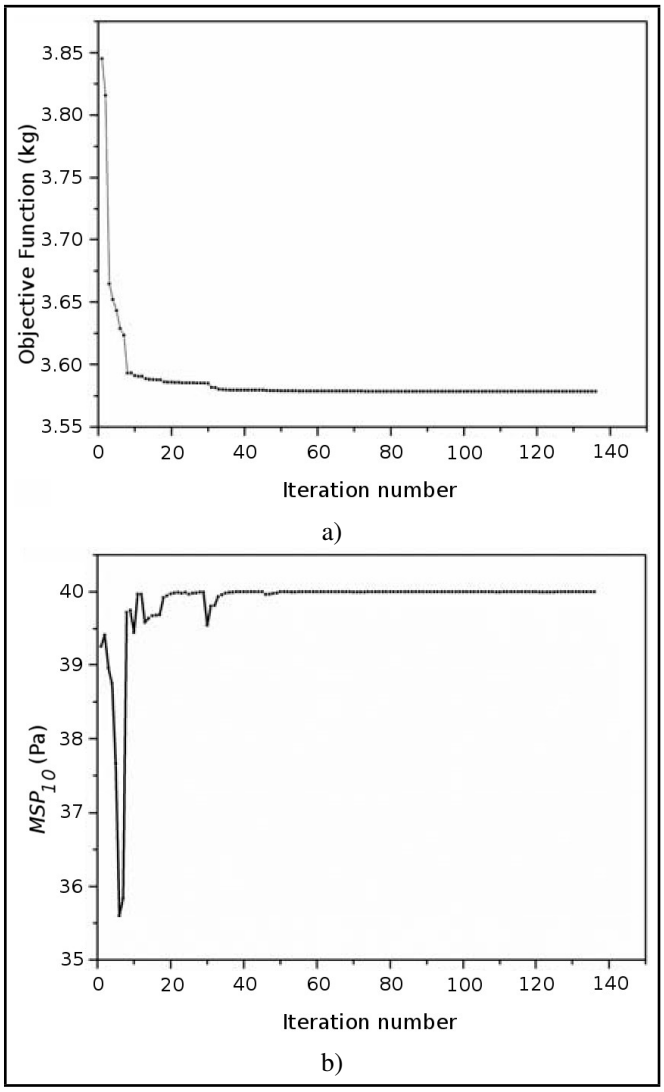

Figure 8. Iterative curves of the safety factor-based optimization ($n = 1.352$): a) objective function and b) MSP.

[10] Hagiwara, I. and Ma, Z. Sensitivity Calculation Method for Conducting Modal Frequency Response Analysis of Coupled Acoustic-structural Systems, *JSME International Journal Series III*, **35** (1), (1992). http://dx.doi.org/10.1299/jsmec1988.35.14

[11] Hagiwara, I., Kozukue, W., and Ma, Z.D. The Development of Eigenmode Sensitivity Analysis Methods for Coupled Acoustic-structural Systems and Their Application to Reduction of Vehicle Interior Noise, *Finite Elements in Analysis and Design*, **14** (2), 235–248, (1993). http://dx.doi.org/10.1016/0168-874x(93)90023-j

[12] Papadopoulos, C. I. Redistribution of the Low Frequency Acoustic Modes of a Room: A Finite Element-based Optimisation method, *Applied Acoustics*, **62** (11), 1267–1285, (2001). http://dx.doi.org/10.1016/s0003-682x(01)00002-0

[13] Denli, H. and Sun, J. Optimization of Boundary Supports for Sound Radiation Reduction of Vibrating Structures, *Journal of Vibration and Acoustics*, **130** (1), (2008). http://dx.doi.org/10.1115/1.2776345

[14] Christensen, S. T., Sorokin, S. V., and Olhoff, N. On Analysis and Optimization in Structural Acoustics – Part I: Problem Formulation and Solution Techniques, *Structural Optimization*, **16** (2-3), 83–95, (1998). http://dx.doi.org/10.1007/s001580050009

[15] Christensen, S. T., Sorokin, S. V., and Olhoff, N. On Analysis and Optimization in Structural Acoustics – Part II: Exemplifications for Axisymmetric Structures, *Structural Optimization*, **16** (2-3), 96–107, (1998). http://dx.doi.org/10.1007/s001580050010

[16] Elishakoff, I. and Ferracuti, B. Fuzzy Sets Based Interpretation of the Safety Factor, *Fuzzy Sets and Systems*, **157** (18), 2495–2512, (2006). http://dx.doi.org/10.1016/j.fss.2006.06.009

[17] Wang, X., Qiu, Z., and Elishakoff, I. Non-probabilistic Set-theoretic Model for Structural Safety Measure, *Acta Mechanica*, **198** (1-2), 51–64, (2008). http://dx.doi.org/10.1007/s00707-007-0518-9

[18] Elishakoff, I. and Starnes Jr, J. H. Safety factor and the non-deterministic approaches, Proc. of the 1999 AIAA/ASME/ASCE/AHS/ASC structrures, Structural Dynamics, and Materials Conference and Exhibit, (1999). http://dx.doi.org/10.2514/6.1999-1614

[19] Ranjbar M., Hardtke H. J., Fritze D., et al. Finding the best design within limited time: a comparative case study on methods for optimization in structural acoustics. *Journal of Computational Acoustics*, **18** (2), 149–164, (2010). http://dx.doi.org/10.1142/s0218396x10004139

[20] Ranjbar M., Marburg S., and Hardtke H. J. Structural-acoustic optimization of a rectangular plate: A tabu search approach, *Finite Elements in Analysis and Design*, **50**, 142–146, (2012). http://dx.doi.org/10.1016/j.finel.2011.09.005

[21] Marburg S. and Hardtke H. J. A general concept for design modification of shell meshes in structural-acoustic optimizationPart II: Application to a floor panel in sedan interior noise problems. *Finite Elements in Analysis and Design*, **38** (8)737–754, (2002). http://dx.doi.org/10.1016/s0168-874x(01)00102-0

[22] Fritze D., Marburg S., and Hardtke H. J. FEM–BEM-coupling and structural–acoustic sensitivity analysis for shell geometries, *Computers & structures*, 143–154, **83** (2), (2005). http://dx.doi.org/10.1016/j.compstruc.2004.05.019

Frequency Identification of Flexible Hub-Beam System Using Control Data

Xie Yong, Liu Pan and Cai Guo-Ping

Department of Engineering Mechanics, State Key Laboratory of Ocean Engineering, Shanghai Jiaotong University, Shanghai 200240, China

(Received 24 March 2014; accepted: 17 September 2014)

This paper studies the parameter identification of a flexible hub-beam system based on the input-output data. Firstly, the first-order approximation coupling (FOAC) model is presented. Then, active position control for the system is studied using optimal tracking control theory. Finally, the observer/Kalman filter identification (OKID) and eigensystem realization algorithm (ERA) method are applied to identify the frequency of the system. In the simulations, the effectiveness of the identification method presented in this paper is verified by comparing the identification results of several different external excitations. Simulation results indicate that the anticipated position of the system may be traced by the proposed controller, and the residual vibration of the beam may be suppressed as well. The frequency of the system can be effectively identified using OKID and ERA. It is feasible and effective to identify the frequency using the control data.

1. INTRODUCTION

Spacecraft is composed of a central body and several flexible attachments. It is a typical rigid-flexible dynamic system with characteristics of dense frequencies and small damping. System assembly on the ground (1G gravity environment) is very difficult in many circumstances because of the flexibility of the structures; it is even more difficult to do vibration experiments on structures due to factors such as air damping, gravity effect, etc. Moreover, in some cases, the experimental apparatus may not be able to meet the experimental requirement of tests on the ground. On the other hand, flexible parameters of spacecraft, especially the natural frequencies of flexible solar array, may have great effect on the control of the spacecraft's attitude, since the flexible parameters will be used in control design. Due to the difference between ground and space environments, vibration behaviour of the solar array in two environments is different, too. So, the flexible parameters obtained by experiments on the ground cannot reflect the actual state of spacecraft in outer space. Therefore, it is necessary to study the on-orbit identification technology for the spacecraft to improve the accuracy in identifying flexible parameters. Since the flexible parameters obtained by the on-orbit identification are based on the real vibration of a spacecraft in outer space, it is more likely that these parameters are of high accuracy, and then control design based on these parameters can ensure high accuracy of attitude control. Furthermore, a system dynamic model may be modified by comparing the on-orbit test with the ground test so as to establish the quantitative relationships among the on-orbit test, the ground test, and the dynamic simulation. This will be helpful for the follow-up development of the spacecraft. The on-orbit identification needs the vibration response of spacecraft under certain excitation, which could be provided by the attitude manoeuvre, which means the realization of on-orbit identification is possible.

On-orbit parameter identification is conducted by directly using the input and output data, with no need of the exact dynamic model of the system. Generally speaking, the parameter identification methods can be divided into frequency domain methods and time domain methods, and the time domain method has better performance than the frequency domain method. Theoretical studies and engineering applications of the on-orbit identification technique have been completed in past research. For example, Haugse, et al.[1] developed an accelerometer measurement system to gather data from an operational, on-orbit, and deployed space vehicle, and Fast Fourier Transform (FFT), Power Spectral Density (PSD) and Eigensystem Realization Algorithm (ERA) are employed for system modal identification. Kim, et al.[2] presented a data processing strategy to generate equivalent free-decay responses from structural response data and used a free-decay time-domain modal identification technique for modal identification of Space Station Freedom. Tokio Kasai, et al.[3] used the extended Kalman filter (EKF) technique to extract the modal parameters of a satellite with flexible solar panels. On the Engineering Test Satellite VI, impulse and random excitation were applied to the central body, and the measurement data were packed and downloaded via S-band digital serial telemetry for the off-line analysis by the ERA method. The identified modal parameters were then used in the synthesis of control law.[4–8]

On the International Space Station (ISS), the shuttle booster ignition pulse was used as an excitation to finish an on-orbit modal parameter identification test five times. The dynamic responses of the Shuttle-ISS mated structure were measured by the Shuttle payload bay video camera photogrammetric system, the Internal Wireless Instrumentation System (IWIS) ac-

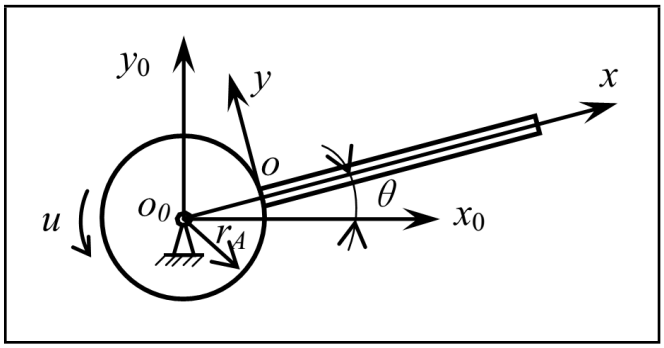

Figure 1. Structural model of the flexible hub-beam system.

celerometers, and the IWIS strain gauges. The measured data were processed and analysed based on the ERA to identify the structural modal parameters, including frequencies, damping, and mode shapes.[9,10] On the Mir Space Station, the external excitations used in on-orbit modal experiment included Shuttle and Mir thruster firings, Shuttle-Mir and Progress-Mir dockings crew exercise and push offs, and ambient noise during night-to-day and day-to-night orbital transitions. The data from the Mir Auxiliary Sensor Unit (MASU), which contains a total of 19 accelerometers, were used for modal identification by a time-domain free-decay method based on the ERA.[11–14] It can be concluded from above that some practical work on spacecraft parameter identification has been done recently. However all the tests above are specially designed for parameter identification, which is separated from other space missions. Every space mission is extremely expensive, as is well known. We are then inspired to consider the following question: Can the attitude manoeuvre data of spacecraft be directly used for parameter identification? We need the dynamic response of spacecraft, which could be exactly provided by the attitude manoeuvre of spacecraft, to realize the on-orbit identification. If possible, it is unnecessary to carry out solely on-orbit identification, saving costs on space missions. And it may also provide new methods for parameter identification in other fields.

In this paper, a frequency identification technique is investigated using a flexible hub-beam system as the object of the research, and the feasibility of identification using control data of the system is verified. The hub-beam system is a typical rigid-flexible coupling dynamic system. This system is applied to many engineering objects in practice, such as spacecraft, robots, turbine blades, etc. Today there are many studies on modelling and active control of the flexible hub-beam system. This paper is organized as follows: Section 2 briefly presents the first-order approximation coupling (FOAC) model for a flexible hub-beam system. Active controller design using optimal trajectory theory is presented in Section 3. Section 4 presents the OKID and ERA methods for the parameter identification. The numerical simulation results are shown in Section 5, and finally, Section 6 generalizes the conclusions of the research.

2. THE FIRST-ORDER APPROXIMATION COUPLING MODEL

A hub-beam rotating in the horizontal plane is considered here, as shown in Fig. 1, where the hub is a rigid body and the beam is flexible. The coordinate system $o_0 - x_0y_0$ is an inertial frame, while the coordinate system $o - xy$ is fixed to the end of the beam, and this beam is fixed to the hub. The effect of gravity on the hub and the beam is neglected. The flexible beam is characterized by its length L, Young's modulus E, cross-sectional area moment of inertia I, mass density per unit volume ρ, and cross-sectional area A. The radius of the hub is r_A, u is an external rotating torque acting on the hub, and θ describes the angular rotation of the hub. In the past few decades, researchers have proposed various dynamic models for the flexible hub-beam system, among which the zero-order approximation coupling (ZOAC) model and the first-order approximation coupling (FOAC) model are the most famous. The ZOAC model assumes the deformation in structural dynamics is small where axial and transverse displacements at any point in the beam are uncoupled; it may result in divergence to the system dynamic problem with high rotational speed, and it is only capable of solving cases with low rotational speed. In the FOAC model, the second-order coupling term of axial displacement caused by the transverse displacement of the flexible beam is considered, so the FOAC model is capable of both cases with low or high rotational speed. Cai, et al. conducted thorough studies on these two models. Details can be found in their research referenced in this study.[15–18] In this paper, the FOAC model is adopted to describe the flexible hub-beam system, and is given below.

In many of the sources referenced here,[15,16,18] the FOAC model of the hub-beam system is analysed in detail using the Hamilton's theory and the assumed-mode discretization method. It is expressed as

$$\mathbf{M}\ddot{\mathbf{Y}} + (2\dot{\theta}\mathbf{G} + \mathbf{C}_t)\dot{\mathbf{Y}} + \mathbf{K}\mathbf{Y} = \mathbf{Q} + \mathbf{F}; \qquad (1)$$

where

$$\mathbf{Y} = \begin{bmatrix} \theta \\ \mathbf{q}_1 \\ \mathbf{q}_2 \end{bmatrix}, \quad \mathbf{M} = \begin{bmatrix} J_H + M_{\theta\theta} & \mathbf{M}_{\theta q_1} & \mathbf{M}_{\theta q_2} \\ \mathbf{M}_{q_1\theta} & \mathbf{M}_{q_1 q_1} & \mathbf{0} \\ \mathbf{M}_{q_2\theta} & \mathbf{0} & \mathbf{M}_{q_2 q_2} \end{bmatrix},$$

$$\mathbf{G} = \begin{bmatrix} 0 & \mathbf{0} & \mathbf{0} \\ \mathbf{0} & 0 & \mathbf{G}_{q_1 q_2} \\ \mathbf{0} & \mathbf{G}_{q_2 q_1} & \mathbf{0} \end{bmatrix}, \quad \mathbf{Q} = \begin{bmatrix} Q_\theta \\ \mathbf{Q}_{q_1} \\ \mathbf{0} \end{bmatrix}, \quad \mathbf{F} = \begin{bmatrix} u \\ \mathbf{0} \\ \mathbf{0} \end{bmatrix},$$

$$\mathbf{K} = \begin{bmatrix} 0 & \mathbf{0} & \mathbf{0} \\ \mathbf{0} & \mathbf{K}_{q_1 q_1} & \mathbf{0} \\ \mathbf{0} & 0 & \mathbf{K}_{q_2 q_2} \end{bmatrix}, \quad \mathbf{C}_t = \begin{bmatrix} C_H & \mathbf{0} & \mathbf{0} \\ \mathbf{0} & \alpha_1 \mathbf{M}_1 & \mathbf{0} \\ \mathbf{0} & 0 & \alpha_2 \mathbf{M}_2 \end{bmatrix} +$$

$$\frac{\beta_1}{\rho A}\begin{bmatrix} M_{\theta\theta} & \mathbf{M}_{\theta q_1} & \mathbf{M}_{\theta q_2} \\ \mathbf{M}_{q_1\theta} & \mathbf{M}_{q_1 q_1} & \mathbf{0} \\ \mathbf{M}_{q_2\theta} & \mathbf{0} & \mathbf{M}_{q_2 q_2} \end{bmatrix} + \frac{\beta_2 \dot{\theta}\,\mathrm{sgn}(\dot{\theta})}{\rho A}\begin{bmatrix} C_{12} & \mathbf{C}_{21}^T & \mathbf{C}_{31}^T \\ \mathbf{C}_{21} & \mathbf{C}_{22} & \mathbf{0} \\ \mathbf{C}_{31} & \mathbf{0} & \mathbf{C}_{33} \end{bmatrix};$$

and where $\mathbf{q}_1$ and $\mathbf{q}_2$ are $n \times 1$ vectors representing modal coordinates of axial and transverse vibrations of the beam, respectively. The parameter $M_{\theta\theta}$ is a scalar representing the

total rotary inertia of the hub-beam system; $\mathbf{M}_{q_1q_1} = \mathbf{M}_1$ and $\mathbf{M}_{q_2q_2} = \mathbf{M}_2$, in which $\mathbf{M}_1$ and $\mathbf{M}_2$ are $n \times n$ generalized elastic mass matrices of the beam; $\mathbf{M}_{\theta q_1} = \mathbf{M}_{q_1\theta}^T$ and $\mathbf{M}_{\theta q_2} = \mathbf{M}_{q_2\theta}^T$ are $1 \times n$ vectors representing inertia effects caused by nonlinear coupling between large rotating motion and elastic deformation; $\mathbf{G}_{q_1q_2}$ and $\mathbf{G}_{q_2q_1}$ are $n \times n$ matrices resulted from gyroscopic effects; C_H is the viscous damping coefficient of the bearing of hub; α_1 and α_2 are the damping coefficients of the beam in axial and transverse directions, respectively; β_1 and β_2 are the viscous and square damping coefficients caused by the windward side of the beam, respectively; C_{11} is a scalar; $\mathbf{C}_{21}$ and $\mathbf{C}_{31}$ are both $n \times 1$ vectors; $\mathbf{C}_{22}$ and $\mathbf{C}_{33}$ are both $n \times n$ matrices; $\mathbf{K}_{q_1q_1}$ and $\mathbf{K}_{q_2q_2}$ are $n \times n$ stiffness matrices; Q_θ is a scalar; and $\mathbf{Q}_{q_1}$ is a $n \times 1$ vector. These quantities are defined as follows:

$$M_{\theta\theta} = J_1 + \mathbf{q}_1^T\mathbf{M}_1\mathbf{q}_1 + \mathbf{q}_2^T\mathbf{M}_2\mathbf{q}_2 + 2(r_A\mathbf{U}_{01} + \mathbf{U}_{11})\mathbf{q}_1 - \mathbf{q}_2^T(r_A\mathbf{D}_0 + \mathbf{D}_1)\mathbf{q}_2; \tag{2}$$

$$\mathbf{M}_{q_1\theta} = \mathbf{M}_{\theta q_1}^T = -\mathbf{R}\mathbf{q}_2; \tag{3}$$

$$\mathbf{M}_{\theta q_2} = \mathbf{M}_{q_2\theta}^T = r_A\mathbf{U}_{02} + \mathbf{U}_{12} + \mathbf{q}_1^T\mathbf{R}; \tag{4}$$

$$\mathbf{M}_{q_1q_1} = \mathbf{M}_1 = \int_0^L \rho A\mathbf{\Phi}_1^T\mathbf{\Phi}_1\,dx; \tag{5}$$

$$\mathbf{M}_{q_2q_2} = \mathbf{M}_2 = \int_0^L \rho A\mathbf{\Phi}_2^T\mathbf{\Phi}_2\,dx; \tag{6}$$

$$\mathbf{G}_{q_1q_2} = -\mathbf{G}_{q_2q_1}^T = -\mathbf{R}; \tag{7}$$

$$\mathbf{K}_{q_1q_1} = \mathbf{K}_1 - \dot\theta^2\mathbf{M}_1; \tag{8}$$

$$\mathbf{K}_{q_2q_2} = \mathbf{K}_2 - \dot\theta^2\mathbf{M}_2 + \dot\theta^2(r_A\mathbf{D}_0 + \mathbf{D}_1); \tag{9}$$

$$Q_\theta = -2\dot\theta\big[(\mathbf{q}_1^T\mathbf{M}_1\dot{\mathbf{q}}_1 + \mathbf{q}_2^T\mathbf{M}_2\dot{\mathbf{q}}_2) + (r_A\mathbf{U}_{01} + \mathbf{U}_{11})\dot{\mathbf{q}}_1 - \mathbf{q}_2^T(r_A\mathbf{D}_0 + \mathbf{D}_1)\dot{\mathbf{q}}_2\big]; \tag{10}$$

$$\mathbf{Q}_{q_1} = \dot\theta^2(r_A\mathbf{U}_{01}^T + \mathbf{U}_{11}^T); \tag{11}$$

$$C_{11} = \int_0^L \rho A(r_A + x)^3dx + \mathbf{q}_1^T\Big[r_A\mathbf{M}_1 + \int_0^L \rho Ax\mathbf{\Phi}_1^T\mathbf{\Phi}_1dx\Big]\mathbf{q}_1 + \mathbf{q}_2^T\Big[r_A\mathbf{M}_2 + \int_0^L \rho Ax\mathbf{\Phi}_2^T\mathbf{\Phi}_2dx\Big]\mathbf{q}_2 + 2\Big[r_A^2\mathbf{U}_{01} + 2r_A\mathbf{U}_{11} + \int_0^L \rho Ax^2\mathbf{\Phi}_1dx\Big]\mathbf{q}_1 - \mathbf{q}_2^T\Big[r_A^2\mathbf{D}_0 + 2r_A\mathbf{D}_1 + \int_0^L \rho Ax^2\mathbf{S}(x)dx\Big]\mathbf{q}_2; \tag{12}$$

$$\mathbf{C}_{21} = -\Big[r_A\mathbf{R} + \int_0^L \rho Ax\mathbf{\Phi}_1^T\mathbf{\Phi}_2dx\Big]\mathbf{q}_2; \tag{13}$$

$$\mathbf{C}_{31} = r_A^2\mathbf{U}_{02}^T + 2r_A\mathbf{U}_{12}^T + \int_0^L \rho Ax^2\mathbf{\Phi}_2^Tdx + \Big[r_A\mathbf{R} + \int_0^L \rho Ax\mathbf{\Phi}_2^T\mathbf{\Phi}_1dx\Big]\mathbf{q}_1; \tag{14}$$

$$\mathbf{C}_{22} = r_A\mathbf{M}_1 + \int_0^L \rho Ax\mathbf{\Phi}_1^T\mathbf{\Phi}_1dx; \tag{15}$$

$$\mathbf{C}_{33} = r_A\mathbf{M}_2 + \int_0^L \rho Ax\mathbf{\Phi}_2^T\mathbf{\Phi}_2dx; \tag{16}$$

where $\mathbf{K}_1$ and $\mathbf{K}_2$ in Eqs. (8) and (9) are $n \times n$ generalized elastic stiffness matrices of the beam. Parameters $\mathbf{\Phi}_1(x)$ and $\mathbf{\Phi}_2(x)$ in the above equations are $1 \times n$ vectors. They represent mode functions of axial and transverse vibrations of the beam, respectively, and they assume mode functions of the cantilever beam. The constant parameters in Eqs. (2)–(11) are given as follows:

$$J_1 = \int_0^L \rho A(r_A + x)^2dx; \tag{17}$$

$$\mathbf{K}_1 = \int_0^L EA\mathbf{\Phi}_1'^T\mathbf{\Phi}_1'dx; \tag{18}$$

$$\mathbf{K}_2 = \int_0^L EI\mathbf{\Phi}_2''^T\mathbf{\Phi}_2''dx; \tag{19}$$

$$\mathbf{U}_{0j} = \int_0^L \rho A\mathbf{\Phi}_jdx, \qquad j = 1, 2; \tag{20}$$

$$\mathbf{U}_{1j} = \int_0^L \rho Ax\mathbf{\Phi}_jdx, \qquad j = 1, 2; \tag{21}$$

$$\mathbf{D}_0 = \int_0^L \rho A\mathbf{S}(x)dx; \tag{22}$$

$$\mathbf{D}_1 = \int_0^L \rho Ax\mathbf{S}(x)dx; \tag{23}$$

$$\mathbf{R} = \int_0^L \rho A\mathbf{\Phi}_1^T\mathbf{\Phi}_2dx; \tag{24}$$

where J_1 is a scalar; $\mathbf{U}_{0j}$ and $\mathbf{U}_{1j}$ are both $1 \times n$ vectors; and $\mathbf{D}_0$, $\mathbf{D}_1$, and $\mathbf{R}$ are all $n \times n$ matrices. The parameter $\mathbf{S}(x)$ in Eqs. (22) and (23) is the coupling shape function, and this $n \times n$ matrix, discussed in sources used here,[15,16,18] is given by

$$\mathbf{S}(x) = \int_0^x \mathbf{\Phi}_2'^T(\xi)\mathbf{\Phi}_2'(\xi)d\xi. \tag{25}$$

3. ACTIVE CONTROL DESIGN

The FOAC model given above is nonlinear and time-varying. Control design directly using this model is difficult, since nonlinear control theory is still under intensive and continuous development, though nowadays linear control theory is comprehensive, and linear control design has many practical applications. Here, we linearise the FOAC model, and use a linear optimal tracking control method to design a controller to control the flexible hub-beam system.

3.1. Linearisation of the FOAC Model

The effect of axial vibrations of the flexible beam on system dynamics is much smaller than that of transverse vibrations, and can be neglected. In classical linearisation for the flexible hub-beam system, it is often assumed that the angular velocity of rotational motion is small, so the related terms and their higher order terms are neglected.[19] Increment of rotary inertia of the beam caused by its elastic deformation is also small, which results in the omission of terms related to $\mathbf{q}_1$ and $\mathbf{q}_2$ in Eq. (2).[19] So, the linearised model of hub-beam system can be

written as[18,19]

$$\begin{bmatrix} J_H+J_1 & \mathbf{M}_{\theta q_2} \\ \mathbf{M}_{q_2\theta} & \mathbf{M}_2 \end{bmatrix}\begin{bmatrix} \ddot{\theta} \\ \ddot{\mathbf{q}}_2 \end{bmatrix} + \begin{bmatrix} C_H+\frac{\beta_1}{\rho A}J_1 & \frac{\beta_1}{\rho A}\mathbf{M}_{\theta q_2} \\ \frac{\beta_1}{\rho A}\mathbf{M}_{q_2\theta} & (\alpha_2+\frac{\beta_1}{\rho A})\mathbf{M}_2 \end{bmatrix}\begin{bmatrix} \dot{\theta} \\ \dot{\mathbf{q}}_2 \end{bmatrix} + \begin{bmatrix} 0 & \mathbf{0} \\ \mathbf{0} & \mathbf{K}_2 \end{bmatrix}\begin{bmatrix} \theta \\ \mathbf{q}_2 \end{bmatrix} = \begin{bmatrix} u \\ \mathbf{0} \end{bmatrix}; \tag{26}$$

where J_1, $\mathbf{M}_{\theta q_2}$, $\mathbf{M}_{q_2\theta}$, $\mathbf{M}_2$, and $\mathbf{K}_2$ are given by Eqs. (17), (4), (6) and (19), respectively. In the expressions of $\mathbf{M}_{\theta q_2}$ and $\mathbf{M}_{q_2\theta}$, the term of $\mathbf{q}_1^T\mathbf{R}$ should be neglected.

In matrix form, Eq. (26) may be written as

$$\hat{\mathbf{M}}\ddot{\hat{\mathbf{Y}}} + \hat{\mathbf{C}}\dot{\hat{\mathbf{Y}}} + \hat{\mathbf{K}}\hat{\mathbf{Y}} = \overline{\mathbf{H}}u; \tag{27}$$

where $\hat{\mathbf{Y}} = \begin{bmatrix} \theta \\ \mathbf{q}_2 \end{bmatrix}$, $\hat{\mathbf{M}} = \begin{bmatrix} J_H+J_B & \mathbf{M}_{\theta q_2} \\ \mathbf{M}_{q_2\theta} & \mathbf{M}_2 \end{bmatrix}$, $\hat{\mathbf{C}} = \begin{bmatrix} C_H+\frac{\beta_1}{\rho A}J_1 & \frac{\beta_1}{\rho A}\mathbf{M}_{\theta q_2} \\ \frac{\beta_1}{\rho A}\mathbf{M}_{q_2\theta} & (\alpha_2+\frac{\beta_1}{\rho A})\mathbf{M}_2 \end{bmatrix}$, $\hat{\mathbf{K}} = \begin{bmatrix} 0 & \mathbf{0} \\ \mathbf{0} & \mathbf{K}_2 \end{bmatrix}$, and $\overline{\mathbf{H}} = \begin{bmatrix} 1 \\ \mathbf{0} \end{bmatrix}$.

In state-space formulation, Eq. (27) becomes

$$\dot{\mathbf{x}} = \overline{\mathbf{A}}\mathbf{x} + \overline{\mathbf{B}}u; \tag{28}$$

where $\mathbf{x} = \begin{bmatrix} \hat{\mathbf{Y}} \\ \dot{\hat{\mathbf{Y}}} \end{bmatrix}$, $\overline{\mathbf{A}} = \begin{bmatrix} \mathbf{0} & \mathbf{I}_{2(n+1)\times 2(n+1)} \\ -\hat{\mathbf{M}}^{-1}\hat{\mathbf{K}} & -\hat{\mathbf{M}}^{-1}\hat{\mathbf{C}} \end{bmatrix}$, and $\overline{\mathbf{B}} = \begin{bmatrix} \mathbf{0} \\ \hat{\mathbf{M}}^{-1}\overline{\mathbf{H}} \end{bmatrix}$.

3.2. Controller Design

The optimal tracking controller is investigated in this section. The desired state trajectory of the system is assumed to be given by $\mathbf{x}_d = \left[\hat{\mathbf{Y}}_d^T,\ \dot{\hat{\mathbf{Y}}}_d^T\right]^T$, where $\hat{\mathbf{Y}}_d^T = \left[\theta_d,\ \mathbf{q}_{2d}^T\right]^T$. The following state error vector is defined as

$$\mathbf{e} = \mathbf{x}_d - \mathbf{x}; \tag{29}$$

and the performance index is defined as

$$J = \frac{1}{2}\int_0^\infty \left(\mathbf{e}^T\mathbf{Q}\mathbf{e} + \overline{R}u^2\right)dt; \tag{30}$$

where $\mathbf{Q}$ is a $2(n+1)\times 2(n+1)$ weighting matrix, which is positive definite and symmetric, and $\overline{R}$ is a positive weighting scalar. The optimal tracking control law may be obtained as[20]

$$u = -\overline{R}^{-1}\overline{\mathbf{B}}^T\mathbf{P}\mathbf{x} + \overline{R}^{-1}\overline{\mathbf{B}}^T\left[\mathbf{P}\overline{\mathbf{B}}\overline{R}^{-1}\overline{\mathbf{B}}^T - \overline{\mathbf{A}}^T\right]^{-1}\mathbf{Q}\mathbf{x}_d; \tag{31}$$

where $\mathbf{P}$ is the solution of the Riccati equation

$$\mathbf{P}\overline{\mathbf{A}} + \overline{\mathbf{A}}^T\mathbf{P} - \mathbf{P}\overline{\mathbf{B}}\overline{R}^{-1}\overline{\mathbf{B}}^T\mathbf{P} = -\mathbf{Q}. \tag{32}$$

In the controller Eq. (31), the first term is a linear function of state $\mathbf{x}$, representing the regulating role of negative feedback. The second term is a linear function of the desired state $\mathbf{x}_d$, representing a driving action resulting from $\mathbf{x}_d$.

4. PARAMETER IDENTIFICATION OF THE SYSTEM

In this section, parameter identification technology will be investigated for the system. The observer/Kalman filter identification (OKID) and eigensystem realization algorithm (ERA) will be used in the parameter identification. These two methods are both time-domain identification techniques and have successful applications in spacecraft.

4.1. Description for OKID Technique

The OKID is a time-domain identification technique, proposed by Juang, et al.[21] Consider the following discrete linear system

$$\begin{cases} \mathbf{x}(k+1) = \mathbf{A}\mathbf{x}(k) + \mathbf{B}u(k) \\ \mathbf{y}(k) = \mathbf{C}\mathbf{x}(k) + \mathbf{D}u(k) \end{cases}; \tag{33}$$

where $\mathbf{x}$ is $2(n+1)$-dimensional state vector; u is the input torque; and $\mathbf{y}$ is $q\times 1$ output vector. The matrices $\mathbf{A}$, $\mathbf{B}$, $\mathbf{C}$, and $\mathbf{D}$ are the system matrix, input matrix, output matrix, and influence matrix, respectively. From the recursive relations of Eq. (33), one can obtain the expression of the system output at $k\overline{T}$ moment ($\overline{T}$ denotes the data sampling period) as

$$\begin{aligned} \mathbf{y}(k) &= \mathbf{C}\mathbf{A}^k\mathbf{x}(0) + \sum_{\tau=0}^{k-1}\mathbf{C}\mathbf{A}^\tau\mathbf{B}u(k-\tau-1) + \mathbf{D}u(k) \\ &= \mathbf{C}\mathbf{A}^k\mathbf{x}(0) + \sum_{\tau=0}^{k-1}\mathbf{Y}_\tau u(k-\tau-1) + \mathbf{D}u(k); \end{aligned} \tag{34}$$

where $\mathbf{Y}_\tau = \mathbf{C}\mathbf{A}^\tau\mathbf{B}$ and $\mathbf{D}$ are the system Markov parameters to be identified. If the initial condition of the system is zero or given, i.e., if $\mathbf{x}(0)$ at $k=0$ is known, the system Markov parameters can be determined directly using Eq. (34).[21] However, for a practical engineering structure, the exact value of initial condition is difficult to determine. Even though the structure is at an equilibrium state and does not suffer from any external excitation, the zero initial condition cannot be exactly guaranteed; yet, there are always certain affecting factors that make it impossible for the initial condition to be zero. Errors may occur inevitably when the system Markov parameters are identified using Eq. (34) based on the input-output data of the system. To eliminate the influence of the initial conditions on the identification of system Markov parameters, we firstly construct a state observer whose Markov parameter equation is independent of the initial condition, and by solving this equation based on the input-output data to get the observer's parameters, and then by establishing the relationship of Markov parameters between the observer and the original system, we finally work out the Markov parameters of the original system. The detailed process is described below.

The following state observer is constructed as[21]

$$\begin{cases} \widehat{\mathbf{x}}(k+1) = \mathbf{A}\widehat{\mathbf{x}}(k) + \mathbf{B}u(k) - \mathbf{F}\left[\mathbf{y}(k) - \widehat{\mathbf{y}}(k)\right] \\ \qquad\qquad = (\mathbf{A}+\mathbf{F}\mathbf{C})\widehat{\mathbf{x}}(k) + (\mathbf{B}+\mathbf{F}\mathbf{D})u(k) - \mathbf{F}\mathbf{y}(k) \\ \widehat{\mathbf{y}}(k) = \mathbf{C}\widehat{\mathbf{x}}(k) + \mathbf{D}u(k) \end{cases}; \tag{35}$$

where $\mathbf{F}$ is the weighting matrix of the observer. The eigenvalues of $\mathbf{A}+\mathbf{FC}$ are adjusted by the selection of $\mathbf{F}$ such that the state $\widehat{\mathbf{x}}(k)$ of the observer approaches the real state $\mathbf{x}(k)$ of the system. The output of the observer at $k\overline{T}$ moment can be written as

$$\widehat{\mathbf{y}}(k)=\mathbf{C}(\mathbf{A}+\mathbf{FC})^k\widehat{\mathbf{x}}(0)+\sum_{\tau=0}^{k-1}\widehat{\mathbf{Y}}_\tau\left[u^T(k-\tau-1)\ \ \mathbf{y}^T(k-\tau-1)\right]^T+\mathbf{D}u(k); \quad (36)$$

where $\widehat{\mathbf{Y}}_\tau$ and $\mathbf{D}$ are the observer Markov parameters; $\widehat{\mathbf{Y}}_\tau$ is expressed as

$$\widehat{\mathbf{Y}}_\tau=\left[\mathbf{C}(\mathbf{A}+\mathbf{FC})^\tau(\mathbf{B}+\mathbf{FD})\ \ -\mathbf{C}(\mathbf{A}+\mathbf{FC})^\tau\mathbf{F}\right]=\left[\widehat{\mathbf{Y}}_\tau^{(1)}\ \ \widehat{\mathbf{Y}}_\tau^{(2)}\right]; \quad (37)$$

where $\widehat{\mathbf{Y}}_\tau^{(1)}=\mathbf{C}(\mathbf{A}+\mathbf{FC})^\tau(\mathbf{B}+\mathbf{FD})$ and $\widehat{\mathbf{Y}}_\tau^{(2)}=-\mathbf{C}(\mathbf{A}+\mathbf{FC})^\tau\mathbf{F}$.

By selecting $\mathbf{F}$ to make the pole of $\mathbf{A}+\mathbf{FC}$ on the origin, the eigenvalue equation of $\mathbf{A}+\mathbf{FC}$ will be $(\lambda-\lambda_i)^{2(n+1)}$; where λ_i is the i-th eigenvalue. Then by the Hamilton-Cayley theorem, we have $(\mathbf{A}+\mathbf{FC})^{2(n+1)}=\mathbf{0}$. From Eqs. (33) and (34) and by some derivation, the state error equation can be written as

$$\mathbf{x}(k+1)-\widehat{\mathbf{x}}(k+1)=(\mathbf{A}+\mathbf{FC})[\mathbf{x}(k)-\widehat{\mathbf{x}}(k)]. \quad (38)$$

By the recurrence of the state error equation, when $k\geq n$, we have

$$\begin{aligned}\mathbf{x}(k+1)-\widehat{\mathbf{x}}(k+1)&=(\mathbf{A}+\mathbf{FC})[\mathbf{x}(k)-\widehat{\mathbf{x}}(k)]\\&=(\mathbf{A}+\mathbf{FC})^2[\mathbf{x}(k-1)-\widehat{\mathbf{x}}(k-1)]\\&\ \ \vdots\\&=(\mathbf{A}+\mathbf{FC})^{2(n+1)}[\mathbf{x}(k-2n-1)-\widehat{\mathbf{x}}(k-2n-1)]\\&=\mathbf{0}.\end{aligned} \quad (39)$$

From Eq. (39), when $k\geq 2(n+1)$, the state $\widehat{\mathbf{x}}(k)$ of the observer will converge to the real state $\mathbf{x}(k)$, i.e., $\mathbf{x}(k)=\widehat{\mathbf{x}}(k)$ $(k\geq 2(n+1))$. So, from the second equation of Eq. (35), the output $\widehat{\mathbf{y}}(k)$ of the observer will converge to the real output $\mathbf{y}(k)$ when $k\geq 2(n+1)$, i.e., $\mathbf{y}(k)=\widehat{\mathbf{y}}(k)$ $(k\geq 2(n+1))$. From Eq. (37), we know that $\widehat{\mathbf{Y}}_\tau=\mathbf{0}$ when $\tau\geq 2(n+1)$. Therefore, when $k\geq 2(n+1)$, Eq. (36) can be written as

$$\mathbf{y}(k)=\sum_{\tau=0}^{2n+1}\widehat{\mathbf{Y}}_\tau\left[u(k-\tau-1)\ \ \mathbf{y}^T(k-\tau-1)\right]^T+\mathbf{D}u(k),\quad k\geq 2(n+1). \quad (40)$$

Equation (40) holds strictly and is independent of the initial condition of the system. But Eq. (36) is subject to the initial condition. Using the least squares to solve Eq. (40), the Markov parameters $\widehat{\mathbf{Y}}_\tau$ and $\mathbf{D}$ of the observer can be obtained.[21] The relationship of Markov parameters between the original system and the observer is[21,22]

$$\mathbf{Y}_\tau=\mathbf{CA}^\tau\mathbf{B}=\widehat{\mathbf{Y}}_\tau^{(1)}+\sum_{k=0}^{\tau-1}\widehat{\mathbf{Y}}_k^{(2)}\widehat{\mathbf{Y}}_{\tau-k-1}+\widehat{\mathbf{Y}}_\tau^{(2)}\mathbf{D}. \quad (41)$$

Based on the input-output data of the system, Markov parameters of the observer can be obtained from Eq. (40), and Markov parameters of the original system can be obtained from Eq. (41). The minimal state-space realization of the system can be determined by using the eigensystem realization algorithm (ERA) given in the following Section 4.2. From the above process, we can observe that the specific value of $\mathbf{F}$ is not needed in the entire calculation for Markov parameters.

4.2. Eigensystem Realization Algorithm (ERA)

The ERA is a well-established algorithm for parameter identification in time domain. It utilizes impulse response data of the system to seek the minimal state-space realization $(\mathbf{A}_r,\mathbf{B}_r,\mathbf{C}_r,\mathbf{D}_r)$ by the singular value decomposition of the Hankel block matrix.

The $(\overline{s}+1)\times(\overline{t}+1)$ Hankel block matrix is constructed as[23,24]

$$\mathbf{H}(\tau)=\begin{bmatrix}\mathbf{Y}_\tau & \mathbf{Y}_{\tau+1} & \cdots & \mathbf{Y}_{\tau+\overline{t}}\\ \mathbf{Y}_{\tau+1} & \mathbf{Y}_{\tau+2} & \cdots & \mathbf{Y}_{\tau+1+\overline{t}}\\ \vdots & \vdots & \ddots & \vdots\\ \mathbf{Y}_{\tau+\overline{s}} & \mathbf{Y}_{\tau+\overline{s}+1} & \cdots & \mathbf{Y}_{\tau+\overline{s}+\overline{t}}\end{bmatrix}. \quad (42)$$

The matrix $\mathbf{H}(\tau)$ can be written as the following form:

$$\mathbf{H}(\tau)=\overline{\mathbf{V}}_{\overline{s}}\mathbf{A}^\tau\overline{\mathbf{W}}_{\overline{t}}; \quad (43)$$

where $\overline{\mathbf{V}}_{\overline{s}}=\left[\mathbf{C}^T\ (\mathbf{CA})^T\ (\mathbf{CA}^2)^T\ \ldots\ (\mathbf{CA}^{\overline{s}})^T\right]^T$, $\overline{\mathbf{W}}_{\overline{t}}=\left[\mathbf{B}\ \mathbf{AB}\ \mathbf{A}^2\mathbf{B}\ \ldots\ \mathbf{A}^{\overline{t}}\mathbf{B}\right]$ are the controllable and observable matrices of the system, respectively. It is well known that for the system with the order $2(n+1)$, the minimal dimension of the system matrix is $2(n+1)\times 2(n+1)$. If $\overline{s}+1\geq 2(n+1)$, $\overline{t}+1\geq 2(n+1)$, and the system is controllable and observable, the rank of $\overline{\mathbf{V}}_{\overline{s}}$ and $\overline{\mathbf{W}}_{\overline{t}}$ will be both n; therefore, the rank of the Hankel block matrix $\mathbf{H}(\tau)$ will be $2(n+1)$. By performing the singular value decomposition of $\mathbf{H}(0)$, we have

$$\mathbf{H}(0)=\mathbf{UNV}^T; \quad (44)$$

where $\mathbf{U}$ and $\mathbf{V}$ are both unitary matrix, and $\mathbf{N}$ is the eigenvalue diagonal matrix, given by

$$\mathbf{N}=\mathrm{diag}(d_1,d_2,\ldots,d_r,d_{r+1},\ldots),\quad d_1\geq d_2\geq\ldots\geq d_r\geq d_{r+1}\geq\ldots\geq 0. \quad (45)$$

Assuming that the order of minimal realization of the system is r, r can be determined using the following singular value truncation threshold ε:

$$\frac{d_r}{d_1}\geq\varepsilon,\qquad\frac{d_{r+1}}{d_1}\leq\varepsilon. \quad (46)$$

Let $\mathbf{U}_r$ be the first r columns of $\mathbf{U}$, let $\mathbf{V}_r$ be the first r columns of $\mathbf{V}$, and let $\mathbf{N}_r=\mathrm{diag}(d_1,d_2,\ldots,d_r)$. Now define the following matrices:

$$\mathbf{E}_q^T=\left[\mathbf{I}_q\ \mathbf{0}_{q\times(l-1)q}\right],\qquad\mathbf{E}_m^T=\left[\mathbf{I}_m\ \mathbf{0}_{m\times(l-1)m}\right]; \quad (47)$$

where $\mathbf{I}_q$ and $\mathbf{I}_m$ are q-dimensional and m-dimensional unit matrices, respectively. The minimal realization $(\mathbf{A}_r, \mathbf{B}_r, \mathbf{C}_r, \mathbf{D}_r)$ of the system can be determined as[23,24]

$$\begin{aligned}\mathbf{A}_r &= \mathbf{N}_r^{-1/2}\mathbf{U}_r^T\mathbf{H}(1)\mathbf{V}_r\mathbf{N}_r^{-1/2},\\ \mathbf{B}_r &= \mathbf{N}_r^{1/2}\mathbf{V}_r\mathbf{E}_m,\\ \mathbf{C}_r &= \mathbf{E}_q^T\mathbf{U}_r\mathbf{N}_r^{1/2}.\end{aligned} \tag{48}$$

By solving the eigenvalues of $\mathbf{A}_r$, we can obtain

$$\boldsymbol{\psi}^{-1}\mathbf{A}_r\boldsymbol{\psi} = \boldsymbol{\Lambda}, \qquad \boldsymbol{\Lambda} = \mathrm{diag}(\overline{\lambda}_1, \overline{\lambda}_2, \ldots, \overline{\lambda}_{2(n+1)}); \tag{49}$$

where $\boldsymbol{\psi}$ is the eigenvector matrix of $\mathbf{A}_r$ and $\overline{\lambda}_i$ $(i = 1, 2, \ldots, 2(n+1))$ is the i-th eigenvalue. Define the following parameter:

$$s_i = \frac{\ln(\overline{\lambda}_i)}{T}, \qquad i = 1, 2, \ldots, 2(n+1); \tag{50}$$

where T is the data sampling period. Then, the natural frequency ω_i can be obtained as

$$\omega_i = \sqrt{[\mathrm{Re}(s_i)]^2 + [\mathrm{Im}(s_i)]^2}, \quad i = 1, 2, \ldots, 2(n+1); \tag{51}$$

where $\mathrm{Re}(s_i)$ and $\mathrm{Im}(s_i)$ are the real part and imaginary part of s_i, respectively.

5. NUMERICAL SIMULATIONS

In this section, numerical simulations are carried out to demonstrate the effectiveness of the identification method proposed in this paper. The radius of the hub is assumed to be $r_A = 0.05$ m, and its rotary inertia is $J_H = 0.30$ kgm^2. The properties of the flexible beam are given as follows: The length is $L = 1.8$ m, the cross-section area is $A = 2.5 \times 10^{-4}$ m^2, the area rotary inertia is $I = 1.3021 \times 10^{-10}$ m^4, the mass density is $\rho = 2.766 \times 10^3$ kg/m^3, and the modulus of elasticity is $E = 6.90 \times 10^{10}$ N/m^2. The damping parameters adopted in Yang's study of dynamic modelling theory[25] are set to $\alpha_1 = \alpha_2 = 0.011$, $\beta_1 = 0$, $\beta_2 = 0.0353$, and $C_H = 0$. For the flexible cantilever beam with no large motion, the fundamental frequency is 0.622 Hz.

Assume that the following rotating torque is put on the hub:

$$u(t) = \begin{cases} u_0 \sin\left(\frac{2\pi}{T}t\right), & 0 \le t \le T \\ 0 & t > T \end{cases}; \tag{52}$$

where $T = 2$ s and $u_0 = 1$ Nm. The tip transverse response of the beam and the time history of angle displacement of large motion of the hub are displayed in Fig. 2. The domain frequency of the tip transverse response of the beam based on the FOAC model is the first-order frequency (1.381 Hz), and the weightiness of the second order frequency is very small. Due to the effect of large motion, the first-order frequency now is 2.2 times that of the fundamental frequency without rotation. This is the so-called dynamic stiffening phenomenon, which results from the additional stiffness caused by the coupling of

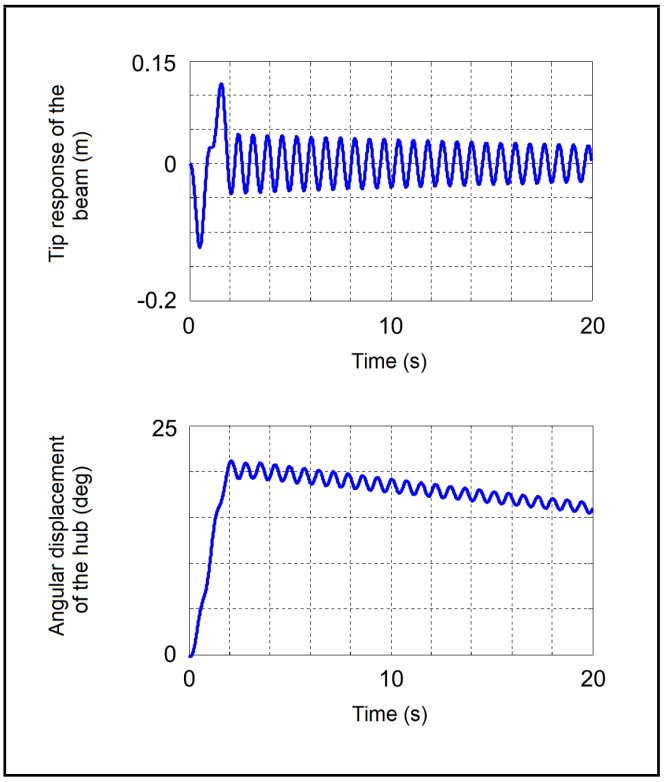

Figure 2. The tip response of the beam and the time history of angular displacement of the hub.

large rotation of the rigid hub and small elastic vibration of the flexible beam.[25] In Yang's study, dynamics experiments of flexible hub-beam system were done, in which several beams of different lengths were taken into account, and the experimental results indicate that the domain vibration frequency of the beam with rotation is always about 2.2 times that of the fundamental frequency of the beam without rotation.[25] Based on this conclusion, the first-order frequency is set to be the target of parameter identification.

In the identification simulations, three cases are considered: white-noise excitation, position control, and constant-speed rotation control. A white-noise case means that the external torque on the hub is a white-noise signal. A position control case means that a controller on the hub is designed to drive the system from one position to another, and the residual vibration of the beam should be suppressed by this controller after the arrival of position. Constant-speed rotation control means that a controller is designed to drive the system to rotate with a constant angular velocity, and the residual vibration of the beam should be suppressed. The angular displacement and angular velocity of the hub, and the tip transverse response of the beam, will be used as the output of the system in the parameter identifications. The detailed input-output arrangements are:

- Case 1: white-noise torque is used as the input of the system; the angular velocity of the hub and the tip transverse response of the beam are used as the output of the system, respectively.

- Case 2: the position controller is used as the input; the angular displacement of the hub and the tip transverse re-

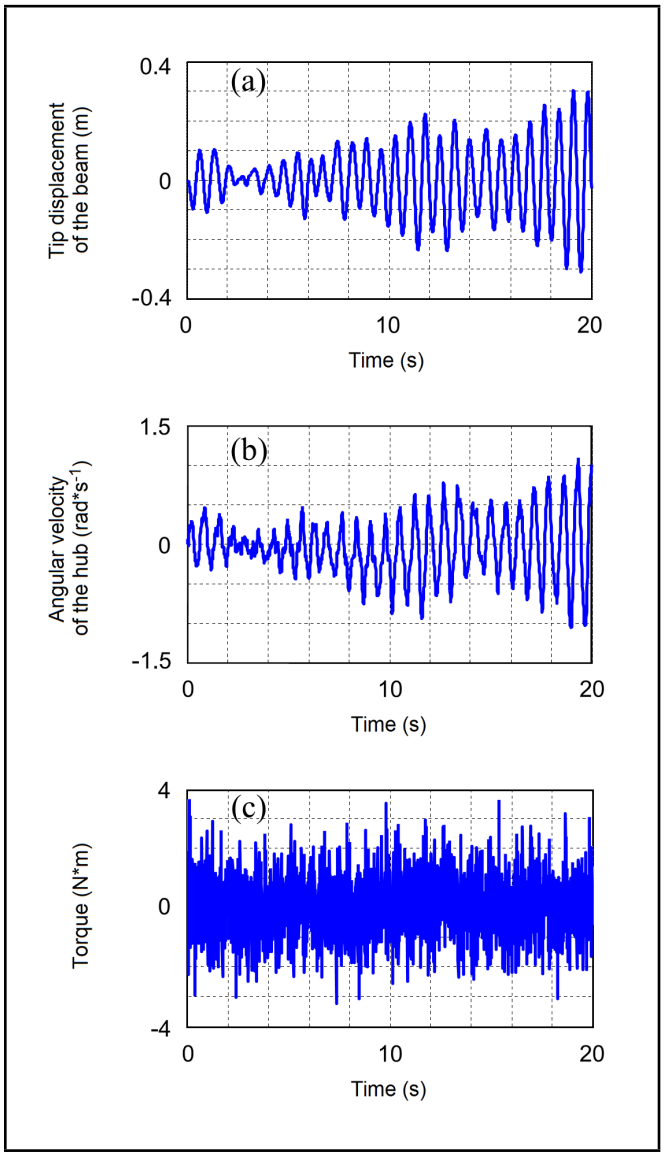

Figure 3. The responses of the system under white-noise excitation: (a) tip displacement of the beam, (b) angular velocity of the hub, and (c) white-noise excitation.

sponse of the beam are used as the output, respectively.

- Case 3: the constant-speed rotation controller is used as the input; the angular velocity of the hub and the tip transverse response of the beam are used as the output, respectively.

Then, parameter identifications will be done for the above three cases. The data sampling period is all chosen as 100 Hz in the simulations. First, we consider the white-noise case. The tip transverse response of the beam, the time history of angular velocity of the hub, and white noise torque are displayed in Fig. 3. So, the input and output data of the system are both known; thus the OKID and ERA may be used to identify the first-order frequency of the system, and the results are given in the third and fourth rows of Table 1. The theoretical result is given in the second row of Table 1 for comparison, as well. We can observe from Table 1 that the identification results are very close to the theoretical ones, which proves the validity of the methods in this paper.

Table 1. The identification results of the first-order frequency of the system.

Case	Output signal	Frequency (Hz)	Error (%)
Theoretical results		1.3810	
White-noise excitation	Tip transverse response of beam	1.3841	0.224475
	Angular velocity of beam	1.3834	0.173787
Position control	Tip transverse response of beam	1.3762	0.347574
	Angular displacement of hub	1.3722	0.637219
Constant-speed control	Tip transverse response of beam	1.3811	0.007241
	Angular velocity of hub	1.3810	0.000000

Next, we consider the active position control of a flexible hub-beam system. The desired position trajectory adopted by Cai, et al. and Zhang[18,19] is used here, given by

$$\theta = \begin{cases} \frac{2\theta_0}{T^2}t^2 & t \le \frac{T}{2} \\ \frac{\theta_0}{2} + \frac{2\theta_0}{T}\left(t - \frac{T}{2}\right) - \frac{2\theta_0}{T^2}\left(t - \frac{T}{2}\right)^2 & \frac{T}{2} < t \le T \\ \theta_0 & t > T \end{cases}. \tag{53}$$

Equation (53) indicates that the system rotates with an accelerated motion from the initial condition. The angular velocity of the system reaches its maximum value at the moment $T/2$, and then the system rotates with a decelerated motion, and the angular velocity turns zero after the moment T. The controller to be designed is required to drive the system to a desired position and suppress the residual vibration of beam after arrival. Assume that the end position of angular displacement in Eq. (53) is $\theta_0 = \pi/3 = 60°$. The parameter $T = 2$ s is taken in Eq. (53). In designing the active controller, the weighting matrix and the weighting scalar in Eq. (32) are chosen as $\mathbf{Q} = \mathrm{diag}(1000, 100, 10, 1, 1, 1)$, and $\overline{R} = 1$. The responses of the system are given in Fig. 4. It is observed from Fig. 4 that the desired position may be achieved and the residual vibration of the beam may be suppressed. Using the OKID and ERA to identify the vibration frequency, the results are shown in rows 5 and 6 of Table 1, and they are also very close to the theoretical value.

Finally, we consider the constant-speed rotation control of the hub-beam system. It is assumed that the system rotates with an accelerated motion from the initial condition. The aim of control design is to drive the system to rotate from the zero moment and reach an angular velocity $\dot{\theta}$ at moment T. Then, the system is required to rotate with this constant angular velocity $\dot{\theta}$. At the same time, residual vibration of the beam should be suppressed by this controller. $\dot{\theta} = 1$ rad/s and $T = 2$ s here. In controller design, the weighting matrix $\mathbf{Q}$ and the weighting scalar $\overline{R}$ are the same as the above cases. The responses of the system are displayed in Fig. 5. Using the input and output data to identify the vibration frequency of the system, the results are shown in rows 7 and 8 of Table 1. Similar to the above two cases, the identification results are almost identical to the theoretical one, and the identification precision

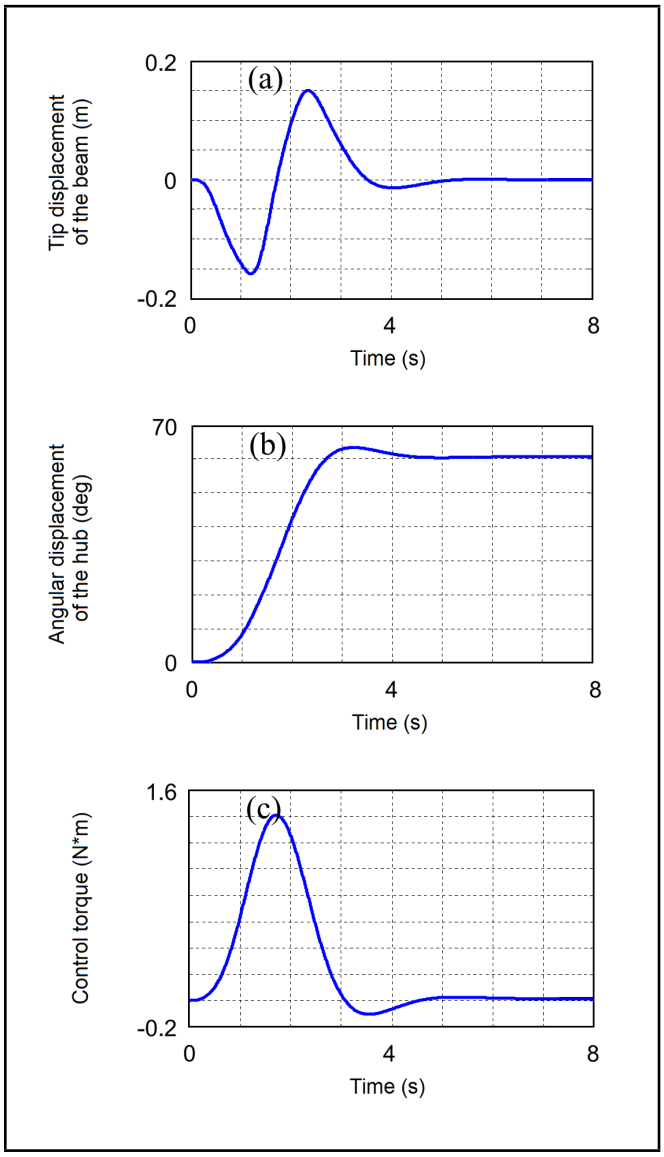

Figure 4. The responses of the system for the position control case: (a) tip displacement of the beam, (b) angular displacement of the hub, and (c) control torque.

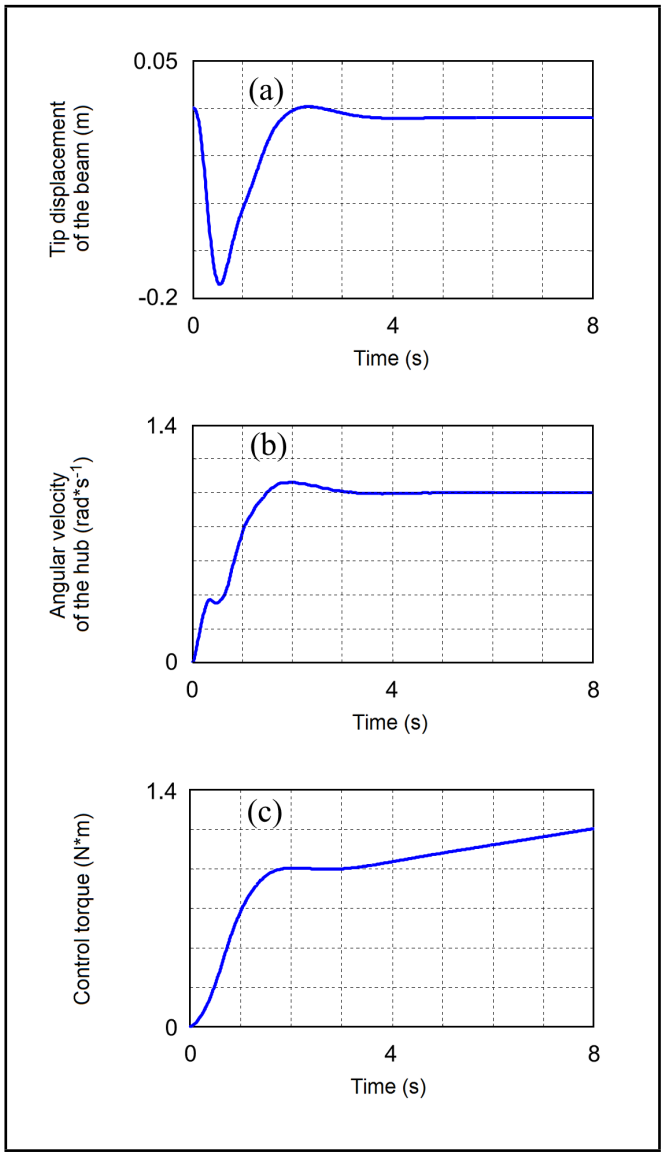

Figure 5. The responses of the system for the constant-speed case: (a) tip displacement of the beam, (b) angular velocity of the hub, and (c) control torque.

is higher than in the above two cases, as well.

From the above simulations we can draw a conclusion that the first-order frequency of the system can be effectively identified using the OKID and ERA as long as the input and output data of the system are known. This technique may possibly be applied to the on-orbit identification of spacecraft. The on-orbit identification needs the vibration response of spacecraft, and the attitude manoeuvre of spacecraft exactly provides an excitation, so it can be accomplished without adding additional space missions.

6. CONCLUSIONS

In this paper, active control and parameter identification are studied based on a flexible hub-beam system. The first-order approximation coupling (FOAC) model is introduced. The optimal tracking control theory is used for the active control of the system. A parameter identification technology is presented using the OKID and ERA. The research results indicate that the desired position of the system may be achieved by using the controller, and the residual vibration of the beam can be suppressed, as well. The system frequency may be identified effectively by the OKID and ERA, no matter what kind of external torque is put on the hub. It is feasible and effective to obtain the system frequency using the control data.

ACKNOWLEDGEMENT

This work was supported by the Key Project (11132001) and the General Project (11272202) of Natural Science Foundation of China, the Aviation Science Foundation of China (20120157002), and the Key Scientific Project of Shanghai Municipal Education Commission (14ZZ021).

REFERENCES

[1] Haugse, E. D., Juengst, C. D., Salus, W. L., and Lollock, J. A. On orbit system identification, *A collection of technical papers : 37th AIAA/ASME/ASCE/AHS/ASC Structures,*

Structural Dynamics, and Materials Conference, **4**, 2398–2407, American Institute of Aeronautics and Astronautics, Washington, DC, (1996).

[2] Kim, H. M., Van Horn, D. A., and Doiron, H. H. Free-decay time-domain modal identification for large space structures, *Journal of Guidance, Control, and Dynamics*, **17** (3), 513–519, (1994).

[3] Kasai, T., Komatsu, K., and Sano, M. Modal parameter identification of controlled structures, *Journal of Guidance, Control, and Dynamics*, **20** (1), 184–186, (1997).

[4] Yamaguchi, I. and Kida, T. ETS-VI on-orbit system identification experiments, *JSME International Journal*, **40** (4), 623–629, (1997).

[5] Adachi, S. and Yamaguchi, I. On-orbit system identification experiments on Engineering Test Satellite-VI, *Control Engineering Practice*, **7**, 831–841, (1999).

[6] Yamaguchi, I., Kida, T., and Kasai, T. Experimental demonstration of LSS system identification by eigensystem realization algorithm, *Proceedings of American Control Conference*, Seattle, Washington, 407–411, (1995).

[7] Ishikawa, S., Yamada, K., Yamaguchi, I., Chida, Y., and Adachi, S. ETS-VI on-orbit parameter estimation by random excitation, *Proceedings of Astrodynamics Symposium*, Halifax, Nova Scotia, Canada, (1995).

[8] Kasai, T., Komatsu, K., and Sano, M. Modal parameter identification of controlled flexible structures, *AIAA Journal of Guidance, Control, and Dynamics*, **20** (2), 184–186, (1997).

[9] Kaouk, M., McNeill, S., Haley, S., et al. Shuttle-ISS flight-7A on orbit test verification: pre and post flight analysis, Society for Experimental Mechanics, Boeing Company, (2003).

[10] Kaouk, M., Haley, S., Bartkowicz, T., et al. Modal analysis and correlation of International Space Station 4A mated configuration, Society for Experimental Mechanics, Boeing Company, (2002).

[11] Kim, H. M. and Bokhour, E. B. Mir structural dynamics experiment: a flight experiment development, *Proceedings of the 38th AIAA SDM Conference*, Kissimmee, Florida, 577–585, (1997).

[12] Kim, H. M. and Kaouk, M. Mir structural dynamics experiment: first phase test and data analysis, *Proceedings of the 39th AIAA SDM Conference*, Long Beach, CA, 204–212, (1998).

[13] Kim, H. M. and Kaouk, M. Mir structural dynamics experiment: first phase test and model refinement, *Proceedings of the 40th SDM Conference*, St. Louis, MO, (1999).

[14] Shuttle-Mir Docking Mission 5: Structural mathematical Models. STS-81, WG-03 Operations and Systems Integration Document, NASA-JSC Document #WG-3/RSC E/NASA/000/3412-5, (1996).

[15] Cai, G-P., Hong, J. Z., and Yang, S. X. Dynamic analysis of a flexible hub-beam system with tip mass, *Mechanics Research Communications*, **32** (2), 173–190, (2005).

[16] Cai, G-P. and Lim, C. W. Active control of a flexible hub-beam system using optimal tracking control method, *International Journal of Mechanical Sciences*, **48** (10), 1150–1162, (2006).

[17] Cai, G-P. and Lim, C. W. Optimal tracking control of a flexible hub-beam system with time delay, *Multibody System Dynamics*, **16** (4), 331–305, (2006).

[18] Cai, G-P., Hong, J. Z., and Yang, S. X. Model study and active control of a rotating flexible cantilever beam, *International Journal of Mechanical Sciences*, **46** (6), 871–889, (2004).

[19] Zhang, L. T. Study of control simulations of a flexible manipulator system, Master Thesis in Shanghai Jiaotong University, China, (2002).

[20] Hu, S. S. *Automatic Control Theory*, Defence Industry Press, Beijing, China, (1998).

[21] Juang, J. N., Phan, M., Horta, L. G., and Longman, R. W. Identification of observer/Kalman filter Markov parameters: theory and experiments, *Journal of Guidance, Control, and Dynamics*, **16**, 320–329, (1993).

[22] Dong, X.-J., Meng, G., and Peng, J.-C. Vibration control of piezoelectric smart structures based on system identification technique: numerical simulation and experimental study, *Journal of Sound and Vibration*, **297** (3–5), 680–693, (2006).

[23] Juang, J. N. and Phan, M. *Identification and Control of Mechanical Systems*, Cambridge University Press, New York, (2001).

[24] Li, D.-B. *Experimental Modal Analysis and Application*, Science Press, Beijing, (2001).

[25] Yang, H. Study of dynamic modelling theory and experiment for rigid-flexible coupling systems, PhD Thesis in Shanghai Jiaotong University, (2002).

Exact Solution for a Free Vibration of Thermoelastic Hollow Cylinder Under GNIII Model

Ibrahim A. Abbas

Department of Mathematics, Faculty of Science and Arts — Khulais, University Of Jeddah, Saudi Arabia
Nonlinear Analysis and Applied Mathematics Research Group (NAAM), Department of Mathematics, King Abdulaziz University, Jeddah, Saudi Arabia
Department of Mathematics, Faculty of Science, Sohag University, Sohag, Egypt.

(Received 12 April 2014; accepted 17 February 2015)

The exact analytic solutions are obtained with the use of the eigenvalue approach for a free vibration problem of a thermoelastic hollow cylinder in the context of Green and Naghdi theory (GNIII). The dispersion relations for the existence of various types of possible modes of vibrations in the considered hollow cylinder are derived in a compact form and the validation of the roots for the dispersion relation is presented. To illustrate the analytic results, the numerical solution of various relations and equations has been carried out to compute the frequency, thermoelastic damping and frequency shift of vibrations in a hollow cylinder of copper material with MATHEMATICA and MATLAB software.

1. INTRODUCTION

In the literature concerning thermal effects in continuum mechanics, several parabolic and hyperbolic theories for describing the heat conduction were developed. These hyperbolic theories were also called theories of second sound and there the flow of heat was modelled with finite propagation speed, which contrasts with the classical model based on the Fouriers law leading to infinite propagation speed of heat signals as in.[1–9] Green and Naghdi[10,11] proposed GNII and GNIII, which is a generalized thermoelasticity theory based on entropy equality rather than the usual entropy inequality. An important feature of this theory, which was not present in other thermoelasticity theories, was that it does not accommodate the dissipation of thermal energy. GN theory seems to be idealistic from a physical point of view. The genesis lies in the fact that the thermoelastic model of the GN theory was an idealized material model. During the last years, different problems were considered by using Green and Naghdi theories, as in Abd El-Latief et al.,[12] Youssef,[13] Mukhopadhyay et al.,[14] Sharma et al.,[15] Prasad et al.,[16] Othman et al.,[17] Abbas,[18] and Abbas et al.[19] A survey article of representative theories in the range of generalized thermoelasticity is given by Hetnarski and Ignaczak.[20]

The vibrations in thermoelastic materials have many applications in various fields of science and technology, namely aerospace, atomic physics, thermal power plants, and chemical pipes. The cylinders were frequently used as structural components and their vibrations were obviously important for practical design. Abbas studied the natural frequencies of a poroelastic hollow cylinder.[21] Abd-alla and Abbas investigated the magnetoelastic longitudinal wave propagation in a transversely isotropic circular cylinder.[22] Mykityuk studied the thermoelastic vibrations of a thick-walled cylinder of time-varying thickness.[23] Zhitnyaya analyzed an uncoupled problem of the thermoelastic vibrations of a cylinder.[24] Marin and Lupu studied the harmonic vibrations in thermoelasticity of micropolar bodies.[25] Erbay et al. investigated thermally induced vibrations in a generalized thermoelastic solid with a cavity.[26] Sharma et al. solved the vibration analysis of a transversely isotropic hollow cylinder by using the matrix Frobenius method.[27] Nayfeh and Younis presented a model for thermoelastic damping in microplates.[28,29] Rezazadeh et al. studied the thermoelastic damping in a micro-beam resonator using modified couple stress theory.[30]

The present article is devoted to study the frequency, frequency shifts and damping due to thermal variations in homogenous isotropic hollow cylinder, in the context of Green and Naghdi of type III model of non-classical (generalized) thermoelasticity.

2. BASIC EQUATION AND FORMULATION OF THE PROBLEM

Following Green and Naghdi, the basic equations of the thermoelasticity theory for homogeneous isotropic material in the absence of body forces and heat sources were considered as the equations of motion[10,11]:

$$\sigma_{ij,j} = \rho \frac{\partial^2 u_i}{\partial t^2}; \tag{1}$$

where ρ was the density of the medium, t was the time, σ_{ij} were the components of stress tensor, and u_i were the components of displacement vector. The equation of heat conduction is:

$$\left(K^*_{ij} T_{,j} + K_{ij} \dot{T}_{,j}\right) = \frac{\partial^2}{\partial t^2} \left(\rho c_e + \gamma T_0 e\right); \tag{2}$$

where T is the temperature, c_e was the specific heat at constant strain, K_{ij} was the thermal conductivity, K^*_{ij} was the material constant characteristic of the theory, T_0 was the reference temperature; $\gamma = (3\lambda + 2\mu)\alpha_t$, α_t was the coefficient of linear thermal expansion. The constitutive equations were given by:

$$\sigma_{ij} = 2\mu e_{ij} + \left[\lambda e - \gamma(T - T_0)\right] \delta_{ij}; \tag{3}$$

with $e = e_{ii},\ i, j = r, \theta, z$, where λ, μ were the Lame's constants and δ_{ij} was the Kronecker symbol.

Let us consider an elastic hollow cylinder of an isotropic homogeneous medium whose state could be expressed in terms of the space variable r and the time variable t. In a cylindrical coordinate system (r, θ, z), for the axially symmetric problem $u_r = u_r(r, z, t)$, $u_\theta = 0$, $u_z = u_z(r, z, t)$. Furthermore, if only the axisymmetric plane strain problem was considered, we had $u_r = u(r, t)$ and $u_\theta = u_z = 0$. Thus, the strain-displacement relations are

$$e_{rr} = \frac{\partial u}{\partial r}, \quad e_{\theta\theta} = \frac{u}{r}, \quad e_{zz} = e_{rz} = e_{r\theta} = e_{\theta z} = 0. \quad (4)$$

The stress-strain relations are

$$\sigma_{rr} = 2\mu\frac{\partial u}{\partial r} + \lambda\left(\frac{\partial u}{\partial r} + \frac{u}{r}\right) - \gamma(T - T_0); \quad (5)$$

$$\sigma_{\theta\theta} = 2\mu\frac{u}{r} + \lambda\left(\frac{\partial u}{\partial r} + \frac{u}{r}\right) - \gamma(T - T_0). \quad (6)$$

It was assumed that there were no body forces and heat sources in the medium, the equation of motion and energy equation hadthe form:

$$\frac{\partial \sigma_{rr}}{\partial r} + \frac{\sigma_{rr} - \sigma_{\theta\theta}}{r} = \rho\frac{\partial^2 u}{\partial t^2} \quad (7)$$

$$K^*\frac{1}{r}\frac{\partial}{\partial r}\left(r\frac{\partial T}{\partial r}\right) + K\frac{1}{r}\frac{\partial}{\partial r}\left(r\frac{\partial^2 T}{\partial t \partial r}\right) = \frac{\partial^2}{\partial t^2}\left(\rho c_e T + \gamma T_0\left(\frac{\partial u}{\partial r} + \frac{u}{r}\right)\right). \quad (8)$$

It was convenient to change the preceding equations into the dimensionless forms. To do this, the dimensionless parameters were introduced as

$$(r', u') = \frac{(r, u)}{c\chi}, \quad t' = \frac{t}{\chi}, \quad \omega' = \omega\chi,$$
$$(\sigma'_{rr}, \sigma'_{\theta\theta}) = \frac{1}{\lambda + 2\mu}(\sigma_{rr}, \sigma_{\theta\theta}), \quad T' = \frac{T - T_0}{T_0}, \quad (9)$$

where, $c^2 = \frac{\lambda+2\mu}{\rho}$, $\chi = \frac{K}{\rho c_e c^2}$. From Eq. (9) into Eqs. (5) to (8), one may obtain (here dashes are ignored for convenience):

$$\frac{\partial^2 u}{\partial r^2} + \frac{1}{r}\frac{\partial u}{\partial r} - \frac{u}{r^2} - a_2\frac{\partial T}{\partial r} = \frac{\partial^2 u}{\partial t^2}; \quad (10)$$

$$\left(\varepsilon_1 + \frac{\partial}{\partial t}\right)\left(\frac{\partial^2 T}{\partial r^2} + \frac{1}{r}\frac{\partial T}{\partial r}\right) = \frac{\partial^2}{\partial t^2}\left(T + \varepsilon_2\left(\frac{\partial u}{\partial r} + \frac{u}{r}\right)\right); \quad (11)$$

$$\sigma_{rr} = \frac{\partial u}{\partial r} + a_1\frac{u}{r} - a_2 T; \quad (12)$$

$$\sigma_{\theta\theta} = a_1\frac{\partial u}{\partial r} + \frac{u}{r} - a_2 T \quad (13)$$

where $a_1 = \frac{\lambda}{\lambda+2\mu}$, $a_2 = \frac{\gamma T_0}{\lambda+2\mu}$, $\varepsilon_1 = \frac{K^*}{\rho c_e c^2}$, $\varepsilon_2 = \frac{\gamma}{\rho c_e}$. The boundary conditions for stress free and isothermal surfaces of the cylinder may be expressed as:

$$\sigma_{rr}(a, t) = \sigma_{rr}(b, t) = 0; \quad T(a, t) = T(b, t) = 0; \quad (14)$$

where a and b are the inner and outer radii of the cylinder respectively.

3. THE EXACT SOLUTION OF THE MODEL

We considered cylindrical time-harmonic vibrations so that:

$$u(r, t) = \bar{u}(r)e^{i\omega t}, \quad T(r, t) = \overline{T}e^{i\omega t}; \quad (15)$$

where ω was the non-dimensional circular frequency of vibrations. By placing Eq. (15) into Eqs. (10) and (11), we get:

$$\frac{d^2\bar{u}}{dr^2} + \frac{1}{r}\frac{d\bar{u}}{dr} - \frac{\bar{u}}{r^2} = -\omega^2\bar{u} + a_2\frac{d\overline{T}}{dr}; \quad (16)$$

$$\frac{d^2\overline{T}}{dr^2} + \frac{1}{r}\frac{d\overline{T}}{dr} = -\omega^2\left(\varepsilon_3\overline{T} + \varepsilon_4\left(\frac{d\bar{u}}{dr} + \frac{\bar{u}}{r}\right)\right) \quad (17)$$

where $\varepsilon_3 = \frac{1}{\varepsilon_1 + i\omega}$ and $\varepsilon_4 = \frac{\varepsilon_2}{\varepsilon_1 + i\omega}$. By differentiating Eq. (17) with respect to r and using Eq. (16) we got:

$$\frac{d^2}{dr^2}\left(\frac{d\overline{T}}{dr}\right) + \frac{1}{r}\frac{d}{dr}\left(\frac{d\overline{T}}{dr}\right) - \frac{1}{r^2}\left(\frac{d\overline{T}}{dr}\right) = -\omega^2\left(-\omega^2\varepsilon_4\bar{u} + (\varepsilon_3 + \varepsilon_4 a_2)\frac{d\overline{T}}{dr}\right). \quad (18)$$

Equations (16) and (18) could be written in a vector-matrix differential equation as follows:

$$L\mathbf{V} = \mathbf{A}\mathbf{V} \quad (19)$$

where $L \equiv \frac{d^2}{dr^2} + \frac{1}{r}\frac{d}{dr} - \frac{1}{r^2}$ was the Bessel operator, $\mathbf{V} = \begin{bmatrix}\bar{u} & \frac{d\overline{T}}{dr}\end{bmatrix}^T$ and $\mathbf{A} = \begin{bmatrix}A_{11} & A_{12}\\ A_{21} & A_{22}\end{bmatrix}$, with $A_{11} = -\omega^2$, $A_{12} = a_2$, $A_{21} = \omega^4\varepsilon_4$, $A_{22} = -\omega^2(\varepsilon_3 + a_2\varepsilon_4)$.

Let us now proceed to solve Eq. (19) by the eigenvalue approach proposed by Das at al.,[31] Abbas,[32–34,36] and Youssef et al.[35] The characteristic equation of the matrix $\mathbf{A}$ takes the form:

$$A_{11}A_{22} - A_{12}A_{21} - (A_{22} + A_{11})\lambda + \lambda^2 = 0. \quad (20)$$

The roots of the characteristic Eq. (20), which were also the eigenvalues of matrix $\mathbf{A}$, were of the form $\lambda = \lambda_1$, $\lambda = \lambda_2$. The eigenvector $\mathbf{X} = \begin{bmatrix}x_1 & x_2\end{bmatrix}^T$, which corresponded to the eigenvalue λ, could be calculated as:

$$x_1 = A_{12}, \quad x_2 = \lambda - A_{11}. \quad (21)$$

From Eq. (20), we could easily calculate the eigenvector $\mathbf{X}_j$, which corresponded to the eigenvalue λ_j, $j = 1, 2$. For further reference, we shall use the following notations:

$$\mathbf{X}_1 = [\mathbf{X}]_{\lambda=\lambda_1}, \quad \mathbf{X}_2 = [\mathbf{X}]_{\lambda=\lambda_2}. \quad (22)$$

The solution of Eq. (20) could be written as follows:

$$\mathbf{V} = \mathbf{X}_1\left(A_1 I_1(p_1 r) + A_2 K_1(p_1 r)\right) + \mathbf{X}_2\left(A_3 I_1(p_2 r) + A_4 K_1(p_2 r)\right); \quad (23)$$

where $p_1 = \sqrt{\lambda_1}$, $p_2 = \sqrt{\lambda_2}$, I_1, K_1 were the modified of Bessels functions and A_1, A_2, A_3, A_4 were arbitrary constants to be determined. Upon using Eq. (23), the displacement and temperature gradient were obtained as:

$$\bar{u}(r) = x_1^1\left(A_1 I_1(p_1 r) + A_2 K_1(p_1 r)\right) + x_1^2\left(A_3 I_1(p_2 r) + A_4 K_1(p_2 r)\right); \quad (24)$$

$$\frac{d\overline{T}}{dr} = x_2^1 \left(A_1 I_1(p_1 r) + A_2 K_1(p_1 r)\right) + x_2^2 \left(A_3 I_1(p_2 r) + A_4 K_1(p_2 r)\right); \quad (25)$$

where x_i^j was the component number i of the eigenvector number j. Thus, the exact solutions of field variables could be written for r and t as:

$$u(r,t) = \left[x_1^1 \left(A_1 I_1(p_1 r) + A_2 K_1(p_1 r)\right) + x_1^2 \left(A_3 I_1(p_2 r) + A_4 K_1(p_2 r)\right)\right] e^{i\omega t}; \quad (26)$$

$$T(r,t) = \left[\frac{x_2^1}{p_1} \left(A_1 I_0(p_1 r) - A_2 K_0(p_1 r)\right) + \frac{x_2^2}{p_2} \left(A_3 I_0(p_2 r) - A_4 K_0(p_2 r)\right)\right] e^{i\omega t}; \quad (27)$$

$$\begin{aligned}\sigma_{rr}(r,t) = {} & A_1 \left[\frac{(p_1^2 x_1^1 - \beta x_2^1)}{p_1} I_0(p_1 r) + \frac{x_1^1(\xi-1)}{r} I_1(p_1 r)\right] + \\ & A_2 \left[\frac{(\beta x_2^1 - p_1^2 x_1^1)}{p_1} K_0(p_1 r) + \frac{x_1^1(\xi-1)}{r} K_1(p_1 r)\right] + \\ & A_3 \left[\frac{(p_2^2 x_1^2 - \beta x_2^2)}{p_2} I_0(p_2 r) + \frac{x_1^2(\xi-1)}{r} I_1(p_2 r)\right] + \\ & A_4 \left[\frac{(\beta x_2^2 - p_2^2 x_1^2)}{p_2} K_0(p_2 r) + \frac{x_1^2(\xi-1)}{r} K_1(p_2 r)\right]; \end{aligned} \quad (28)$$

$$\begin{aligned}\sigma_{\theta\theta}(r,t) = {} & A_1 \left[\frac{(p_1^2 \xi x_1^1 - \beta x_2^1)}{p_1} I_0(p_1 r) - \frac{x_1^1(\xi-1)}{r} I_1(p_1 r)\right] + \\ & A_2 \left[\frac{(\beta x_2^1 - p_1^2 \xi x_1^1)}{p_1} K_0(p_1 r) - \frac{x_1^1(\xi-1)}{r} K_1(p_1 r)\right] + \\ & A_3 \left[\frac{(p_2^2 \xi x_1^2 - \beta x_2^2)}{p_2} I_0(p_2 r) - \frac{x_1^2(\xi-1)}{r} I_1(p_2 r)\right] + \\ & A_4 \left[\frac{(\beta x_2^2 - p_2^2 \xi x_1^2)}{p_2} K_0(p_2 r) - \frac{x_1^2(\xi-1)}{r} K_1(p_2 r)\right]. \end{aligned} \quad (29)$$

4. DISPERSION RELATIONS

We assumed that the thermoelastic hollow cylinder was subjected to traction-free and isothermal boundary conditions, Eq. (15), at its surfaces ($r = a, b$). By applying boundary conditions, which were Eqs. (15), (27), and (28), we obtain a system of four homogeneous linear algebraic equations in unknowns A_1, A_2, A_3, and A_4. This system would have a nontrivial solution if and only if the determinant of the coefficients A_1, A_2, A_3, and A_4 vanished and such a requirement of nontrivial solution lead to dispersion equations given by:

$$\Delta = \det(L_{ij}) = 0, \quad i,j = 1,2,3,4; \quad (30)$$

where,

$$L_{11} = \frac{(p_1^2 x_1^1 - a_2 x_2^1)}{p_1} I_0(p_1 a) + \frac{x_1^1(a_1-1)}{a} I_1(p_1 a);$$

$$L_{12} = \frac{(a_2 x_2^1 - p_1^2 x_1^1)}{p_1} K_0(p_1 a) + \frac{x_1^1(a_1-1)}{a} K_1(p_1 a);$$

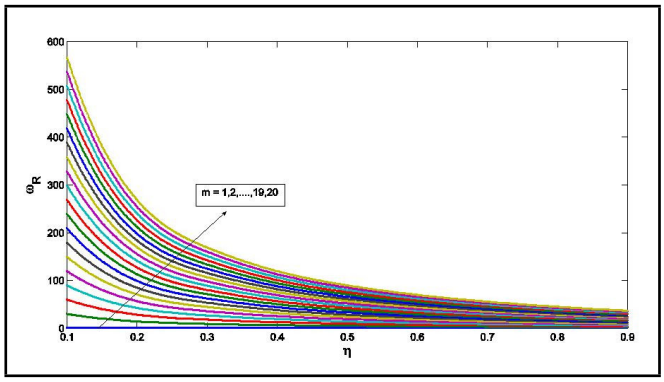

Figure 1. Non-dimensional frequency ω_R verses the length to mean radius ratio η.

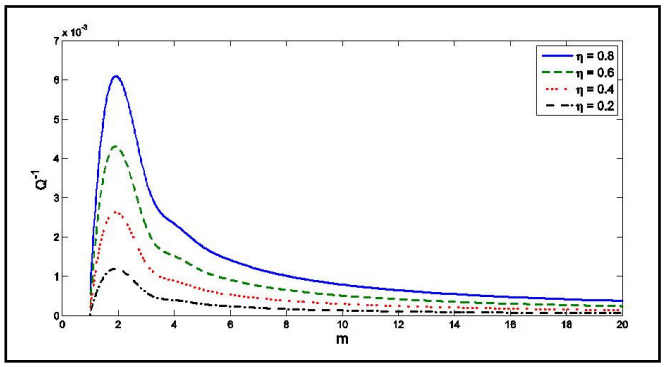

Figure 2. Thermoelastic damping Q^{-1} versus m for different values of η.

$$L_{13} = \frac{(p_2^2 x_1^2 - a_2 x_2^2)}{p_2} I_0(p_2 a) + \frac{x_1^2(a_1-1)}{a} I_1(p_2 a);$$

$$L_{14} = \frac{(a_2 x_2^2 - p_2^2 x_1^2)}{p_2} K_0(p_2 a) + \frac{x_1^2(a_1-1)}{a} K_1(p_2 a);$$

$$L_{21} = \frac{(p_1^2 x_1^1 - a_2 x_2^1)}{p_1} I_0(p_1 b) + \frac{x_1^1(a_1-1)}{b} I_1(p_1 b);$$

$$L_{22} = \frac{(a_2 x_2^1 - p_1^2 x_1^1)}{p_1} K_0(p_1 b) + \frac{x_1^1(a_1-1)}{b} K_1(p_1 b);$$

$$L_{23} = \frac{(p_2^2 x_1^2 - a_2 x_2^2)}{p_2} I_0(p_2 b) + \frac{x_1^2(a_1-1)}{b} I_1(p_2 b);$$

$$L_{24} = \frac{(a_2 x_2^2 - p_2^2 x_1^2)}{p_2} K_0(p_2 b) + \frac{x_1^2(a_1-1)}{b} K_1(p_2 b);$$

$$L_{31} = \frac{x_2^1}{p_1} I_0(p_1 a), \qquad L_{32} = -\frac{x_2^1}{p_1} K_0(p_1 a)$$

$$L_{33} = \frac{x_2^2}{p_2} I_0(p_2 a), \qquad L_{34} = -\frac{x_2^2}{p_2} K_0(p_2 a)$$

$$L_{41} = \frac{x_2^1}{p_1} I_0(p_1 b), \qquad L_{42} = -\frac{x_1^2}{p_1} K_0(p_1 b)$$

$$L_{43} = \frac{x_2^2}{p_2} I_0(p_2 b), \qquad L_{44} = -\frac{x_2^2}{p_2} K_0(p_2 b)$$

5. NUMERICAL RESULTS AND DISCUSSION

The copper material had been chosen for the purposes of numerical evaluations in the space-time domain. From the material constants, we got the non-dimensional values of the problem as Abbas:[37]

$$\mu = 3.86 \times 10^{10} (\text{kg})(\text{m})^{-1}(\text{s})^{-2};$$

Table 1. The validation of the roots for the dispersion relation.

m	$\eta = 0.4$		$\eta = 0.8$	
	ω	Δ	ω	Δ
1	$0.7062 + 0.00002$i	$4.2 \times 10^{-16} - 1.5 \times 10^{-17}$i	$0.5628 + 0.00016$i	$9.9 \times 10^{-16} + 1.1 \times 10^{-15}$i
2	$6.3247 + 0.00825$i	$-3.2 \times 10^{-16} - 6.9 \times 10^{-16}i$	$2.4331 + 0.00738$i	$-1.0 \times 10^{-16} + 1.8 \times 10^{-17}$i
5	$25.143 + 0.00839$i	$5.1 \times 10^{-19} - 2.4 \times 10^{-19}$i	$9.4425 + 0.00834$i	$5.0 \times 10^{-16} - 7.1 \times 10^{-17}$i
10	$56.553 + 0.00839$i	$-23 \times 10^{-18} - 4.4 \times 10^{-19}$i	$21.213 + 0.00839$i	$-2.0 \times 10^{-18} + 7.1 \times 10^{-18}$i
15	$87.967 + 0.0084$i	$7.3 \times 10^{-19} + 1.3 \times 10^{-18}$i	$32.991 + 0.00839$i	$1.7 \times 10^{-17} + 4.8 \times 10^{-18}$i
20	$119.38 + 0.0084$i	$-3.1 \times 10^{-19} - 1.8 \times 10^{-18}$i	$44.771 + 0.00839$i	$-2.7 \times 10^{-17} + 1.5 \times 10^{-18}$i

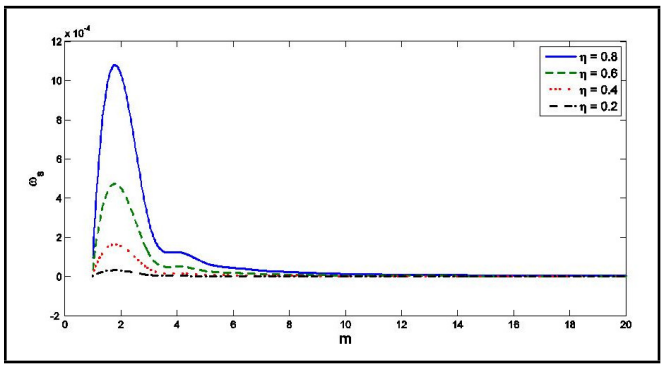

Figure 3. Frequency shift ω_s versus m for different values of η.

$$\begin{aligned}
\lambda &= 7.76 \times 10^{10}(\text{kg})(\text{m})^{-1}(\text{s})^{-2};\\
c_e &= 3.831 \times 10^{2}(\text{m})^{2}(\text{K})^{-1}(\text{s})^{-2};\\
K &= 3.68 \times 10^{2}(\text{kg})(\text{m})(\text{K})^{-1}(\text{s})^{-3};\\
\rho_0 &= 8.954 \times 10^{3}(\text{kg})(\text{m})^{-3};\\
\alpha_t &= 17.8 \times 10^{-6}(\text{K})^{-}1;\\
T_0 &= 293(\text{K}); \quad a = 1. \qquad (31)
\end{aligned}$$

The numerical computation had been carried out with the help of MATHEMATICA and MATLAB files for the length to mean radius ratio $\left(\eta = \frac{b-a}{R}\right)$, where $a = 1$, $b > a$, $R = \frac{a+b}{2}$. Due to the presence of a dissipation term in the heat conduction equation, the frequency equation in the general complex transcendental equation provided us with a complex frequency value, $\omega^m = \omega_R^m + i\omega_I^m$, where m was the mode number that corresponded to the roots of the transcendental Eq. (30) and ω_R^m and ω_I^m were the real part and imaginary parts of frequency ω^m. The thermoelastic damping factor was given by:

$$Q^{-1} = 2\left|\frac{\omega_I^m}{\omega_R^m}\right|.$$

The frequency shift due to thermal variations was defined as:

$$\omega_s = \left|\frac{\omega_R^m - \omega_o^m}{\omega_o^m}\right|;$$

where ω_o^m was the frequency in elastic hollow cylinder.

The calculation of the roots of the dispersion relation Eq. (30) represented a major task and required a rather extensive effort of numerical computation. The frequency spectrum ω^m versus the different values of the length to mean radius ratio η for the first twenty modes was computed by the interval halving method. The validation of the roots for the dispersion relation is presented in Table 1.

The first twenty modes of non-dimensional frequency ω_R verses the length to radius ratio η are presented in Fig. 1. It was observed that the non-dimensional frequency ω_R decreased with an increasing length to mean radius ratio. The thermoelastic damping Q^{-1} versus m for different values of the length to mean radius ratio η are presented in Fig. 2, from which it is seen that the thermoelastic damping Q^{-1} increased initially to attain its maximum peak value at the second mode before it decreased in order to become ultimately asymptotic with increasing m. Figure 3 shows the variation of the frequency shift ω_s versus m for different values of the length to mean radius ratio η. It could be inferred that the frequency shift ω_s increased sharply to attain its maximum peak value at the second mode and then decreased to become ultimately asymptotic with increasing m.

6. CONCLUSIONS

The exact solution for a free vibration of thermoelastic hollow cylinder under GNIII model has been done with the help of the eigenvalue approach. The eigenvalue approach is applied successfully to get an explicit, totally analytic, and uniformly valid solution for the current problem. The validation of the roots for the dispersion relation is also presented. The closed form solution obtained here opens the scope of further studies in mathematics, science, and engineering disciplines.

REFERENCES

[1] Lord, H. W. and Y. Shulman. A generalized dynamical theory of thermoelasticity, *Journal of the Mechanics and Physics of Solids*, **15**(5),299–309, (1967).

[2] Green, A. E. and K. A. Lindsay. Thermoelasticity, *Journal of Elasticity*, **2**(1), 1–7 (1972).

[3] Dhaliwal, R. S. and H. H. Sherief. Generalized thermoelasticity for anisotropic media, *Quarterly of Applied Mathematics*, **38**(1), 1–8 (1980).

[4] Sherief, H. H. and M. N. Anwar. A problem in generalized thermoelasticity for an infinitely long annular cylinder, *International Journal of Engineering Science*, **26**(3), 301–306, (1988).

[5] Sherief, H. H. and M. A. Ezzat. A problem in generalized magneto-thermoelasticity for an infinitely long annular cylinder, *Journal of Engineering Mathematics*, **34**(1–4), 387–402, (1998).

[6] Abbas, I. A. and A. M. Zenkour. LS model on electro-magneto-thermoelastic response of an infinite functionally graded cylinder, *Composite Structures*, **96**, 89–96, (2013).

[7] Abbas, I. A. Generalized magneto-thermoelastic interaction in a fiber-reinforced anisotropic hollow cylinder, *International Journal of Thermophysics*, **33**(3): 567–579, (2012).

[8] . Abd-alla, A. N. and I. Abbas. A problem of generalized magnetothermo-elasticity for an infinitely long, perfectly conducting cylinder. *Journal of Thermal Stresses*, **25**(11), 1009–1025, (2002).

[9] Abbas, I. A. and H. M. Youssef. A nonlinear generalized thermoelasticity model of temperature-dependent materials using finite element method, *International Journal of Thermophysics*, **33**(7), 1302–1313, (2012).

[10] Green, A. E. and P. M. Naghdi. Thermoelasticity without energy dissipation, *Journal of Elasticity*, **31**(3), 189–208, (1993).

[11] Green, A. E. and P. M. Naghdi. On undamped heat waves in an elastic solid, *Journal of Thermal Stresses*, **15**(2), 253–264, (1992).

[12] Abd El-Latief, A. M. and S. E. Khader. Exact solution of thermoelastic problem for a one-dimensional bar without energy dissipation, *ISRN Mechanical Engineering, 2014*, (2014).

[13] Youssef, H. M. State-space approach to two-temperature generalized thermoelasticity without energy dissipation of medium subjected to moving heat source, *Applied Mathematics and Mechanics (English Edition)*, **34**(1),63–74, (2013).

[14] Mukhopadhyay, S. and R. Kumar. A problem on thermoelastic interactions without energy dissipation in an unbounded medium with a spherical cavity, *Proceedings of the National Academy of Sciences India Section A — Physical Sciences*, **79**(1), 135–140, (2009).

[15] Sharma, S., K. Sharma, and R. R. Bhargava. Effect of viscosity on wave propagation in anisotropic thermoelastic with Green–Naghdi theory type-II and type-III, *Materials Physics and Mechanics*, **16**(2), 144–158, (2013).

[16] Prasad, R., S. Das, and S. Mukhopadhyay. A two-dimensional problem of a mode i crack in a type III thermoelastic medium, *Mathematics and Mechanics of Solids*, **18**(5), 506–523, (2013).

[17] Othman, M. I. A. and S. Y. Atwa. Thermoelastic plane waves for an elastic solid half-space under hydrostatic initial stress of type III, *Meccanica*, **47**(6), 1337–1347, (2012).

[18] Abbas, I. A. A GN model for thermoelastic interaction in an unbounded fiber-reinforced anisotropic medium with a circular hole, *Applied Mathematics Letters*, **26**(2), 232–239, (2013).

[19] Abbas, I. A. and A. M. Zenkour. The effect of rotation and initial stress on thermal shock problem for a fiber-reinforced anisotropic half-space using green-naghdi theory, *Journal of Computational and Theoretical Nanoscience*, **11**(2), 331–338, (2014).

[20] Hetnarski, R. B. and J. Ignaczak. Generalized thermoelasticity, *Journal of Thermal Stresses*, **22**(4), 451–476, (1999).

[21] Abbas, I. Natural frequencies of a poroelastic hollow cylinder, *Acta Mechanica*, **186**(1–4), 229–237, (2006).

[22] Abd-alla, A. N. and I. A. A. Abbas. Magnetoelastic longitudinal wave propagation in a transversely isotropic circular cylinder, *Applied Mathematics and Computation*, **127**(2–3), 347–360, (2002).

[23] Mykityuk, Y. I. Thermoelastic vibrations of a thick-walled cylinder of time-varying thickness, *Soviet Applied Mechanics*, **5**(11), 1237–1240, (1972).

[24] Zhitnyaya, V. G. The uncoupled problem of thermoelastic vibrations of a cylinder, *Journal of Mathematical Sciences*, **92**(5), 4190–4192, (1998).

[25] Marin, M. and M. Lupu. On harmonic vibrations in thermoelasticity of micropolar bodies, *Journal of Vibration and Control*, **4**(5), 507–518, (1998).

[26] Erbay, HA., S. Erbay, and S. Dost. Thermally induced vibrations in a generalized thermoelastic solid with a cavity, *Journal of Thermal Stresses*, **14**(2), 161–171, (1991).

[27] Sharma, J. N., H. Singh, and Y. D. Sharma. Vibration analysis of a transversely isotropic hollow cylinder by using the matrix Frobenius method, *Journal of Thermal Stresses*, **34**(9), 934–957, (2011).

[28] Nayfeh, A. H. and M. I. Younis. A model for thermoelastic damping in microplates, (2004)

[29] Nayfeh, A. H. and M. I. Younis, Modeling and simulations of thermoelastic damping in microplates, *Journal of Micromechanics and Microengineering*, **14**(12), 1711–1717, (2004).

[30] Rezazadeh, G., et al. Thermoelastic damping in a microbeam resonator using modified couple stress theory, *Acta Mechanica*, **223**(6), 1137–1152, (2012).

[31] Das, N. C., A. Lahiri, and R. R. Giri. Eigenvalue approach to generalized thermoelasticity, *Indian Journal of Pure and Applied Mathematics*, **28**(12), 1573–1594, (1997).

[32] Abbas, I. A. Eigenvalue approach to fractional order generalized magneto-thermoelastic medium subjected to moving heat source, *Journal of Magnetism and Magnetic Materials*, **377**, 452–459, (2015).

[33] Abbas, I. A. Eigenvalue approach in a three-dimensional generalized thermoelastic interactions with temperature-dependent material properties, *Computers & Mathematics with Applications*, **68**(12), 2036–2056, (2014).

[34] Abbas, I. A. Eigenvalue approach for an unbounded medium with a spherical cavity based upon two-temperature generalized thermoelastic theory, *Journal of Mechanical Science and Technology*, **28**(10), 4193–4198, (2014).

[35] Youssef, H. M. and I. A. Abbas. Fractional order generalized thermoelasticity with variable thermal conductivity, *Journal of Vibroengineering*, **16**(8), 4077–4087, (2014).

[36] Abbas, I. A. A GN model based upon two-temperature generalized thermoelastic theory in an unbounded medium with a spherical cavity, *Applied Mathematics and Computation*, **245**, 108–115, (2014).

[37] Abbas, I. Generalized magneto-thermoelasticity in a nonhomogeneous isotropic hollow cylinder using the finite element method, *Archive of Applied Mechanics*, **79**(1), 41–50, (2009).

The Effect of Crack Geometry on the Nondestructive Fault Detection in a Composite Beam

Sadettin Orhan

Ankara Yıldırım Beyazıt University, Mechanical Engineering Department, Ankara, Turkey

Murat Lüy

Kırıkkale University, Electrical & Electronics Eng. Dept., 71450, Kırıkkale, Turkey

M. Hüsnü Dirikolu

Istanbul University, Mechanical Eng. Dept., 34320, Istanbul, Turkey

Gazi Mustafa Zorlu

TCDD, Ankara,Turkey

(Received 26 April 2014; accepted: 9 March 2015)

Defects in structures may be inherited from materials and manufacturing or they develop during service. Defects may cause catastrophic failure, which is why their detection and classification are important issues. Many aspects of defects have already been dealt with, but with wider applications of non-destructive testing methods to composite materials. However, the effect of arbitrary and random defect geometry on the applicability of these methods has been overlooked. In order to investigate this issue, this study carries out a free vibration analysis of a specially orthotropic cracked cantilever beam that was manufactured by Pultrusion. A new crack model, unlike the widely known V-shaped crack, is introduced and the effect of crack depth on the natural frequency is investigated, both experimentally and numerically. The results obtained from both the new- and the V-shaped models are compared with each other, and it is revealed that the results are not sensitive to the geometry change.

1. INTRODUCTION

Composites were used in various structural applications in the civil, automotive, and aerospace industries. One typical application of composites in structures are beams. A defect on a composite beam, which develops with time, can destroy it. Recent research has been directed to the detection or diagnoses of the development of defects in composites under dynamic loading. Initially, in composite failure detection research, Krawczuk et al.[1] found that natural frequencies of a cracked structural composite member beam were influenced by a crack in the member: the increase in crack depth had caused a decrease in the calculated natural bending frequencies. Song et al.,[2] on the other hand, analysed that the bending free vibration of a cantilever laminated composite beam was weakened by multiple surface cracks. The governing equations of the composite beam with open cracks were accounted for in transverse shear and inertia effects. Kisa[3] presented a new method for the numerical modelling of the free vibration of a cantilever composite beam that had multiple open and non-propagating cracks. The author had observed the frequency ratios to decrease under fibre angle increases. Wang et al.[4] studied the coupled bending and torsional vibration of a fiber-reinforced composite cantilever with an edge surface crack. They concluded that changes in natural frequencies and the corresponding mode shapes depended on fiber orientation and fiber volume fraction. Finally, Hamid and Hamada[5] investigated a composite beam with different fiber angles and a single crack. They stated that the natural frequency and the damping ratio increased when fiber angle rose for a constant crack location and depth.

Table 1. The mechanical properties of the pultruded GFRP composite beam.

E_1	E_2	E_3	G_{12}	G_{13}	G_{23}	v_{12}	v_{13}	v_{23}	Density
10^9 Pa						-			kg/m^3
25	8.5	8.5	3	3	3.9	0.23	0.23	0.09	1800

In this study, a new crack model is introduced together with the known V-shaped crack model in order to investigate the effect of defect geometry change on the natural frequencies and mode shapes under free vibration loading. These examinations were carried out using both experimental and finite element analyses.

2. MATERIAL PROPERTIES

Material properties in the principal material directions 1, 2, and 3 of the pultruded glass fibre reinforced composite beam were determined. The beam had a solid cross-section with 45 mm height, 29 mm width, and a length of 1400 mm. The 1-axis lies along the fibre's direction and the shear modulus G_{23} were calculated from Eq. (1):

$$G_{23} = \frac{E_2}{2(1+\nu_{23})}. \tag{1}$$

The properties are given in Tab. 1.

3. NUMERICAL MODELLING

ANSYS 8.1[6] finite element package had been used to model the beam with an assumed open crack. The crack was created at 745 mm away from the cantilevered end. Eight different crack depths, namely $d = 5, 10, 15, 20, 25, 30,$ and 35 mm,

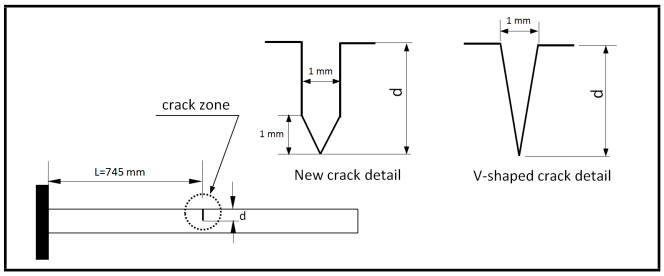

Figure 1. The schematic representation of the cracked cantilever beam.

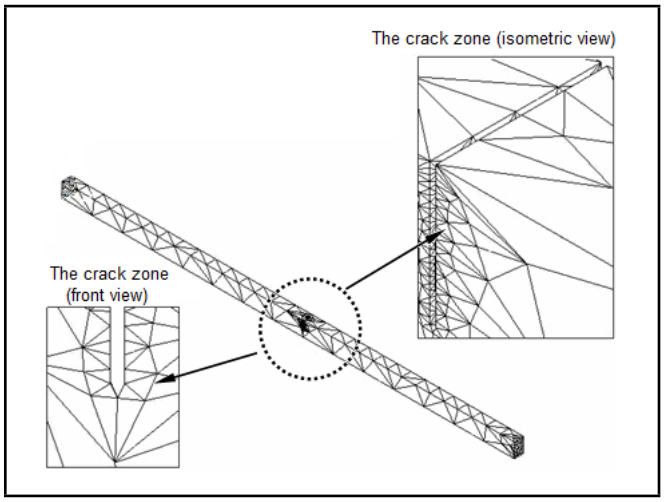

Figure 2. The overall appearance of the new finite element model and cracked zone.

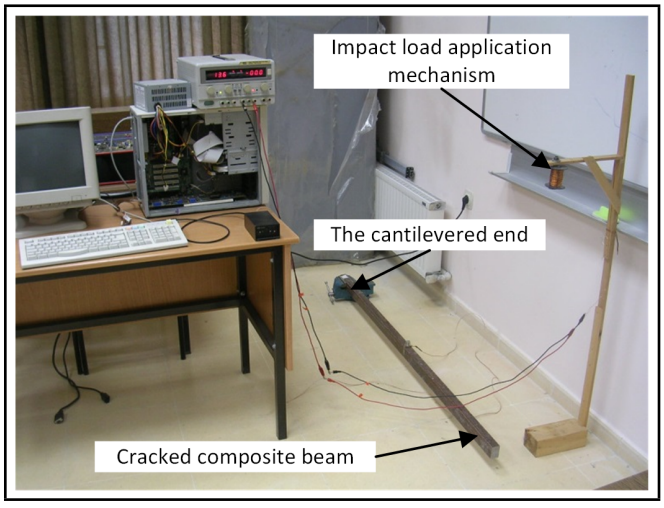

Figure 3. The experimental setup.

were studied. Lines were created by joining defined keypoints and the areas were obtained by connecting these lines. The three-dimensional beam models were obtained by extrusion of the corresponding areas along the width direction. Then, the model was meshed by *Solid45* elements existing in the Ansys element library. Because the crack zone was the most critical, finer elements along the crack edges were created with constant 1 mm side length divisions. The overall appearance of the schematics and the finite element model are shown in Figs. 1 and 2, respectively.

Displacements and rotations of the left end of the beam in all directions were constrained. Hence, the cantilever boundary conditions were imposed. The upper side and the tip of the

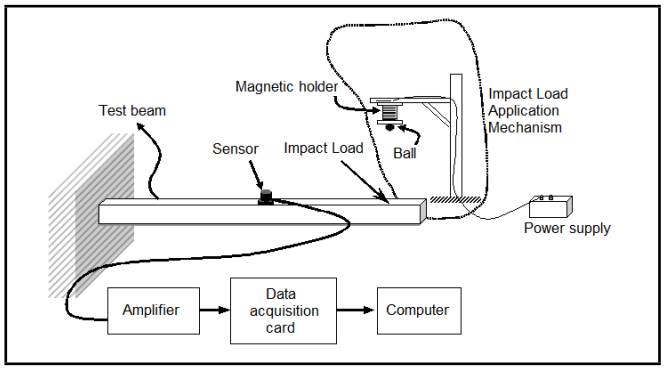

Figure 4. The schematic drawing of the experiment.

crack were modelled in the shape of a combination of a rectangle and a V, as shown in Fig. 2. This was a different approach from previous research, where the whole crack had been modelled in a V-shape. In fact, cracks created on beams in real life have a rectangular upper side and a V-shape towards the crack tip.

4. EXPERIMENTS

Both intact ($d = 0$) and cracked ($d = 5$, 10, 15, 20, 25, 30, and 35 mm) specially orthotropic composite beams had been placed successively on the prepared setup for free vibration analysis. The experimental setup and its schematic drawing are shown in Figs. 3 and 4, respectively.

The intact beams were constrained from their left ends along a 100 mm length by the aid of a vice. An accelerometer was located at a point that is 700 mm away from the cantilever end. Free vibration was simulated by dropping a steel ball with a weight of 2.04 gram from a constant height of 800 mm. Free vibration signals obtained through the accelerometer were amplified with an amplifier, which had a constant gain of 10 and transferred to the computer through a data acquisition card. The vibration signals were sampled with 100 kHz on a data acquisition card. The data was then transferred to and recorded on the computer in 165 ms. The computer recorded a total number of 16,384 data. Then, a program written in MATLAB was used to calculate Fast Fourier Transform of the vibration signals.

Later, artificial cracks that had widths of 1 mm and depths of 5, 10, 15, 20, 25, 30, and 35 mm, respectively, and 745 mm away from the cantilever end were made by the aid of a hand saw. Experiments executed for the intact beam were also performed for every cracked beam, and the obtained data were saved to the computer.

5. RESULTS AND DISCUSSION

In this study, free vibrations of intact and later cracked beams that had different crack depths are investigated both experimentally and numerically. The natural frequencies of the beams are determined and then the relationship between the depth of the crack and the variation in the natural frequency is investigated. The first four experimental and finite element natural frequencies of the intact beam and the beams with the new crack model, along with the results of the V-shaped crack geometries, are presented in Tab. 2, where f represents the corresponding natural frequency and d shows the depth of crack with appropriate subscripts. Specifically, d_0 indicates the intact beam. Fig. 5 gives the lateral mode shapes for the 25 mm cracked depth, namely d_{25}.

Table 2. The first four natural frequencies for the two crack geometries.

Natural Freq. [Hz]	d_0	d_5	d_{10}	d_{15}	d_{20}	d_{25}	d_{30}	d_{35}
f_{1exp}	18.80	18.75	18.75	18.75	18.75	18.75	18.75	18.75
f_{1fem_New}	13.80	13.78	13.73	13.64	13.49	13.21	12.68	11.46
$f_{1_fem_V}$	13.80	13.78	13.74	13.65	13.50	13.24	12.74	11.62
f_{2exp}	118.75	118.74	112.50	112.48	99.99	93.75	81.24	68.74
f_{2fem_New}	85.35	84.87	83.28	80.65	76.58	70.65	62.62	52.09
$f_{2_fem_V}$	85.35	84.91	83.44	80.86	76.93	71.20	63.41	53.04
f_{3exp}	331.23	331.23	324.96	324.95	318.73	312.48	306.22	299.98
f_{3fem_New}	234.29	234.17	233.80	233.17	232.21	230.84	229.01	226.67
$f_{3_fem_V}$	234.29	234.18	233.83	233.23	232.30	230.98	229.21	226.90
f_{4exp}	624.96	612.46	606.20	599.96	587.46	568.71	556.21	543.71
f_{4fem_New}	446.65	444.74	438.63	429.01	415.22	397.26	376.43	353.99
$f_{4_fem_V}$	446.65	444.90	439.20	429.74	416.34	398.78	378.23	355.66

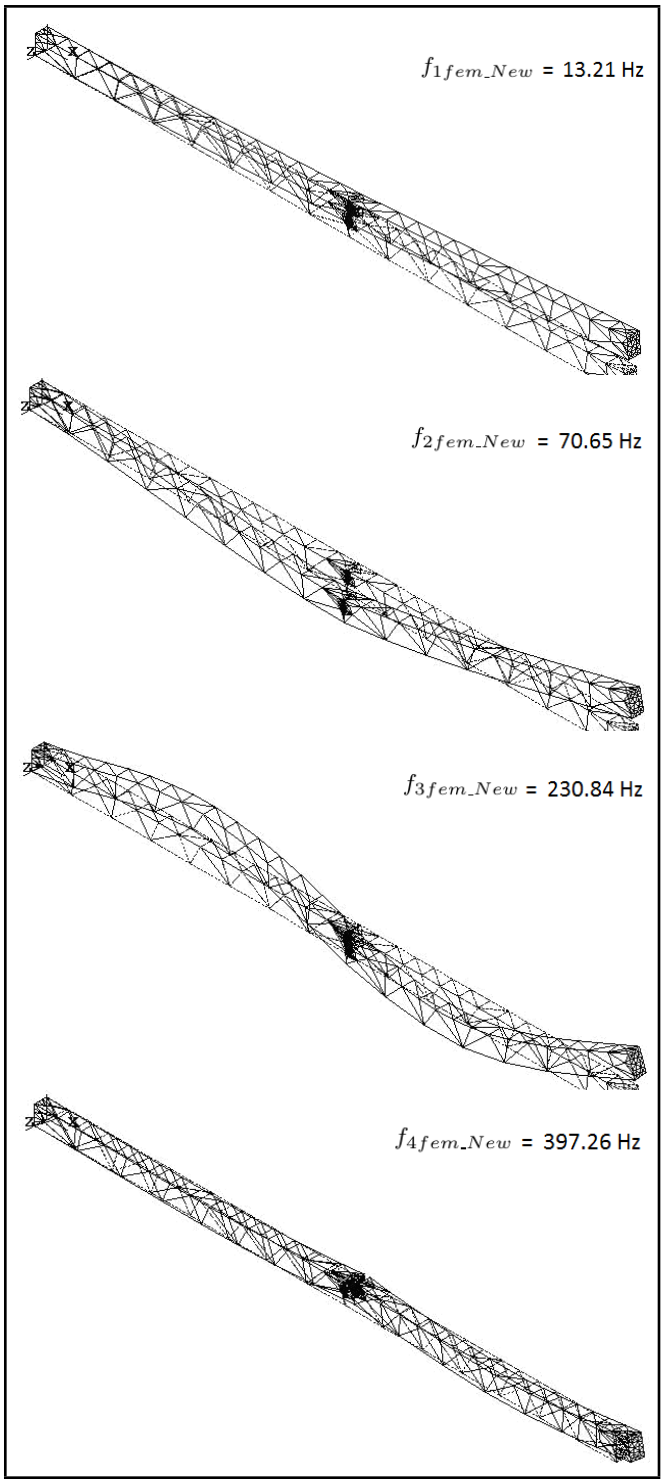

Figure 5. The mode shapes for the 25 mm cracked depth, namely d_{25}.

It is possible to diagnose the defects that arise in the course of time in structures by free vibration analysis. In this study, free vibrations of intact and cracked orthotropic composite beams that have different crack shapes are investigated both experimentally and numerically.

First of all, it has been found that the natural frequencies decrease when the depth of the crack increases in both experimental and finite element analyses for the new crack model. Additionally, as the depth of the crack increases, the error between finite element estimates and experiments varies from 22% to 39%. This is believed to happen due to the structural instability created from higher crack lengths. Finally, the finite element natural frequency results obtained from both the new- and the V-shaped crack models are compared with each other and a maximum difference of 1.82% was determined. This result reveals that composite structures are insensitive to a change in crack shape geometry as long as vibration characteristics are concerned.

In conclusion, vibration monitoring on more complex structures can be coupled with finite element free vibration analysis in order to determine the severity of defects in such structures.

REFERENCES

[1] Krawczuk, M., Ostachowicz, W. and Zak, A. Modal analysis of cracked, unidirectional composite beam, *Composites Part B: Engineering*, **28**, 641–650, (1997). http://dx.doi.org/10.1016/S1359-8368(97)82238-X

[2] Song, O., Ha, T. W. and Librescu, L. Dynamics of anisotropic composite cantilevers weakened by multiple transverse open cracks, *Engineering Fracture Mechanics,* **70**, 105–123, (2003). http://dx.doi.org/10.1016/S0013-7944(02)00022-X

[3] Kisa. M. Free vibration analysis of a cantilever composite beam with multiple cracks, *Composite Science and Technology,* **64**, 1391–1402, (2004). http://dx.doi.org/10.1016/j.compscitech.2003.11.002

[4] Wang, K. and Inman, D. J. Coupling of bending and torsion of a cracked composite beam, *22nd international modal analysis conference (IMAC),* 26–29 January, Michigan, USA, 1460–1472, (2004). http://sem-proceedings.com/22i/sem.org-IMAC-XXII-Conf-s30p01-Coupling-Bending-Torsion-Cracked-Composite-Beam.pdf

[5] Abd El-Hamid Hamada, A. An investigation into the eigennature of cracked composite beams, *Composite Structures*, **38** (l–4),45–55, (1997). http://dx.doi.org/10.1016/S0263-8223(97)00040-8

[6] *ANSYS Release 8.1*, ANSYS Inc., (2004).

Fault Diagnosis For Exhaust Fan Using Experimental Predictive Maintenance Method

Hamdi Taplak

Mechanical Engineering Department, Erciyes University, 38039 Kayseri, Turkey

Emrah Kurt

Afsin-Elbistan Thermal Power Plant, Kahramanmaras, Turkey

Mehmet Parlak

Department of Mechanical Engineering, Faculty of Engineering and Architecture, Nevsehir Haci Bektas Veli University, Nevsehir, Turkey
Graduate School of Natural and Applied Sciences, Erciyes University, Kayseri 38039, Turkey

(Received 23 June 2014; accepted: 3 February 2015)

Unexpected machine failures cause a decrease in production and increase in cost so that predictive maintenance methods have everyday importance. The main principle of predictive maintenance methods is to decide maintenance time of machines by monitoring machine performance during operations and resolving the failure when the machines stop.

In this study, failures of the exhaust fan system used in Afsin-Elbistan B Thermal Power Plant were monitored by using predictive maintenance methods that rely on vibration analysis. The failures were periodically measured from four points on the bearings of fans and motors with a vibration analyzer. Identified failures on the system have been respectively removed with analysis of measurements. After all failures have been removed, it has been noted that vibration values decreased when measured again from the aforementioned four point. With using the predictive maintenance method, failures can be identified before the failures cause negative results whereby both unnecessary machine stops can be prevented and the cost of operation can be decreased.

1. INTRODUCTION

In practical applications, predictive maintenance can use different techniques, such as the analysis of vibrations, the analysis of the potential contaminants in the lubrication system, the control of energy consumption, the control of the temperature in selected positions or the analysis of the noise generated by the machine; in conclusion, the measurement of the parameter or parameters that could be considered representative of the operation of the machine. Among these techniques, the analysis of vibration is the most frequently used and undoubtedly the most effective technique to detect mechanical defects in rotating machinery.[1,2] The maintenance based on the analysis of vibration has been enforced in plants that have mass production since the 1970's. Petroleum, chemical, steel, and paper industries have adopted this technique and have increased their rate of profit thanks to an increment of production and fewer machine stops.

Unexpected machine failure cause both hitch of production schedule and increasing cost with financial loss, which explains why maintenance based on vibration analysis has high importance in industry. The main principles of predictive maintenance include monitoring the machine performance during production, determining the maintenance time and turning off the machine at a convenient time to resolve the predetermined faults.

Even well-designed machines experience slight vibration. The machine elements wear off through continued use. Some machine elements might be deformed, and their dynamical features may change. Clearance between elements, that run together, increases eccentirity and cause imbalance problems. All of these factors cause rising vibration amplitude. Information about machine condition can be obtained by analyzing the vibrations.

When the machines have specific failures, they give some signal intended for the failures. The best signal can be obtained from vibrations of the machines. A vibration is a reaction force against internal and external forces of mechanical elements of a machine. Vibration analyses offer good results on the rotating machines, especially fans, pumps, engines, and gearboxes. There is a great deal of literature available that describes the type of vibration signals to be expected for faults in typical systems and the analysis tehniques that can be used for early detection of faults.[3]

The vibration analysis technique includes vibration measurement and its evaluation. First, vibration signals are collected by the vibration analyzer equipped with a sensor in the time domain by processing FFT, and the information gained from the vibration signals can be used to predict failures, to reduce vibration and to repair failures caused by vibration.[4]

Failures commonly found in fans include imbalance, misalignment, looseness, bearing fault, gear fault, hydraulic and

aerodynamic problems, resonance, etc. In this study, mechanical looseness, bearing faults, rubber damper faults, and engine faults in the used systems were determined using predictive maintenance techniques and have been resolved. Some studies on the topic of fault detection have been done by using the vibration analysis. Orhan et al. presented and examined the vibration monitoring and analysis case studies in machineries that were running in real operating conditions. They determined the failures on the machines in their early stages by using the spectral analysis.[4]

Trebuna et al. analyzed causes of excessive vibration of one of the two fans in the steelworks that provide exhaustion of vapor and residues produced during melting of steel scrap. During operation, the excessive vibration of the problematic fan led to the initiation of cracks in the concrete foundation and the repeated damage to the bearings. Under such conditions, whole equipment can be damaged and collapse. A complex approach was applied to solve this problem. The approach includes experimental and numerical modal analysis of the fan's rotating wheel as well as a series of operational measurements to assess the actual technical condition of the problematic fan and determine possible damages.[5]

McFadden and Smith have modelled the vibration that has been created by single and multiple damages in the inner race of rolling element bearing and have verified the obtained results with experimental results.[6]

Akturk and Gohar have conducted studies on a shaft-bearing system. Change of ball size in the bearing has been investigated regarding the effects of radial and axial vibration. In order to do this, they have created a software and presented results on time-frequency domain.[7]

Ibrahim et al. described the application of vibration analysis technique in the diagnosis of cooler fan of a centrifugal compressor high vibration. To describe this, they collected the data from machinery and showed that the vibration amplitudes for radial directions tend to be high near the coupling of motortogear input by analyzing the data. After essential works have been realized, they managed to reduce and fix, within the acceptable limits the vibration amplitude.[8]

Geramitchioski and Trajcevski investigated vibration produced by rolling bearings defect in the motor-fan machinery and showed the procedure for prediction of rolling bearings defect.[9]

Albraik et al. investigated the correlations between pump performance parameters and surface vibration for the purpose of both pump condition monitoring and performance assessment. They used five impellers to investigate and compare relations between damaged and healthy pump: one impeller in good condition and four others with different defects.[10]

Spychala et al. investigated damages of military aerial ships after exploitation and obtained the vibration answer on simulated damages.[11]

Choi et al. studied to find out the cause of high vibration at cyrogenic pumps-motor system in LNG terminal. They estimated motor rotor bar problems by the vibration analysis and confirmed the results with current analysis.[12]

Ali et al. studied on the effects of working under different speeds at two loading conditions on an electric motor. They showed that the vibration amplitude was affected by changing both load and speed.[13]

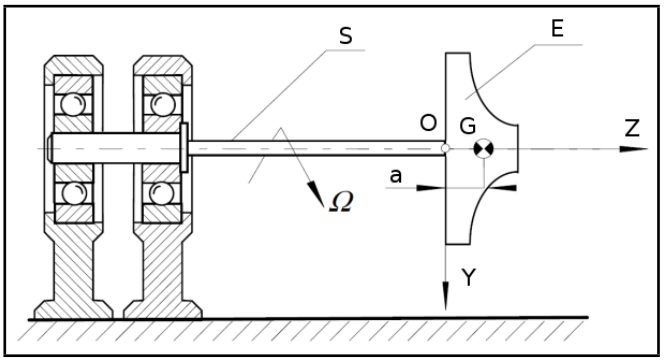

Figure 1. Physical model of fan.[14]

As seen on the publications, vibration analysis technique is frequently used to determine the faults. In these publications, researchers only focused to estimate one fault by vibration analysis. In this study, such as mechanical looseness, bearing faults, rubber damper faults, and engine faults, four different faults in the used systems had been determined with predictive maintenance technique and the faults have been resolved. In addition, the difference in vibration level between before and after maintenance can be clearly seen in Table 2.

2. THEORY

2.1. Determining the Physical and Mathematical Model of the System

Rotor system seen in Fig. 1 represents the physical model of the exhaust fan. Let us accept shaft 'S' on this model is flexible and has no mass. Let us consider fan disc element 'E' as a rigid object fixed to shaft at the point 'O'. Point O is choosen as the centre of XYZ absolute system coordinates. Gravity centre 'G' is far away as 'a' from origin 'O'. This disc element has the mass of 'm' and Z axis is the symmetry axis of the object. Because of this inertia moment on X and Y axis are equal and defined as $I_x = I$ and $I_y = I$. The rotor is rotating with angular velocity of 'Ω'.[14] In this situation, mathematical model of the system is

$$m\ddot{X} + c\dot{X} + kX = F_G; \tag{1}$$

where

$$m = \begin{bmatrix} m & 0 & ma & 0 \\ 0 & m & 0 & ma \\ ma & 0 & I + ma^2 & 0 \\ 0 & ma & 0 & I + ma^2 \end{bmatrix}$$

$$k = \begin{bmatrix} k_{11} & 0 & k_{12} & 0 \\ 0 & k_{11} & 0 & k_{12} \\ k_{21} & 0 & k_{22} & 0 \\ 0 & k_{21} & 0 & k_{22} \end{bmatrix} \quad c = \begin{bmatrix} 0 & 0 & 0 & 0 \\ 0 & 0 & 0 & 0 \\ 0 & 0 & 0 & I_z\Omega \\ 0 & 0 & -I_z\Omega & 0 \end{bmatrix}$$

$$X = \begin{bmatrix} X \\ Y \\ f_X \\ f_Y \end{bmatrix} \quad F_G = \begin{bmatrix} 0 \\ mg \\ 0 \\ mga \end{bmatrix}; \tag{2}$$

Equations of motion of the rigid element are

$$\begin{aligned} m\ddot{x} + ma\ddot{f}_x &= F_x + UF_x \\ m\ddot{y} + ma\ddot{f}_y &= F_y + mg + UF_y; \end{aligned} \tag{3}$$

$$\begin{aligned} I\ddot{f}_z + I_z\Omega\dot{f}_y &= M_x - F_x a + UM_x \\ I\ddot{f}_y + I_z\Omega\dot{f}_x &= M_y - F_y a + UM_y. \end{aligned} \tag{4}$$

Mathematical model of unbalanced rigid object is determined as below after F_x and F_y are removed from Eq. (4) using Eq. (3):

$$m\ddot{x} + c\dot{x} = R + F_G + F_U; \tag{5}$$

where

$$m = \begin{bmatrix} m & 0 & ma & 0 \\ 0 & m & 0 & ma \\ ma & 0 & I + ma^2 & 0 \\ 0 & ma & 0 & I + ma^2 \end{bmatrix}$$

$$c = \begin{bmatrix} 0 & 0 & 0 & 0 \\ 0 & 0 & 0 & 0 \\ 0 & 0 & 0 & I_z\Omega \\ 0 & 0 & -I_z\Omega & 0 \end{bmatrix}$$

$$X = \begin{bmatrix} X \\ Y \\ f_X \\ f_Y \end{bmatrix} \quad F_G = \begin{bmatrix} 0 \\ mg \\ 0 \\ mga \end{bmatrix}; \tag{6}$$

$$F_U = \begin{bmatrix} UF_x \\ UF_y \\ UM_x \\ UM_y \end{bmatrix} = \begin{bmatrix} S\Omega^2 cos(\Omega t + f_S) \\ S\Omega^2 sin(\Omega t + f_S) \\ D\Omega^2 cos(\Omega t + f_D) \\ D\Omega^2 sin(\Omega t + f_D) \end{bmatrix}. \tag{7}$$

Because of this mathematical model of the system considered can be rewriten as

$$m\ddot{X} + c\dot{X} + kX = F_G + F_U. \tag{8}$$

Partial solution of the equation below is

$$m\ddot{X} + c\dot{X} + kX = F_G. \tag{9}$$

Coordinates of balance position of the system is

$$X_S = \begin{bmatrix} X_S \\ Y_S \\ f_{X_s} \\ f_{Y_s} \end{bmatrix} = k^{-1}F_G. \tag{10}$$

If few symbols (notations) are used considering Fig. 2

$$X = X_S + x; \tag{11}$$

equations of motion can be rewriten as

$$m\ddot{x} + c\dot{x} + kx = F_U; \tag{12}$$

where,

$$x = \begin{bmatrix} x \\ y \\ f_x \\ y_y \end{bmatrix}. \tag{13}$$

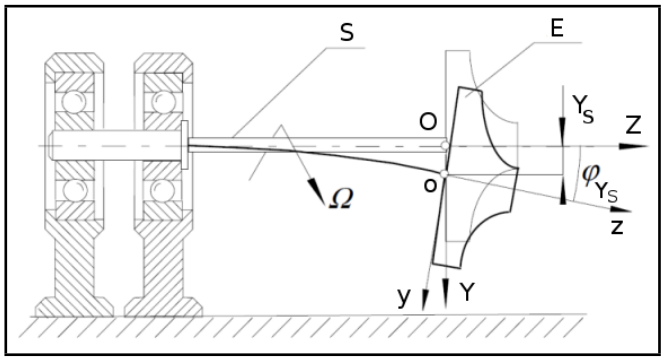

Figure 2. Sudden Position of the Disc As Fixed System Coordinates.[14]

Vector x determines the sudden position of the disc as xyz fixed system coordinates seen at Fig. 2. If Eq. (13) is written at Eq. (12);

$$\begin{aligned} m\ddot{x} + ma\ddot{f}_x + k_{11}x + kf_x &= S\Omega^2 cos(\Omega t + f_S) \\ m\ddot{y} + ma\ddot{f}_y + k_{11}y + kf_y &= S\Omega^2 sin(\Omega t + f_S); \end{aligned} \tag{14}$$

$$\begin{aligned} ma\ddot{x} + (I + ma^2)\ddot{f}_x + I_z\Omega\dot{f}_y + kx + k_{22}f_x \\ = D\Omega^2 cos(\Omega t + f_D) \\ ma\ddot{y} + (I + ma^2)\ddot{f}_y - I_z\Omega\dot{f}_y + k_y + k_{22}f_y \\ = D\Omega^2 sin(\Omega t + f_D). \end{aligned} \tag{15}$$

Complex forms of the equations of motion can be determined as below if right sides of Eqs. (14) or (15) are multiplied with unit vector (i) and added to Eq. (15).

$$\begin{aligned} m\ddot{z} + ma\ddot{f}_z + k_{11}z + kf_z &= S\Omega^2 e^{(\Omega t + f_s)} \\ ma\ddot{z} + (I + ma^2)\ddot{f}_z - iI\Omega\dot{f}_z + kz + k_{22}f_z \\ = D\Omega^2 e^{i(\Omega t + f_D)}; \end{aligned} \tag{16}$$

where,

$$\begin{aligned} z &= x + iy \\ f_z &= f_x + if_y. \end{aligned} \tag{17}$$

3. EXPERIMENTAL STUDY

3.1. Exhaust Fan System

In industry, cost and quality are gaining importance day, by day and efficiency is becoming a ciritical factor for success in rivalry environment. It is necessary to keep working performance of manufacturing systems at the highest level possible and making maintenance continuously with up-to-date maintenance techniques for corporations to work more efficiently. Predictive maintenance methods, which are being used widespreadly, vibration analysis, failure determinations, and removal activities from this methods are raising its importance in most of the corporations of today's rivalry environment. Important stipulations of industrial corporations include using predictive maintenance application methods effectively, correctly gathering data, interpreting in a timely manner, giving net decisions for results, and applying these decisions suitably to the techniques.

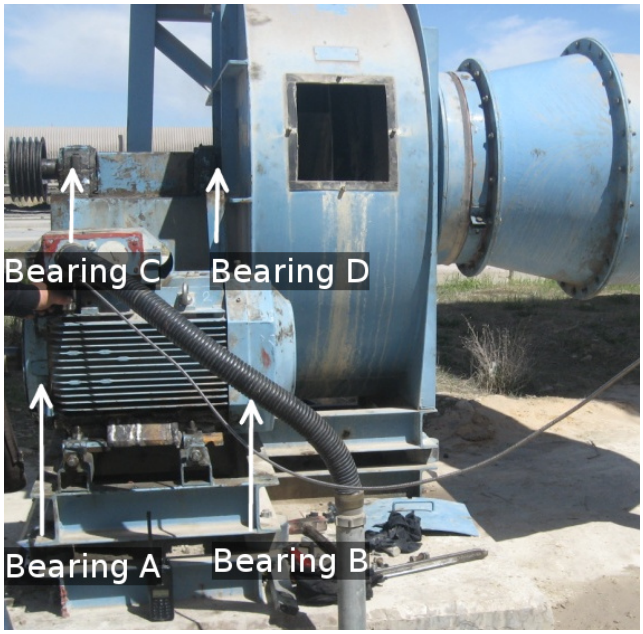

a)

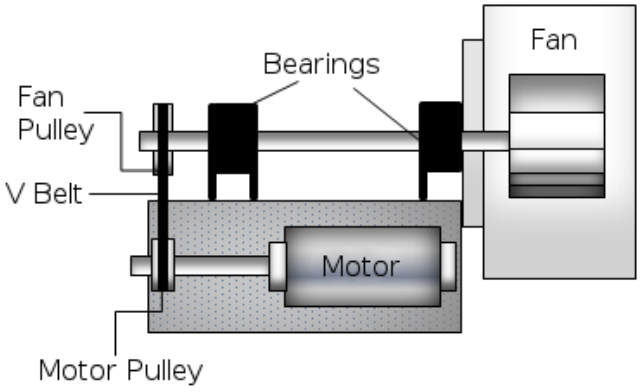

b)

Figure 3. a) View of the exhaust fan system used on experimental study. b) Schematic representation of exhaust fan.

In this work, studies made to determine and to remove probable failures of the system with vibration analysis and determined results are summarized to the extent of predictive maintenance applications on exhaust fan systems.

3.1.1. The information about fans used on experiment

As shown in Fig. 3a, the exhaust fan system, situated on a flue gas purification system in Afsin Elbistan B Thermal Power Plant, has been used in experimental work. Repairing motor supports, changing the rubber damper, changing bearings, adjusting the pulley, and cleaning the dust on the fan of this system have been completed; additionally, an attempt has been made to minimize vibration on the fan by analyzing spectrum analysis graph.

3.1.2. Technical features of the fan

In this study, the vibration has been measured with DCX-RT/ExpertAlert vibration analyzer. First, the information of exhaust fan has to be identified on the analyzer to measure vibration of the system.

Table 1. Technical features of fan.

Trademark	Alfer Engineering ltd corp.
Type/Size	AL-B3-630
Flow	26000 m^3/h
Temperature	20° C
Total Pressure	350 mmss
Year of manufacture	2002
Fan Speed	1723 rpm
Motor Speed	1475 rpm
Motor	ABB Motors
Diameter of motor pulley	94 mm
Diameter of fan pulley	81 mm
Length of belt	2700 mm

Figure 5. Measurement of vibrations of Bearing A.

3.2. Measurements and Analysis on the Fan

3.2.1. The first measurement

In the experimental analysis, vibration has been measured from four points on the fan bearings and motor bearings with analyzer before cracked motor supports havent been welded with arc welding and damaged fan bearings havent been replaced with new ones. After repair operations, ie., welding cracked motor supports (Fig. 4b), and replacing damaged fan bearings with new ones (Fig. 4c), vibration has been measured from four points again (Fig. 5). Second measurements showed the amplitude at the peak of 1x increased. The belts have been demounted to identify whether the vibration was caused by fan or motor, and vibration of motor bearings have only been measured. As a result, analysis of the vibration showed that there was no problem on the motor. Third, demounted belts have been mounted again and performed necessary adjustments. When the vibration of bearings were measured again, it showed that the amplitude at the peak of 1x comparatively decreased. In addition, measurements showed that amplitude of vibration on Bearing A and Bearing B was high at the peak of 1x and amplitude of vibration on Bearing C and Bearing D was high at the peak of 1x, 2x, 3x, and 4x. It was found that worn or loose belt problems occurred at the third and fourth multiples of belt frequency. Misalignment of belt-pulley is seen at the peak of 2x, and mechnaical looseness

Figure 4. a) Cracked motor support. b) Welding of cracked motor support. c) Damaged bearing. d) Mounting of new bearing.

is seen at the peak of 3x.
Belt Frequency = (3,142*1723 rpm*81 mm)/2700 mm = 162 rd/s
Fourth, bolts that fix the fan and motor to ground have been fastened. While the bolts were being fastened, it was discovered that the rubber dampers were sclerous, so that all nine rubber dampers have been changed. Finally, adustment of belt-pulley has been done and the vibrations have been measured again.

4. RESULTS AND DISCUSSION

4.1. Results

In the experimental study, vibration measurements have been done from four points on fan bearings and motor bearings, and results have been analyzed. By evaluation of the results, vibration values on four bearings have been minimized. Vibration values and graphs of the labeled four bearings have been respectively given for before maintenance and after maintenance.

As shown in Fig. 6, while the vibration value on the Bearing A was 20 mm/s on one orders radial direction before maintenance, after maintenance the value decreased to 4 mm/s (Fig. 7). In addition, it is clearly seen that while the vibration

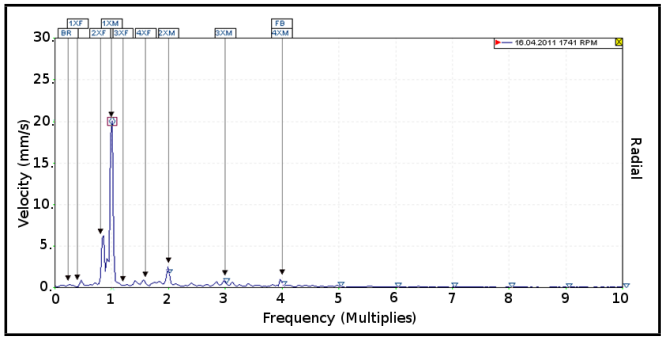

Figure 6. Spectrum analysis graph for Bearing A before maintenance.

value on Bearing B was 11 mm/s on one order's axial direction before maintenance (Fig. 8), after maintenance the value decreased to 2 mm/s (Fig. 9).

As shown in Fig. 10, the vibration value on the Bearing C was 15 mm/s on one orders radial direction before maintenance, and after maintenance the value have been decreased to 3 mm/s (Fig. 11). In addition, it is clearly seen that while the vibration values on the Bearing D were 11.5 and 12 mm/s on one orders radial and axial direction before maintenance, respectively (Fig. 12 and Fig. 14); after maintenance, the values have been decreased to 8 mm/s and 1 mm/s, respectively

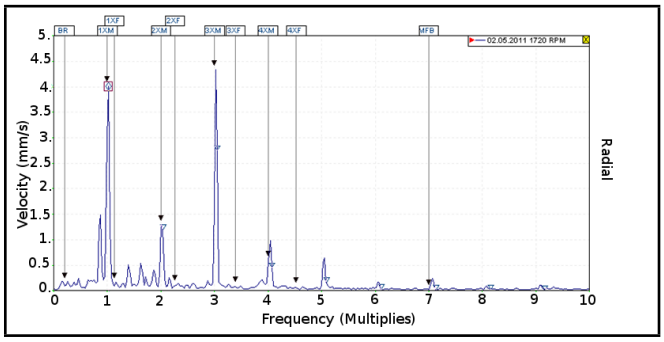

Figure 7. Spectrum analysis graph for Bearing A after maintenance.

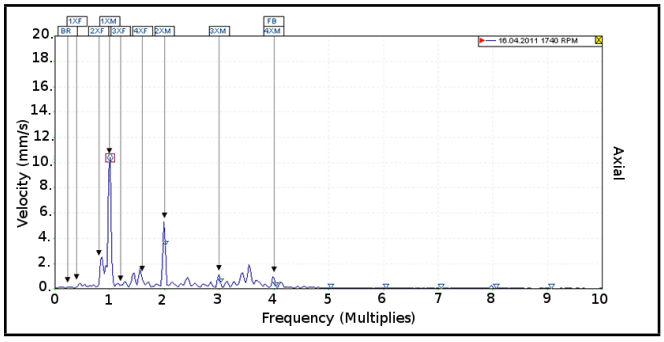

Figure 8. Spectrum analysis graph for Bearing B before maintenance.

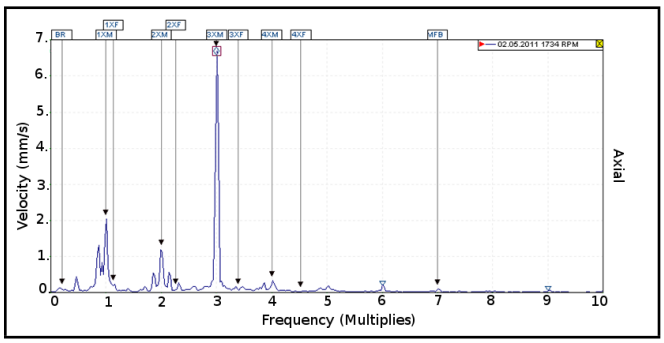

Figure 9. Spectrum analysis graph for Bearing B after maintenance.

Table 2. Vibration values before and after maintenance.

Measurement point	Vibration values before maintenance	Vibration values after maintenance	Percentage of change
Bearing A (radial)	20 mm/s	4 mm/s	80,00%
Bearing B (axial)	11 mm/s	2 mm/s	81,80%
Bearing C (radial)	15 mm/s	3 mm/s	80,00%
Bearing D (radial)	11,5 mm/s	8 mm/s	30,43%
Bearing D (axial)	12 mm/s	1 mm/s	91,67%

(Fig. 13 and Fig. 15). Consequently, vibration values have been markedly reduced after analysis and maintenance procedures had been done (Table 2).

4.2. Discussion

When unexpected failures occur on machines, maintenance takes longer because of the level of difficulty and time consuming of assurance of relay. This leads to storing extra relay for factories that do not perform planned and programmed maintenance. Storing extra relay increases cost and creates additional cost for finished shelf life of relays. Relay can be provided on

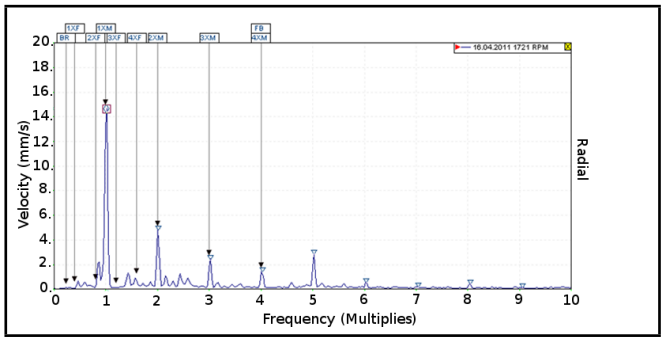

Figure 10. Spectrum analysis graph for Bearing C before maintenance.

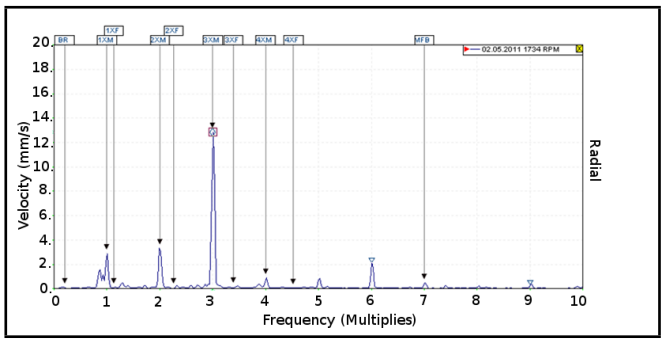

Figure 11. Spectrum analysis graph for Bearing C after maintenance.

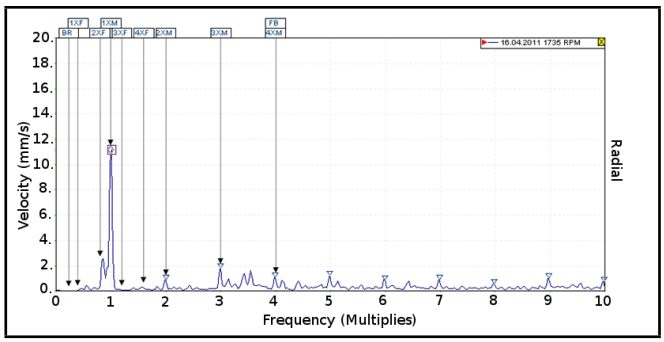

Figure 12. Spectrum analysis graph for Bearing D before maintenance (radial).

time by using predictive maintenance method; the machine is monitored constantly, and time of faults can be predicted so that it doesn't need to store extra relay.

As seen in Table 2, while vibration value before maintenance on Bearing A was 20 mm/s, this value decreased to 4 mm/s after maintenance. The same situation can be also seen for other bearings. The largest decline on Bearing D was 91.67%. It can be said that Bearing D damaged largely before maintenance. This situation shows that predictive maintenance has high importance.

The cost of labor can be reduced by using predictive maintenance method rather than industries employing extra workers to run after failures because of sudden machine failures.
Although the equipment and specialists required for predictive maintenance method may seem to be an increase in cost, the difference will payoff in a short time. Overall, predictive maintenence method decreases cost and production loss.

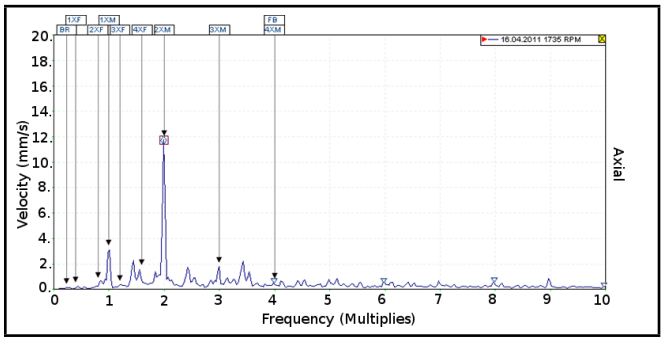

Figure 13. Spectrum analysis graph for Bearing D after maintenance (radial).

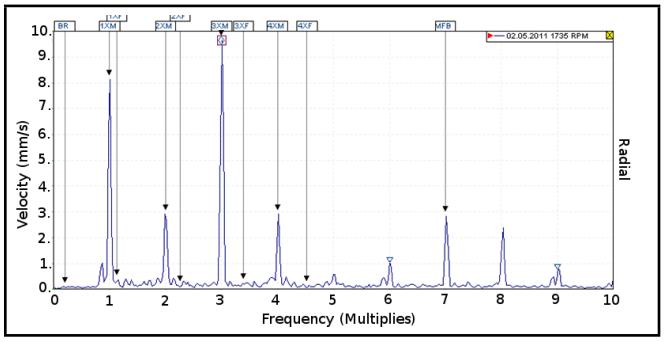

Figure 14. Spectrum analysis graph for Bearing D before maintenance (axial).

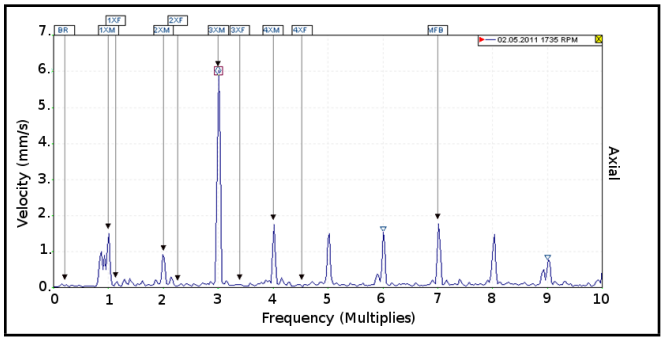

Figure 15. Spectrum analysis graph for Bearing D after maintenance (axial).

REFERENCES

[1] Tsang AHC. Condition-based maintenance: tools and decision making. *J. Quality Maintenance Eng*, 3–17, (1995). http://dx.doi.org/10.1108/13552519510096350

[2] Girdhar, P., Scheffer, C., In practical machinery vibration analysis and predictive maintenance, Oxford, (2004). http://dx.doi.org/10.1016/b978-075066275-8/50001-1

[3] I. E. Alguindigue, L. A. Buczak, R. E. Uhrig, Monitoring and diagnosis of rolling element bearings using artificial neural networks, *IEEE Trans Ind Electron*, **40** (2), 209–217, (1993). http://dx.doi.org/10.1109/41.222642

[4] Orhan, S., Aktürk, N., Çelik, A., Vibration monitoring for defect diagnosis of Rolling element bearings as a predictive maintenance tool: Comprehensive case studies, *NDT&E International*, **39**, 293–298, (2006). http://dx.doi.org/10.1016/j.ndteint.2005.08.008

[5] Trebuna, F., Simcak, F., Bocko, J., Hunady, R., Pastor, M., Complex approach to the vibrodiagnostic analysis of excessive vibration of the exhaust fan, *Engineering Failure Analysis*, **37**, 86–95, (2014). http://dx.doi.org/10.1016/j.engfailanal.2013.11.015

[6] McFadden, P. D., Smith, J. D., Model for the vibration produced by a single point defect in a Rolling element bearing, *Journal of Sound and Vibration*, **96**(1a), 69–82, (1984). http://dx.doi.org/10.1016/0022-460x(84)90595-9

[7] Aktürk, N., Gohar, R., The effect of Ball Size Variation on Vibrations Associated with Ball-Bearings, *Proc. I. Mech. E.*, 212 Part j, 101–109, (1998). http://dx.doi.org/10.1243/1350650981541921

[8] Ibrahim, I., Rani, A. M. A., Zainuddin, A., Anua, M. R. M., Centrifugal compressor cooler fan high vibration: a case study, *Australian Journal of Mechanical Engineering*, **9** (1), 1–9, (2012). http://dx.doi.org/10.1080/14484846.2012.11464613

[9] Geramitchioski, T., Trajcevski, L., Prediction of rolling bearings defect in motor-fan using vibration signal analysis, *Machine Design*, **3** (3), 211–216, (2011).

[10] Albraik, A., Althobiani, F. G., Ball, A., Diagnosis of centrifugal pump faults using vibration methods, *Journal of Physics: Conference Series*, **364**, 2012. http://dx.doi.org/10.1088/1742-6596/364/1/012139

[11] Spychala, J., Szczekala, M., Zokowski, M., Diagnosis of the jet-propelled engine by vibration analysis, *Transport Problems*, **4** (3), 75–81, (2009).

[12] Choi, B., Kim, H., Gu, D., Kim, H., Jeong, H., Diagnosis of cryogenic pump-motor systems using vibration and current signature analysis, *Journal of Mechanical Science and Technology*, **20** (7), 972–980, (2006). http://dx.doi.org/10.1007/bf02915996

[13] Ali, M. K., Youssef, M. F. H., Hamaad, M. A., El Butch, A. A., A study on fault diagnosis by vibration analysis at different loading and speed conditions, ASAT-13, **13**, 1–11, (2009).

[14] J. M. Krodkiewski, Dynamics of Rotors, The University of Melbourne, Department of Mechanical Engineering, (2000).

Dynamic Analysis of Draft Gear and Draft Pad of Freight Wagon due to Localized Defects using FEM

Sachin S. Harak, Satish C. Sharma and S. P. Harsha

Vibration and Noise Control Lab., Mechanical & Industrial Engineering Department, Indian Institute of Technology, Roorkee – 247667, Uttarakhand State, India

(Received 26 November 2013; accepted 12 October 2015)

The present work investigates the effect of a crack on the modal frequency of a draft pad. Initially, the first five mode shapes of a healthy draft pad and the first seven mode shapes of healthy draft gear considering compressed draft pads are determined using the finite element approach. A mathematical model of the draft pad is formulated to predict the effect of the crack on its modal frequency. A semi-elliptical shaped crack is modelled in the lateral and longitudinal direction of the draft pad. It is observed that if the crack lies in the zone of minimum modal displacement, then the frequency drop is minimal, and if the crack lies in the zone of maximum modal displacement, then the frequency drop is significant. Various damage scenarios are simulated by varying the width and aspect ratio of the crack in order to identify its effect on the modal frequency. It is seen that if the aspect ratio is varied while the crack's width is maintained constant, then the frequency drop is linear, whereas if the crack's width is varied while the aspect ratio is maintained constant, then the frequency drop is parabolic. This study provides a tool for monitoring exciting frequencies of draft gear and shows how each modal frequency is affected by the crack due to parameters like aspect ratio, crack width, and crack location/orientation.

1. INTRODUCTION

The longitudinal dynamics of freight wagons largely depends on the dynamics of draft gear and consequently the draft pad(s). Draft gear is a key part of autocouplers in freight wagons, as they function like a cushioning device absorbing shocks in the form longitudinal forces arising due to train operations like accelerating or braking. The draft gear (RF-361) under consideration is manufactured by Miner Enterprises Inc., USA. It is normally used in open hopper/coal wagons and bulk commodity wagons. Freight wagons in Indian Railways are loaded with RF-361 draft gear. The various components of the draft gear illustrated in Fig. 1a are six draft pads with a top follower, three shoes, and a wedge. The draft pad shown in Fig. 1b consists of a rubber compound sandwiched between two steel plates and is perfectly bonded to them. All these components are assembled in housing with the three shoes arranged circumferentially around the wedge. The wedge and shoes operate between the top follower and the draft gear housing. The applied forces reach the draft pads through the wedge and shoes. Each pad has an ultra-high capacity natural rubber spring package to absorb the high longitudinal forces arising due to operations like acceleration and/or braking and also due to changes in track topography. These forces, being repetitive in nature, accelerate the damage to the draft pads in the presence of defects. These draft pads, when used in damaged conditions, cause the longitudinal forces to be transmitted to the wagon, which compromises the safety of the laden goods.

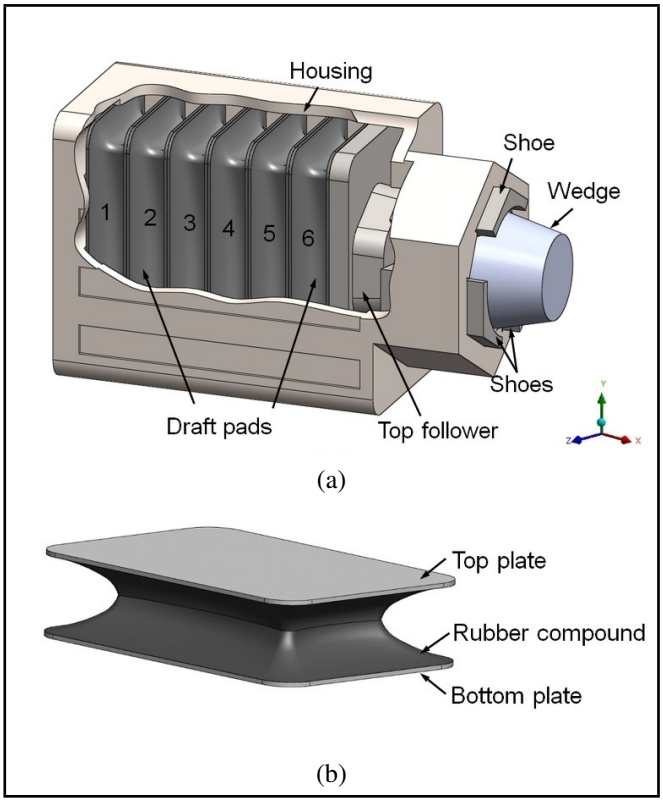

Figure 1. (a) A cross-sectional view of draft gear unit (RF-361) and (b) a typical draft pad (RF-8).

A review shows that the longitudinal in-train forces are responsible for several problems including broken draft gear and even causing freight wagons to be pulled off the inside of curves.[1] Initial efforts by researchers were aimed at reducing longitudinal oscillations in passenger trains. Measurements and simulations of in-train forces were carried out by Duncan and Webb to achieve reduction in longitudinal oscillations.[2] Work by Chen was aimed at developing a mathematical model to calculate transient responses of a coupler and to identify the coupling speed.[3] Experimental efforts by McClanachan et al. helped determine the occurrences of coupler impacts combined with pitching motions in the wagon body.[4] The impacts were simulated using the train-wagon interaction model in NUCARS and ADAMS/Rail. The fatigue life of three different wagon connection coupling systems that had draft gear with and without self-locking features was evaluated by Cole

and Sun.[5] A numerical procedure was developed by Belforte et al. to investigate the dynamics of heavy freight trains.[6] The proposed methodology by Belforte et al. combined a numerical model designed for the longitudinal dynamics of the whole trainset called TrainSet Dynamics simulator (TSDyn) with a multibody code named Modular Non-Stationary TRAMcar dynamics simulator originally developed to analyse the dynamics of modular tramcars (MoNSTram) and used for a more detailed investigation of the response of a trainset segment.

The effect of train braking delay time (for long, medium, and short brake application time) at different train forward velocities on longitudinal dynamics of trains was studied by Nasr and Mohammadi.[7] Cole et al. added modelling of coupler angles to a normal longitudinal simulation for a comprehensive study of lateral components of coupler forces, as these forces affected the stability of long and heavier trains.[8] Qi et al. improved the efficiency and safety of the wagons during positioning operations by optimizing the design speed of the positioner based on the simulation of longitudinal train dynamics. This was achieved by replacing the traditional draft gear model with nonlinear spring and linear damping with a more detailed model based on the achievement of contact and impact mechanics while considering the coupler slack.[9] Recently, Wu et al. developed a new technology called the Train dynamics and energy analyser/train simulator (TDEAS) by modelling three aspects: wagon connection systems, air brake systems, and train energy components in order to perform detailed whole trip longitudinal train dynamics and energy analyses and to act as a driving simulator for heavy haul trains.[10] The simulator uses advanced wedge-spring draft gear models that can simulate a wider spectrum of friction draft gear behaviour.

The present work concentrates on the effect of a crack on the natural frequency of a draft pad, as it plays a significant role in predicting the fatigue behaviour of the components subjected to repetitive loads. Initially the first five mode shapes of a healthy draft pad and the first seven mode shapes of healthy draft gear were determined by using the finite element approach. These mode shapes were compared to establish the participating mode shapes of the draft pad in the draft gear. Furthermore, the effect of the crack on participating mode shapes of the draft pad was determined by using the finite element approach. A mathematical model of the draft pad is formulated to predict the effect of the crack on its modal frequency. The crack was modelled by using a semi-elliptical shape in two directions, viz., lateral and longitudinal direction of the draft pad. Various damage scenarios were simulated by varying the width as well as the aspect ratio of the crack to identify its effect on modal frequency.

2. MODAL ANALYSIS USING FINITE ELEMENT APPROACH

Modal analysis determines the natural frequencies and mode shapes of a continuous structure. For a free vibration analysis, the natural frequencies (ω_i) and the mode shapes (ϕ_i) were calculated using the following relation: $([K] - \omega_i^2[M])\phi_i = 0$.[11] Here, the finite element was used to setup the system equations of motion, which were solved for natural frequencies and mode shapes using Eigen-value analysis. For evaluating mode shapes, the material was assumed to behave linearly elastic neglecting nonlinearities.

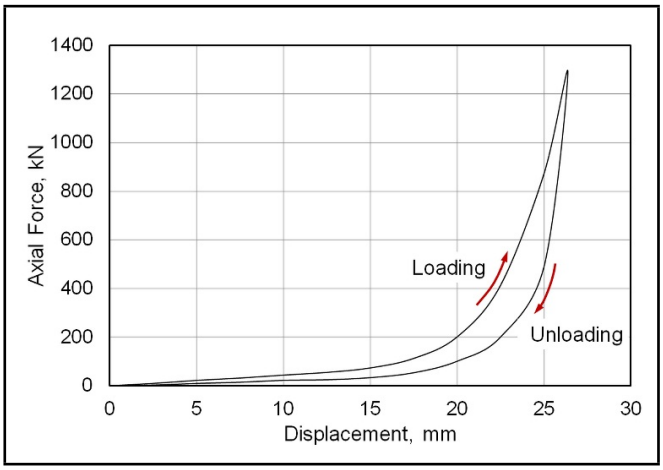

Figure 2. A typical manufacturer's draft pad response data.

2.1. Model For Modal Analysis

For vibration-based analysis, which is model dependent, an accurate numerical model was important to use. Thus, three dimensional models of the draft pad and draft gear were created using *Solidworks* and exported to ANSYS environment for numerical analysis.

2.1.1. Draft pad

The draft pad used in this study is illustrated in Fig. 1b. It is available commercially as "RF-8" and confirms to "Drg. No. WD-90076" of Indian Railways. The draft pad consists of a rubber compound sandwiched between two steel plates and is perfectly bonded to them. The material properties of steel are Young's modulus: 200×10^9 N/m^2, Poisson's ratio: 0.30, and material density: 7850 kg/m^3. The material properties for the rubber compound were derived from experimental data, which was a non-linear plot of force and displacement as illustrated in Fig. 2. This plot is an outcome of a uniaxial test on a draft pad. Young's modulus and Poisson's ratio were determined with the help of a material model calibration software. The hysteresis due to visco-elastic behaviour of rubber compound was responsible for dissipating the longitudinal shock loads. The damping ratio (ζ) was evaluated to be 0.05 and the same was considered during simulation. The numerical values are: Young's modulus= 21.94×106 N/m^2 and Poisson's ratio= 0.4978. The material density was specified by the manufacturer and is 1220 kg/m^3. The effective life span of natural rubber under operating conditions was considered to be 15 years. However, periodic maintenance was scheduled every five years and includes replacement of failed draft pads.[12] This indicates that the average life of almost all draft pads is around five years. Hence, changes in the properties of rubber compounds due to ageing were not included for the proposed dynamic analysis. The boundary condition for modal analysis of a draft pad thus included fixing all nodes at the outer surface of bottom plate.

2.1.2. Draft gear

Fig. 1a illustrates the sectional view of draft gear. The various components of the draft gear consisted of six draft pads with a top follower, three shoes, and a wedge. The material properties taken were the same as those in the earlier case. For the boundary conditions, all nodes at the bottom surface of the housing were fixed, whereas the interface between adjacent pads were assumed to be bonded type since the pads were

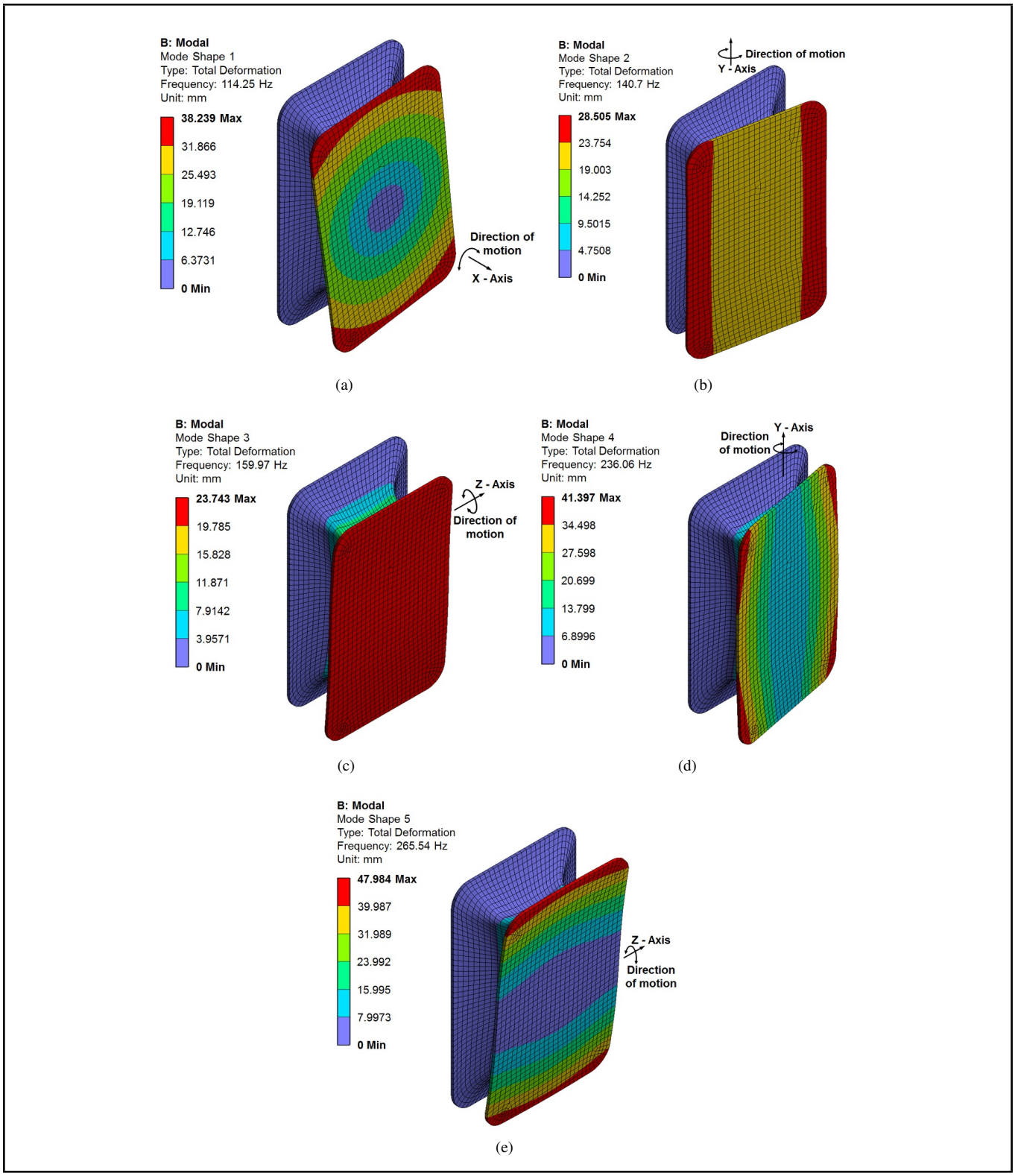

Figure 3. Mode shapes of the draft pad: (a) the first mode shape at 114.25 Hz (b) the second mode shape at 140.70 Hz (c) the third mode shape at 159.97 Hz (d) the fourth mode shape at 236.06 Hz and (e) the fifth mode shape at 265.54 Hz.

in constant compression within the draft gear.

2.2. Mode Shapes and Frequencies of Draft Pad and Draft Gear

The modal frequencies of an individual draft pad (for the rst five modes) and draft gear (for first seven modes) were obtained using the finite element package (ANSYS) and presented in Tables 1 and 2 respectively.

Table 1. The first five modal frequencies of an individual draft pad in Hz.

Mode	1	2	3	4	5
Frequency	114.25	140.7	159.97	236.06	265.54

Table 2. The first seven modal frequencies of draft gear in Hz.

Mode	1	2	3	4	5	6	7
Frequency	61.97	69.99	77.75	121.12	132.88	147.97	174.22

The first five mode shapes of an individual draft pad are illustrated in Fig. 4. Hence, it is seen that:

- The first mode shape, Fig. 3a, describes oscillatory motion of the rubber compound and the top plate about the x-axis of the draft pad.
- The second mode shape, Fig. 3b, shows oscillation of the rubber compound and the top plate about the y-axis. However, the y-axis about which the oscillation occurs doesnt coincide with the draft pad y-axis but passes through the base plate of the draft pad.
- The third mode shape, Fig. 3c, describes oscillation of the rubber compound and the top plate about the z-axis. The z-axis doesn't coincide with the draft pad z-axis but passes through the base plate of draft pad.
- The fourth mode shape, Fig. 3d, shows oscillation of the rubber compound and the top plate about the y-axis. The y-axis is contained by the top plate, as seen in the illustration.
- The fifth mode shape, Fig. 3e, indicates oscillatory motion of the rubber compound and the top plate z-axis. As seen in the illustration, the z-axis is contained by the top plate.

A comparison of the mode shapes of each draft pad in the draft gear with mode shapes of an individual draft pad was done. It was observed that the individual draft pad's rst ve mode shapes dominated the behaviour of each draft pad in the draft gear for all seven mode shapes (of the draft gear). This was because the draft pads housed in the draft gear had their own individual behaviour, which cumulatively resulted in different mode shapes of the draft gear. These mode shapes of the draft gear had no resemblance with mode shapes of an individual draft pad. Fig. 4a describes the rst mode shape of a draft gear. The draft gear housing was very stiff compared to the draft pad, and thus had a very poor modal response. Hence, it had been hidden in this view. The modal behaviour of each draft pad was presented separately. It was seen that all the draft pads oscillated about the longitudinal (x) axis of the draft gear. Each draft pad exhibited modal behaviour close to its rst mode shape. A symmetry in modal behaviour was observed at the interface of the third and fourth pads for all seven mode shapes of the draft gear. Hence, the modal behaviour of only the rst three draft pads is presented in the illustrations.

For the second mode of the draft gear, a linear displacement of the interface between pad 3 and pad 4 in the lateral (z) direction was observed, which caused the draft pads to exhibit modal behaviour close to its second mode shape. The third mode showed linear displacement of the interface between pad 3 and pad 4 in the vertical (y) direction, causing the draft pads to exhibit modal behaviour close to its third mode shape. For the fourth mode shape, the interface between pad 3 and pad 4 remained fixed, and the interfaces between the pads (1 and 2; pads 2 and 3; pads 4 and 5; and pads 5 and 6) oscillates about the longitudinal (x) axis in the opposite sense. As a result, modal behaviour corresponding to the first mode shape of the draft pad was observed in some of the draft pads.

The fifth mode shape showed oscillation of the interface between pad 3 and pad 4 about the vertical (y) axis. The result was that some draft pads exhibited fourth modal behaviour of an individual draft pad. The remaining draft pads exhibited higher modal behaviour. The sixth mode shape showed oscillation of the interface between pad 3 and pad 4 about the lateral (z) axis. As a result, some draft pads exhibited third modal behavior while some exhibited fifth modal behaviour of an individual draft pad. In the seventh mode shape, the interfaces between pads 2 and 3 and pads 4 and 5 remained fixed, and the interfaces between pads 1 and 2; 3 and 4; and 5 and 6 oscillated about the longitudinal (x) axis, which caused every single pad to execute motion in accordance to the first mode shape. The oscillatory motion of the interface between pads 1 and 2, 5 and 6, and 3 and 4 was opposed. This modal relationship between pads in the draft gear as well as an individual draft pad is summarized in Table 3.

3. THE EFFECT OF CRACKS ON MODAL FREQUENCIES

As per the fundamentals of vibration, the natural frequency (ω_n) for any mechanical system is affected by two parameters: mass (m) and stiffness (K). The effect of these two parameters is generally defined by the equation:

$$\omega_n = \sqrt{K/m}. \tag{1}$$

The natural frequency is directly proportional to the stiffness of the system. Thus, any parameters that affect the stiffness of the system also affect its natural frequency. Hooke's law can also be used to correlate system stiffness with other parameters. As per Hooke's law:

$$\sigma = E \cdot \varepsilon; \tag{2}$$

or

$$\frac{W}{A} = E\frac{\delta l}{l}. \tag{3}$$

The terms in Eqs. (2) and (3) carry their usual meaning. The stiffness for any system that obeys Hookes law can thus be written as:

$$K = \frac{W}{\delta l} = E\frac{A}{l}. \tag{4}$$

It is seen that the stiffness of any system is affected by its Young's modulus, cross-sectional area, and thickness. Thus, these parameters have a similar impact on the system's natural frequency. The crack's presence affects the cross-sectional area of the system and tends to reduce it. A reduced area results in reduced stiffness and, consequently, a reduced natural frequency, which is seen in Eqs. (1) and (4).

While considering any crack, variation in the area of a crack is effected by the crack's width and aspect ratio. When the crack's width is constantly maintained and the aspect ratio is varied, it is seen that the area is the function of a single parameter:

$$A = f(\textit{depth of crack}). \tag{5}$$

From Eq. (5) it is observed that changing the aspect ratio while maintaining the crack width constant results in linear variation of the area. If the variation in area is effected by varying the crack width and maintaining aspect ratio constant, then area of the crack is function of two parameters, viz., crack width and depth of crack. Thus,

$$A = f(\textit{crack width}, \textit{depth of crack}). \tag{6}$$

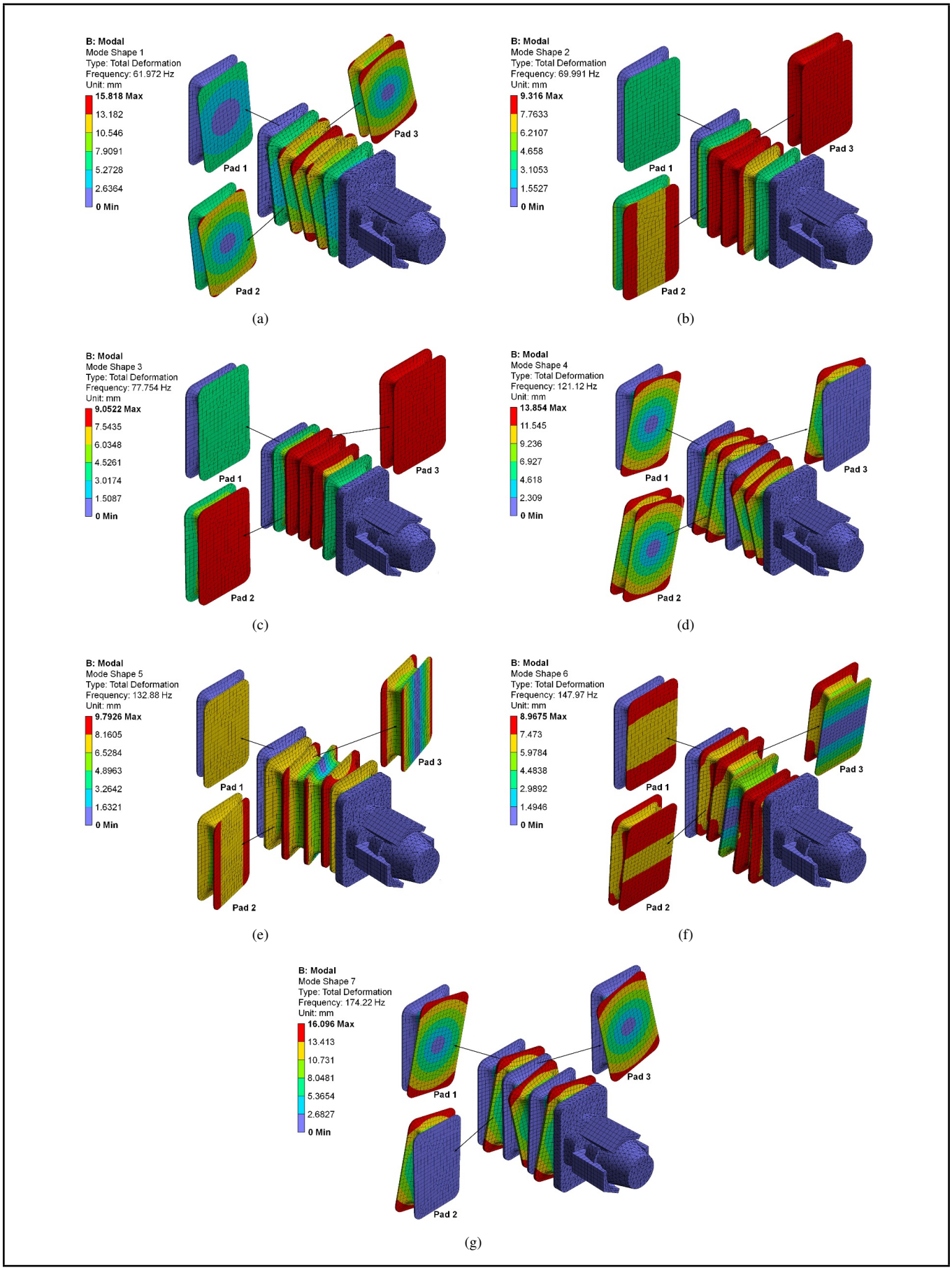

Figure 4. Mode shapes of the draft gear with housing hidden for the (a) first modal frequency (b) the second modal frequency (c) the third modal frequency (d) the fourth modal frequency (e) the fifth modal frequency (f) the sixth modal frequency and (g) the seventh modal frequency.

Table 3. Participating mode shapes of an individual draft pad in the modal behaviour of draft gear.

Draft gear		Participating modes of various draft pads (of draft gear)					
Mode No.	Frequency	Pad 1	Pad 2	Pad 3	Pad 4	Pad 5	Pad 6
1	061.97	Mode 1	Mode 1	Mode 1	Mode 1	Mode 1	Mode 1
2	069.99	Mode 2	*	Mode 2	Mode 2	*	Mode 2
3	077.75	Mode 3	Mode 3	*	*	Mode 3	Mode 3
4	121.12	Mode 1	*	Mode 1	Mode 1	*	Mode 1
5	132.88	*	Mode 4	*	*	Mode 4	*
6	147.97	*	Mode 5	Mode 3	Mode 3	Mode 5	*
7	174.22	Mode 1	Mode 1	Mode 1	Mode 1	Mode 1	Mode 1

* Indicates a higher mode of an individual draft pad.

Under such circumstances, variation in the area is either parabolic or second order. This reduction in stiffness will consequently reduce the natural frequency. Thus, for a draft pad, the presence of a crack should cause a reduction in natural frequency, as seen in Eqs. (5) and (6).

3.1. Mathematical Model of Draft Pad

As discussed earlier, the effect of the crack was to reduce the stiffness of the system. Hence, a mathematical relationship between the natural frequency and the stiffness of the system was necessary to predict the idealized behaviour of the system in the presence of the crack. From simulation, it was observed that all the mode shapes of the draft pad exhibited an oscillatory motion about either the x, y, or z axis. The same could also be observed in Fig. 4. All of these modal behaviours could be approximated by a single degree of freedom model as shown in Fig. 5a. The bottom plate was grounded and the mass of the top plate and the rubber compound was lumped as a single mass and represented as m_p. The stiffness of the rubber compound was represented by two stiffnesses, K_1 and K_2, such that:

$$K_{pad} = K_1 + K_2 \tag{7}$$

The mass was free to oscillate about its centroid. The stiffnesses, K_1 and K_2, are located at distances a and b respectively from the centroid and represent the crack's location in the plane of the crack. This proposed model was used to determine the parameters affecting the modal frequency.

Figure 5b shows the forces acting on the draft pad. Here, $K_1.a\theta$ and $K_2.b\theta$ are the restoring forces opposing the inertia couple $I\ddot{\theta}$. The equation of motion for the mass m_p can be determined by using D'Alembert's principle:

$$I\ddot{\theta} = -K_1 \cdot a\theta \cdot a - K_2 \cdot b\theta \cdot b; \tag{8}$$

or

$$I\ddot{\theta} + (K_1 \cdot a^2 + K_2 \cdot b^2)\theta = 0; \tag{9}$$

and

$$\omega_n = \sqrt{\frac{(K_1 \cdot a^2 + K_2 \cdot b^2)}{I}}. \tag{10}$$

It can be seen from Eq. (10) that the stiffnesses, K_1 and K_2, of the mass m_p directly impacted the natural frequency of the system. Thus, the presence of the crack that reduced the area caused a reduction in stiffness and consequently the natural frequency. Hence, for the draft pad, the natural frequency was dependent on the presence of the crack (in the form of reduced values of stiffnesses K_1 or K_2) and the location of the crack in its own plane.

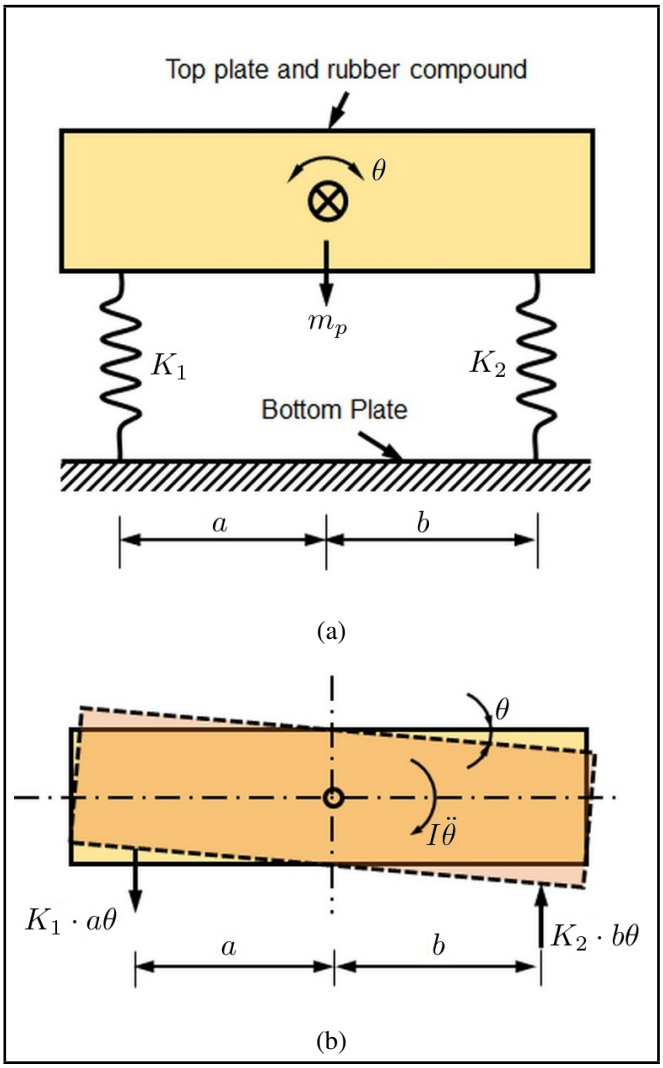

Figure 5. (a) The mathematical model of the draft pad and (b) the free body diagram of the draft pad.

3.2. Modelling a Crack in 3D CAD Model of Draft Pad

An analysis of the types of pad failures was carried out in a maintenance workshop of Indian Railways located in Jagadhri, Haryana State, India, which is the largest amongst those in the northern part of the country. It handles as much as 40 draft gear units daily, apart from other maintenance activities. The shape of the crack was finalized after a careful analysis of the draft pads, which failed during operation. The following are some important illustrations that were instrumental in finalizing the shape and location of the cracks.

As reported by the operators in the workshop, nearly 80% of the draft pads that were replaced for being faulty had cracks either in the lateral or longitudinal orientation with their widths

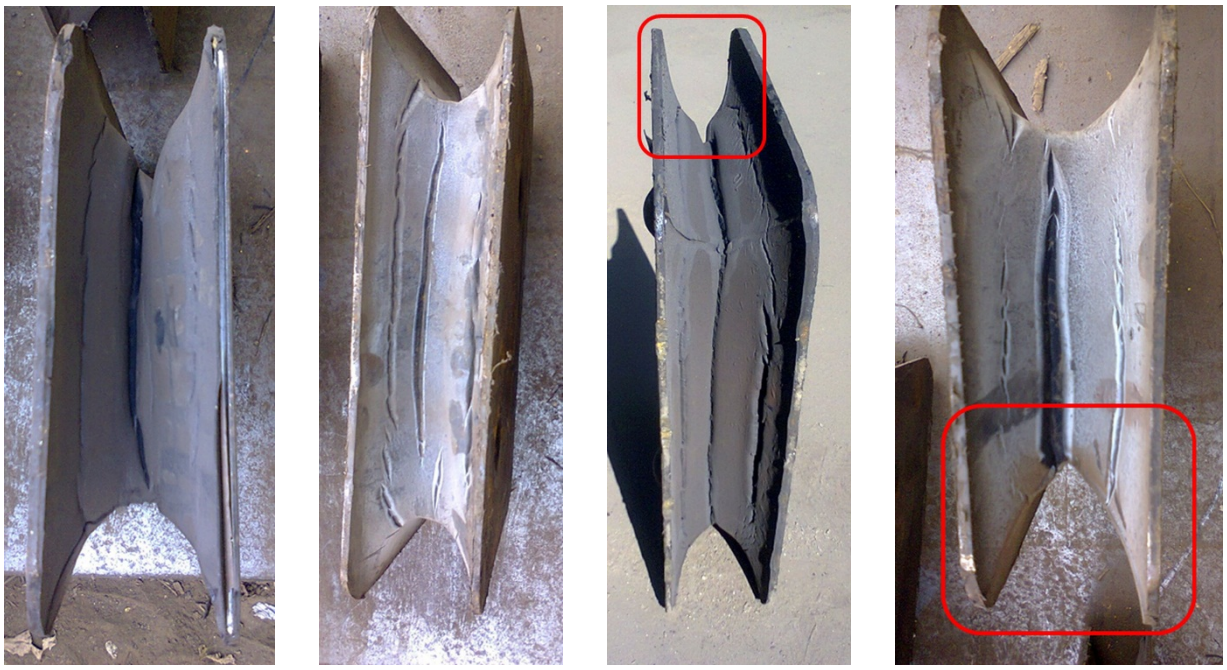

Figure 6. The crack location on the draft pad in (a) the lateral orientation, (b) the longitudinal orientation, (c), and (d) permanent set of rubber compound in the longitudinal direction.

spanning to cover the entire length of the rubber compound in either direction, as seen in Figs. (6a) and (6b). It was also observed that the crack's shape could not be defined by uniform geometry, but its width was spread along the entire length in either the lateral or longitudinal direction of the pad. However, for the simulation, realistic results were achieved by approximating the shape of the crack as semi-elliptical. This semi-elliptical shape, when defined with an aspect ratio, helped in analysing the dynamics of the draft pad. Furthermore, Figs. (6c) and (6d) describe a permanent set in the rubber compound/draft pad due to the impacting load on the draft gear. This permanent set was observed only on one side of the draft pad, especially the one with a greater length (longitudinal orientation), rather than on the diagonal corners. The effect of such deformation (set), along with fatigue loading, was to promote failure of the rubber compound along the longitudinal direction. Hence, cracks were assumed to be located along the lateral and longitudinal directions rather than at the diagonal corners for current analysis.

The effect of the crack on natural / modal frequency is determined for two different locations on the minimum cross-section of the draft pad, which lies at the geometric centre. Since it is the area and not the volume that affects the natural frequency, the crack's thickness was not treated with importance. Figure 7 illustrates a semi-elliptical crack as part of an ellipse defined by major axis x and minor axis y. The major axis represents the width of the crack, whereas the semi-minor axis represents the depth of the crack. The aspect ratio for an ellipse is defined as the ratio of its major axis to the minor axis.

Since the crack is semi-elliptical, its aspect ratio was defined by the ratio of the semi-major and the semi-minor axis. Mathematically, the aspect ratio was considered as x/y and was the same as in the case of the crack's lateral and longitudinal orientation. Figures 6a and 6b show the crack spreading along 70–85% of the entire lateral and longitudinal length at the concerned cross-section. Hence, for the cracks located in these two directions, the width's (x) maximum size was assumed to be 65 mm. This maximum crack size was in proportion to the maximum spread. A lower limit of 40 mm was considered and the crack size was varied in step of 5 mm. The size (y) of the crack was also varied to achieve aspect the ratios of 0.4, 0.5, 0.6, 0.7, and 0.8. Table 4 below summarizes the crack sizes for different crack widths and aspect ratios.

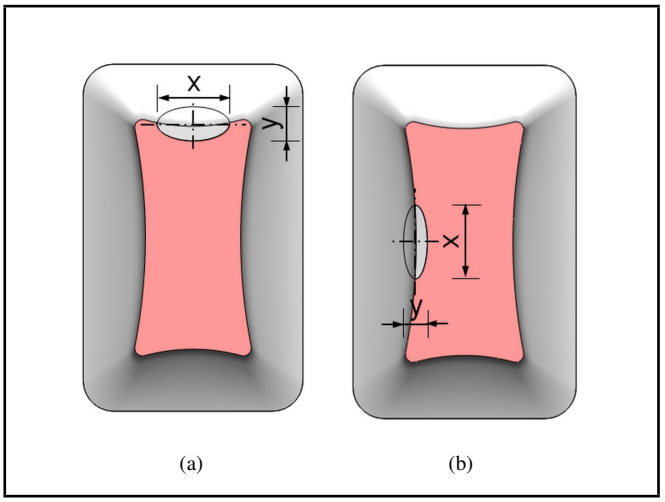

Figure 7. The semi-elliptical crack in the (a) lateral direction and (b) the longitudinal direction.

4. RESULTS AND DISCUSSION

4.1. Effect of Crack Aspect Ratio on Modal Frequency

Figures 8 to 12 show the frequency drop for different aspect ratios of a semi-elliptical crack. This variation is plotted as a

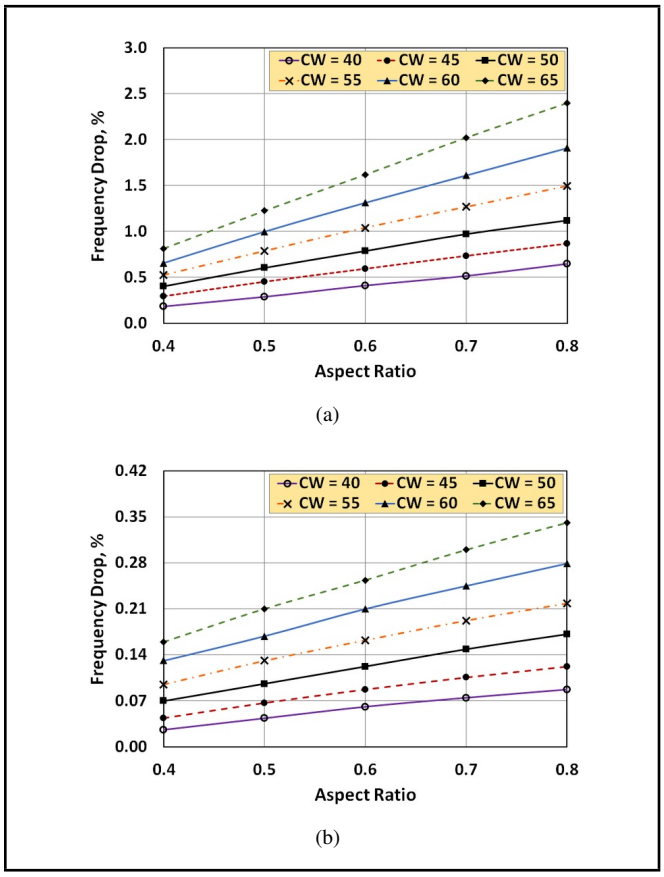

Figure 8. The effect of the aspect ratio on the first modal frequency for (a) the lateral crack and (b) the longitudinal crack.

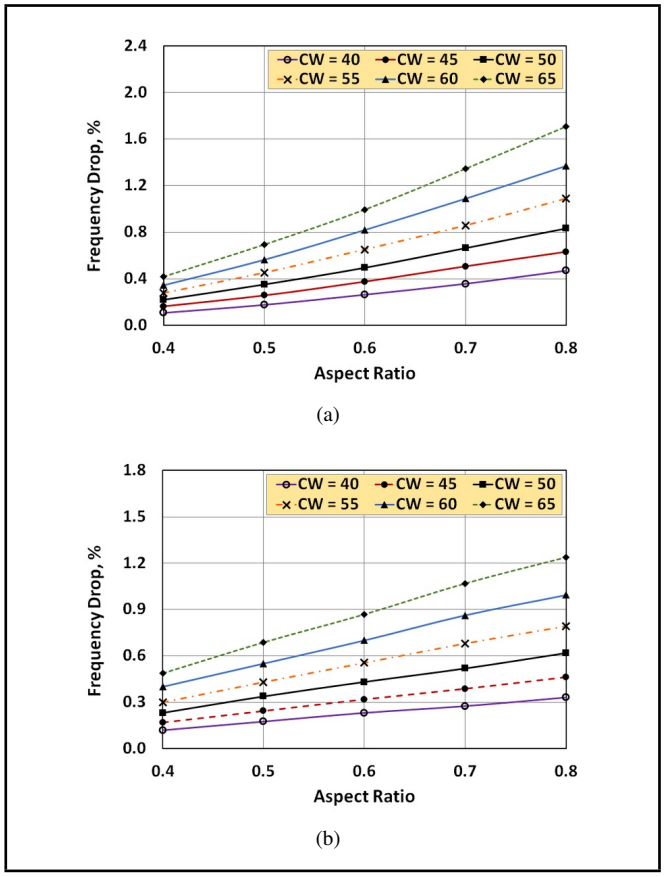

Figure 10. The effect of the aspect ratio on the third modal frequency for (a) the lateral crack and (b) the longitudinal crack.

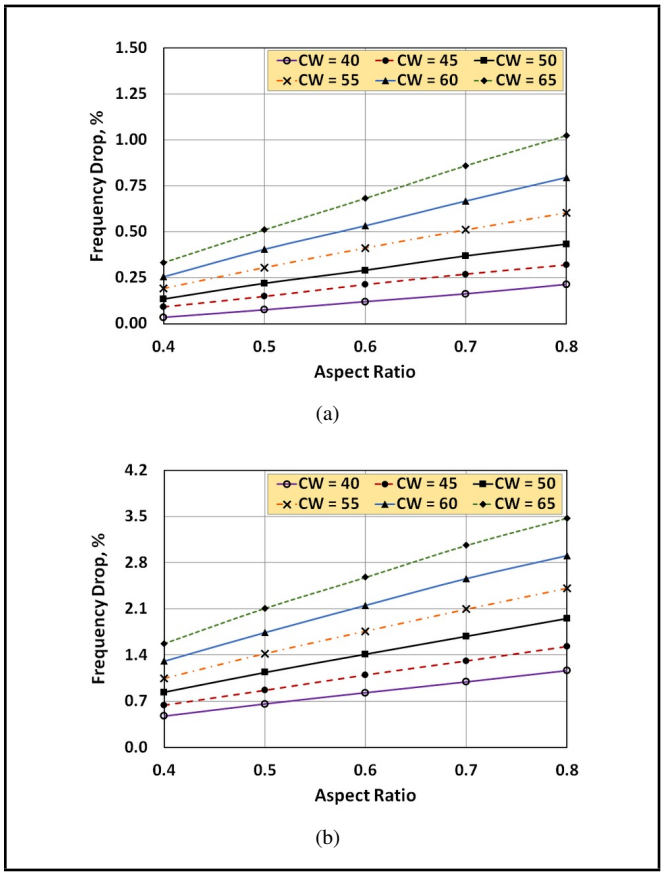

Figure 9. The effect of the aspect ratio on the second modal frequency for (a) the lateral crack and (b) the longitudinal crack.

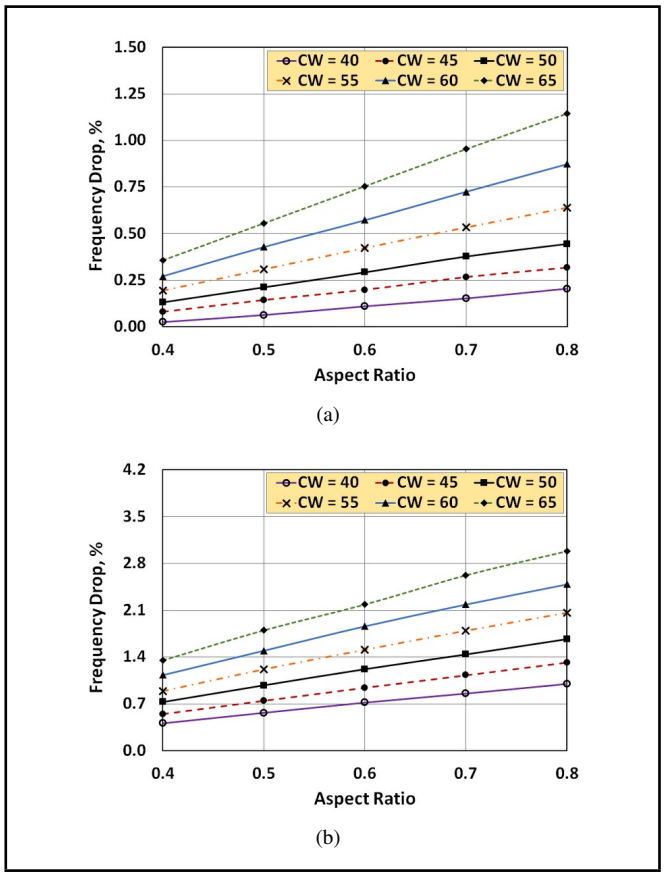

Figure 11. The effect of the aspect ratio on the fourth modal frequency for (a) the lateral crack and (b) the longitudinal crack.

Table 4. Depth of the crack for different crack widths and aspect ratios.

Crack width, mm	Aspect ratio				
(major axis 'x')	0.4	0.5	0.6	0.7	0.8
40	8.00	10.00	12.0	14.00	16.0
45	9.00	11.25	13.5	15.75	18.0
50	10.0	12.50	15.0	17.50	20.0
55	11.0	13.75	16.5	19.25	22.0
60	12.0	15.00	18.0	21.00	24.0
65	13.0	16.25	19.5	22.75	27.0

function of the crack width for various modes. The plots reveal that each mode responds differently to the presence of the crack with variation in the aspect ratio. As mentioned in earlier section, the top plate and rubber compound in the first mode shape exhibit an oscillatory motion about the x-axis. This motion is controlled by a component of stiffness in the z direction. From Figs. 8a and 8b, it is evident that as the aspect ratio of the crack increases, the frequency drops. This drop in frequency is almost linear in case of the lateral as well as the longitudinal crack, and the linearity is observed for all the crack widths. It is further observed that the given mode responds differently to the crack's location. For the lateral crack, the drop is significant (maximum 2.40%), whereas in the longitudinal crack, it is negligible (maximum 0.34%), which indicates a sensitivity of the first mode shape to the presence of the lateral crack.

Similarly for the second mode, where the top plate and rubber compound tend to oscillate about y-axis of the base plate of draft pad, the frequency drop is linear, as seen in Figs. 9a and 9b. The maximum magnitude of the drop is barely 1% in the case of the lateral crack, whereas for the longitudinal crack for this drop has a significant value (maximum 3.4%). Thus, the crack's presence in the lateral direction has a minimal effect on the second modal frequency, even for crack widths as high as 65 mm, whereas their presence in the longitudinal orientation causes a drop in frequency of up to 3.5% for the maximum crack width. For the third mode shape, the top plate and rubber compound oscillate about the z-axis of the base plate. The frequency drop in the presence of a lateral and longitudinal crack is nearly the same and almost linear, as seen in Figs. 10a and 10b. Moreover, the frequency is not significantly affected. The fourth mode shape shows behaviour similar to that of the second mode. The only difference is that in the second mode, the top plate and rubber compound oscillate about the y-axis of the base plate, whereas for the fourth mode, the top plate and rubber compound oscillate about the y-axis of the top plate. The maximum decrease is 1.14% for the crack in the lateral direction, whereas the maximum decrease is 3.4% in the longitudinal direction, as seen in Figs. 11a and 11b.

Fifth mode shape describes the oscillatory motion of the top plate and rubber compound about z-axis of the top plate. This mode shape is most responsive to the presence of lateral crack as compared to all other mode shapes and least responsive to the presence of longitudinal crack as seen from Figs. 12a and 12b.

4.2. The Effect of Crack Width on Modal Frequency

Figures 13 to 17 show the frequency drop for different widths (x) of a semi-elliptical crack. This variation is plotted as a function of the aspect ratio for various modes. It is clear from the plots that for all mode shapes, the frequency drops with an increasing crack width. The increasing aspect ratio further enhances this frequency drop. A significant aspect re-

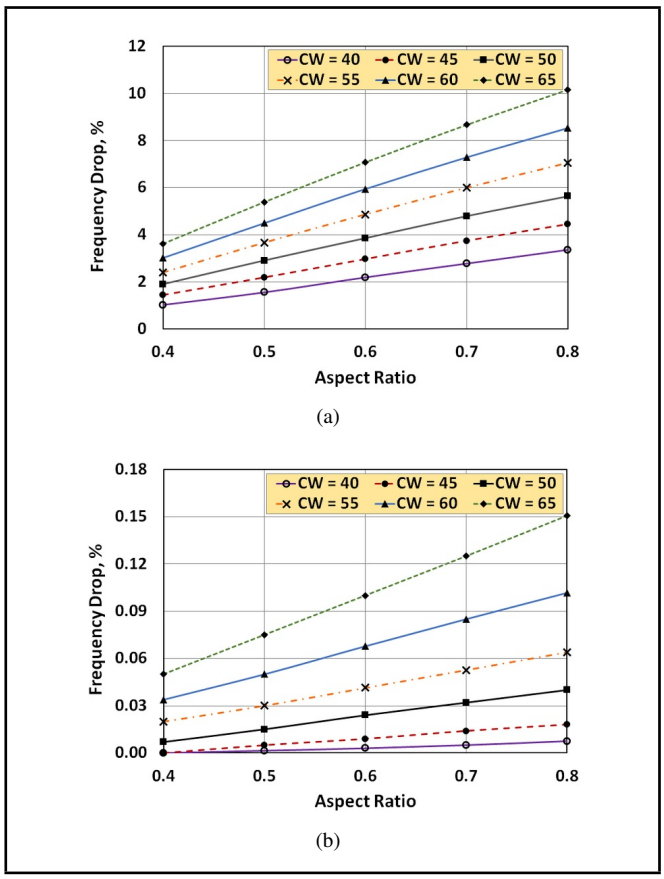

Figure 12. The effect of the aspect ratio on the fifth modal frequency for (a) the lateral crack and (b) the longitudinal crack.

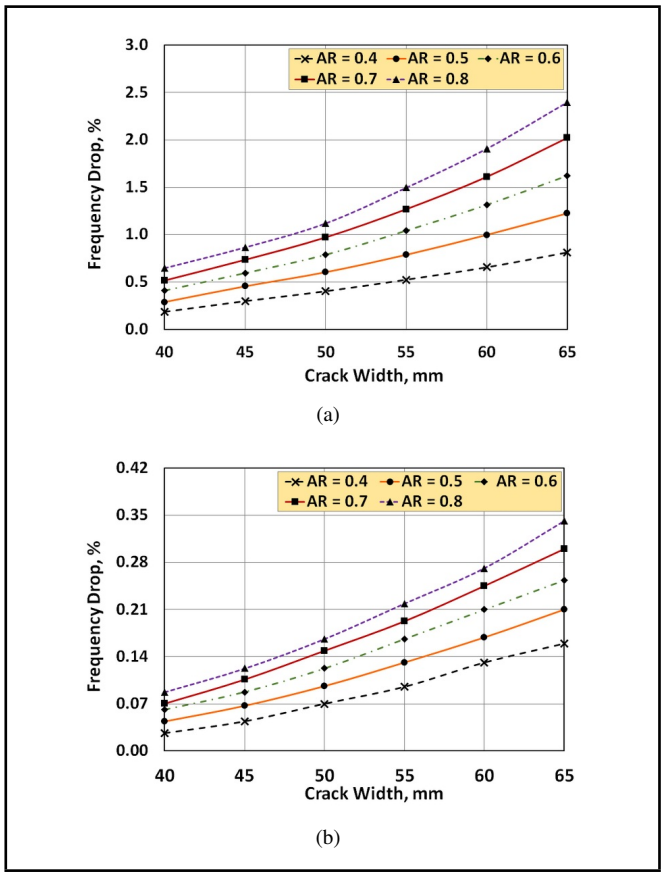

Figure 13. The effect of the crack width on the first modal frequency for (a) the lateral crack and (b) the longitudinal crack.

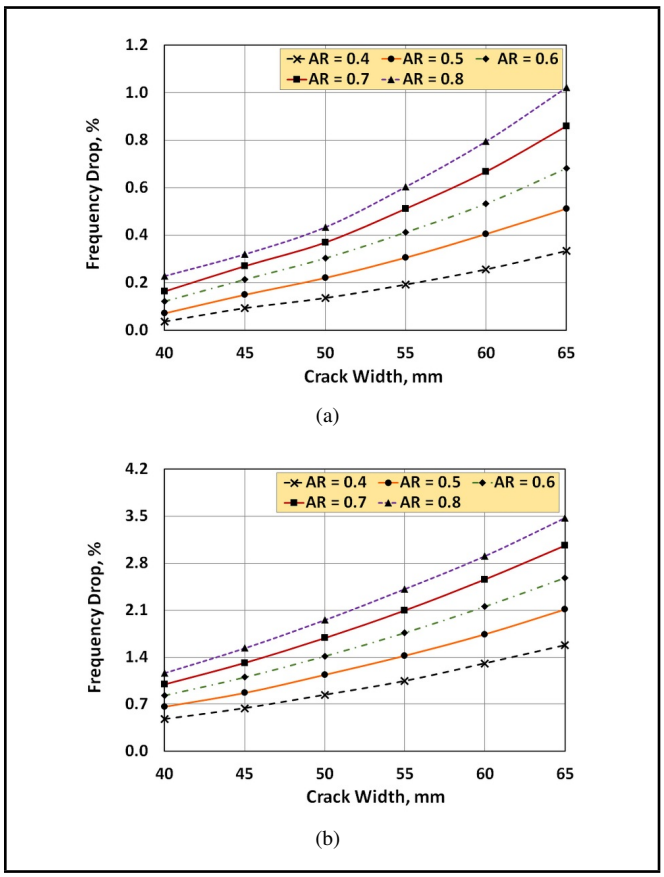

Figure 14. The effect of the crack width on the first modal frequency for (a) the lateral crack and (b) the longitudinal crack.

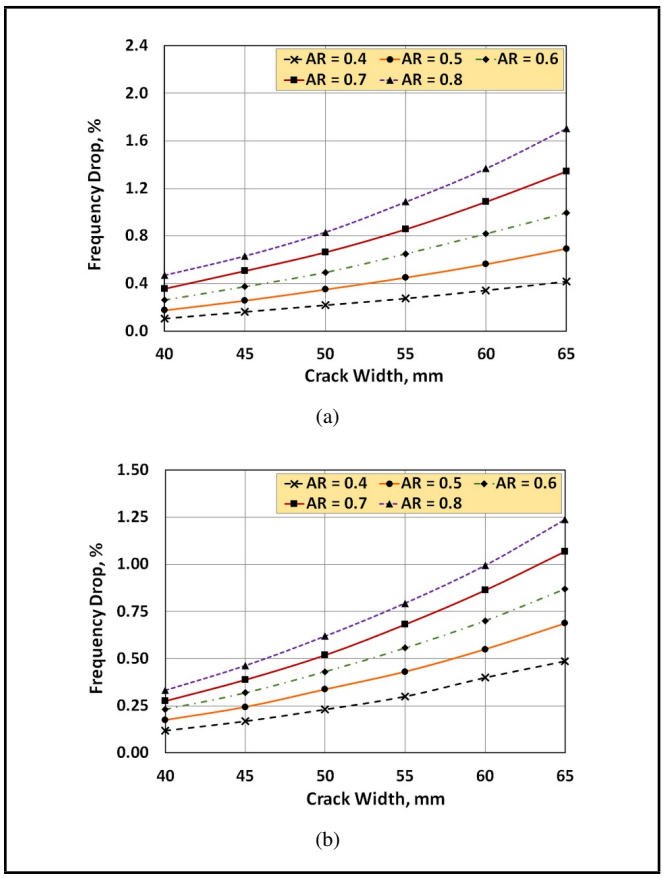

Figure 15. The effect of the crack width on the first modal frequency for (a) the lateral crack and (b) the longitudinal crack.

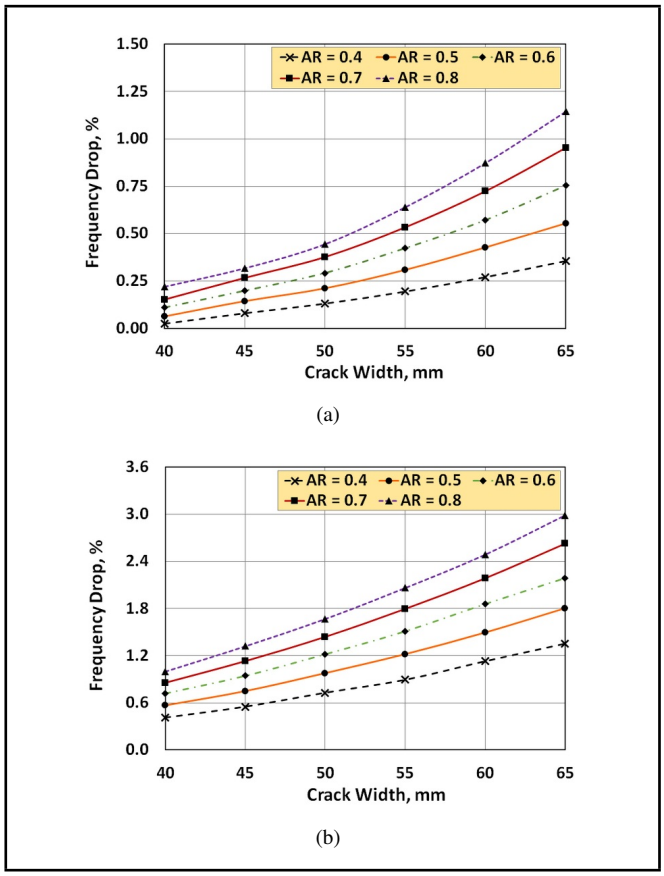

Figure 16. The effect of the crack width on the first modal frequency for (a) the lateral crack and (b) the longitudinal crack.

garding the frequency drop is that it is parabolic in nature.

Figures 13a and 13b show that the first mode shape is more sensitive to the lateral crack than to the longitudinal crack. Variation in the crack width in the lateral direction causes a significant frequency drop, as compared to the longitudinal direction. The second mode, as seen from Figs. 14a and 14b, is more sensitive to the longitudinal crack width variation as compared to the lateral crack's width variation. Figs. 15a and 15b show that the third mode shape responds equally to the lateral as well as the longitudinal crack variation. The fourth mode shape has a response similar to that of the second mode shape for the lateral and longitudinal cracks, as seen from Figs. 16a and 16b. The fifth mode shape is greatly affected by the lateral cracks than the longitudinal cracks. This mode responds very poorly to the longitudinal cracks, as seen in Figs. 17a and 17b.

5. CONCLUSIONS

In this work, a modal analysis of draft gear comprising of six compressed draft pads is done with healthy and defective draft pads so that the effect of a defect (i.e. a crack), on the natural frequency of the draft pad can be studied. The mode shapes and frequencies for an individual draft pad and a draft gear are obtained using the finite element approach. Critical observations reveal that crack parameters, such as crack width, crack aspect ratio, and crack location/orientation, influence the dynamic behaviour of the draft pad. The following observations are noteworthy because they reveal the dynamics of the draft pad:

- If the aspect ratio is varied while maintaining the crack

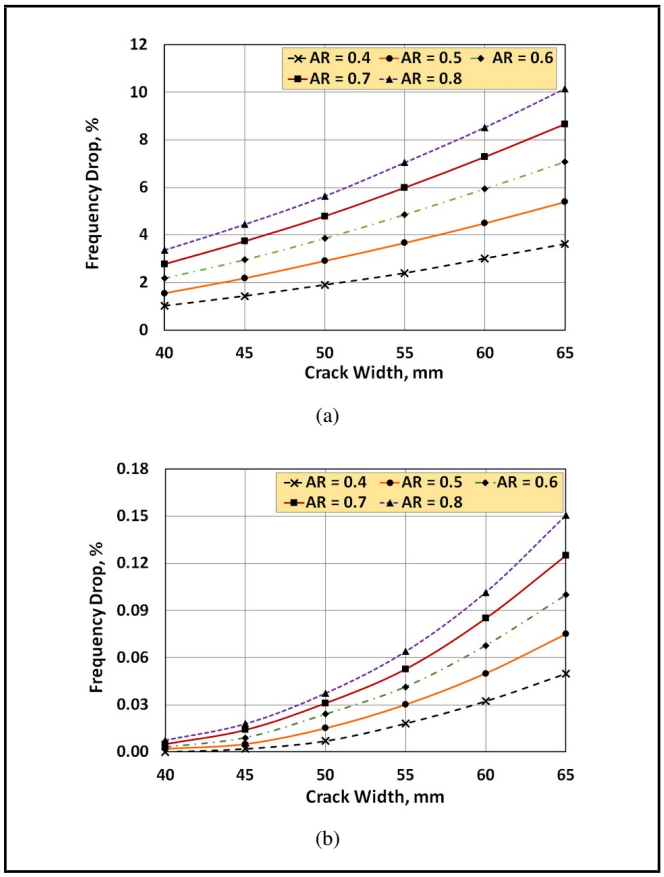

Figure 17. The effect of the crack width on the first modal frequency for (a) the lateral crack and (b) the longitudinal crack.

width constant, then the frequency drop is linear. This linear behaviour can be attributed to the variation of the aspect ratio. Since the crack width is constantly maintained, and the aspect ratio is varied, the reduction in the area becomes a function of depth only.

- If the crack width is varied while constantly maintaining the aspect ratio, then the frequency drop is parabolic. This second order variation can be attributed to the constant value of the aspect ratio, which makes it necessary to change the width while changing the depth.

- It is observed that if the crack lies in the zone of minimum modal displacement, then the frequency drop is minimal. Additionally, if the crack lies in the zone of maximum modal displacement, then the frequency drop is significant.

- It is also observed that frequency reduction is the function of stiffness rather than mass because the presence of the crack affects the area more than the volume. Hence, the presence of the crack is noted through changes in stiffness rather than in mass.

The above observations can be confirmed from Eqs. (4), (5), (6), and (10). Thus, the finite element approach can be used as a reliable tool for predicting dynamic responses of draft pads. This prediction can help to determine the extent to which the frequency values in Table 3, which can vary. If the loading frequency to which the draft gear is subjected due to acceleration and braking of the locomotive are equivalent to the values in Table 3 then failure of draft pads would occur. It is necessary to test the draft pads at these values to determine the fatigue response. Hence, a range of frequency values are identified against which a draft pad must be tested for fatigue response against the cyclic loading of 10 Hz.[12] This study provides a tool for monitoring exciting frequencies of draft gear and shows how each modal frequency is affected by the crack due to parameters like aspect ratio, crack width, and crack location/orientation.

REFERENCES

[1] Garg, V. K. and Dukkipati, R. V. *Dynamics of railway vehicle systems,* Academic Press, Canada, (1984). http://dx.doi.org/10.1016/B978-0-12-275950-5.50014-6

[2] Duncan, I. B. and Webb, P. A. The longitudinal behaviour of heavy haul trains using remote locomotives, *Fourth Int. Heavy Haul Conf.*, Brisbane, 579–583, 1989.

[3] Chen, O. Dynamic simulation of Taipei EMU train, *Veh. Syst. Dyn.: Int. J. Veh, Mech. Mob.*, **30** (2), 143–167, (1998). http://dx.doi.org/10.1080/00423119808969441

[4] McClanachan, M., Cole, C., Roach, D. and Scown B. An investigation of the effect of bogie and wagon pitch associated with longitudinal train dynamics, *Veh. Syst. Dyn.: Int. J. Veh, Mech. Mob.*, **33** (Supplement), 374–385, (1999).

[5] Cole, C. and Sun, Y. Q. Simulated comparisons of wagon coupler systems in heavy haul trains, *Proc. Inst. Mech. Eng. F J. Rail Rapid Transit*, **220** (3), 247–256, (2006). http://dx.doi.org/10.1243/09544097JRRT35

[6] Belforte, P., Cheli, F., Diana, G., and Melzi, S. Numerical and experimental approach for the evaluation of severe longitudinal dynamics of heavy freight trains, *Veh. Syst. Dyn.: Int. J. Veh, Mech. Mob.*, **46** (S1), 937–955, (2008). http://dx.doi.org/10.1080/00423110802037180

[7] Nasr, A. and Mohammadi, S. The effects of train delay time on in-train forces, *Proc. Inst. Mech. Eng. F J. Rail Rapid Transit*, **224** (3), 523–534, (2010). http://dx.doi.org/10.1243/09544097JRRT306

[8] Cole, C., McClanachan, M., Spiryagin, M., and Sun, Y. Q. Wagon instability in long trains, *Veh. Syst. Dyn.: Int. J. Veh, Mech. Mob.*, **50** (Supplement), 303–317, (2012). http://dx.doi.org/10.1080/00423114.2012.659742

[9] Qi, Z., Huang, Z., and Kong, X. Simulation of longitudinal dynamics of long freight trains in positioning operations, *Veh. Syst. Dyn.: Int. J. Veh, Mech. Mob.*, **50** (9), 1409–1433, (2012). http://dx.doi.org/10.1080/00423114.2012.661063

[10] Wu, Q., Luo, S., and Cole, C. Longitudinal dynamics and energy analysis for heavy haul trains, *J. Mod. Transport.*, **22** (3), 127–136, (2014). http://dx.doi.org/10.1007/s40534-014-0055-x

[11] Rao, S. S. *Mechanical Vibrations,* Pearson Education, New Delhi, India, (2009).

[12] Research Design & Standards Organisation, Ministry of Railways, Lucknow - 226011. Amendment No. 3 of September, 1993 to Indian Railways Schedule Of Technical Requirement No. 55-Bd-90 For Rubber Springs of High Capacity Draft Gear For Centre Buffer Couplers of Bg Bogie Wagons Having 625.5 mm Draft Gear Pocket, (1993).

Effects of Young's Modulus on Disc Brake Squeal using Finite Element Analysis

Ali Belhocine

Mechanical Engineering Dept., USTO Oran University, B.P 1505 El - Mnaouer, USTO 31000, Oran, Algeria

Nouby M. Ghazaly

Mechanical Engineering Dept., Faculty of Engineering, South Valley University, Qena-83523, Egypt

(Received 9 July 2014; accepted 24 June 2016)

This paper is concerned with the disc brake squeal problem of passenger cars. The objective of this study is to develop a finite element model of the disc brake assembly in order to improve the understanding of the influence of Young's modulus on squeal generation. A detailed finite element model of the whole disc brake assembly that integrates the wheel hub and steering knuckle is developed and validated by using experimental modal analysis. Stability analysis of the disc brake assembly is conducted to find unstable frequencies. A parametric study is carried out to look into the effect of changing Young's modulus of each brake's components on squeal generation. The simulation results indicate that Young's modulus of the disc brake components plays an important role in generating the squeal noise.

1. INTRODUCTION

Passenger cars have historically been one of the essential methods of ground transportation for people who want to move from one place to another. The braking system acts as one of the most fundamental safety-critical components in modern passenger cars. Therefore, the braking system of a vehicle is a significant system, especially when the vehicles are slowing down or stopping. Due to the braking operation, the brake system generates an unwanted high frequency sound called squeal noise. It occurs in the frequency range between 1 and 16 kHz and leads to customer dissatisfaction and increases warranty costs. Although substantial research has been conducted into predicting and eliminating brake squeal since the 1930s, it is still rather difficult to predict its occurrence.[1] As described in some of the recent review papers,[2–5] theories on brake squeal mechanisms have been put forward on six major classes: stick-slip, sprag-slip, negative friction velocity slope, hammering excitation, splitting the doublet modes, and mode coupling of structures. These mechanisms are essential for better understanding of squeal noise.

In recent years, the finite element (FE) method has become the preferred method to study brake squeals. The capabilities of FE models, with a huge number of freedom, have enabled an accurate representation of the brake system. The analysis of disc brake squeal using the FE model could reflect each detail of the brake design, while this demanded a lot of effort to do significant changes in the geometry of components.[6] Due to a general lack of confidence in FE models, the dynamic testing of structures had become a standard procedure for model validation and updating. Over the past years, modal testing and analysis had become a fast- developing technique for the experimental evaluation of the dynamic properties of structures.[7] Several types of analyses had been performed on disc brake systems through FEA, in an attempt to understand the noise and to develop a predictive design tool. There were two numerical methods that are used to study this problem: transient dynamic analysis[8,9] and complex eigenvalue analysis.[10–13] Currently, the complex eigenvalue method is the most commonly preferred method. Generally, the existence of complex eigenvalues with positive real parts indicated the presence of instability and the magnitude of the real part is used to represent the level of system instability or squeal propensity.

Reduction and elimination of the brake squeal was an important task for the improvement of the vehicle passengers' comfort. Many researchers, in their studies on brake systems tried to reduce squeal noise by changing the factors associated with the brake squeal. For example, Liles[14] found that shorter pads, damping, a softer disc, and a stiffer back plate could reduce squeal, while in contrast, a higher friction coefficient and wear of the friction materials were prone to squeal. Lee et al.[15] reported that reducing back plate thickness led to less uniform contact pressure distributions and consequently increased the squeal propensity. Kung et al.[10], in their simulations, showed that instability of the disc brake was dependent upon a range of disc Young's modulus. Liu et al.[12] commented that the squeal could be reduced by decreasing the friction coefficient, increasing the stiffness of the disc, using damping material on the back of the pads, and modifying the shape of the brake pads. Recently, Nouby et al.[16] introduced a combined approach of complex eigenvalue analysis (CEA) and designed experiments to get optimal design for the brake system. They reported that the brake squeal propensity could be reduced by increasing Young's modulus of the back plate and by modifying the shape of the friction material by adding chamfer and slots.

In FEA, several researchers varied the geometric details of the brake assembly model. For instance, some researchers[12,17] considered only the disc brake and two pads. Zhu et al.[18] added the finger and piston to the FE model. Dai and Teik[19] developed a FE model that consisted of a rotor, a caliper, a mounting bracket, a piston, and brake pads to analyze the design of the disc brake pad structure for squeal noise reduction. Some authors[20–22] used a more detailed FE model, which consisted of a disc, a piston, a caliper, a carrier, piston and finger pads, two bolts and two guide pins.

An extension of the FE models discussed earlier in this work

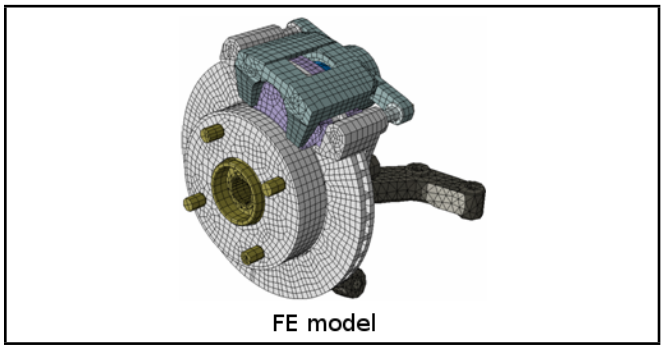

Figure 1. A commercial disc brake corner.

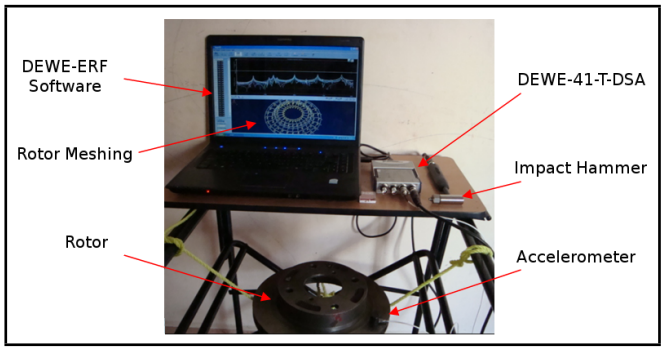

Figure 2. Experimental Modal Analysis set-up.

on a three-dimensional model of a validated FE model of the disc brake assembly that incorporated the wheel hub and steering knuckle was considered. Experimental modal analysis of a disc brake system was first used to develop and validate the FE model to improve accuracy of simulation results. Then, stability of the disc brake assembly with frequencies ranging from 1 kHz to 10 kHz was examined by using FE software ABAQUS. A preliminary FE simulation was carried out to predict unstable frequencies by applying complex eigenvalue analysis to the FE model. Finally, the parametric study as a guide was conducted to evaluate the influence of the Young's modulus on the disc brake components.

2. FINITE ELEMENT MODEL

A detailed three dimensional FE model of a vented disc brake assembly that had been used in this work is shown in Fig. 1. All disc brake system components, except a rubber seal (attached to the piston), two rubber washers (attached to the guide pins), and the pad insulator, have been included in the model. The FE model consisted of a disc, a piston, a caliper, an anchor bracket, a wheel hub, a steering knuckle, piston and finger pads, two bolts, and two guide pins. All the disc brake components were modeled in order to achieve as accurate a representation of a real disc brake as possible.

The FE model uses up to 19,000 solid elements and approximately 78,000 Degrees of Freedom (DOFs). The disc, brake pads, piston, wheel hub, guide pins, and bolts were developed by using 8-node (C3D8) linear solid elements, while other components were developed by using a combination of 8-node (C3D8), 6-node (C3D6) and 4-node (C3D4), linear solid elements. Details for each of the components are given in Table 1.

In the brake assembly FE model, all the disc brake components were integrated together to form an assembly model and all the boundary conditions and component interfaces were considered. Contact interaction between disc brake components was represented by a combination of node-to- surface and surface-to-surface contact elements. The surface of the disc was defined as the master surface, since it had a coarser mesh than the pad and the disc was made of a stiffer material. The pad was therefore treated as the slave surface. This enables the slave surface to potentially contact the entire master surface.

3. VALIDATION OF THE FE MODEL

The purpose of this section was to ensure that accuracy of the dynamical properties of the FE model agreed with those

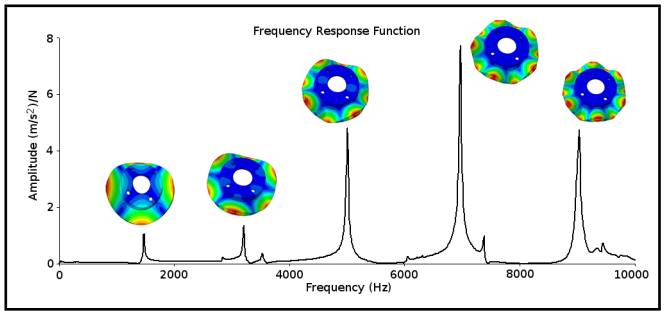

Figure 3. FRF measured for the brake rotor.

of the physical component. Two validation stages were established (i.e., modal analysis at component and assembly levels). Frequency Response Functions (FRF) measurements using impact hammer and accelerometer were recorded by DEWE/FRF software. Fig. 2 shows the experimental modal analysis set-up.

First, modal analysis at the component level was carried up to frequencies of 10 kHz. The FRF result for brake rotor was performed at free-free boundary conditions, as shown in Fig. 3. An accurate representation of the component model formed one of the validation stages for good squeal correspondence between experiments and predictions. In order to correct the predicted frequencies with the experimental results, an FE updating was used to reduce the relative errors between the two sets of results by tuning material. The baseline material properties of the disc brake components after FE updating are listed in Table 2. It was found that the predicted natural frequencies for brake rotor was quite close to those obtained in the measured data, as listed in Table 3. Similarly, validation of the other brake components was performed. A good agreement between the predicted results and the measured data for the brake components was also found, as listed in Appendix A.

The second validation stage was to perform dynamic characteristics of the complete assembly with boundary conditions. In experimental modal analysis, the individual components were fixed on a brake test rig under applied pressure of 1 MPa. Fig. 4 shows the results of the FRF measured for the disc brake assembly. A similar condition was also applied to the FE brake assembly model. In this validation, measurements were taken on the disc, as it had a regular shape than the other components. The analysis results show that a good agreement was found between the predicted results and the measured data, as shown in Table 4.

Table 1. Element details of the disc brake components.

Disc brake Components		Types of Element	No. of Elements	No. of Nodes
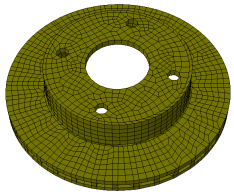	Disc	C3D8	2559	4988
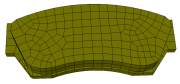	Friction Material Back plate	C3D8 C3D8	320 233	558 526
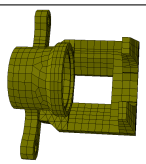	Caliper	C3D8 C3D6 C3D4	2334	2370
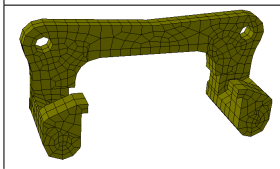	Anchor Bracket	C3D8 C3D4	1036	1644
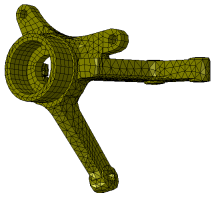	Steering Knuckle	C3D8 C3D6 C3D4	9868	3585
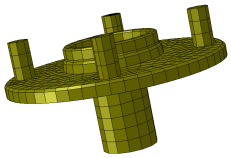	Wheel Hub	C3D8	1654	2786
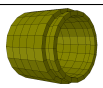	Piston	C3D8	357	576
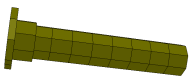	Guide pin	C3D8	292	414
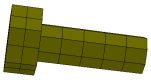	Bolt	C3D8	58	123

Table 2. Material properties of the disc brake component.

Components	Density (kg m^{-3})	Young's Modulus (GPa)	Poisson's ratio
Disc	7155	125	0.23
Friction material	2045	2.6	0.34
Back plate	7850	210	0.30
Caliper	7005	171	0.27
Anchor Bracket	7050	166	0.27
Steering Knuckle	7625	167	0.29
Wheel Hub	7390	168	0.29
Piston	8018	193	0.27
Guide pin	2850	71	0.30
Bolt	7860	210	0.30

Table 3. Comparisons between the predicted results and measured data for the brake rotor.

Mode	1	2	3	4	5
Exp. (Hz)	1464	3198	4992	6957	9020
FEA (Hz)	1453	3225	5062	7067	9170
Error (%)	-0.7	0.8	1.4	1.5	1.6

Table 4. Comparisons between the predicted results and measured data for brake assembly.

Mode	1	2	3	4	5
Exp. (Hz)	1611	3222	5065	7043	9130
FEA (Hz)	1562	3174	5184	6597	9452
Error (%)	-3	-1.4	2.3	-6.3	3.5

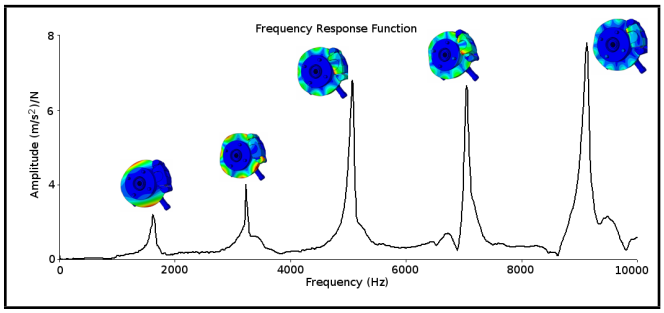

Figure 4. FRF measured for the disc brake assembly.

4. CONTACT ANALYSIS

In recent years, the complex eigenvalue analysis has become the preferred method to investigate the stability of brake system modes. Complex eigenvalues usually result from the frictional coupling of brake components due to the off-diagonal terms that arise in the stiffness matrix of the system, causing it to be unsymmetrical. The positive real parts of the complex eigenvalues indicated the degree of instability of the disc brake assembly and reflected the likelihood of squeal occurrence. Complex eigenvalues with positive real parts were identified as unstable modes and corresponding frequencies, which always appeared in complex conjugate pairs. The complex eigenvalue analysis in ABAQUS was used to determine instability in disc brake assembly.[14] In order to perform the complex eigenvalue analysis using ABAQUS, four main steps were required. They are as follows:

- Nonlinear static analysis for applying brake-line pressure.
- Nonlinear static analysis to impose rotational speed on the disc.
- Normal mode analysis to extract natural frequency of undamped system.
- Complex eigenvalue analysis that incorporated the effect of friction coupling.

The complex eigenvalue analysis was examined between 1 kHz and 10 kHz by using the ABAQUS version 6.8 with brake-line pressure of 0.7 MPa, a rotational speed of 5 rad/s to assess the brake propensity as the friction coefficient values. The influence of friction coefficient of the pad-rotor interface was performed. The unstable modes for varying μ from 0.1 to 0.5 were plotted as real parts versus frequency in Fig. 5 to illustrate how the instability increases with friction level. It was found that the propensity for squeal increases with higher coefficients of friction. This was because the higher coefficient of friction causes the variable frictional forces to be higher resulting in the tendency to excite greater number of unstable modes.

In this study, the baseline model for investigating the effects of elastic modulus of the main disc brake components on squeal generation was considered at $= 0.5$. It was found that at $= 0.5$, there were five unstable frequencies predicted at 2777 Hz, 7573 Hz, 8530 Hz, 9453 Hz, and 9722 Hz, as shown in Fig. 6.

5. PARAMETRIC STUDIES

The aim of this section is to propose parametric studies in order to examine the effects of material properties of the disc brake components on disc brake squeal generation. Fieldhouse and Steel[23] suggested that the source of a noisy brake may lie as much in basic mechanical design as inappropriate material choice. When the components were in an assembly, there may have been a significant redistribution of stiffness and mass throughout the structure if a component's material property was changed. This in turn will change the natural frequencies of the assembly as a whole as well as potentially varying the strain energy distribution during vibration. As a consequence, it was necessary to design the entire brake components so that their natural frequencies in the audible range were as isolated as possible to avoid mode coupling. In this study, the effect of elastic modulus for disc brake components was examined using parametric studies in order to reduce squeal generation. Theoretically, this was thought to have been achieved when either the positive real parts of eigenvalues of the baseline model were reduced or the predicted unstable frequencies in the baseline model totally disappeared. Details of the parametric study of Young's modulus of the disc brake components are discussed below.

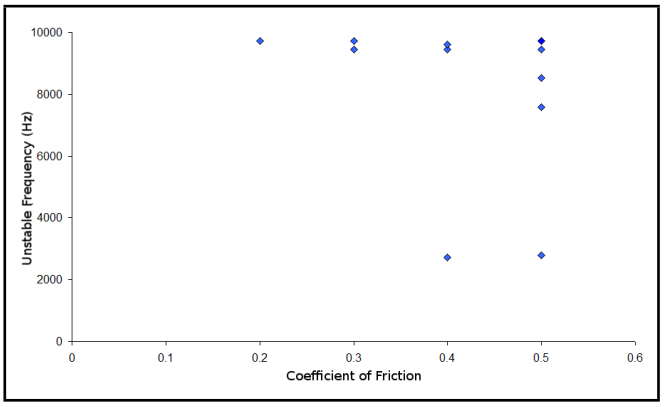

Figure 5. Predicted unstable frequencies for varying coefficient of friction values.

5.1. Influence of Rotor Young's Modulus

Disc brake rotors in wide use today are made of gray cast irons, because they have acceptable thermal properties, sufficient mechanical strength, satisfactory wear resistance, and good damping properties, they are cheap and relatively easy to cast. Gray cast irons differ somewhat to steels and most other structural metals in that the Young's modulus could be varied significantly by changing carbon equivalent. This allowed the rotors to be manufactured with Young's modulus that runs from below 100 GPa through to approximately 140 GPa.

In this section, variation of Young's modulus of the brake rotor from 100 GPa to 140 GPa was simulated. Where the baseline Young's modulus of the disc is 125 GPa. The density and Poisson's ratio of these variants was assumed to be as the same as the baseline model. Fig. 7 presents the real parts versus frequency for different Young's modulus of the rotor. From the simulation results, it was found that increasing Young's modulus of the rotor to 140 GPa was capable of eliminating positive real parts for unstable frequencies of 2777 Hz, 8530 Hz, and 9722 Hz. On the other hand, by reducing Young's modulus of the rotor to 100 GPa, a new unstable frequency had appeared at approximately 5100 Hz. Additionally, the number of unstable frequencies was unchanged, but their magnitudes were increased, especially at frequencies of 2777 Hz, 7573 Hz, 9453 Hz, and 9722 Hz. In theory, the higher positive real parts,

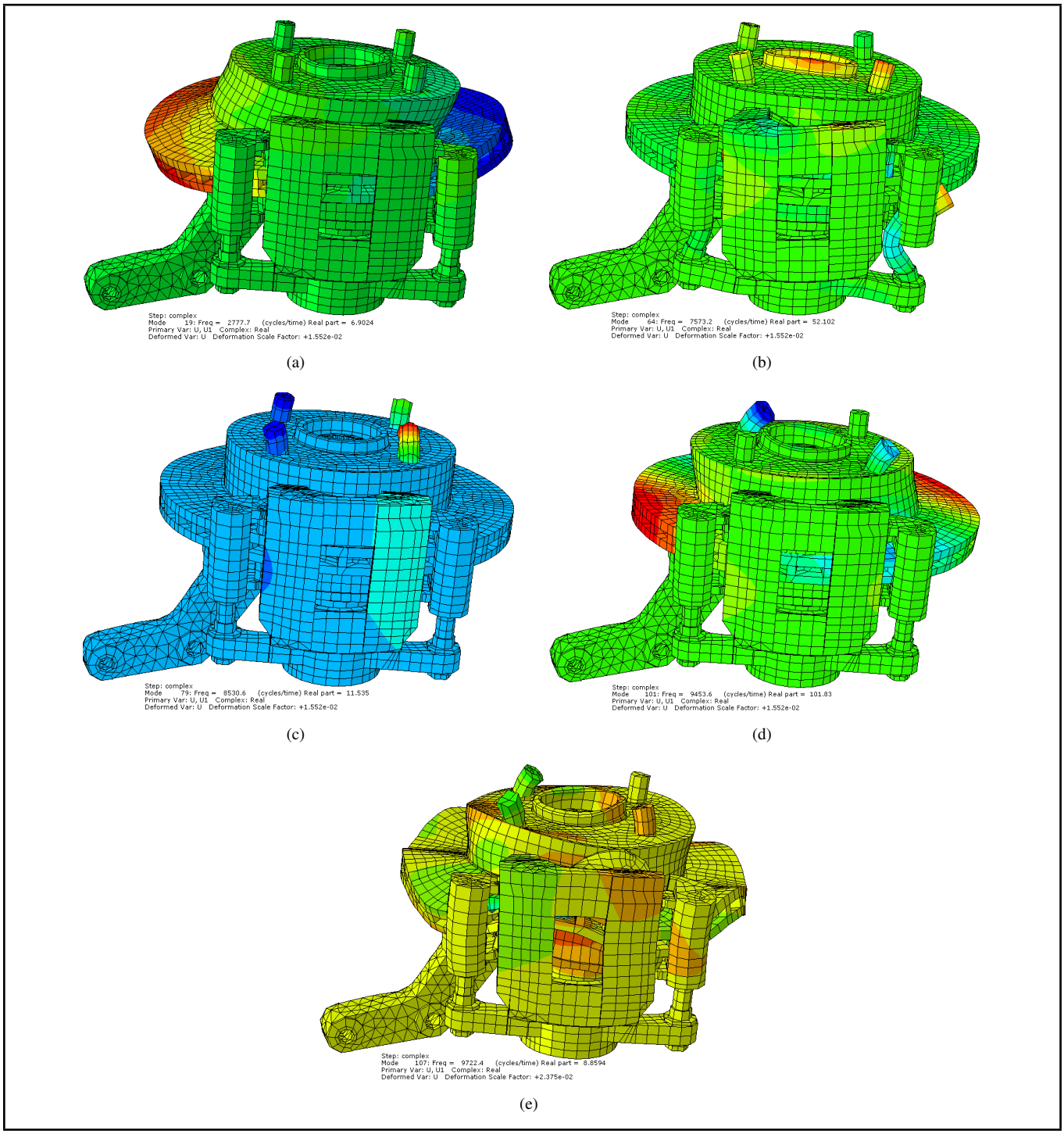

Figure 6. Predicted unstable frequencies of the disc brake corner for the baseline model at = 0.5: (a) 2777 Hz (b) 7573 Hz (c) 8530 Hz (d) 9453 Hz and (e) 9722 Hz.

the more tendency the squeal to occur. Overall, it was observed that the rotor Young's modulus had a significant effect on the stability of the system. Increasing Young's modulus of the disc may be reducing the brake squeal generation. Similar evaluations have been carried out by Liu et al.[12] Also, Dunlap[24] reported that increased rotor stiffness was directionally correct for reduction in squeal propensity.

5.2. Influence of Friction Material Young's Modulus

It was necessary to investigate the effect of the friction material stiffness on the squeal propensity for the design of a quiet brake system, since changes in the pad stiffness could alter the mode coupling between the pads and rotor. In this section, variation of Young's modulus of the friction material from 0.5 GPa to 4 GPa was simulated. These values of Young's modulus were in the range readily attained within brake pads available in the market.[25] Where the baseline Young's modulus of the disc is 2.6 GPa. The other properties, such as Poisson's ratio and density of these variants, were assumed to be the same as the baseline model. Similarly, Young's modulus of other components was also unchanged. Having simulated the variation of Young's modulus of the friction material, it can be seen from Fig. 8 that increasing Young's modulus of the friction material to 4 GPa was capable of eliminating positive

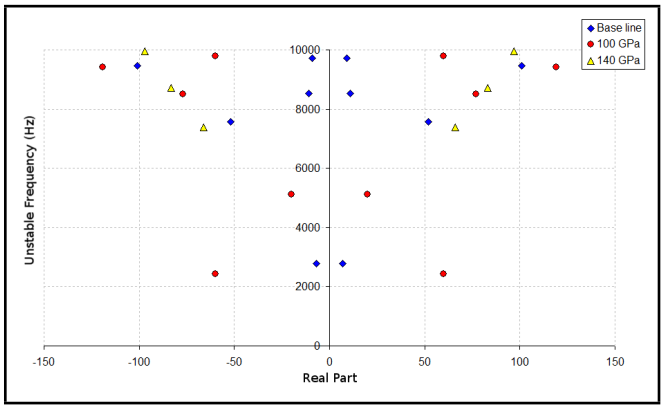

Figure 7. The Effect of Young's modulus of the rotor on the brake squeal generation.

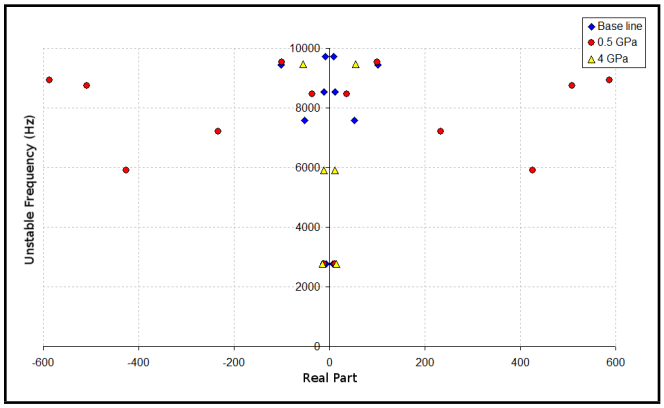

Figure 8. The effect of Young's modulus on the friction material on the brake squeal generation.

real parts for unstable frequencies of 7573 Hz, 8530 Hz, and 9722 Hz, and of reducing the positive real part for unstable frequency of 9453 Hz. On the other hand, reducing Young's modulus of the friction material to 0.5 GPa by increasing the overall number of unstable frequencies and the real parts especially at high frequency squeal.

From the predicted results, it can be concluded that stiffer friction material causes the system to be more stable and reduces squeal generation. This finding seems to agree with that from Liles.[14] Also, Papinniemi[21] reported that increasing pad Young's modulus reduced the overall number of unstable modes and indicated that the overall system stability would be enhanced with higher modulus pads. The most probable physical explanation for this would be a reduction in pad deformation.

5.3. Influence of Anchor Bracket Young's Modulus

The anchor bracket was made from ductile cast iron component that was used for housing the caliper and pads in brake assembly. This anchor bracket was attached to the steering knuckle. The baseline Young's modulus of the bracket was 166 GPa. In this section, the baseline Young's modulus of the bracket was varied approximately up to $\pm 10\%$. The other properties, such as Poisson's ratio and density, were kept constant throughout the parametric study. Similarly, Young's modulus of the other components was also unchanged. From the complex eigenvalue analysis, it was seen that the anchor bracket had a significant affect on the stability of the system.

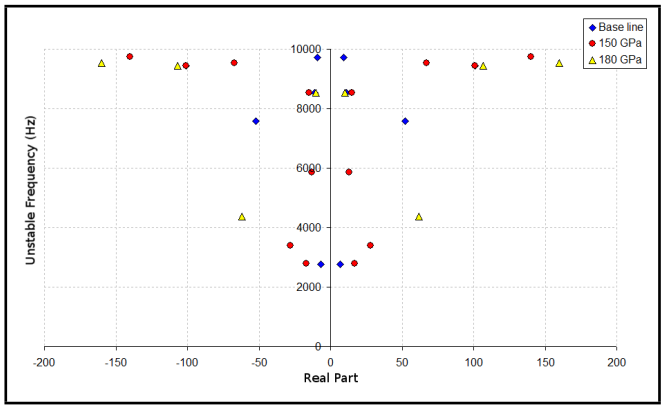

Figure 9. The effect of Young's modulus of the bracket on the brake squeal generation.

As seen in Fig. 9, increasing the modulus to 180 GPa reduced the number of unstable modes to just three. On the other hand, reducing the Young's modulus to 150 GPa had less of an impact with unstable frequencies still present at 2777 Hz, 8530 Hz, 9453 Hz, and 9722 Hz. In addition, a new unstable frequencies had appeared in frequencies of 3403 Hz, 5873 Hz, and 9530 Hz. Dessouki[26] concluded that the common countermeasure for caliper bracket induced squeal was to introduce mass loading to the caliper bracket or alternatively to stiffen the bracket. This finding seems to agree with the current simulation results, where was observed that increasing Young's modulus of the anchor bracket may be reducing the brake squeal generation.

5.4. Influence of Back Plate Young's Modulus

The disc brake pads consisted of two parts: friction plates, which were made of organic materials, and back plates made of steel. In this study, the baseline Young's modulus of the back plates of the pads was 210 GPa. Steel did not show much variation in modulus, but an alternative case was run with the back plates modulus set to 190 GPa and 200 GPa. In Fig. 10, it is seen that reducing Young's modulus of the back plate to 190 GPa makes it capable of eliminating positive real parts for unstable frequencies of 2777 Hz, 7573 Hz, and 8530 Hz. However, a new unstable mode appeared at approximately 4330 Hz, so the overall noise performance of the system could be significantly improved by reducing the number of unstable frequencies to just three. On the other hand, reducing Young's modulus of the back plate to 200 GPa had less of an impact with unstable frequencies still present at 2777 Hz, 7573 Hz, 9453 Hz, and 9722 Hz. However, the unstable frequency of 8530 Hz was eliminated. Compared to the baseline case, setting back plates modulus to 200 GPa reduced the number of unstable frequencies to just four.

From simulation results, it was observed that the stiffer back plates cause a higher squeal propensity. This was because the friction material connected to the back plates was very soft compared with the back plate material. Hence, the higher stiffness of the back plates, the greater the uneven deformation and vibration magnitude of the pad, and the higher the damping coefficient.

5.5. Influence of Caliper Young's Modulus

The base line Young's modulus of the caliper was 171 GPa. In this section, the baseline Young's modulus of the caliper

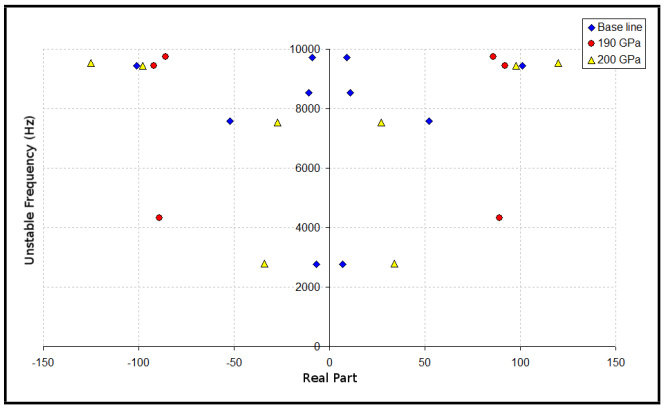

Figure 10. The effect of Young's modulus on the back plate of the brake squeal generation.

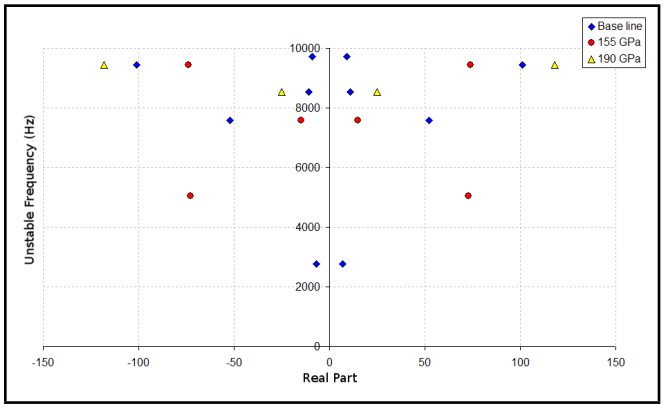

Figure 11. The effect of Young's modulus on the caliper of the brake squeal generation.

was varied approximately up to ±10%. The other properties, such as Poisson's ratio and density, were kept constant throughout the parametric study. Similarly, Young's modulus of other components was also unchanged. Having simulated the variation of Young's modulus of the caliper, it can be seen from Fig. 11 that the caliper also had a significant affect on the stability of the system. Reducing the modulus to 155 GPa reduced the number of unstable modes to just three. On the other hand, increasing Young's modulus of the caliper to 190 GPa was capable of suppressing positive real parts for unstable frequencies of 2777 Hz, 7573 Hz, and 9722 Hz. Compared to the baseline case, setting the caliper modulus to 190 GPa reduced the number of unstable frequencies to just two.

In his simulations, Liles[7] suggested that varying the caliper Young's modulus did not much affect instability of the disc brake model. Additionally, Papinniemi[21] reported that caliper stiffness may not be beneficial for overall system stability. However, in this study, the resulted show that varying caliper Young's modulus somewhat had an effect on the number of unstable frequencies. By varying this value, it seemed that the unstable frequencies were varied from one to another even though some of them remain.

5.6. Influence of Steering Knuckle Young's Modulus

The base line Young's modulus of the steering knuckle was 167 GPa. In this section, the baseline Young's modulus of the steering knuckle was varied approximately up to ±10%. The other properties, such as Poisson's ratio and density, were kept

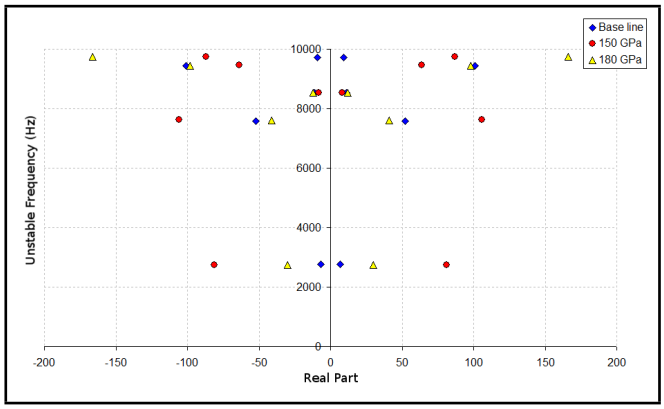

Figure 12. The effect of Young's modulus on the steering knuckle of the brake squeal generation.

constant throughout the parametric study. Similarly, Young's modulus of the other components was also left unchanged. The results in Fig. 12, show real and imaginary parts of the complex eigenvalues when Young's modulus of the friction material varies from 150 GPa to 180 GPa. It was found that the number of unstable frequencies was unchanged for varying Young's modulus of the steering knuckle but their magnitudes vary nonlinearly. It was also observed that at frequencies 2777 Hz and 7573 Hz, increasing Young's modulus of the steering knuckle lead to reduce the real values. However, at frequencies 8530 Hz, 9453 Hz, and 9722 Hz the real parts varied nonlinearly. It was concluded that Young's modulus of the steering knuckle may not be beneficial for overall system stability.

5.7. Influence of Wheel Hub Young's Modulus

The base line Young's modulus of the wheel hub was 168 GPa. In this section, the baseline Young's modulus of the wheel hub was varied approximately up to ±10%. The other properties, such as Poisson's ratio and density, were kept constant throughout the parametric study. Similarly, Young's modulus of other components was also unchanged. From the complex eigenvalue analysis, it was found that there were unstable frequencies that increased Young's modulus of the wheel hub to 190 GPa and was capable of eliminating positive real parts for unstable frequencies of 2777 Hz and 8530 Hz. However, a new unstable mode appeared at approximately 5800 Hz. From Fig. 13, setting the wheel hub modulus to 190 GPa reduced the number of unstable frequencies to just four. On the other hand, reducing Young's modulus of the wheel hub to 155 GPa had less of an impact with unstable frequencies still present at 7573 Hz, 9453 Hz, and 9722 Hz. However, the unstable frequencies of 2777 Hz and 8530 Hz were eliminated. Compared to the baseline case, setting the wheel hub modulus to 155 GPa reduced the number of unstable frequencies to just three. The results of the simulations indicate a range of instability in terms of the wheel hub Young's modulus.

6. CONCLUSIONS

This study investigated the effect of Young's modulus variations of the disc brake components on the squeal propensity using a detailed three-dimensional finite element model. Prior to the stability analysis using complex eigenvalue analysis, a

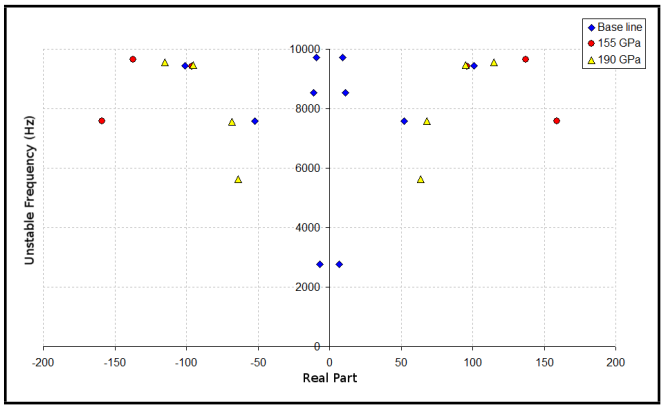

Figure 13. The effect of Young's modulus on the wheel hub of the brake squeal generation.

reasonably agreement is achieved between predicted and experimental results in terms of dynamic characteristics of the developed FE model. The simulation result showed that instability of the disc brake made it sensitive to Young's modulus variations of the disc brake components. It is worth noting that some of those variations reduce the number of unstable frequencies and consequently provide better squeal performance. In particular, increasing Young's modulus of the rotor, friction material, anchor bracket, and back plate. On the other hand, the variations of Young's modulus of the caliper and wheel hub have somewhat effect on the squeal generation. It is also observed that the variation of Young's modulus of the steering knuckle has little influence on the brake to alter its tendency to generate squeal noise.

ACKNOWLEDGEMENTS

The authors would like to thank Mr. Govardhana Giri of ATALON Testing and Consulting Engineers for his help in conducting modal testing experiments.

REFERENCES

[1] Papinniemi, A., Lai, J. C. S., Zhao, J., and Loader, L. Brake squeal: a literature review, *Appl Acoust.*, **63** (4), 391–400, (2002). http://dx.doi.org/10.1016/s0003-682x(01)00043-3

[2] Kinkaid, N. M., O'Reilly, O. M., and Papadopoulos, P. Automotive disc brake squeal, *J. Sound Vib.*, **267** (1), 105–166, (2003). http://dx.doi.org/10.1016/s0022-460x(02)01573-0

[3] Nouby, M. G., El-Sharkawy, M., and Ibrahim, A. A Review of Automotive Brake Squeal Mechanisms, *J. Mech. Design. Vib.*, **1** (1), 5–9, (2014).

[4] Carlo, C., Riccardo, C., Giampiero, M., Gianpiero, R., and Roberto, S. Brake comfort – a review. *Vehicle. Sys. Dyn.*, **47** (8), 901–947, (2009). http://dx.doi.org/10.1080/00423110903100432

[5] Ouyang, H., Nack, W. V., Yuan, Y., and Chen, F. Numerical analysis of automotive disc brake squeal: a review, *Int. J Veh. Noise Vib.*, **1** (3/4), 207–231, (2005). http://dx.doi.org/10.1504/ijvnv.2005.007524

[6] Joe, Y. G., Cha, B. G., Sim, H. J., Lee, H. J., and Oh, J. E. Analysis of disc brake instability due to friction-induced vibration using a distributed parameter model, *Int. J. Auto. Tech.*, **9** (2), 161–171, (2008). http://dx.doi.org/10.1007/s12239-008-0021-x

[7] Ewins, D. J., *Modal testing: theory and practice*, Research Studies Press. (2001).

[8] Nouby, M., Sujatha, C., and Srinivasan, K. Modelling of Automotive Disc Brake Squeal and Its Reduction Using Rotor Design Modifications, *Int. J. Veh Noise. Vib.*, **7** (2), 129–148, (2011). http://dx.doi.org/10.1504/ijvnv.2011.040571

[9] Hu, Y., Mahajan, S., and Zhang, K. Brake Squeal DOE Using Nonlinear Transient Analysis, SAE Paper 1999-01-1737, (1999). http://dx.doi.org/10.4271/1999-01-1737

[10] Kung, S. W., Dunlap, K. B., and Ballinger R. S., Complex eigenvalue analysis for reducing low frequency brake squeal, SAE 2000-01-0444, (2000). http://dx.doi.org/10.4271/2000-01-0444

[11] Abdo, J., Nouby, M., Mathivanan, D., and Srinivasan, K. Reducing disc brake squeal through FEM approach and experimental design technique, *Int. J. Veh. Noise. Vib*, **6** (2/3/4), 230–246, (2010). http://dx.doi.org/10.1504/ijvnv.2010.036688

[12] Liu, P., Zheng, H., Cai, C., Wang, Y. Y., Lu, C., Ang, K. H., and Liu G. R. Analysis of disc brake squeal using the complex eigenvalue method, *Appl Acoust.*, **68** (6), 603–615,(2007). http://dx.doi.org/10.1016/j.apacoust.2006.03.012

[13] Abu-Bakar, A. R. and Ouyang, H. A prediction methodology of disc brake squeal using complex eigenvalue analysis, *Int. J. Vehicle Des.*, **46** (4), 416–435, (2008). http://dx.doi.org/10.1504/ijvd.2008.020307

[14] Liles, G. D., Analysis of disc brake squeal using finite element methods, SAE 891150, (1989). http://dx.doi.org/10.4271/891150

[15] Lee, Y. S., Brooks, P. C., Barton, D. C., and Crolla D. A., A study of disc brake squeal propensity using a parametric finite element model, *In I Mech E Conference Transaction*, *European Conference on Noise and Vibration*, 191–201, (1998).

[16] Nouby, M., Mathivanan, D., and Srinivasan K. A combined approach of complex eigenvalue analysis and design of experiments (DOE) to study disc brake squeal, *Int. J. Eng. Sci. Tech.*, **1** (1), 254–271, (2009). http://dx.doi.org/10.4314/ijest.v1i1.58084

[17] Mario, T. J., Samir, N. Y., and Roberto, J. Analysis of brake squeal noise using the finite element method: A parametric study, *Appl Acoust.*, **69** (2), 147–162, (2008). http://dx.doi.org/10.1016/j.apacoust.2007.10.003

[18] Hassan, M. Z., Brooks, P. C., and Barton, D. C. A predictive tool to evaluate disk brake squeal using a fully coupled thermo-mechanical finite element model, *Int. J. Vehicle Des*, **51** (1/2), 124–142, (2009). http://dx.doi.org/10.1504/ijvd.2009.027118

Table 5. Comparisons between the predicted results and measured data for brake components.

Components	Mode	Exp. (Hz)	FE (Hz)	Error (%)	Mode shape
Anchor bracket	1	878	880	0.2	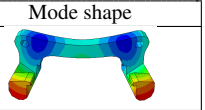
	2	1770	1755	-0.8	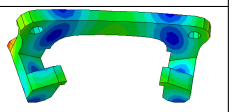
	3	3341	3164	-5.2	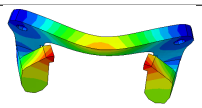
Caliper	1	2282	2293	-1.7	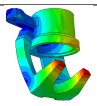
	2	3769	3960	5	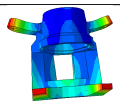
	3	5017	5182	3.2	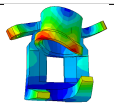
Brake Pad	1	2819	2889	2.4	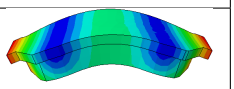
	2	7067	6735	-4.6	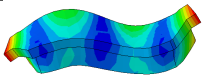
Piston	1	7287	7392	1.4	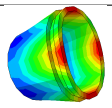
Steering knuckle	1	1232	1211	-1.7	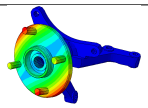
and wheel hub	2	2138	2242	4.8	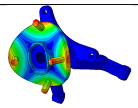
	3	4856	4421	8.9	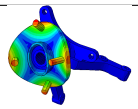

[19] Dai, Y. and Teik, C. L. Suppression of brake squeal noise applying finite element brake and pad model enhanced by spectral-based assurance criteria, *Appl Acoust.*, **69** (3), 196–214, (2008). http://dx.doi.org/10.1016/j.apacoust.2006.09.010

[20] Abu-Bakar, A. R. *Modelling and Simulation of Disc Brake Contact Analysis and Squeal*, PhD Thesis, Department of Engineering, University of Liverpool, (2005).

[21] Papinniemi, A. *Vibro–Acoustic Studies of Brake Squeal*, PhD Thesis, The University of New South Wales, (2007).

[22] Lou, G., Wu, T. W., and Ba, Z. Disk brake squeal prediction using the ABLE algorithm, *J Sound Vib.*, **272** (3/5), 731–748, (2004). http://dx.doi.org/10.1016/s0022-460x(03)00416-4

[23] Fieldhouse, J. D. and Steel, W. P. A study of brake noise and the influence of the centre of pressure at the disc/pad interface, the coefficient of friction and caliper mounting geometry, *Proc. I Mech E Part D, J. Automobile Engineering*, **217** (11), 957–973, (2003). http://dx.doi.org/10.1243/095440703770383866

[24] Dunlap K. B., Riehle M. A., and Longhouse, R. E. An investigation overview of automotive disc brake noise, *SAE Paper* 1999-01-0142, (1999). http://dx.doi.org/10.4271/1999-01-0142

[25] Lee, Y. S., Brooks, P. C., Barton, D. C., and Crolla, D. A. A Predictive Tool to Evaluate Disc Brake Squeal Propensity Part 3: Parametric Design Study, *Int. J. Vehicle Des.*, **31** (3), 330–353, (2003). http://dx.doi.org/10.1504/ijvd.2003.003364

[26] Dessouki, O., Brake, G., Lowe, B., and Chang, W. K. Disc brake squeal: diagnosis and prevention, *SAE paper*, 2003-01-1618, (2003). http://dx.doi.org/10.4271/2003-01-1618

APPENDIX A

Comparisons between the predicted results and measured data for brake components are presented in Table 5.

Acoustic Characteristic Analysis of Prestressed Cylindrical Shells in Local Areas

Lu-yun Chen

State Key Laboratory of Ocean Engineering, Shanghai Jiaotong University, Shanghai 200240, PR China

Yong Liu

China Ship Scientific Research Center, Shanghai Branch, Shanghai 214082, PR China

(Received 20 July 2014; accepted 5 November 2015)

The influence of prestress on dynamic responses and acoustic radiation for thin cylindrical shells is analyzed in this study. The strain-displacement equation of cylindrical shells with prestress in local areas is established based on the Flügge theory. The structural-acoustic radiation formulation for prestressed cylindrical shells in local areas is instituted by using the variational principle. A numerical analysis is then carried out. The numerical results are validated by comparing the influence of prestress on acoustic radiation power and directivity. This study shows that prestress significantly affects the dynamic characteristics of cylindrical shells.

1. INTRODUCTION

Prestress (initial stress) exists in complex structures because of welding residual stress, structural manufacturing defects, material thermal effects, and static external loading. Prestress resists or aids structural deformation and alters the static and dynamic characteristics of complex structures. For example, the natural frequencies of a structure increase or decrease with prestress distribution. Several studies have demonstrated the influence of prestress on structural-acoustic radiation. A previous study analyzed the structure buckling and vibration problem of composite sandwich plates with initial stress through the higher-order finite element theory.[1] The influence of prestress on the vibration frequency of concrete bridges was also investigated using the prestress stiffness matrix.[2] Regarding uniform Euler-Bernoulli beams under linearly varying fully tensile, the structure natural frequencies may be increased or decreased, and parameters change the forbidden frequencies of the mechanical system, considering the pre-stress force.[3] The influence of temperature was also determined by specifying the arbitrary high temperature on the outer surface and the ambient temperature on the inner surface of cylindrical shells. In this case, the prestressed state was induced by thermal loading.[4] The potential influence of prestress on resonance frequencies was also assessed, and the results showed that prestress depended on water depth.[5] Moreover, prestress can be used as a parameter to change the natural frequencies of a mechanical system in a proposed model of the prestressed structure.[6]

Thin cylindrical shells are widely used in complex structures, such as aerospace, marine, mechanical, and civil constructs. Research on the vibration and acoustic radiation of cylindrical shells has been a hot topic these past few years. A non-linear finite element model based on Murnaghan third-order elastic theory was applied to analyze the resonance structure, and the results showed that natural frequencies increased with increasing compressive stress.[7] The free-vibration characteristics of cylindrical shells were also investigated for a general class of elastic-support boundary conditions which considered depth-water pressure.[8] Moreover, several studies have investigated cylindrical shell dynamic problems with prestress distribution. A previous study reported the output power flow for an infinite ring-stiffened cylindrical shell submerged in fluid induced by a cosine harmonic circumferential line force under a uniform external hydrostatic pressure field and compared the influence of depth-water pressure.[9] The effect of variation in flow velocities and hydrostatic pressures on the dynamic behavior of fluid-conveying shells, as well as that of support conditions on free vibration, were further studied; a 3D method for prestress distribution was also established.[10,11] Simultaneous effects of a prestress condition, including its linear and nonlinear parts and the elastic foundation on natural frequencies of shells under various boundary conditions, were extensively examined.[12] The structure dynamic response of cylindrical shells subjected to harmonic excitation at low natural frequencies was discussed by comparing five different nonlinear cylindrical shell theories.[13] The free vibration and instability characteristics of a ring-stiffened cylindrical shell that conveys internal fluid was analyzed using motion equations based on the Flügge theory. The effects of fluid velocity and ring stiffener parameters on the natural frequency and stability characteristics of the shell were also assessed.[14] The effect of prestress on dynamic responses of fluid and initial stresses for the pipeline were further investigated using the integral equation; the result showed that the influence of prestress at high frequencies is essential.[15] The vibration problem of cylindrical shells was also evaluated using the differential quadrature method to resolve the prestressed structure problem.[16]

However, most studies focused on models of uniformly distributed prestress, such as hydrostatic pressure or water pressure, although fluid velocity deduces pressure. To the best of the author's knowledge, few results have investigated the prestress problem of local area distribution, despite its wide existence in engineering design and manufacturing. With this reason, to analyze the dynamic response and acoustic radiation characteristics of a prestressed complex structure in local areas is necessary. This study aimed to describe the low-frequency dynamic and acoustic responses of a prestressed cylindrical shell structure. The basic equations of structural-acoustic characteristics for cylindrical shells were established using the classical Flügge theory. The developed model was used to determine the influence of prestress on the local area. A general mathematical model capable of analyzing the dynamic behav-

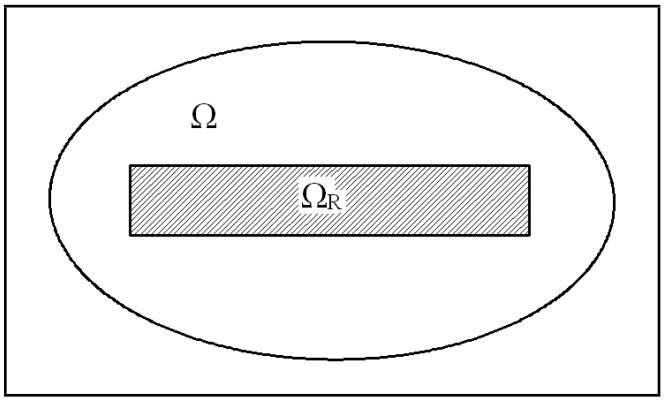

Figure 1. Prestress distribution in local areas.

ior of thin cylindrical shells with and without local area distribution as well as the overall and non-uniform distribution of prestress, were developed using the elasticity model. Finally, the effectiveness of the proposed models was confirmed through numerical calculations.

This paper is organized as follows: a brief literature review of the structural-acoustic radiation and prestress in Section 1. The basic model of prestress in local areas of a thin plate is demonstrated in Section 2. The motion governing the equations for cylindrical shells is presented in Section 3. Methods for addressing prestressed cylindrical shells in local areas in Section 4. The structural-acoustic radiation function of cylindrical shells is then established in Section 5. Acoustic radiation power and directivity are numerically analyzed in Section 6 to illustrate the validity and efficiency of the proposed method. Finally, concluding remarks are provided in Section 7.

2. PRESTRESS MODEL

2.1. Prestress Model in Local Areas

An elastic isotropic thin plate was used to establish a prestress distribution model in local areas. As shown in Fig. 1, the structure domain Ω contains the sub-domain Ω_R (more than one domain Ω_R in the domain Ω). Prestress exists in the subdomain Ω_R.

2.2. Prestress Equation

The prestress value was defined as zero in the absence of prestress in the design domain Ω_R. The unified prestress equation of the thin plate structure was also established. A thin plate was subjected to dynamic external loading, static external loading, and initial stress. The structure stress in the design domain can be expressed as $\boldsymbol{\sigma} = \{\sigma_{xx}, \sigma_{yy}, \sigma_{zz}, \tau_{xy}, \tau_{xz}, \tau_{yz}\}$. Thus, in the structure dynamic response, prestress consists of two parts: initial and static loading stresses. The initial stress consists of initial stress, welding residual stress, and material thermal effects, whereas the static loading stress is due to static external loading. Only prestress caused by static external loading was analyzed in this study.

According to the thin plate theory, the structure stress in the thin plate can be expressed as $\sigma_{zz} = \tau_{xz} = \tau_{yz} = 0$, where z is the direction of the plate thickness. The structure stress function can be written as $\boldsymbol{\sigma} = \{\sigma_{xx}, \sigma_{yy}, 0, \tau_{xy}, 0, 0\}$. Moreover, the cylindrical polar coordinate system indicates that the structure stress is represented by $\boldsymbol{\sigma} = \{\sigma_{xx}, \sigma_{\theta\theta}, \tau_{x\theta}\}$.

According to the Flügge theory and the structure elasticity theory, structure stresses, namely σ_{xx}, $\sigma_{\theta\theta}$, and $\tau_{x\theta}$, are related to the strain for homogeneous and isotropic materials and can be expressed as: $\sigma_{xx} = \frac{E}{1-\mu^2}(\varepsilon_{xx} + \mu\varepsilon_{\theta\theta})$, $\sigma_{\theta\theta} = \frac{E}{1-\mu^2}(\varepsilon_{\theta\theta} + \mu\varepsilon_{xx})$, and $\tau_{x\theta} = \frac{E}{2(1+\mu)}\gamma_{x\theta}$ respectively. The structure-strain displacements, ε_{xx} and $\varepsilon_{\theta\theta}$, are in axial and circumferential directions respectively. The structure shear strain, $\gamma_{x\theta}$, is in the coordinate system, E is the structural material Young's modulus, and μ is the Poisson ratio.

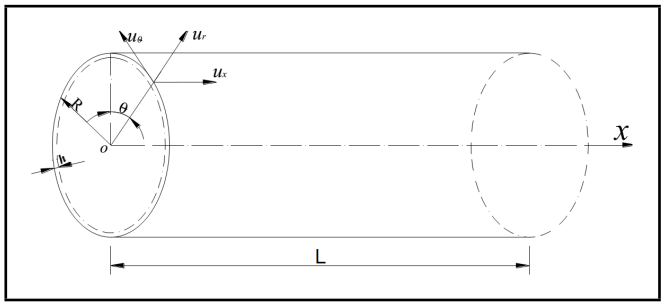

Figure 2. Coordinate system for a cylindrical shell.

For isotropic materials, the structure prestress in local areas can be written as $\boldsymbol{\sigma}^0 = \{\sigma^0_{xx}, \sigma^0_{yy}, \sigma^0_{zz}, \tau^0_{xy}, \tau^0_{xz}, \tau^0_{yz}\}$. If $\sigma^0 = 0$, then prestress does not exist in the structure design domain. Prestress has no influence on the shear strain in the thin plate. Only two principal directions of prestress are considered, and the stress can be stated as $\sigma^0_{zz} = \tau^0_{xy} = \tau^0_{xz} = \tau^0_{yz} = 0$. Prestress can be rewritten with a cylindrical polar coordinate system as $\boldsymbol{\sigma}^0 = \{\sigma^0_{xx}, \sigma^0_{\theta\theta}\}$.

The cylindrical structure stress of the thin plate subjected to state loading, dynamic loading, and prestress can be expressed as $\boldsymbol{\sigma} = \boldsymbol{\sigma}^0 + \boldsymbol{\sigma}^f = \{\sigma^0_{xx}, \sigma^0_{\theta\theta}, 0, 0, 0, 0\} + \{\sigma^f_{xx}, \sigma^f_{\theta\theta}, 0, \tau^f_{x\theta}, 0, 0\}$, where $\boldsymbol{\sigma}^0$ is the local-area prestress, and $\boldsymbol{\sigma}^f$ is caused by dynamic external loading.

3. MOTION EQUATIONS OF CYLINDRICAL SHELLS

In this study, the dynamic response problem of prestress in the local areas of cylindrical shells was formulated in a cylindrical polar coordinate system.

3.1. Free Vibration Formulations of Cylindrical Shells

The structure of isotropic, infinite, and thin cylindrical shells in a fluid medium contains the region Ω_S with the boundary Γ_S. The dynamic response of the shells was determined in a cylindrical polar coordinate system (x, θ, r), as shown in Fig. 2, where the x-axis is the axis of the shell and r and θ are the radial and circumferential directions respectively.

The general assumptions in the structural-acoustic analysis for cylindrical shells include the following: the structure material is isotropic and linearly elastic; the fluid medium is isotropic, inviscid, and incompressible; the acoustic wave equation is linear; the deformation of the shell is small; the shell and fluid gravity force are neglected; and the shell thickness t is smaller than the shell's mean radius. In addition, only the low- and middle-frequency domains of acoustic radiation are discussed in this study, while structure-fluid coupling are not.

Figure 2 shows the circular cylindrical shell structure with thickness t, length L, and radius of the middle surface R.

Therefore, the dynamic displacement vector $\mathbf{u}$ in the cylindrical polar coordinate system can be expressed as:

$$\mathbf{u} = \{u_x(x,\theta,r,t), u_\theta(x,\theta,r,t), u_r(x,\theta,r,t)\}^T; \quad (1)$$

where u_x, u_θ, and u_r represent the displacements of an arbitrary point on the middle surface of shell axial, tangential, and radial displacements respectively. The superscript T is the transposition of a vector/matrix in the equation. Dynamic displacement in the middle surface of the cylindrical shell structure can be obtained using the classical Flügge theory and can be expressed as:

$$u_x = \sum_{n=-\infty}^{\infty} \int_{-\infty}^{\infty} U_x(k_x) e^{(in\theta + ik_x x)} dx,$$

$$u_\theta = \sum_{n=-\infty}^{\infty} \int_{-\infty}^{\infty} U_\theta(k_x) e^{(in\theta + ik_x x)} dx,$$

and

$$u_r = \sum_{n=-\infty}^{\infty} \int_{-\infty}^{\infty} U_r(k_x) e^{(in\theta + ik_x x)} dx,$$

where U_x, U_θ, and U_r are the shell spectral displacement amplitudes of the axial, tangential, and radial directions respectively. The parameter k_x is the wave number in the axial direction.

3.2. Strain-displacement Equation of Cylindrical Shells

The cylindrical shell structure loaded by residual stress or static loading can resist or aid structure deformation. The strain field associated with the vibration of a prestressed cylindrical shell consists of prestress and dynamic stress. As such, the strain-displacement relations include several nonlinear terms. Therefore, the total strain field $\boldsymbol{\varepsilon}$ for prestressed cylindrical shells may be represented as the cylindrical polar coordinate system using:

$$\boldsymbol{\varepsilon} = \boldsymbol{\varepsilon}^0 + \boldsymbol{\varepsilon}^f = \{\varepsilon^0_{xx}, \varepsilon^0_{\theta\theta}, 0, 0, 0, 0\} + \{\varepsilon^f_{xx}, \varepsilon^f_{\theta\theta}, 0, \gamma^f_{x\theta}, 0, 0\}; \quad (2)$$

where $\boldsymbol{\varepsilon}$ is the strain vector of the cylindrical shell and $\boldsymbol{\varepsilon}^0$ is the strain vector caused by local-area prestress. Only the linear strain was discussed in this study, such as $\{\varepsilon^0_{xx}, \varepsilon^0_{\theta\theta}, 0, 0, 0, 0\}$, where ε^0_{xx} and $\varepsilon^0_{\theta\theta}$ are the axial and circumferential strains by prestress respectively.

The structure strain, $\boldsymbol{\varepsilon}^f = \{\varepsilon^f_{xx}, \varepsilon^f_{\theta\theta}, 0, \gamma^f_{x\theta}, 0, 0\}$, is the dynamic strain components in the cylindrical coordinate system and includes strain and shear strain, which was caused by harmonic external loading. Based on the classical Flügge theory, ε^f_{xx}, $\varepsilon^f_{\theta\theta}$, and $\gamma^f_{x\theta}$ are strain components in the cylindrical coordinate system.

In the middle surface of the structure, the relationship of the strain-displacement equation for the thin cylindrical shell structure can be expressed as: $\varepsilon^f_{xx} = \frac{\partial u_x}{\partial x}$, $\varepsilon^f_{\theta\theta} = \frac{1}{R}\frac{\partial u_\theta}{\partial \theta} + \frac{u_r}{R}$, and $\gamma^f_{x\theta} = \frac{1}{R}\frac{\partial u_x}{\partial \theta} + \frac{\partial u_\theta}{\partial x}$. The strain-displacement equation can be written in vector form as: $\boldsymbol{\varepsilon}^f = \{u_{x,x}, \frac{1}{R}(u_{\theta,\theta} + u_r), 0, \frac{1}{R}u_{x,\theta} + u_{\theta,x}, 0, 0\}^T$. Meanwhile, the strain-displacement equation can be rewritten in matrix form as:

$$\boldsymbol{\varepsilon}^f = \mathbf{Y}\boldsymbol{\zeta}; \quad (3)$$

where $\mathbf{Y} = \begin{bmatrix} 1&0&0&0&0&0 \\ 0&1&0&0&0&0 \\ 0&0&0&0&0&0 \\ 0&0&0&1&1&0 \\ 0&0&0&0&0&0 \\ 0&0&0&0&0&0 \end{bmatrix}$ and $\boldsymbol{\zeta} = \{\zeta_1, \zeta_2, \zeta_3, \zeta_4, \zeta_5, \zeta_6\}^T$.

Furthermore, $\zeta_1 = u_{x,x}$, $\zeta_2 = \frac{1}{R}(u_{\theta,\theta} + u_r)$, $\zeta_4 = \frac{1}{R}(u_{x,\theta})$, and $\zeta_5 = u_{\theta,x}$.

3.3. The Stress-Strain Equation of the Cylindrical Shell

In the cylindrical shell structure, the general constituent stress-strain relationship between the stress and strain vectors can be obtained by using the following equation:

$$\boldsymbol{\sigma} = \mathbf{D}\boldsymbol{\varepsilon} = \boldsymbol{\sigma}^0 + \mathbf{D}\boldsymbol{\varepsilon}^f; \quad (4)$$

where $\boldsymbol{\sigma}^0$ is the prestress vector, viz. $\boldsymbol{\sigma}^0 = \{\sigma^0_{xx}, \sigma^0_{\theta\theta}\}$ and σ^0_{xx}, $\sigma^0_{\theta\theta}$ are the normal prestress vector components in the cylindrical coordinate system, and $\mathbf{D}$ represents the shell stress-strain matrix. For the isotropic material structure, the constitutive relationship matrix $\mathbf{D}$ can be expressed as:

$$\mathbf{D} = \frac{E}{(1+\mu)(1-2\mu)} \begin{bmatrix} 1-\mu & \mu & \mu & 0 & 0 & 0 \\ \mu & 1-\mu & \mu & 0 & 0 & 0 \\ \mu & \mu & 1-\mu & 0 & 0 & 0 \\ 0 & 0 & 0 & 0.5-\mu & 0 & 0 \\ 0 & 0 & 0 & 0 & 0.5-\mu & 0 \\ 0 & 0 & 0 & 0 & 0 & 0.5-\mu \end{bmatrix};$$

where E is the Young's modulus, and μ is the Poisson ratio.

3.4. Governing Formulation of the Cylindrical Shell

In a small shell element with unit length, the displacement vector of the cylindrical shell $\mathbf{u}$ was governed by the motion equation. The dynamic displacement parameter of the cylindrical shell is $\mathbf{u} = \{u_x, u_\theta, u_r\}^T$. In the structure domain Ω_S, the appropriate function for the shell domain can be expressed as:

$$\rho_S \ddot{\mathbf{u}} - \nabla \cdot \boldsymbol{\sigma} = 0 \quad \text{in} \quad \Omega_S; \quad (5)$$

where ρ_S is the density of the cylindrical shell, dot represents a derivative with respect to time, and Ω_S is the shell solution domain.

If fluid-structural coupling is weak and can be neglected, especially for air, the influence of acoustic pressure on the structure can also be neglected, and the shell's motion equation can be proposed. If the distribution function of prestress is defined, the amplitude and frequency of external loading is also given. Combining the boundary condition and substituting Eqs. (3) and (4) into Eq. (5) yields the following equation that governs the motion of the cylindrical shell:

$$\int_{\Omega_S} \delta\boldsymbol{\varepsilon}^T \mathbf{D}\boldsymbol{\varepsilon}\, d\Omega_S + \int_{\Omega_S} \delta\mathbf{u}^T \rho\ddot{\mathbf{u}}\, d\Omega_S - \int_{\Omega_S} \delta\mathbf{u}^T \mathbf{f}\, d\Omega_S = 0; \quad (6)$$

where $\mathbf{u}$ is the cylindrical shell displacement vector, such as $\mathbf{u} = \{u_x, u_\theta, u_r\}^T$, $\boldsymbol{\rho}_S$ represents the inertia force acceleration matrix, and $\mathbf{f}$ is the vector of the shell body force.

These motion equations of shell in the acoustic medium can be rewritten in a variational formula by using the Hamilton

principle. Hence, the following motion equation can be obtained:

$$\int_{\Omega_S} \delta(\boldsymbol{\varepsilon}^0+\boldsymbol{\varepsilon}^f)^T \mathbf{D}(\boldsymbol{\varepsilon}^0+\boldsymbol{\varepsilon}^f)\, d\Omega_S + \int_{\Omega_S} \delta\overline{\mathbf{u}}^T \mathbf{N}_S^T \rho_S \mathbf{N}_S \ddot{\overline{\mathbf{u}}}\, d\Omega_S - \int_{\Omega_S} \delta\overline{\mathbf{u}}^T \mathbf{N}_S^T \mathbf{f}\, d\Omega_S = 0; \tag{7}$$

where the first, second, and third parts represent strain energy variation in the structure, kinetic energy variation in the structure, and external force acting on the structure of the virtual variation in external forces respectively.

4. SOLUTION OF MOTION EQUATION

4.1. Structure Discretization

In Eq. (7), the governing motion of the cylindrical shell subjected to boundary conditions was solved by using the finite element method (FEM). The cylindrical shell was also discretized by introducing cylindrical frustums, in which the shell displacement variable $\mathbf{u}(x,\theta,r,t)$ and the variational form $\delta\mathbf{u}(x,\theta,r,t)$ can be expressed as:

$$\mathbf{u}(x,\theta,r,t) = \{\mathbf{N}_S\overline{\mathbf{u}}_x, \mathbf{N}_S\overline{\mathbf{u}}_\theta, \mathbf{N}_S\overline{\mathbf{u}}_r\}^T = \mathbf{N}\overline{\mathbf{u}}; \tag{8a}$$

$$\delta\mathbf{u}(x,\theta,r,t) = \{\delta(\mathbf{N}_S\overline{\mathbf{u}}_x), \delta(\mathbf{N}_S\overline{\mathbf{u}}_\theta), \delta(\mathbf{N}_S\overline{\mathbf{u}}_r)\}^T = \delta\overline{\mathbf{u}}^T\mathbf{N}^T; \tag{8b}$$

where $\overline{\mathbf{u}} = \{\overline{\mathbf{u}}_x, \overline{\mathbf{u}}_\theta, \overline{\mathbf{u}}_r\}^T$ represents the nodal displacement vector. $\overline{\mathbf{u}}_x$, $\overline{\mathbf{u}}_\theta$, and $\overline{\mathbf{u}}_r$ are the nodal displacement in the axial, tangential, and radial directions respectively. $\mathbf{N}_S$ denotes the shape function matrix of the element and $\mathbf{N}$ is the assembled shape function matrix. The relationship between matrix $\mathbf{N}$ and matrix $\mathbf{N}_S$ can be obtained by using $\mathbf{N} = \begin{bmatrix} \mathbf{N}_S & 0 & 0 \\ 0 & \mathbf{N}_S & 0 \\ 0 & 0 & \mathbf{N}_S \end{bmatrix}$.

Defining $d\boldsymbol{\zeta} = \mathbf{G}\, d\overline{\mathbf{u}}$, then there is $d\boldsymbol{\varepsilon} = d\boldsymbol{\varepsilon}^f = \mathbf{YG}\, d\overline{\mathbf{u}}$. The transformation matrix $\mathbf{G}$ can be defined as $\mathbf{G} = \begin{bmatrix} \mathbf{N}_{S,x}^T & 0 & 0 & \frac{\mathbf{N}_{S,x}^T}{R} & 0 & 0 \\ 0 & \frac{\mathbf{N}_{S,x}^T}{R} & 0 & \mathbf{N}_{S,x}^T & 0 & 0 \\ 0 & \frac{\mathbf{N}_{S,x}^T}{R} & 0 & 0 & 0 & 0 \end{bmatrix}^T$. The linear strain-displacement matrix $\mathbf{A}$ can be obtained by substituting the transformation matrix $\mathbf{G}$ into Eq. (4). In addition, the differential equations of the structural dynamic strain can be expressed as:

$$d\boldsymbol{\varepsilon}^f = \mathbf{YG}\, d\overline{\mathbf{u}} = \mathbf{A}\, d\overline{\mathbf{u}} = \begin{bmatrix} \frac{\partial \mathbf{N}_S}{\partial x} & 0 & 0 \\ 0 & \frac{\partial \mathbf{N}_S}{R\,\partial x} & \frac{\mathbf{N}_S}{R} \\ 0 & 0 & 0 \\ \frac{\partial \mathbf{N}_S}{R\,\partial \theta} & \frac{\partial \mathbf{N}_S}{\partial x} & 0 \\ 0 & 0 & 0 \\ 0 & 0 & 0 \end{bmatrix} d\overline{\mathbf{u}}. \tag{9}$$

4.2. Motion Function of the Cylindrical Shell

Nonlinear terms (second- and third-order) were neglected under low shell deformation and only the nonlinear strain-displacement relationship were used to derive the geometric stiffness matrix during standard discretization. The following equation governing the motion of the shell in the global coordinate system was obtained using the variational principle. By substituting Eqs. (3), (8), and (9) into Eq. (7), a motion equation can be yielded, which governs the motion of the cylindrical shell system as a standard discretization form:

$$\int_{\Omega_S} \mathbf{N}_S^T \rho_S \mathbf{N}_S^T \ddot{\overline{\mathbf{u}}}\, d\Omega_S + \int_{\Omega_S} \mathbf{A}^T\mathbf{DA}\overline{\mathbf{u}}\, d\Omega_S + \int_{\Omega_S} \mathbf{G}^T\mathbf{SG}\overline{\mathbf{u}}\, d\Omega_S - \int_{\Omega_S} \mathbf{f}\, d\Omega_S = 0; \tag{10}$$

where $\ddot{\overline{\mathbf{u}}}$ is the shell nodal acceleration vector, $\overline{\mathbf{u}}$ is the shell nodal displacement vector, and the matrix $\mathbf{S}$ is provided by the structural prestress matrix and can be written as: $\mathbf{S} = \begin{bmatrix} \sigma_{xx}^0\mathbf{I}_2 & \tau_{x\theta}^0\mathbf{I}_2 & \tau_{x\gamma}^0\mathbf{I}_2 \\ \tau_{x\theta}^0\mathbf{I}_2 & \sigma_{\theta\theta}^0\mathbf{I}_2 & \tau_{\theta\gamma}^0\mathbf{I}_2 \\ \tau_{x\gamma}^0\mathbf{I}_2 & \tau_{\theta\gamma}^0\mathbf{I}_2 & \sigma_{\gamma\gamma}^0\mathbf{I}_2 \end{bmatrix}$, where $\mathbf{I}_2$ is a unit matrix of order 2. The local area prestress $\sigma^0 = \{\sigma_{xx}^0, \sigma_{\theta\theta}^0, 0, 0, 0, 0\}$ is substituted into matrix $\mathbf{S}$, which can be written as: $\mathbf{S} = \begin{bmatrix} \sigma_{xx}^0\mathbf{I}_2 & 0 & 0 \\ 0 & \sigma_{\theta\theta}^0\mathbf{I}_2 & 0 \\ 0 & 0 & 0 \end{bmatrix}$.

The integral equation can then be obtained as:

$$\mathbf{m}_S\ddot{\overline{\mathbf{u}}} + \mathbf{k}_S\overline{\mathbf{u}} + \mathbf{f} = 0; \tag{11}$$

where $\mathbf{f}$ is the elemental matrix of external loading, $\mathbf{m}_S$ is the elemental mass matrix and represented as $\mathbf{m}_S = \int_{\Omega_S} \mathbf{N}_S^T\rho_S\mathbf{N}_S^T\, d\Omega_S$; $\mathbf{k}_S = \mathbf{k}_0 + \mathbf{k}_\sigma$ is the elemental stiffness matrix, $\mathbf{k}_0 = \int_{\Omega_S} \mathbf{A}^T\mathbf{DA}\, d\Omega_S$ is the elemental stiffness matrix of the cylindrical shell without prestress, and $\mathbf{k}_\sigma = \int_{\Omega_S} \mathbf{G}^T\mathbf{SG}\, d\Omega_S$ is the additional part of the elemental stiffness matrix for the cylindrical shell with prestress and defined as prestress stiffness matrix. The structural stiffness matrix was modified due to the the existence of prestress in the local area. Thus, the overall stiffness matrix was altered, the effect of fluid-structural coupling was neglected, and the mass matrix was not affected by prestress.

If the viscous damping matrix is considered, then the viscous damping matrix $\mathbf{c}_S$ in the differential equation can be expressed as:

$$\mathbf{m}_S\ddot{\overline{\mathbf{u}}} + \mathbf{c}_S\dot{\overline{\mathbf{u}}} + \mathbf{k}_S\overline{\mathbf{u}} + \mathbf{f} = 0. \tag{12}$$

The nodal displacement vector matrix was obtained by substituting the displacement vector equation and the harmonic loading equation into Eq. (12). In addition, the nodal normal velocity vector $\mathbf{v}_n(\omega)$ can be obtained. The nodal particle normal velocity was used as boundary condition in the acoustic radiation analysis with the boundary element method (BEM).

5. ACOUSTIC RADIATION FUNCTION

Structure vibration induces acoustic radiation. BEM was used to calculate the acoustic radiation behavior (acoustic pressure and acoustic radiation power) with structure response (harmonic normal velocity) as the boundary condition. Only the low-middle frequency domains of the exterior acoustic radiation of the continuum structure were analyzed in this study, which only considered the steady-state response of the vibrating structure. The standard acoustic wave equations were reduced to the Helmholtz equation in the harmonic response problem. For an arbitrary shape structure, the governing differential equation and boundary condition in steady-state linear acoustics is the classical 3D Helmholtz equation as follows:

$$\nabla^2\mathbf{p}(x,\theta,r,t) + k^2\mathbf{p}(x,\theta,r,t) = 0; \tag{13}$$

$$\frac{\partial^2\mathbf{w}}{\partial t^2} = -\frac{1}{\rho}\frac{\partial\mathbf{p}(x,\theta,r,t)}{\partial r}\Big|_{r=R}; \tag{14}$$

where $\mathbf{p}$ is the acoustic pressure of the acoustic field point, k ($= \omega/c$) denotes the wave number, and ω and c are the angular frequency and speed of sound respectively, and ∇^2 is the Laplace operator. The acoustic wave assumes harmonic time variations throughout the analysis with $e^{i\omega t}$ dependence suppressed for simplicity.

At the structure-fluid boundaries Γ_S, the acoustic pressure must satisfy the Neumann boundary condition $\partial\mathbf{p}/\partial\mathbf{n} = -i\omega\rho\mathbf{v}_n$, where $\mathbf{v}_n$ is the nodal normal velocity of the structure, ρ is the density of the fluid medium, and $\mathbf{n}$ is the outer-normal unit vector of the structure surface. Moreover, the acoustic pressure $\mathbf{p}$ precisely and automatically satisfies the Sommerfeld condition at infinity, $\lim_{r\to\infty}[\mathbf{r}(\partial\mathbf{p}/\partial\mathbf{r} - ik\mathbf{p})] = 0$. The associated form of the pressure field of the cylindrical shell can be expressed by applying the variable separation method to solve the acoustic wave equation:

$$\mathbf{p}(x,\theta,r) = \sum_{n=-\infty}^{\infty} P_n(x) H_n^{(1)}(kr) e^{in\theta}; \tag{15}$$

where n is the expansion coefficient, $H_n^{(1)}(kr)$ is the n-th order Hankel function of the first kind, $P_n(x)$ is the pressure amplitude, and $k = \sqrt{k_f^2 - k_x^2}$, $k_f = \omega/c$. In addition, the radial velocity $\mathbf{v}_n(\vec{r})$ in the acoustic field is $\mathbf{v}_n(\vec{r}) = -\frac{1}{i\omega\rho}\frac{\partial\mathbf{p}}{\partial\mathbf{r}}$.

In this study, the acoustic medium was defined as air. The feedback coupling between the acoustic medium and the vibrating structure was also neglected because of its weak influence. The acoustic radiation field quantities were relevant to acoustic radiation pressure and power. However, acoustic pressure varies according to spatial position, and the calculation is time consuming. Acoustic power was a suitable parameter to be used for quantifying the radiation on the structure surface. Acoustic power is also related to the characteristics of structure vibration and does not change with spatial position. Therefore, the power parameter of acoustic radiation is preferred over the acoustic pressure parameter for structural-acoustic analysis and evaluation. In the acoustic field domain, the acoustic radiation power describes the energy flow of an assumed integral surface and can be defined as:

$$\Pi = \frac{1}{2}\int_{\Gamma} \mathrm{Re}\{\mathbf{p}(\vec{r}) \cdot \mathbf{v}_n^*(\vec{r})\}\, d\Gamma; \tag{16}$$

where "Re" represents the real part of a complex variable, $\mathbf{p}(\vec{r})$ is the acoustic pressure at the acoustic field point, as shown in Eq. (15), $\mathbf{v}_n^*(\vec{r})$ is the field-point normal complex conjugate operator velocity of fluid-particle, and Γ is the integral surface of acoustic domain. After omitting the acoustic transmission loss and absorption of the boundary and source points, the acoustic radiation power of the exterior acoustic field is equal to that of the source point surface. The structure surface radiation acoustic power can be written as:

$$\Pi = \frac{1}{2}\mathrm{Re}\int_{\Gamma} \mathbf{p}_f \mathbf{v}_n^*\, d\Gamma; \tag{17}$$

where Γ is the structure-fluid interface, $\mathbf{p}_f$ is the acoustic pressure on the structural surface, and $\mathbf{v}_n^*$ is the nodal normal complex conjugate velocity on the structural surface. In the vibration structure, $\mathbf{p}_f = \rho c\mathbf{v}_n$ exits, where the phase angle between acoustic pressure $\mathbf{p}_f$ and the normal velocity $\mathbf{v}_n^*$ is 0.

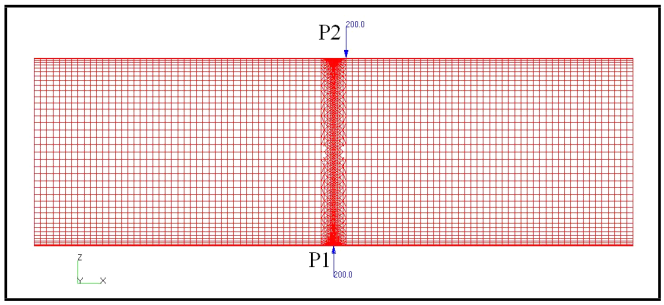

Figure 3. Finite element model of the cylindrical shell.

6. NUMERICAL RESULTS AND DISCUSSION

A cylindrical shell structure under external harmonic excitation in air was used to demonstrate the influence of prestress in local areas on the structural-acoustic characteristics of the shells. In the numerical examples, FEM was used to analyze structural dynamic response, whereas BEM was applied to deal with the exterior acoustic radiation problem, structure vibration, acoustic power, and acoustic directivity. This study only focused on the steady-state dynamic response of the vibrating structure.

6.1. Model Description

A finite thin cylindrical shell structure with supported boundary condition immersed in fluid was used in this study, as shown in Fig. 3. The radius, length, and thickness of the cylindrical shell are 1.5, 4.8, and 0.01 m respectively. The cylindrical shell structure was discretized using FEM. In the model, the zero point of the overall coordinate system is located at the center of the cylindrical shell.

The material of the cylindrical shell structure is steel with mechanical performance parameters as follows: density, $\rho = 7800$ kg/m^3; modulus of elasticity, $E = 210$ GPa; and the Poisson ratio, $\mu = 0.3$. The total weight of the cylindrical shell is 1764.0 kg, whereas the fundamental frequency is $\omega = 7.6$ Hz.

In the structural-acoustic analysis, the acoustic properties of the fluid (i.e. air) are isotropic and homogeneous, with density (ρ) of 1.225 kg/m^3, speed of sound (c) of 343 m/s, acoustic power reference value (W_0) of 1×10^{-12} Watt, and acoustic pressure reference value (p_0) of 2×10^{-5} Pa.

A time-harmonic line force loading on the shell structure was also observed. The first concentrated loading is $\mathbf{f}(t) = F\sin(2\pi ft)$, with a prescribed amplitude of $P < 0, 0, 200.0 >$ N. The frequency of the external force is $f = 61$ Hz, which was applied to a point on P1, as shown in Fig. 3. The second concentrated loading is $\mathbf{f}(t) = F\sin(2\pi ft)$, with a prescribed amplitude of $P < 0, 0, -200.0 >$ N. The frequency of the external force is $f = 61$ Hz, which was applied to a point on P2, as shown in Fig. 3.

6.2. Structure Prestress

Prestress of the cylindrical shell structure was induced by ring static loading. A uniform distribution of static loading was observed on the cylindrical shell structure, as shown in Fig. 3. The length of the static loading region is 0.2 m on the axis direction. The amplitude of the static surface force is 1.6×10^6 Pa, and the normal direction of the force is inward.

The deformation parameter of the cylindrical shell structure was obtained according to the numerical analysis of the structure subjected to static loading. In addition, the contour maps

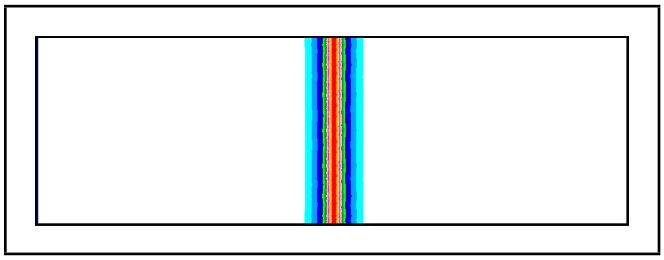

Figure 4. Contour maps of prestress distribution.

Table 1. Comparison of mode frequencies.

Mode order	Without prestress	With prestress
1	7.6	7.2
2	9.1	8.9
3	12.0	11.0
4	20.0	19.4
5	20.1	20.0
6	33.8	32.5

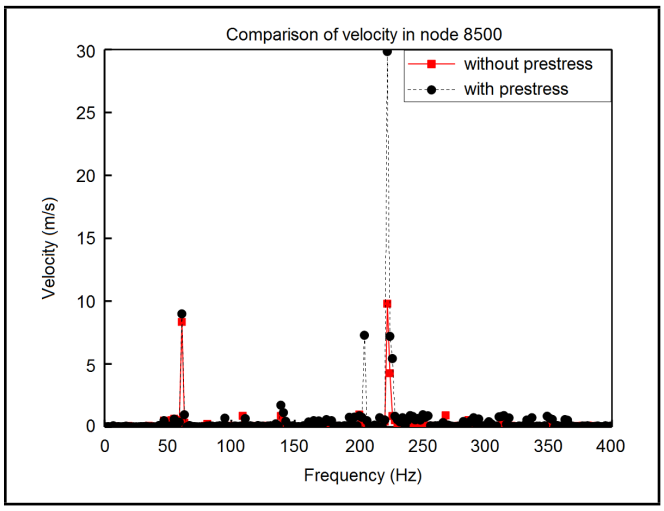

Figure 5. Comparison of velocity.

of the structure stress distribution are illustrated in Fig. 4. The structure stress is concentrated in the center of the shell structure near the static loading region. Far from the static loading region, the stress is very small and can be omitted. The maximum value of the structure stress of the shell structure is 107 MPa. The structure stress is defined as local-area prestress in the dynamic response analysis.

6.3. Vibration of the Cylindrical Shell

The dynamic characteristic of the cylindrical shell structure changed with prestress distribution. Table 1 shows the mode frequencies of the structure with or without prestress distribution. The influence of prestress on the dynamic behavior of the shell structure is considered significant.

The vibration characteristics of the cylindrical shell were compared in the absence or presence of prestress distribution. The velocity of the cylindrical shell structure can be calculated using the FEM code. Frequency variation in the analysis ranges from 0 Hz to 400 Hz, and the frequency step size is 2 Hz. Figure 5 demonstrates the comparison of the node velocity of the defined point located on the static loading region with or without prestress.

As shown in Fig. 5, the influence of prestress on the dynamic behavior of the cylindrical shell structure is evident.

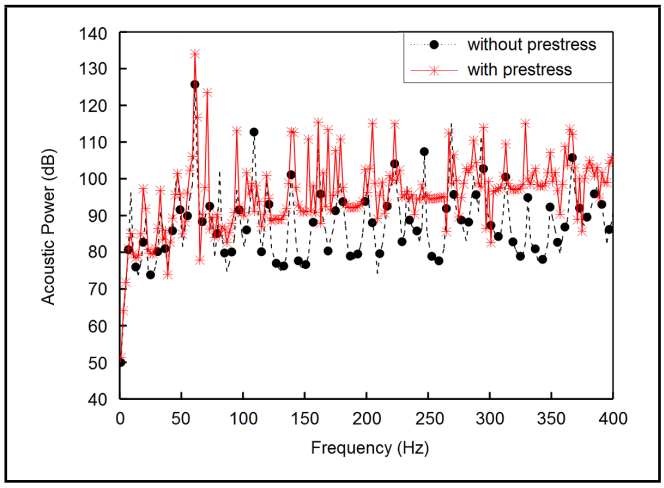

Figure 6. Comparison of acoustic power.

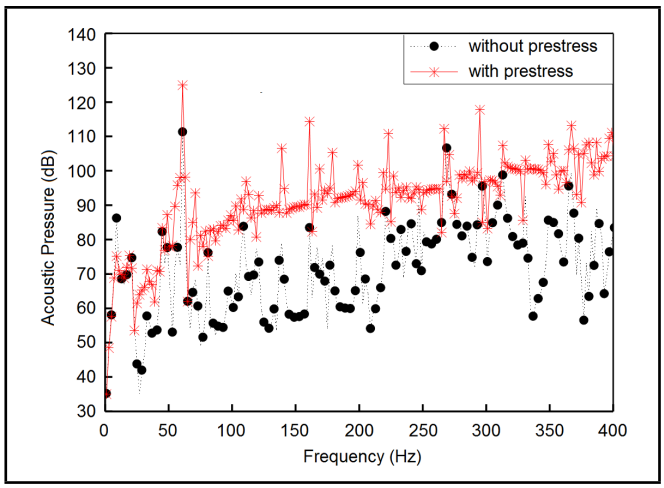

Figure 7. Comparison of acoustic pressure.

6.4. Acoustic Radiation of the Cylindrical Shell

Acoustic pressure in the field point and acoustic radiation power were obtained using the BEM code combined with the normal velocity of the cylindrical shell structure. Frequency variation in radiated acoustic power ranges from 0 Hz to 400 Hz, and the frequency step size is 2 Hz. Figure 6 shows the comparison between the acoustic radiation power with and without prestress. As shown in Figs. 6 and 7, the influence of prestress on acoustic radiation power, as well as on acoustic pressure in the field point of the cylindrical shell structure is evident, with the field point located in (0, 5, and 5).

Numerical analysis showed that the stiffness matrix of the cylindrical shell structure and the dynamic response parameter were altered in the presence of prestress. Acoustic radiation power was then changed, and the maximum value of the acoustic radiation power significantly increased.

6.5. Acoustic Directivity Analysis

The influence of prestress, which is located in local areas of the acoustic source point on acoustic pressure directivity was compared. In the directivity analysis, acoustic pressure was compared in the frequency of 61 Hz. The acoustic field was located in the horizontal plane midway along the cylinder length. Figure 8 shows the comparison between the acoustic radiation directivity with and without prestress.

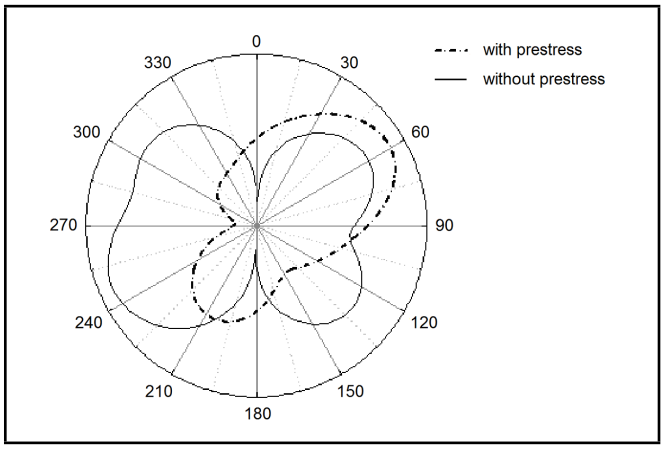

Figure 8. Comparison of the acoustic directivity.

A comparison of Figs. 5, 6, 7, and 8 shows that the dynamic characteristics are significantly reduced. Additionally, the influence of the existing prestress is obvious.

7. CONCLUSIONS

In this study, acoustic radiation power is proposed as a performance index to address vibration and acoustic radiation problem of a prestressed cylindrical shell structure in local area distribution. The following conclusions are drawn through numerical analysis and comparison. The existence of local prestress changes the stiffness of the structure. Prestress distributed in local areas significantly influences sound radiation and is evident in low-frequency band. Meanwhile, the structure of radiation directivity can be changed. Future studies will focus on fluid-structure coupling characteristics at the interface.

FUNDING

This work was partially supported by the State Key Laboratory of Ocean Engineering of Shanghai Jiaotong University. Their support is gratefully acknowledged by the authors.

REFERENCES

[1] Nayak, A. K., Moy, S. S. J., and Shenoi, R. A. A higher order finite element theory for buckling and vibration analysis of initially stressed composite sandwich plates, *Journal of Sound and Vibration*, **286**, 763–780, (2005). http://dx.doi.org/10.1016/j.jsv.2004.10.055

[2] Saiidi, M., Douglas, B., and Feng, S. Prestress force effect on vibration frequency of concrete bridges, *Journal of Structural Engineering*, **120**, 2233–2241, (1994). http://dx.doi.org/10.1061/(asce)0733-9445(1994)120:7(2233)

[3] Naguleswaran, S. Transverse vibration of an uniform Euler-Bernoulli beam under linearly varying axial force, *Journal of Sound and Vibration*, **275**, 47–57, (2004). http://dx.doi.org/10.1016/s0022-460x(03)00741-7

[4] Haddadpour, H., Mahmoudkhani, S., and Navazi, H. M. Free vibration analysis of functionally graded cylindrical shells including thermal effects, *Thin-Walled Structures*, **45**, 591–599, (2007). http://dx.doi.org/10.1016/j.tws.2007.04.007

[5] Hamed, E. and Frostig, Y. Natural frequencies of bonded and unbonded prestressed beams prestress force effects, *Journal of Sound and Vibration*, **295**, 28–39, (2006). http://dx.doi.org/10.1016/j.jsv.2005.11.032

[6] Bigoni, D., Gei, M., and Movchan, A. B. Dynamics of a prestressed stiff layer on an elastic half space: filtering and band gap characteristics of periodic structural models derived from long-wave asymptotics, *Journal of the Mechanics and Physics of Solids*, **56**, 2494–2520, (2008). http://dx.doi.org/10.1016/j.jmps.2008.02.007

[7] Lundqvist, P. and Rydén, N. Acoustoelastic effects on the resonance frequencies of prestressed concrete beams-short-term measurements, *NDT & E International*, **50**, 36–41, (2012). http://dx.doi.org/10.1016/j.ndteint.2012.04.010

[8] Zhou, H. J., Li, W. Y., Lv, B. L., et al. Free vibrations of cylindrical shells with elastic-support boundary conditions, *Applied Acoustics*, **73**, 751–756, (2012). http://dx.doi.org/10.1016/j.apacoust.2012.02.008

[9] Zhu, X., Ye, W. B., and Li, T. Y. The elastic critical pressure prediction of submerged cylindrical shell using wave propagation method, *Ocean Engineering*, **58**, 22–26, (2013). http://dx.doi.org/10.1016/j.oceaneng.2012.09.008

[10] Zhang, Y. L., Daniel, G. G., and Jason, M. R. Vibration of prestressed thin cylindrical shells conveying fluid, *Thin-Walled Structures*, **41**, 1103–1127, (2003). http://dx.doi.org/10.1016/s0263-8231(03)00108-3

[11] Zhang, Y. L., Reese, J. M., and Gorman, D. G. Finite element analysis of the vibratory characteristics of cylindrical shells conveying fluid, *Computer methods in applied mechanics and engineering*, **191**, 5207–5231, (2002). http://dx.doi.org/10.1016/s0045-7825(02)00456-5

[12] Bakhtiari-Nejad, F. and Bideleh, S. M. M. Nonlinear free vibration analysis of prestressed circular cylindrical shells on the Winkler/Pasternak foundation, *Thin-Walled Structures*, **53**, 26–39, (2012). http://dx.doi.org/10.1016/j.tws.2011.12.015

[13] Amabili, M. A. comparison of shell theories for large-amplitude vibrations of circular cylindrical shells: Lagrangian approach, *Journal of Sound and Vibration*, **264**, 1091–1125, (2003). http://dx.doi.org/10.1016/s0022-460x(02)01385-8

[14] Zhou, X. P. Vibration and stability of ring-stiffened thin-walled cylindrical shells conveying fluid, *Acta Mechanica Solida Sinica*, **25**, 168–176, (2012). http://dx.doi.org/10.1016/s0894-9166(12)60017-2

[15] Belyankova, T. I. and Kalinchuk, V. V. The dynamic contact problem for a prestressed cylindrical tube filled with a fluid, *Journal of Applied Mathematics and Mechanics*, **73**, 209–219, (2009). http://dx.doi.org/10.1016/j.jappmathmech.2009.04.011

[16] Hu, X. J. and Redekop, D. Prestressed vibration analysis of a cylindrical shell with an oblique end, *Journal of Sound and Vibration*, **277**, 429–435, (2004). http://dx.doi.org/10.1016/j.jsv.2003.11.051

Nonlinear Vibrations and Chaos in Rectangular Functionally Graded Plates with Thermo-mechanical Coupling

Seyedeh Elnaz Naghibi

School of Engineering and Materials Science, Queen Mary, University of London, London, UK

Mojtaba Mahzoon

School of Mechanical Engineering, Shiraz University, Shiraz, Iran

(Received 19 August 2014; accepted 19 April 2016)

We analyze the nonlinear dynamics of a simply supported, rectangular, and functionally graded plate in terms of a newly derived coupled system of thermo-elasticity and energy equations, which is then expanded here in derivations and explored for chaotic responses through a parameter study in the state space.[1] The plate properties vary linearly in thickness. Three-dimensional stress-strain relations are considered in general case and nonlinear strain-displacement relations are deployed to account for the plate's large deflection. A lateral harmonic force is applied on the plate, and there is a heat generation source within it and the surfaces are exposed to free convection. By integrating over the thickness, four new thermal parameters are introduced, which together with the mid-plane displacements constitute a system of seven partial differential equations. These equations are changed into ordinary differential equations in time using Galerkin's approximation and solved by using the 4th order Runge-Kutta method. Finally, a parameter study is performed and the appropriate conditions resulting in chaotic solutions are determined by using numerical features such as the Lyapunov exponent and power spectrum.

NOMENCLATURE

$\overline{u}, \overline{v}, \overline{w}$	Particles displacements in x, y, z directions
u, v, w	Midplane displacements in x, y, z directions
A, B, C	Dimensionless amplitudes of u, v, w
V	Dimensionless amplitude of $\dot{w}$
ε_{ij}	Strain components
σ_{ij}	Stress components
θ	Point-wise plate temperature
θ_0	Initial plate temperature
T	Dimensionless amplitude of θ
$N_\theta, M_\theta, P_\theta, Q_\theta$	Temperature 0th to 3th moments
D, E, F, G	Dimensionless amplitudes of N, M, P, and Q
E	Modulus of elasticity
ν	Poisson's ratio
α	Thermal expansion coefficient
ρ	Density
k	Thermal diffusivity
c	Specific heat capacity
r	Heat generation rate per unit mass
λ	Plate side length to thickness ratio
h	Plate thickness
a, b	Plate side lengths in x and y directions
ω	Frequency of the external force
H	Heat transfer coefficient
q_0	Amplitude of the external force

1. INTRODUCTION

Functionally graded materials (FGMs) are widely used in aeronautic structures, where they are simultaneously subjected to mechanical and thermal loadings. Thus, presenting a model that combines the mechanical and thermal characteristics increase our understanding of their behavior. In this paper, the coupled problem of thermo-elasticity for the nonlinear dynamics of FGM plates was studied, the governing equations were derived, and after achieving the solution, some parameter values for which trajectories show chaotic behavior were determined.

In the field of linear thermo-elasticity Nowacki has made several fundamental contributions, among which was the derivation of the equations of thermo-elastic vibrations of plates in the coupled case.[2] He solved the problem of transverse vibrations when the temperature field varied harmonically with time. Kawamura et al. derived the governing equations for thermally induced vibrations of an FGM plate exposed to sinusoidally varying surface temperature.[3] Xiang and Melnik presented a numerical approach for the general thermo-mechanical problems, which was based on the reduction of the original system of partial differential equations to a system of differential algebraic equations.[4] They tested the method for a two-dimensional, thermo-elasticity problem. Yang and Shen performed an analysis on free and forced vibrations of initially stressed FGM plates with temperature dependent material properties.[5] They also studied partially distributed impulsive loads on FGM plates resting on elastic foundations.[6] Gupta investigated non-linear thickness variation on the thermally-induced vibration of a rectangular plate using a spline technique.[7]

A number of papers have been dedicated to the nonlinear free vibrations of plates. Prabhakara and Chia calculated nonlinear frequencies for free flexural large amplitude vibrations of orthotropic rectangular plates with different boundary conditions and showed that for large values of amplitude, the coupling effect of vibrating modes on the nonlinear frequency of the fundamental mode is significant for orthotropic plates.[8] Allahverdizadeh et al. analyzed free and forced axisymmetric vibrations of a thin circular FGM plate in a thermal environment and determined the stresses and nonlinear natural frequencies using a semi-analytical approach.[9,10] Chang and Chian presented an analytical study on free vibrations of a heated orthotropic rectangular thin plate under various boundary conditions.[11] Xuefeng et al. studied nonlinear thermo-elastic free vibrations of circular plates that had simply supported and clamped boundary conditions.[12,13]

Furthermore, Praveen and Reddy analyzed the static and dynamic response of FGM plates using a plate finite element that accounts for the transverse shear strains, rotary inertia, and moderately large rotations in von Karman sense.[14] Huang and Shen investigated nonlinear vibrations of an FGM plate in thermal environments, accounting for heat conduction and temperature dependent material.[15] Woo and Meguid provided an analytical solution for the coupled large deflection of plates and shallow shells made of functionally graded material. They made use of two-dimensional stress-strain relations and studied the effect of thermo-mechanical coupling on the FGM shell response.[16] In another survey, Woo et al. discussed the effect of material properties, boundary conditions, and thermal loading on nonlinear dynamics of a freely vibrating FGM plate.[17] Chang and Wan presented an analytical method to investigate large amplitude thermo-mechanically coupled vibrations of rectangular elastic thin plates with various boundary conditions.[18] Hao et al. studied the nonlinear dynamics of a simply supported rectangular FGM plate subjected to transverse and in-plane excitations in a time dependent thermal environment.[19] Yeh analyzed large amplitude thermo-mechanically coupled vibrations of simply supported orthotropic rectangular thin plates.[20] He discussed the effect of changing different parameters on thermal damping of the plate. Alijani and Amabili investigated non-linear parametric instability of rectangular FGM plates in thermal environments using a multi-degree-of-freedom energy approach.[21]

Among works done on the chaotic vibrations of plates, we can mention the derivation of the nonlinear dynamic equation of a harmonically forced elliptic plate in the presence of a thermal field by Qiang et al.[22] They used the Melnikov function method to give the critical condition for chaotic motion and to discuss the path to chaos. Ribeiro performed an analysis on geometrically nonlinear vibrations of linear elastic and isotropic plates under the combined effect of thermal fields and mechanical excitations and studied transitions from periodic to non-periodic motions.[23] Both him and Duarte also investigated the effect of fibers' angle in nonlinear thermo-elastic vibrations of composite laminated plates.[24] Lai et al. determined the conditions leading to chaotic motion for large deflections of a simply supported rectangular plate by examining the fractal dimension and the maximum the Lyapunov exponent.[25] They used the same approach to detect chaos in large deflections of rectangular plates with thermo-mechanical coupling.[26] In another investigation, Yeh and Chen found the conditions that resulted in chaos for a simply supported circular plate of thermo-mechanical coupling with variable thickness.[27] Zhang et al. analyzed the nonlinear dynamics and chaos of a simply supported rectangular orthotropic FGM plate in a thermal environment in which heat conduction and temperature-dependent material properties were taken into account.[28] Hao et al. observed chaos in nonlinear dynamics of a rectangular FGM plate in a thermal environment.[29]

However, none of the referred papers have considered the thermo-mechanical coupling for nonlinear forced vibrations of functionally graded plates. The novelty of this paper is the full derivation of the governing equations in the three-dimensional case while accounting for geometrical nonlinearity, non-homogeneity, coupled fields of temperature, and displacement in the extension of our preliminary research, which only includes the general framework for this purpose.[1] Additionally, we have performed a parameter study in the state space to find the parameter values that trigger chaotic solutions. In the following sections, the equations of motion and energy equation are first derived for a nonlinear thermo-elastic FGM plate and then a solution strategy is proposed for solving them. Section three is devoted to a parameter study and discusses the behavior of the resulting responses, with a focus on detecting chaos. Finally, the conclusions are drawn in the last section.

2. METHOD

The first aim of this paper is to derive the equations of motion and the energy equation considering thermo-mechanical coupling for a rectangular plate made of functionally graded material. Equations of motion were derived on the basis of displacement formulation.[30] Lagrangian finite strain tensor is defined as:[31]

$$\varepsilon_{ij} = \frac{1}{2}\left(\frac{\partial u_i}{\partial x_j} + \frac{\partial u_j}{\partial x_i}\right) + \frac{1}{2}\frac{\partial u_m}{\partial x_i}\frac{\partial u_m}{\partial x_j}. \tag{1}$$

Based on Kirchhoff hypothesis, the displacements of various points in the plate thickness are linearly related to those of the mid-plane as:[32]

$$\begin{aligned}\vec{u}(x,y,z,t) &= u(x,y,t) - z\frac{\partial w}{\partial x};\\ \vec{v}(x,y,z,t) &= v(x,y,t) - z\frac{\partial w}{\partial y};\\ \vec{w}(x,y,z,t) &= w(x,y,t).\end{aligned} \tag{2}$$

Substituting Eq. (2) in Eq. (1), strain components in terms of mid-plane displacements were found.[33] Additionally, generalized thermo-elastic constitutive law for isotropic material was given by:[30]

$$\sigma_{ij} = \lambda\varepsilon_{kk}\delta_{ij} + 2\mu\varepsilon_{ij} - (3\lambda + 2\mu)\alpha(\theta - \theta_0); \tag{3}$$

where,

$$\lambda = \frac{E\nu}{(1+\nu)(1-2\nu)}; \tag{4}$$

$$\mu = \frac{E}{2(1+\nu)}. \tag{5}$$

By using Eq. (3), stress tensor components were found in terms of mid-plane displacements as:

$$\sigma_{xx} = \frac{E\nu}{(1+\nu)(1-2\nu)}\left[\frac{\partial u}{\partial x} + \frac{\partial v}{\partial y} + \left(\frac{\partial w}{\partial x}\right)^2 + \left(\frac{\partial w}{\partial y}\right)^2 - z\frac{\partial^2 w}{\partial x^2} - z\frac{\partial^2 w}{\partial y^2}\right] + \frac{E}{(1+\nu)}\left[\frac{\partial u}{\partial x} + \frac{1}{2}\left(\frac{\partial w}{\partial x}\right)^2 - z\frac{\partial^2 w}{\partial x^2}\right] - \frac{E\alpha}{(1-2\nu)}(\theta-\theta_0); \quad (6)$$

$$\sigma_{yy} = \frac{E\nu}{(1+\nu)(1-2\nu)}\left[\frac{\partial u}{\partial x} + \frac{\partial v}{\partial y} + \left(\frac{\partial w}{\partial x}\right)^2 + \left(\frac{\partial w}{\partial y}\right)^2 - z\frac{\partial^2 w}{\partial x^2} - z\frac{\partial^2 w}{\partial y^2}\right] + \frac{E}{(1+\nu)}\left[\frac{\partial v}{\partial y} + \frac{1}{2}\left(\frac{\partial w}{\partial y}\right)^2 - z\frac{\partial^2 w}{\partial y^2}\right] - \frac{E\alpha}{(1-2\nu)}(\theta-\theta_0); \quad (7)$$

$$\sigma_{zz} = \frac{E\nu}{(1+\nu)(1-2\nu)}\left[\frac{\partial u}{\partial x} + \frac{\partial v}{\partial y} + \left(\frac{\partial w}{\partial x}\right)^2 + \left(\frac{\partial w}{\partial y}\right)^2 - z\frac{\partial^2 w}{\partial x^2} - z\frac{\partial^2 w}{\partial y^2}\right] + \frac{E}{(1+\nu)}\left[\frac{1}{2}\left(\frac{\partial w}{\partial x}\right)^2 + \frac{1}{2}\left(\frac{\partial w}{\partial y}\right)^2\right] - \frac{E\alpha}{(1-2\nu)}(\theta-\theta_0); \quad (8)$$

$$\sigma_{xy} = \frac{E}{(1+\nu)}\left[\frac{1}{2}\left(\frac{\partial u}{\partial y} + \frac{\partial v}{\partial x} + \frac{\partial w}{\partial x}\frac{\partial w}{\partial y}\right) - z\frac{\partial^2 w}{\partial x \partial y}\right]; \quad (9)$$

$$\sigma_{xz} = \frac{E}{(1+\nu)}\left[\frac{1}{2}z\frac{\partial^2 w}{\partial x^2}\frac{\partial w}{\partial x} + \frac{1}{2}z\frac{\partial^2 w}{\partial x \partial y}\frac{\partial w}{\partial y} - \frac{1}{2}\frac{\partial u}{\partial x}\frac{\partial w}{\partial x} - \frac{1}{2}\frac{\partial v}{\partial x}\frac{\partial w}{\partial y}\right]; \quad (10)$$

$$\sigma_{yz} = \frac{E}{(1+\nu)}\left[\frac{1}{2}z\frac{\partial^2 w}{\partial y^2}\frac{\partial w}{\partial y} + \frac{1}{2}z\frac{\partial^2 w}{\partial x \partial y}\frac{\partial w}{\partial x} - \frac{1}{2}\frac{\partial u}{\partial y}\frac{\partial w}{\partial x} - \frac{1}{2}\frac{\partial v}{\partial y}\frac{\partial w}{\partial y}\right]; \quad (11)$$

It was assumed that the volume fractions, x_A and x_B, and consequently all extensive properties, varied linearly in thickness. Thus, a plate typical property P was expressed as:

$$P = x_A P_A + x_B P_B = \frac{P_A + P_B}{2} + \frac{z(P_B - P_A)}{h} = P_{\text{avg}} + \frac{z}{h}\Delta P; \quad (12)$$

where A and B are the two types of material used at the lower and upper surfaces respectively.

The equations of motion in the absence of body forces had the form:

$$\sigma_{ij,j} = \rho\ddot{\overline{u}}_i. \quad (13)$$

In order to reduce spatial dimensions of Eq. (13), we integrated both sides of each equation over the thickness. In this way, we let the property variations emerge in the equations of motion. This integration yielded:

$$\frac{\partial N_{xx}}{\partial x} + \frac{\partial N_{xy}}{\partial y} + \sigma_{xz}|_{-h/2}^{h/2} = \rho_{\text{avg}} h\frac{\partial^2 u}{\partial t^2} - \frac{h^2\Delta\rho}{12}\frac{\partial^3 w}{\partial x \partial t^2}; \quad (14)$$

$$\frac{\partial N_{xy}}{\partial x} + \frac{\partial N_{yy}}{\partial y} + \sigma_{yz}|_{-h/2}^{h/2} = \rho_{\text{avg}} h\frac{\partial^2 v}{\partial t^2} - \frac{h^2\Delta\rho}{12}\frac{\partial^3 w}{\partial y \partial t^2}; \quad (15)$$

$$\frac{\partial Q_x}{\partial x} + \frac{\partial Q_y}{\partial y} + \sigma_{zz}|_{-h/2}^{h/2} = \rho_{\text{avg}} h\frac{\partial^2 w}{\partial t^2}; \quad (16)$$

where,

$$N_{xx} = \int_{-h/2}^{h/2}\sigma_{xx}\,dz; \qquad N_{yy} = \int_{-h/2}^{h/2}\sigma_{yy}\,dz;$$
$$N_{xy} = \int_{-h/2}^{h/2}\sigma_{xy}\,dz; \qquad Q_x = \int_{-h/2}^{h/2}\sigma_{xz}\,dz;$$
$$Q_y = \int_{-h/2}^{h/2}\sigma_{yz}\,dz; \qquad \sigma_{zz}|_{-h/2}^{h/2} = q_0\sin(\omega t); \quad (17)$$

and $\sigma_{xz}|_{-h/2}^{h/2}$ and $\sigma_{yz}|_{-h/2}^{h/2}$ can be found from Eqs. (10) and (11). N_{xx}, N_{yy}, and N_{xy} were obtained by directly integrating Eqs. (6), (7), and (9). Thus, the equations of motion in the x and y directions were given by:

$$\frac{E_{\text{avg}}h(1-\nu)}{(1+\nu)(1-2\nu)}\frac{\partial^2 u}{\partial x^2} + \frac{E_{\text{avg}}h}{2(1+\nu)(1-2\nu)}\frac{\partial^2 v}{\partial x \partial y} + \frac{E_{\text{avg}}h}{2(1+\nu)}\frac{\partial^2 u}{\partial y^2} + \frac{E_{\text{avg}}h(3-2\nu)}{2(1+\nu)(1-2\nu)}\frac{\partial w}{\partial x}\frac{\partial^2 w}{\partial x^2} + \frac{E_{\text{avg}}h}{(1+\nu)(1-2\nu)}\frac{\partial w}{\partial y}\frac{\partial^2 w}{\partial x \partial y} - \frac{\Delta E h^2(1-\nu)}{12(1+\nu)(1-2\nu)}\cdot\left(\frac{\partial^3 w}{\partial x^3} + \frac{\partial^3 w}{\partial x \partial y^2}\right) + \frac{E_{\text{avg}}h}{2(1+\nu)}\frac{\partial w}{\partial x}\frac{\partial^2 w}{\partial y^2} - \frac{1}{1-2\nu}\left[E_{\text{avg}}\alpha_{\text{avg}}\frac{\partial}{\partial x}\int_{-h/2}^{h/2}(\theta-\theta_0)\,dz + \frac{(E_{\text{avg}}\Delta\alpha + \alpha_{\text{avg}}\Delta E)}{h}\frac{\partial}{\partial x}\int_{-h/2}^{h/2}z(\theta-\theta_0)\,dz + \frac{\Delta E\Delta\alpha}{h^2}\frac{\partial}{\partial x}\int_{-h/2}^{h/2}z^2(\theta-\theta_0)\,dz\right] = \rho_{\text{avg}}h\frac{\partial^2 u}{\partial t^2} - \frac{h^2\Delta\rho}{12}\frac{\partial^3 w}{\partial x \partial t^2}; \quad (18)$$

$$\frac{E_{\text{avg}}h(1-\nu)}{(1+\nu)(1-2\nu)}\frac{\partial^2 v}{\partial y^2} + \frac{E_{\text{avg}}h}{2(1+\nu)(1-2\nu)}\frac{\partial^2 u}{\partial x \partial y} + \frac{E_{\text{avg}}h}{2(1+\nu)}\frac{\partial^2 v}{\partial x^2} + \frac{E_{\text{avg}}h(3-2\nu)}{2(1+\nu)(1-2\nu)}\frac{\partial w}{\partial y}\frac{\partial^2 w}{\partial y^2} + \frac{E_{\text{avg}}h}{(1+\nu)(1-2\nu)}\frac{\partial w}{\partial x}\frac{\partial^2 w}{\partial x \partial y} - \frac{\Delta E h^2(1-\nu)}{12(1+\nu)(1-2\nu)}\cdot\left(\frac{\partial^3 w}{\partial y^3} + \frac{\partial^3 w}{\partial y \partial x^2}\right) + \frac{E_{\text{avg}}h}{2(1+\nu)}\frac{\partial w}{\partial y}\frac{(\partial^2 w}{\partial x^2} - \frac{1}{1-2\nu}\left[E_{\text{avg}}\alpha_{\text{avg}}\frac{\partial}{\partial y}\int_{-h/2}^{h/2}(\theta-\theta_0)\,dz + \frac{(E_{\text{avg}}\Delta\alpha + \alpha_{\text{avg}}\Delta E)}{h}\frac{\partial}{\partial y}\int_{-h/2}^{h/2}z(\theta-\theta_0)\,dz + \frac{\Delta E\Delta\alpha}{h^2}\frac{\partial}{\partial y}\int_{-h/2}^{h/2}z^2(\theta-\theta_0)\,dz\right] = \rho_{\text{avg}}h\frac{\partial^2 v}{\partial t^2} - \frac{h^2\Delta\rho}{12}\frac{\partial^3 w}{\partial y \partial t^2}. \quad (19)$$

However, in order to derive the equation of motion in the z direction, Q_x and Q_y were obtained by multiplying the equations of motion in the x and y direction by z and integrating them over the thickness. This yielded:

$$\frac{\partial M_{xx}}{\partial x}+\frac{\partial M_{xy}}{\partial y}-Q_x+(z\sigma_{xz})|_{-h/2}^{h/2}= -\frac{h^3}{12}\rho_{\text{avg}}\frac{\partial^3 w}{\partial t^2\partial x}+\frac{h^2}{12}\Delta\rho\frac{\partial^2 u}{\partial t^2}; \quad (20)$$

$$\frac{\partial M_{xy}}{\partial x}+\frac{\partial M_{yy}}{\partial y}-Q_y+(z\sigma_{yz})|_{-h/2}^{h/2}= -\frac{h^3}{12}\rho_{\text{avg}}\frac{\partial^3 w}{\partial t^2\partial y}+\frac{h^2}{12}\Delta\rho\frac{\partial^2 u}{\partial t^2}; \quad (21)$$

where,

$$M_{xx}=\int_{-h/2}^{h/2} z\sigma_{xx}\,dz; \qquad M_{yy}=\int_{-h/2}^{h/2} z\sigma_{yy}\,dz;$$
$$M_{xy}=\int_{-h/2}^{h/2} z\sigma_{xy}\,dz; \quad (22)$$

and $(z\sigma_{xz})|_{-h/2}^{h/2}$ and $(z\sigma_{yz})|_{-h/2}^{h/2}$could be calculated from Eqs. (10) and (11). Differentiating Eq. (20) with respect to x and Eq. (21) with respect to y and substituting the resulting $\frac{\partial Q_x}{\partial x}$ and $\frac{\partial Q_y}{\partial y}$ together with the stress components in Eq. (16), resulted in the equation of motion in the z direction, which was expressed as:

$$\frac{h^2\Delta E(1-\nu)}{12(1+\nu)(1-2\nu)}\left[\frac{\partial^3 u}{\partial y^2\partial x}+\frac{\partial^3 v}{\partial x^2\partial y}+\frac{\partial^3 u}{\partial x^3}+\frac{\partial^3 v}{\partial y^3}\right]+ \frac{(2-3\nu)h^2\Delta E}{6(1+\nu)(1-2\nu)}\left[\left(\frac{\partial^2 w}{\partial x^2}\right)^2+\left(\frac{\partial^2 w}{\partial y^2}\right)^2+\frac{\partial w}{\partial x}\frac{\partial^3 w}{\partial x^3}+ \frac{\partial w}{\partial y}\frac{\partial^3 w}{\partial y^3}+\frac{\partial w}{\partial x}\frac{\partial^3 w}{\partial y^2\partial x}+\frac{\partial w}{\partial y}\frac{\partial^3 w}{\partial x^2\partial y}\right]+ \frac{h^2\Delta E(7-10\nu)}{12(1+\nu)(1-2\nu)}\left(\frac{\partial^2 w}{\partial x\partial y}\right)^2+\frac{h^2\Delta E}{12(1+\nu)}\frac{\partial^2 w}{\partial x^2}\frac{\partial^2 w}{\partial y^2}- \frac{E_{\text{avg}}h^3(1-\nu)}{12(1+\nu)(1-2\nu)}\nabla^4 w-\frac{hE_{\text{avg}}}{(1+\nu)}\left(\frac{\partial^2 u}{\partial x^2}\frac{\partial w}{\partial x}+ \frac{\partial u}{\partial x}\frac{\partial^2 w}{\partial x^2}+\frac{\partial^2 v}{\partial x^2}\frac{\partial w}{\partial y}+\frac{\partial v}{\partial x}\frac{\partial^2 w}{\partial x\partial y}+\frac{\partial^2 u}{\partial y^2}\frac{\partial w}{\partial x}+ \frac{\partial u}{\partial y}\frac{\partial^2 w}{\partial x\partial y}+\frac{\partial v}{\partial y}\frac{\partial^2 w}{\partial y^2}+\frac{\partial^2 v}{\partial y^2}\frac{\partial w}{\partial y}\right)+ \frac{h^3}{12}\rho_{\text{avg}}\frac{\partial^4 w}{\partial t^2\partial x^2}-\frac{h^2}{12}\Delta\rho\frac{\partial^3 u}{\partial x\partial t^2}+\frac{h^3}{12}\rho_{\text{avg}}\frac{\partial^4 w}{\partial t^2\partial y^2}- \frac{h^2}{12}\Delta\rho\frac{\partial^3 v}{\partial y\partial t^2}-\frac{1}{1-2\nu}\left[E_{\text{avg}}\alpha_{\text{avg}}\nabla^2\int_{-h/2}^{h/2} z(\theta-\theta_0)\,dz+ \frac{(E_{\text{avg}}\Delta\alpha+\alpha_{\text{avg}}\Delta E)}{h}\nabla^2\int_{-h/2}^{h/2} z^2(\theta-\theta_0)\,dz+ \frac{\Delta E\Delta\alpha}{h^2}\nabla^2\int_{-h/2}^{h/2} z^3(\theta-\theta_0)\,dz\right]+q_0\sin(\omega t)= \rho_{\text{avg}}h\frac{\partial^2 w}{\partial t^2}. \quad (23)$$

As a result of reducing spatial dimensions of the equations of motion, these equations were changed into integro-differential equations. By introducing the four following parameters, the equations could remain in differential form:

$$N_\theta\equiv\int_{-h/2}^{h/2}(\theta-\theta_0)\,dz; \qquad M_\theta\equiv\int_{-h/2}^{h/2} z(\theta-\theta_0)\,dz;$$
$$P_\theta\equiv\int_{-h/2}^{h/2} z^2(\theta-\theta_0)\,dz; \quad Q_\theta\equiv\int_{-h/2}^{h/2} z^3(\theta-\theta_0)\,dz. \quad (24)$$

To specify these four parameters together with displacement components in the x, y, and z directions, seven independent equations were needed. So far, three equations were derived, and the other four were deduced from the energy equation.

The energy equation for a thermo-elastic continuous media experiencing small temperature changed in the presence of heat generation:[34]

$$\rho r+\nabla(k\nabla\theta)-\rho c\dot{\theta}-\beta\theta_o\dot{\varepsilon}_{mm}=0; \quad (25)$$

where,

$$\beta=3k\alpha=\frac{E\alpha}{(1-2\nu)}. \quad (26)$$

Equation (25) was also integrated over the thickness and solved together with thermo-elasticity equations. However, since we introduced four new thermal variables in Eq. (24), and because we were interested in their dynamics, we still needed three other equations for the closure of the problem. Thus, in addition to mere integration, we multiplied Eq. (25) by z, z^2, and z^3 and integrated over the thickness. As a result, by using Eqs. (1), (12), (24), and (25) and finite integration rules, the four following equations were added to the equations of motion:

$$\rho_{\text{avg}}hr+k_{\text{avg}}\nabla^2 N_\theta+\frac{\Delta k}{h}\nabla^2 M_\theta+k_{\text{avg}}\frac{\partial\theta}{\partial z}\Big|_{-h/2}^{h/2}+ \frac{\Delta k}{h}z\frac{\partial\theta}{\partial z}\Big|_{-h/2}^{h/2}-\rho_{\text{avg}}c_{\text{avg}}\frac{\partial N_\theta}{\partial t}-\frac{(\rho_{\text{avg}}\Delta c+c_{\text{avg}}\Delta\rho)}{h}\frac{\partial M_\theta}{\partial t}- \frac{\Delta c\Delta\rho}{h^2}\frac{\partial P_\theta}{\partial t}-\frac{\theta_0 h}{(1-2\nu)}\left(E_{\text{avg}}\alpha_{\text{avg}}+\frac{\Delta E\delta\alpha}{12}\right)\cdot \left(\frac{\partial^2 u}{\partial t\partial x}+\frac{\partial^2 v}{\partial t\partial y}+2\frac{\partial w}{\partial x}\frac{\partial^2 w}{\partial t\partial x}+2\frac{\partial w}{\partial y}\frac{\partial^2 w}{\partial t\partial y}\right)+ \frac{\theta_0 h^2}{12(1-2\nu)}(E_{\text{avg}}\Delta\alpha+\alpha_{\text{avg}}\Delta E)\left(\frac{\partial^3 w}{\partial t\partial x^2}+\frac{\partial^3 w}{\partial t\partial y^2}\right)=0; \quad (27)$$

$$\frac{h^2\Delta\rho r}{12}+k_{\text{avg}}\nabla^2 M_\theta+\frac{\Delta k}{h}\nabla^2 P_\theta+k_{\text{avg}}z\frac{\partial\theta}{\partial z}\Big|_{-h/2}^{h/2}- k_{\text{avg}}\theta|_{-h/2}^{h/2}+\frac{\Delta k}{h}\left(z^2\frac{\partial\theta}{\partial z}\Big|_{-h/2}^{h/2}-z\theta|_{-h/2}^{h/2}+h\theta_0+N_\theta\right)- \rho_{\text{avg}}c_{\text{avg}}\frac{\partial M_\theta}{\partial t}-\frac{(\rho_{\text{avg}}\Delta c+c_{\text{avg}}\Delta\rho)}{h}\frac{\partial P_\theta}{\partial t}-\frac{\Delta c\Delta\rho}{h^2}\frac{\partial Q_\theta}{\partial t}- \frac{\theta_0 h^2}{12(1-2\nu)}(E_{\text{avg}}\Delta\alpha+\alpha_{\text{avg}}\Delta E)\cdot \left(\frac{\partial^2 u}{\partial t\partial x}+\frac{\partial^2 v}{\partial t\partial y}+2\frac{\partial w}{\partial x}\frac{\partial^2 w}{\partial t\partial x}+2\frac{\partial w}{\partial y}\frac{\partial^2 w}{\partial t\partial y}\right)+ \frac{\theta_0 h^3}{(1-2\nu)}\left(\frac{E_{\text{avg}}\alpha_{\text{avg}}}{12}+\frac{\Delta E\Delta\alpha}{80}\right)\left(\frac{\partial^3 w}{\partial t\partial x^2}+\frac{\partial^3 w}{\partial t\partial y^2}\right)=0; \quad (28)$$

$$\frac{h^3\rho_{\text{avg}}r}{12}+k_{\text{avg}}\nabla^2P_\theta+\frac{\Delta k}{h}\nabla^2Q_\theta+ k_{\text{avg}}\left(z^2\frac{\partial\theta}{\partial z}\Big|_{-h/2}^{h/2}-2z\theta|_{-h/2}^{h/2}+2h\theta_0+2N_\theta\right)+ \frac{\Delta k}{h}\left(z^3\frac{\partial\theta}{\partial z}\Big|_{-h/2}^{h/2}-2z^2\theta|_{-h/2}^{h/2}+4M_\theta\right)-\rho_{\text{avg}}c_{\text{avg}}\frac{\partial P_\theta}{\partial t}- \frac{(\rho_{\text{avg}}\Delta c+c_{\text{avg}}\Delta\rho)}{h}\frac{\partial Q_\theta}{\partial t}-\frac{\Delta c\Delta\rho}{h^2}\frac{\partial}{\partial t}\int_{-h/2}^{h/2}z^4\theta\,dz- \frac{\theta_0h^3}{(1-2\nu)}\left(\frac{E_{\text{avg}}\alpha_{\text{avg}}}{12}+\frac{\Delta E\Delta\alpha}{80}\right)\cdot \left(\frac{\partial^2u}{\partial t\partial x}+\frac{\partial^2v}{\partial t\partial y}+2\frac{\partial w}{\partial x}\frac{\partial^2w}{\partial t\partial x}+2\frac{\partial w}{\partial y}\frac{\partial^2w}{\partial t\partial y}\right)+ \frac{\theta_0h^4}{80(1-2\nu)}(E_{\text{avg}}\Delta\alpha+\alpha_{\text{avg}}\Delta E)\left(\frac{\partial^3w}{\partial t\partial x^2}+\frac{\partial^3w}{\partial t\partial y^2}\right)=0; \tag{29}$$

$$\frac{h^4\Delta\rho r}{80}+k_{\text{avg}}\nabla^2Q_\theta+\frac{\Delta k}{h}\nabla^2\int_{-h/2}^{h/2}z^4\theta\,dz+ k_{\text{avg}}\left(z^3\frac{\partial\theta}{\partial z}\Big|_{-h/2}^{h/2}-3z^2\theta|_{-h/2}^{h/2}+6M_\theta\right)+ \frac{\Delta k}{h}\left(z^4\frac{\partial\theta}{\partial z}\Big|_{-h/2}^{h/2}-3z^3\theta|_{-h/2}^{h/2}+9P_\theta+\frac{3}{4}h^3\theta_0\right)- \rho_{\text{avg}}c_{\text{avg}}\frac{\partial Q_\theta}{\partial t}-\frac{(\rho_{\text{avg}}\Delta c+c_{\text{avg}}\Delta\rho)}{h}\int_{-h/2}^{h/2}z^4\theta\,dz- \frac{\Delta c\Delta\rho}{h^2}\frac{\partial}{\partial t}\int_{-h/2}^{h/2}z^5\theta\,dz-\frac{\theta_0h^4}{80(1-2\nu)}(E_{\text{avg}}\Delta\alpha+\alpha_{\text{avg}}\Delta E)\cdot \left(\frac{\partial^2u}{\partial t\partial x}+\frac{\partial^2v}{\partial t\partial y}+2\frac{\partial w}{\partial x}\frac{\partial^2w}{\partial t\partial x}+2\frac{\partial w}{\partial y}\frac{\partial^2w}{\partial t\partial y}\right)+ \frac{\theta_0h^5}{(1-2\nu)}\left(\frac{E_{\text{avg}}\alpha_{\text{avg}}}{80}+\frac{\Delta E\Delta\alpha}{448}\right)\left(\frac{\partial^3w}{\partial t\partial x^2}+\frac{\partial^3w}{\partial t\partial y^2}\right)=0; \tag{30}$$

where,

$$\nabla^2\equiv\frac{\partial^2}{\partial x^2}+\frac{\partial^2}{\partial y^2}. \tag{31}$$

On the basis of Galerkin's single term approximation, the dependent variables' functionality of the independent variables x, y, z, and t was assumed as:

$$\begin{aligned}
u(x,y,t)&=A(t)\sin\left(\frac{2m\pi x}{a}\right)\sin\left(\frac{2n\pi y}{b}\right);\\
v(x,y,t)&=B(t)\sin\left(\frac{2m\pi x}{a}\right)\sin\left(\frac{2n\pi y}{b}\right);\\
w(x,y,t)&=C(t)\sin\left(\frac{2m\pi x}{a}\right)\sin\left(\frac{2n\pi y}{b}\right);\\
N_\theta(x,y,t)&=h\theta_0D(t)\sin\left(\frac{m\pi x}{a}\right)\sin\left(\frac{n\pi y}{b}\right);\\
M_\theta(x,y,t)&=h^2\theta_0E(t)\sin\left(\frac{m\pi x}{a}\right)\sin\left(\frac{n\pi y}{b}\right);\\
P_\theta(x,y,t)&=h^3\theta_0F(t)\sin\left(\frac{m\pi x}{a}\right)\sin\left(\frac{n\pi y}{b}\right);\\
Q_\theta(x,y,t)&=h^4\theta_0G(t)\sin\left(\frac{m\pi x}{a}\right)\sin\left(\frac{n\pi y}{b}\right);\\
\theta(x,y,z,t)-\theta_0&=(\theta_\infty-\theta_0)T(z,t)\sin\left(\frac{m\pi x}{a}\right)\sin\left(\frac{n\pi y}{b}\right).
\end{aligned} \tag{32}$$

It should be noted that the assumed functions satisfied the problem's boundary conditions, which were simply supported conditions for the displacement components and constant temperature edges for the energy equation:

$$u=v=w=\frac{\partial^2w}{\partial x^2}=0\quad\&\quad\theta=\theta_0\quad\text{at}\quad x=0,a; \tag{33}$$

$$u=v=w=\frac{\partial^2w}{\partial y^2}=0\quad\&\quad\theta=\theta_0\quad\text{at}\quad y=0,b. \tag{34}$$

After substituting the above functions in the governing equations, Eqs. (18) and (19) were weighted by $\sin\left(\frac{2m\pi x}{a}\right)\sin\left(\frac{2n\pi y}{b}\right)$ and Eqs. (23), (27), (28), (29), and (30) by $\sin\left(\frac{m\pi x}{a}\right)\sin\left(\frac{n\pi y}{b}\right)$. Subsequently, the resulting equations were integrated over the plate's surface and a system of seven ordinary differential equations was achieved. These equations were rendered dimensionless by introducing the following parameters:

$$\begin{aligned}
&x=x^*a;\quad y=y^*b;\quad z=z^*h;\quad t=\frac{2\pi t^*}{\omega};\\
&\lambda=\frac{a}{h};\quad u=u^*u_0;\quad v=v_0v^*;\quad w=w^*w_0;\\
&\theta-\theta_0=(\theta_\infty-\theta_0)\theta^*=\Delta\theta_0\theta^*;\quad N_\theta=h\theta_0N_\theta^*;\\
&M_\theta=h^2\theta_0M_\theta^*;\quad P_\theta=h^3\theta_0P_\theta^*;\quad Q_\theta=h^4\theta_0Q_\theta^*;\\
&E_{\text{avg}}=E_BE_{\text{avg}}^*;\quad \alpha_{\text{avg}}=\alpha_B\alpha_{\text{avg}}^*;\quad c_{\text{avg}}=c_Ac_{\text{avg}}^*;\\
&k_{\text{avg}}=k_Bk_{\text{avg}}^*;\quad \rho_{\text{avg}}=\rho_B\rho_{\text{avg}}^*;\\
&\Delta E=E_B\Delta E^*;\quad \Delta\alpha=\alpha_B\Delta\alpha^*;\quad \Delta c=c_A\Delta c^*;\\
&\Delta k=k_B\Delta k^*;\quad \Delta\rho=\rho_B\Delta\rho^*.
\end{aligned} \tag{35}$$

Each material property was non-dimensionalied, with its maximum value belonging to either material type. Material A was considered to be Aremco Macor machinable glass ceramic and material B was considered to be AISI 1010 steel. The values of the properties are given in Table 1 for both material types.[35]

By letting $m=n=1$ and $a=b$, the governing equations for a square plate using a single term Galerkin's approximation was eventually derived as:

$$\frac{\omega^2\rho_{\text{avg}}^*\rho_Ba^2(1+\nu)(1-2\nu)}{16\pi^2E_B}\ddot{A}(t^*)+ \frac{E_{\text{avg}}^*(3-4\nu)\pi^2}{2}A(t^*)=0; \tag{36}$$

$$\frac{\omega^2\rho_{\text{avg}}^*\rho_Ba^2(1+\nu)(1-2\nu)}{16\pi^2E_B}\ddot{B}(t^*)+ \frac{E_{\text{avg}}^*(3-4\nu)\pi^2}{2}B(t^*)=0; \tag{37}$$

$$\frac{(11-18\nu)\Delta E^*\pi^2}{27a}C^2(t^*)-\frac{(1-\nu)E_{\text{avg}}^*\pi^4}{12\lambda}C(t^*)+ \frac{a(1+\nu)\Delta\theta_0\alpha_B\pi^2}{2}\Big[E_{\text{avg}}^*\alpha_{\text{avg}}^*E(t^*)+ \left(E_{\text{avg}}^*\Delta\alpha^*+\alpha_{\text{avg}}^*\Delta E^*\right)F(t^*)+\Delta E^*\Delta\alpha^*G(t^*)\Big]+ \frac{q_0a\lambda^2(1+\nu)(1-2\nu)}{E_B}\sin(2\pi t^*)= \frac{\lambda\omega^2\rho_{\text{avg}}^*\rho_Ba^2(1+\nu)(1-2\nu)}{16\pi^2E_B}\ddot{C}(t^*); \tag{38}$$

Table 1. Material Properties, A (Aremco Macor machinable glass ceramic), B (AISI 1010 steel).

	E (Pa)	α (1/°C)	c (J/kg°C)	k (W/mK)	ρ (kg/m^3)
A	66.9×10^9	7.4×10^{-6}	790	1.464	2520
B	205×10^9	12.2×10^{-6}	448	49.8	7870

$$\frac{4\rho_B\rho^*_{\text{avg}}ra^2}{\pi^2\Delta\theta_0k_B}+\frac{1}{4}\Bigg\{-2\pi^2k^*_{\text{avg}}D(t)-2\pi^2\Delta k^*E(t)+k^*_{\text{avg}}\lambda^2\frac{\partial T}{\partial z^*}\Big|^{1/2}_{-1/2}+\Delta k^*\lambda^2z^*\frac{\partial T}{\partial z^*}\Big|^{1/2}_{-1/2}-\frac{\rho_Bc_A\omega a^2}{2\pi k_B}\Big[\rho^*_{\text{avg}}c^*_{\text{avg}}\dot D(t)+\left(\rho^*_{\text{avg}}\Delta c^*+c^*_{\text{avg}}\Delta\rho^*\right)\dot E(t)+\Delta c^*\Delta\rho^*\dot F(t)\Big]\Bigg\}-\frac{16E_B\alpha_B\omega}{9\pi(1-2\nu)k_B}\frac{\theta_0}{\Delta\theta_0}\left(E^*_{\text{avg}}\alpha^*_{\text{avg}}+\frac{\Delta E^*\Delta\alpha^*}{12}\right)C(t)\dot C(t)-\frac{\pi aE_B\alpha_B\omega}{4(1-2\nu)k_B}\frac{1}{12\lambda}\frac{\theta_0}{\Delta\theta_0}\left(E^*_{\text{avg}}\Delta\alpha^*+\alpha^*_{\text{avg}}\Delta E^*\right)\dot C(t)=0; \tag{39}$$

$$\frac{\rho_B\Delta\rho^*ra^2}{3\pi^2\Delta\theta_0k_B}+\frac{1}{4}\Bigg\{-2\pi^2k^*_{\text{avg}}E(t)-2\pi^2\Delta k^*F(t)+k^*_{\text{avg}}\lambda^2z^*\frac{\partial T}{\partial z^*}\Big|^{1/2}_{-1/2}-k^*_{\text{avg}}\lambda^2T|^{1/2}_{-1/2}+\Delta k^*\lambda^2\left(z^{*2}\frac{\partial T}{\partial z^*}\Big|^{1/2}_{-1/2}-z^*T|^{1/2}_{-1/2}+D(t)\right)-\frac{\rho_Bc_A\omega a^2}{2\pi k_B}\Big[\rho^*_{\text{avg}}c^*_{\text{avg}}\dot E(t)+\left(\rho^*_{\text{avg}}\Delta c^*+c^*_{\text{avg}}\Delta\rho^*\right)\dot F(t)+\Delta c^*\Delta\rho^*\dot G(t)\Big]\Bigg\}-\frac{4E_B\alpha_B\omega}{27\pi(1-2\nu)k_B}\frac{\theta_0}{\Delta\theta_0}\left(E^*_{\text{avg}}\Delta\alpha^*+\alpha^*_{\text{avg}}\Delta E^*\right)C(t)\dot C(t)-\frac{\pi aE_B\alpha_B\omega}{4(1-2\nu)k_B}\frac{1}{\lambda}\frac{\theta_0}{\Delta\theta_0}\left(\frac{E^*_{\text{avg}}\alpha^*_{\text{avg}}}{12}+\frac{\Delta E^*\Delta\alpha^*}{80}\right)\dot C(t)=0; \tag{40}$$

$$\frac{\rho_B\rho^*_{\text{avg}}ra^2}{3\pi^2\Delta\theta_0k_B}+\frac{1}{4}\Bigg\{-2\pi^2k^*_{\text{avg}}F(t)-2\pi^2\Delta k^*G(t)+k^*_{\text{avg}}\lambda^2\left(z^{*2}\frac{\partial T}{\partial z^*}\Big|^{1/2}_{-1/2}-2z^*T|^{1/2}_{-1/2}+2D(t)\right)+\Delta k^*\lambda^2\left(z^{*3}\frac{\partial T}{\partial z^*}\Big|^{1/2}_{-1/2}-2z^{*2}T|^{1/2}_{-1/2}+4E(t)\right)-\frac{\rho_Bc_A\omega a^2}{2\pi k_B}\Big[\rho^*_{\text{avg}}c^*_{\text{avg}}\dot F(t)+\left(\rho^*_{\text{avg}}\Delta c^*+c^*_{\text{avg}}\Delta\rho^*\right)\dot G(t)+\Delta c^*\Delta\rho^*\frac{\partial}{\partial t^*}\int_{-1/2}^{1/2}z^{*4}T\,dz^*\Big]\Bigg\}-\frac{16E_B\alpha_B\omega}{9\pi(1-2\nu)k_B}\frac{\theta_0}{\Delta\theta_0}\left(\frac{E^*_{\text{avg}}\alpha^*_{\text{avg}}}{12}+\frac{\Delta E^*\Delta\alpha^*}{80}\right)C(t)\dot C(t)-\frac{\pi au_0E_B\alpha_B\omega}{320(1-2\nu)k_B}\frac{1}{\lambda}\frac{\theta_0}{\Delta\theta_0}\left(E^*_{\text{avg}}\Delta\alpha^*+\alpha^*_{\text{avg}}\Delta E^*\right)\dot C(t)=0; \tag{41}$$

$$\frac{\rho_B\Delta\rho^*ra^2}{20\pi^2\Delta\theta_0k_B}+\frac{1}{4}\Bigg\{-2\pi^2k^*_{\text{avg}}G(t)-2\pi^2\Delta k^*\int_{-1/2}^{1/2}z^{*4}T\,dz^*+k^*_{\text{avg}}\lambda^2\left(z^{*3}\frac{\partial T}{\partial z^*}\Big|^{1/2}_{-1/2}-3z^{*2}T|^{1/2}_{-1/2}+6E(t)\right)+\Delta k^*\lambda^2\left(z^{*4}\frac{\partial T}{\partial z^*}\Big|^{1/2}_{-1/2}-3z^{*3}T|^{1/2}_{-1/2}+9F(t)\right)-\frac{\rho_Bc_A\omega a^2}{2\pi k_B}\Big[\rho^*_{\text{avg}}c^*_{\text{avg}}\dot G(t)+\left(\rho^*_{\text{avg}}\Delta c^*+c^*_{\text{avg}}\Delta\rho^*\right)\cdot\frac{\partial}{\partial t^*}\int_{-1/2}^{1/2}z^{*4}T\,dz^*+\Delta c^*\Delta\rho^*\frac{\partial}{\partial t^*}\int_{-1/2}^{1/2}z^{*5}T\,dz^*\Big]\Bigg\}-\frac{E_B\alpha_B\omega}{45\pi(1-2\nu)k_B}\frac{\theta_0}{\Delta\theta_0}\left(E^*_{\text{avg}}\Delta\alpha^*+\alpha^*_{\text{avg}}\Delta E^*\right)C(t)\dot C(t)-\frac{\pi aE_B\alpha_B\omega}{4(1-2\nu)k_B}\frac{1}{\lambda}\frac{\theta_0}{\Delta\theta_0}\left(\frac{E^*_{\text{avg}}\alpha^*_{\text{avg}}}{80}+\frac{\Delta E^*\Delta\alpha^*}{448}\right)\dot C(t)=0. \tag{42}$$

Due to the fact that besides temperature integrals, temperature also appeared in the governing equations. As such, a backstepping approach was devised in the programming process. At each time step, dimensionless temperature T, which was only a function of z^*, was approximated by a fifth order polynomial. The coefficients of this polynomial were determined by the four temperature integrals of the preceding step and convection boundary conditions on lateral surfaces as follows:

$$\begin{aligned}D(t^*)&=\int_{-1/2}^{1/2}T(z^*,t^*)\,dz^*;\\ E(t^*)&=\int_{-1/2}^{1/2}z^*T(z^*,t^*)\,dz^*;\\ F(t^*)&=\int_{-1/2}^{1/2}z^{*2}T(z^*,t^*)\,dz^*;\\ G(t^*)&=\int_{-1/2}^{1/2}z^{*3}T(z^*,t^*)\,dz^*;\end{aligned} \tag{43}$$

$$\begin{aligned}k_B\frac{\partial\theta}{\partial z}\Big|_{h/2}&=H(\theta_\infty-\theta|_{h/2})\\ &=H(\theta_\infty-\theta_0+\theta_0-\theta|_{h/2});\end{aligned} \tag{44}$$

$$\begin{aligned}k_A\frac{\partial\theta}{\partial z}\Big|_{-h/2}&=-H(\theta_\infty-\theta|_{-h/2})=\\ &=-H(\theta_\infty-\theta_0+\theta_0-\theta|_{-h/2}).\end{aligned} \tag{45}$$

Using the temperature distribution assumption in Eq. (32) yields:

$$k_B\frac{\Delta\theta_0}{h}\frac{\partial T}{\partial z^*}\Big|_{1/2}\sin(m\pi x^*)\sin(n\pi y^*)=H\Delta\theta_0-H\Delta\theta_0T|_{1/2}\sin(m\pi x^*)\sin(n\pi y^*); \tag{46}$$

$$k_A\frac{\Delta\theta_0}{h}\frac{\partial T}{\partial z^*}\Big|_{-1/2}\sin(m\pi x^*)\sin(n\pi y^*)=-H\Delta\theta_0+H\Delta\theta_0T|_{-1/2}\sin(m\pi x^*)\sin(n\pi y^*). \tag{47}$$

Due to the fact that the convection boundary conditions were point-wise, we satisfied them weakly by integrating over the surfaces:

$$k_B\frac{\partial T}{\partial z^*}\Big|_{1/2}=\frac{\pi^2}{4}hH-hHT|_{1/2}; \tag{48}$$

$$k_A\frac{\partial T}{\partial z^*}\Big|_{-1/2}=-\frac{\pi^2}{4}hH+hHT|_{-1/2}. \tag{49}$$

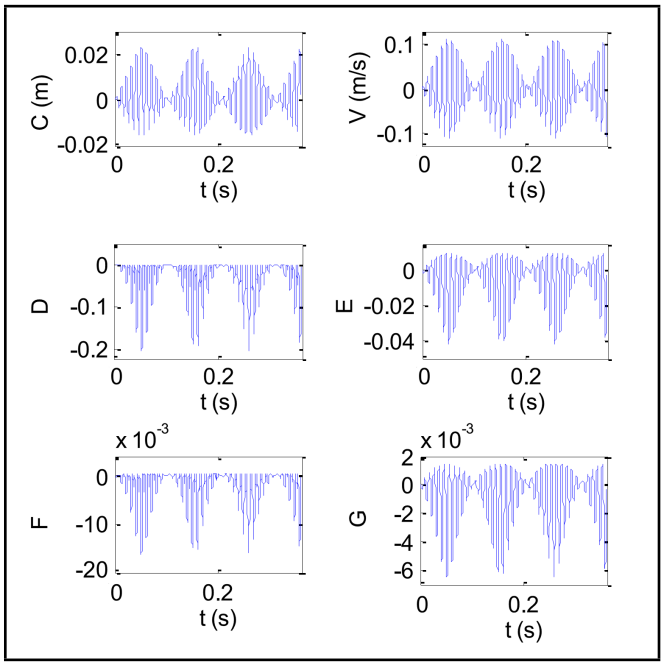

Figure 1. State variables for the base state (Lyapunov exponent = 0.2249).

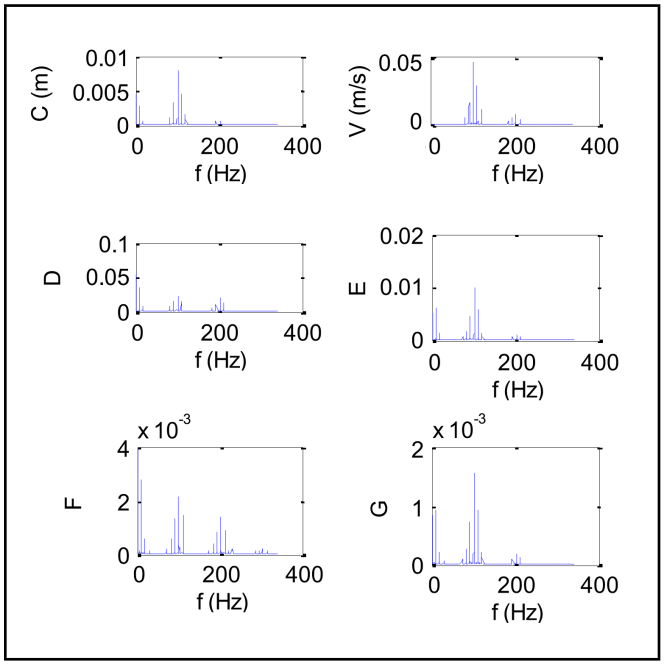

Figure 2. FFT of state variables for the base state (Lyapunov exponent = 0.2249).

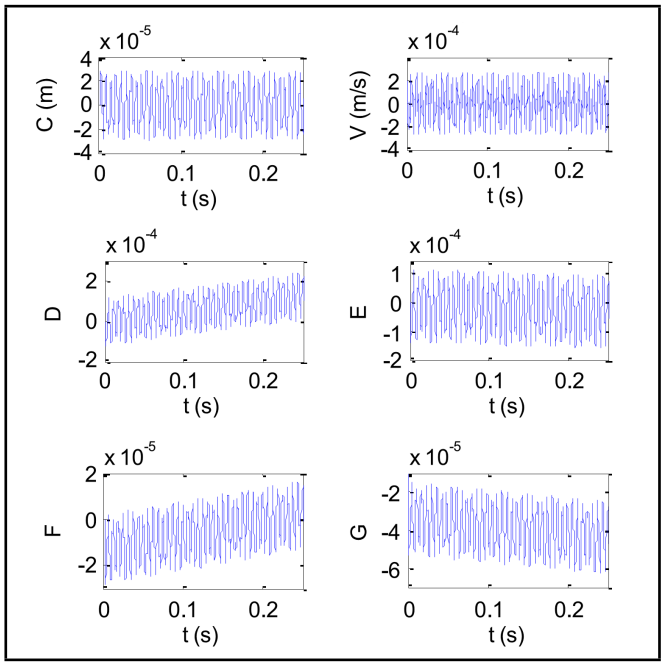

Figure 3. State variables for $\theta_0 = 290$ K, $q_0 = 10000$ N/m^2, $r = 0$ W/kg, $\lambda = 15$, and $\omega = 1000$ rad/s (Lyapunov exponent $= -0.0179$).

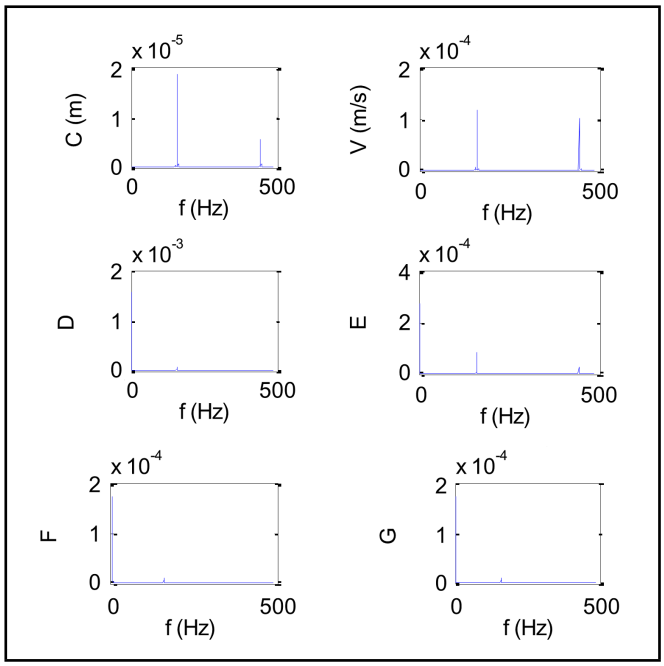

Figure 4. FFT of state variables for $\theta_0 = 290$ K, $q_0 = 10000$ N/m^2, $r = 0$ W/kg, $\lambda = 15$, and $\omega = 1000$ rad/s (Lyapunov exponent $= -0.0179$).

3. RESULTS

Equations (36) and (37), which express in-plane equations of motion, are linear and completely decoupled from parameters C, D, E, F, and G. Therefore, they can be solved separately. Solving Eqs. (38), (39), (40), (41), and (42) involves primarily changing them into six first order differential equations. Afterwards, the solution in the time domain is achieved by using the Runge-Kutta method of fourth order for an 80×80 cm^2 square plate with zero initial conditions for all state variables. The time step is assumed to be 1/50 of the period of applied force and integration is done along 500 periods. To detect chaos, the Lyapunov exponent is calculated for 20 initial points on each trajectory and then averaged as below:[36]

$$\lambda(x_i) = \frac{1}{n} \ln\left(\frac{d_n}{d_0}\right); \tag{50}$$

$$\lambda = \frac{1}{N} \sum_{i=1}^{N} \lambda(x_i). \tag{51}$$

If the sign λ is positive for a trajectory, it is said to be chaotic. d_n is the evolved distance between two point of a trajectory, which were initially at the distance d_0. It should be noted that the distance d indicates the Euclidean norm in six dimensional state space. Fast Fourier transform (FFT) of

Table 2. Maximum lateral displacement, velocity, and average temperature over the thickness and Lyapunov exponent when values of heat generation, initial temperature, and lateral load change (base state: $\theta_{\text{ambient}} = 300$ K, $\omega = 700$ rad/s, and $\lambda = 60$. $r = 0$ W/kg, $\theta_0 = 290$ K, and $q_0 = 1\times10^4$).

	$\delta_{\max}$ (m)	$V_{\max}$ (m/s)	T_{avg} (K)	LE
Base state	0.0233	0.1123	289.9816	0.2249
$r = -100$ W/kg	0.0233	0.1127	288.8077	0.2497
$r = 100$ W/kg	0.0233	0.1121	290.2341	0.2190
$\theta_0 = 295$ K	0.0233	0.1124	294.8742	0.1380
$\theta_0 = 285$ K	0.0233	0.1123	285.0853	0.2764
$q_0 = 5\times10^3$ N/m^2	0.0174	0.0912	290.0027	0.1889
$q_0 = 2\times10^3$ N/m^2	0.0120	0.0669	290.0725	0.2369

Table 3. Maximum lateral displacement, velocity, and average temperature over the thickness and Lyapunov exponent when frequency and side length to thickness ratio change (base state: $\theta_{\text{ambient}} = 300$ K, $\omega = 700$ rad/s, and $\lambda = 60$. $r = 0$ W/kg, $\theta_0 = 290$ K, and $q_0 = 1\times10^4$).

	$\delta_{\max}$ (m)	$V_{\max}$ (m/s)	T_{avg} (K)	LE
Base state	0.0233	0.1123	289.9816	0.2249
$\omega = 900$ rad/s	0.0042	0.0222	290.0487	0.0323
$\omega = 1100$ rad/s	0.0021	0.0100	290.0616	0.0213
$\omega = 1300$ rad/s	0.0014	0.0060	290.0370	-0.0128
$\lambda = 40$	0.011	0.0080	290.0632	-0.0227
$\lambda = 80$	0.0091	0.0422	289.9619	0.0674
$\lambda = 100$	0.00112	0.0368	289.9171	0.0814

the solution time series, which depicts the existing frequencies, can also be an intuitive verification to decide whether a trajectory is chaotic or not.

To investigate the conditions resulting in chaos, θ_0, q_0, r, λ, and ω are treated as control parameters and changed in certain ranges. For different values of these parameters, the Lyapunov exponent, maximum lateral deflection, maximum lateral velocity, and average temperature over the thickness are listed in Tables 2 and 3. Figures 1, 2, 3, and 4 show the state variables and their FFT's for two cases, where the Lyapunov exponent has opposite signs. For the purpose of comparison, the problem is also solved when plate is homogeneously made of steel or ceramic. Table 4 and Fig. 5 illustrate the differences between the thermal and mechanical responses of the homogeneous plates versus the functionally graded plates.

4. CONCLUSIONS

In this paper, the governing equations for thermo-mechanically coupled nonlinear vibrations of a rectangular FGM plate are derived. Using the Galerkin approximation, the equations are changed into ordinary differential equations and solved numerically. The Lyapunov exponent is used as a criterion to recognize chaos and has been computed for various values of control parameters.

According to the results, the Lyapunov exponent is sensitive to the parameters θ_0, q_0, r, λ, and ω. However, among all the mentioned parameters, only λ and ω can cause drastic change in the Lyapunov exponent, especially in its sign. Therefore, the geometry of trajectories in state space is strongly characterized by these two parameters and the response can be chaotic for certain values of them, as listed in Table 3.

Table 4 and Fig. 5 show that the dynamical behavior of a functionally graded plate does not necessarily intermediate ceramic and steel plates, since many new terms emerge in the FGM governing equations through integration over the thickness due to non-homogeneity. This highlights the modeling and analysis of FGM bodies in separate contexts.

Table 4. Maximum lateral displacement, velocity, and average temperature over the thickness and Lyapunov exponent for a plate homogenously made of steel or ceramic versus FGM ($\theta_{\text{ambient}} = 300$ K, $\omega = 1000$ rad/s, and $\lambda = 80$. $r = 0$ W/kg, $\theta_0 = 290$ K, and $q_0 = 1\times10^4$).

	Material A (Ceramic)	FGM	Material B (Steel)
$V_{\max}$ (m/s)	0.0275	0.0140	0.0088
T_{avg} (K)	290.1004	290.0365	290.0657
LE	0.0423	-0.0664	0.0172

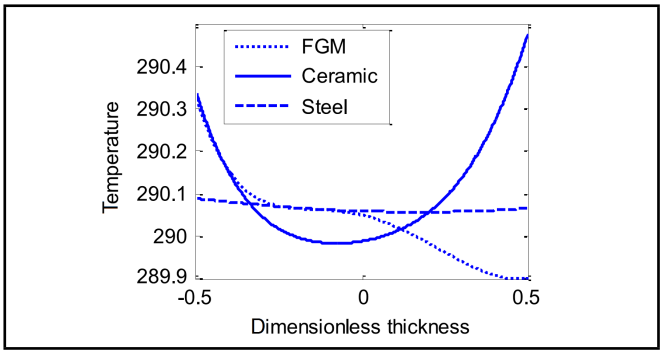

Figure 5. Temperature distribution in thickness for FGM, homogenous steel and ceramic plates ($\theta_{\text{ambient}} = 300$ K, $\omega = 1000$ rad/s, and $\lambda = 80$. $r = 0$ W/kg, $\theta_0 = 290$ K, and $q_0 = 1\times10^4$).

REFERENCES

1 Naghibi, S. E. and Mahzoon M. Chaotic vibrations of rectangular FGM plates with thermo-mechanical coupling, *Proc. of ISME 2012 Iranian Society of Mechanical Engineers*, Shiraz, Iran, (2012).

2 Nowacki, W. *Dynamic Problems of Thermo-elasticity*, Leyden, Noordhoff, (1975).

3 Kawamura, R., Tanigawa, Y., Kusuki, S., and Hamamura, H. Fundamental thermo-elasticity equations for thermally induced flexural vibration problems for inhomogeneous plates and thermo-elastic dynamical responses to a sinusoidally varying surface temperature, *Journal of Engineering Mathematics*, **61**, 143–160, (2007). http://dx.doi.org/10.1007/s10665-007-9190-2

4 Xiang, W. L. and Melnik, R. Differential-algebraic approach to coupled problems of dynamic thermo-elasticity, *Applied Mathematics and Mechanics*, **27** (9), 1185–1196, (2006). http://dx.doi.org/10.1007/s10483-006-0905-z

5 Yang, J. and Shen, H. S. Vibration characteristics and transient response of shear deformable functionally graded plates in thermal environment, *Journal of Sound and Vibration*, **255** (3), 579–602, (2002). http://dx.doi.org/10.1006/jsvi.2001.4161

6 Yang, J. and Shen, H. S. Dynamic response of initially stressed functionally graded rectangular thin plates, *Composite Structures*, **54**, 497–508, (2001). http://dx.doi.org/10.1016/s0263-8223(01)00122-2

7 Gupta, A. K. Non-linear thickness variation on the thermally-induced vibration of a rectangular plate: a spline technique, *International Journal of Acoustics and Vibration*, **19** (2), 131–136, (2014). http://dx.doi.org/10.20855/ijav.2014.19.2341

8 Prabhakara, M. K. and Chia, C. Y. Nonlinear flexural vibrations of orthotropic rectangular plates, *Journal of Sound and Vibration*, **52** (4), 511–518, (1977). http://dx.doi.org/10.1016/0022-460x(77)90367-4

[9] Allahverdizadeh, A., Naei, M. H., and Nikkhah Bahrami, M. Vibration amplitude and thermal effects on the nonlinear behavior of thin circular functionally graded plates, *International Journal of Mechanical Sciences*, **50**, 445–454, (2008). http://dx.doi.org/10.1016/j.ijmecsci.2007.09.018

[10] Allahverdizadeh, A., Naei, M. H., and Nikkhah Bahrami, M. Nonlinear free and forced vibration analysis of thin circular functionally graded plated, *Journal of Sound and Vibration*, **310**, 966–984, (2008). http://dx.doi.org/10.1016/j.jsv.2007.08.011

[11] Chang, W. P. and Chian, J. S. Nonlinear free vibration of heated orthotropic rectangular plates, *International Journal of Solids and Structures*, **22** (3), 267–281, (1986). http://dx.doi.org/10.1016/0020-7683(86)90091-0

[12] Xuefeng, S., Xiaoqing, Z., and Jinxiang, Z. Study of nonlinear thermo-elastic free vibration of simply supported circular plate, *Engineering Mechanics*, **17** (2), 97–101, (2000).

[13] Xuefeng, S., Xiaoqing, Z., and Jinxiang, Z. Thermo-elastic free vibration of clamped circular plate, *Applied Mathematics and Mechanics*, **21** (6), 715–724, (2000).

[14] Praveen, G. N. and Reddy, J. N. Nonlinear transient thermo-elastic analysis of functionally graded ceramic metal plates, *International Journal of Solids and Structures*, **35** (33), 4457–4476, (1998). http://dx.doi.org/10.1016/s0020-7683(97)00253-9

[15] Huang, X. L. and Shen, H. S. Nonlinear vibration and dynamic response of functionally graded plates in thermal environment, *International Journal of Solids and Structures*, **41**, 2403–2427, (2004). http://dx.doi.org/10.1016/j.ijsolstr.2003.11.012

[16] Woo, J. and Meguid, S. A. Nonlinear analysis of functionally graded plates and shallow shells, *International Journal of Solids and Structures*, **38**, 7409–7421, (2001). http://dx.doi.org/10.1016/s0020-7683(01)00048-8

[17] Woo, J., Meguid, S. A., and Ong, L. S. Nonlinear free vibration behavior of functionally graded plates, *Journal of Sound and Vibration*, **289**, 595–611, (2006). http://dx.doi.org/10.1016/j.jsv.2005.02.031

[18] Chang, W. P. and Wan, S. M. Thermo-mechanically coupled nonlinear vibration of plates, *International Journal of Non-Linear Mechanics*, **21** (5), 375–389, (1986). http://dx.doi.org/10.1016/0020-7462(86)90021-1

[19] Hao, Y. X., Zhang, W., Yang, J., and Li, S. Y. Nonlinear dynamic response of a simply supported rectangular functionally graded material plate under the time-dependent thermal-mechanical loads, *Journal of Mechanical Science and Technology*, **25** (7), 1637–1646, (2011). http://dx.doi.org/10.1007/s12206-011-0501-1

[20] Yeh, Y. L. The effect of thermo-mechanical coupling for a simply supported orthotropic rectangular plate on nonlinear dynamics, *Thin Walled Structures*, **43**, 1277–1295, (2005). http://dx.doi.org/10.1016/j.tws.2005.03.002

[21] Alijani, F. and Amabili, M. Nonlinear parametric instability of functionally graded rectangular plates in thermal environments, *Proc. ASME 2012 International Mechanical Engineering Congress and Exposition*, (2012). http://dx.doi.org/10.1115/imece2012-89140

[22] Qiang, H., Nianmei, Z., and Guitong, Y. Chaotic motion of a nonlinear thermo-elastic elliptic plate, *Applied Mathematics and Mechanics*, **20** (9), 960–966, (1999). http://dx.doi.org/10.1007/bf02459058

[23] Ribeiro, P. Thermally induced transition to chaos in plate vibrations, *Journal of Sound and Vibration*, **229**, 314–330, (2007). http://dx.doi.org/10.1016/j.jsv.2006.08.003

[24] Ribeiro, P. and Duarte, R. P. From periodic to chaotic oscillations in composite laminated plates, *Computers & Structures*, **84**, 1629–1639, (2006). http://dx.doi.org/10.1016/j.compstruc.2005.12.006

[25] Lai, H. Y., Chen, C. K., and Yeh, Y. L. Double mode modeling of chaotic and bifurcation dynamics for a simply supported rectangular plate in large deflections, *International Journal of Non-Linear Mechanics*, **37**, 331–343, (2002). http://dx.doi.org/10.1016/s0020-7462(00)00120-7

[26] Yeh, Y. L., Chen, C. K., and Lai, H. Y. Chaotic and bifurcation dynamics for a simply supported rectangular plate of thermo-mechanical coupling in large deflections, *Chaos, Solitons & Fractals*, *13*, 1493–1500, (2002). http://dx.doi.org/10.1016/s0960-0779(01)00158-8

[27] Yeh, Y. L. and Chen, C. K. Chaotic and bifurcation for a simply supported thermo-mechanical coupling circular plate with variable thickness, *Chaos, Solitons & Fractals*, **22**, 1013–1030, (2004). http://dx.doi.org/10.1016/j.chaos.2003.12.102

[28] Zhang, W., Yang, J., and Hao, Y. Chaotic vibrations of an orthotropic FGM rectangular plate based on third order shear deformation theory, *International Journal of Non-Linear Mechanics*, **59**, 619–660, (2010). http://dx.doi.org/10.1007/s11071-009-9568-y

[29] Hao, Y. X., Chen, L. H., Zhang, W., and Lei, J. G. Nonlinear oscillations bifurcation and chaos of functionally graded materials plate, *Journal of Sound and Vibration*, **312**, 862–892, (2008). http://dx.doi.org/10.1016/j.jsv.2007.11.033

[30] Sadd, M. H. *Elasticity Theory, Applications, and Numerics*, Academic Press, Burlington, (2009).

[31] Lai, W. M., Rubin, D., and Krempl, E. *Introduction to Continuum Mechanics*, Butterworth Heinemann, Woburn (1999).

[32] Jones, R. M. *Buckling of Bars, Plates and Shells*, Bull Ridge Corporation, Blacksburg Virginia, (2006).

[33] Timoshenko, S. and Woinovski-Krieger, S. *Theory of Plates and Shells*, McGraw-Hill, Tokyo, (1984).

[34] Coleman, B. D. and Noll, W. The thermodynamics of elastic materials with heat conduction and viscosity, *Archive for Rational Mechanics and Analysis*, **13** (1), 167–178, (1963). http://dx.doi.org/10.1007/bf01262690

[35] MatWeb, LLC. MatWeb, Material Property Data. Retrieved from http://www.matweb.com, (Accessed August 14, 2014).

[36] Hilborn, R. C. *Chaos and Nonlinear Dynamics*, Oxford University Press, New York, (2000).

Response of a Cylindrical Shell with Finite Length Ring Stiffeners

Andrew J. Hull

Undersea Warfare Weapons, Vehicles and Defensive Systems Department, Naval Undersea Warfare Center Division, Newport, Rhode Island 02841 USA

Geoffrey R. Moss

Sensors and Sonar Systems Department, Naval Undersea Warfare Center Division, Newport, Rhode Island 02841 USA

(Received 24 September 2014; accepted 19 April 2016)

This paper derives a spatial domain wave propagation solution of a cylindrical shell that contains periodically spaced ring stiffeners. Previous work in this area has modeled the stiffeners as having a very short or very long length. This paper models the stiffeners as finite length inclusions with forces that have spatial extent in three-dimensions. Furthermore, there is a well-defined separation distance between each stiffener. The new model uses Donnell shell equations with the stiffener forces applied in three-dimensions using Heaviside step functions. These equations of motion are orthogonalized in both the angular and longitudinal directions, resulting in a double fixed index matrix equation. These indices can be varied, which yields a set of double indexed matrix equations that are written together as a single global matrix. This global matrix can be solved, which results in a solution to the system displacements. Two specific external loading cases are investigated and convergence criteria are discussed. One of the models is verified with a comparison to finite element analysis.

1. INTRODUCTION

Reinforced shells were used in a variety of applications. They can be found in undersea vehicles, industrial pipes, hydraulic lines, and marine piers. Reinforcement was typically added to these structures as a method to increase stiffness without adding significant mass. Adding reinforcement changes the structural response of almost any system, and the forces that are introduced by the reinforcement need to be included in an analytical or numerical model that predicts the corresponding response. Unreinforced isotropic thin cylindrical shell models have existed in the literature for a long time and can be found in textbooks on acoustics and applied mechanics.[1,2] Isotropic thick shell cylindrical shells models were also derived for shells without reinforcement.[3] Shell models were extended to include transversely isotropic behavior[4] and general orthotropic behavior.[5]

The inclusion of ring stiffeners in the cylinder increased the stiffness in all three cylindrical directions and changed the character of the infinite cylinder response from a (purely propagating) single longitudinal term expression to a (partially reflective) multi-longitudinal term expression due to the forces of the stiffeners interacting with the wave motion. Historically, research in this area has been divided into two separate approaches: (1) where the length of the stiffener was very short compared to the periodicity of the stiffeners or (2) where the length of the stiffener was relatively long compared its periodicity. Work in the first area (i.e. short stiffeners) was abundant, and various systems were analyzed. Free wave propagation of periodically ring stiffened shells has been studied using finite element analysis[6] applied to various different ring geometries that all had relatively small spatial extent and to determine natural frequencies and modes shapes of ring-stiffened shells.[7] The free vibration analysis of cylindrical shells with ring stiffeners that had non-uniform eccentricity and unequal spacing were investigated using a Ritz analytical method, experimental testing, and finite element analysis,[8] where the stiffeners had a relatively small spatial extent.

A Laplace transfer numerical method to analyze ring stiffened circular thin shells was developed,[9] where the spatial dimensions of the rings were small and the structure was loaded with a transient pressure load. The problem of acoustic radiation from fluid-loaded, ring-supported thin shells subjected to a point forces has been solved[10] in the wavenumber domain. In this paper, both single and double periodic ring supports were considered. The theory of vibrations of a cylinder reinforced by periodically spaced circular T-section ribs along its length has been derived.[11] A method for obtaining the propagation constants of a thin uniform periodically stiffened cylindrical shells with an emphasis on the stop and pass bands of free wave motion has been developed.[12]

Work in the second area (i.e. long stiffeners) generally used wave propagation approaches to model finite length ring-stiffened cylindrical shells by assuming that the structure behaves as an orthotropic shell, a method that is sometimes referred to as "smearing". This was studied for initial hydrostatic pressure using Flugge equations of motion[13] and for fi-

nite length structures with arbitrary boundary conditions with an axial factor term analysis.[14] The effects of energy reflections off of the stiffener edges were absent in these two papers, although these models captured the majority of the wave propagation features of such a system.

This paper derived a spatial domain wave propagation solution for the problem of a cylindrical shell with periodically spaced ring stiffeners that had a significant spatial extent and significant separation. This model was designed to bridge the gap between previous models, where the stiffeners were modeled as extremely short or extremely long. The problem began with the Donnell shell equations of motion written with the stiffener forces applied in three-dimensions using Heaviside step functions. The shell displacements were written as double summations of an unknown wave propagation coefficient multiplied by an indexed circumferential term multiplied by an indexed longitudinal term. The displacement terms were inserted into the differential equations of motion and the Heaviside functions were approximated by a Fourier series. These algebraic equations were then orthogonalized in two spatial dimensions, which resulted in a matrix equation that was dependent on two fixed indices: one an angular index and the other a longitudinal index. By using a finite number of these indices, the fixed index matrix equations were assembled into a global matrix equation, which resulted in a solution to the wave propagation coefficients. By using these coefficients, the displacement field of the shell could be calculated. This problem was investigated for two external forcing conditions: one a ring load and the other a plane wave load. The ring load was verified by comparing the results to a solution generated using finite element theory. Convergence criteria were discussed and the energy distribution of the different mode numbers was investigated.

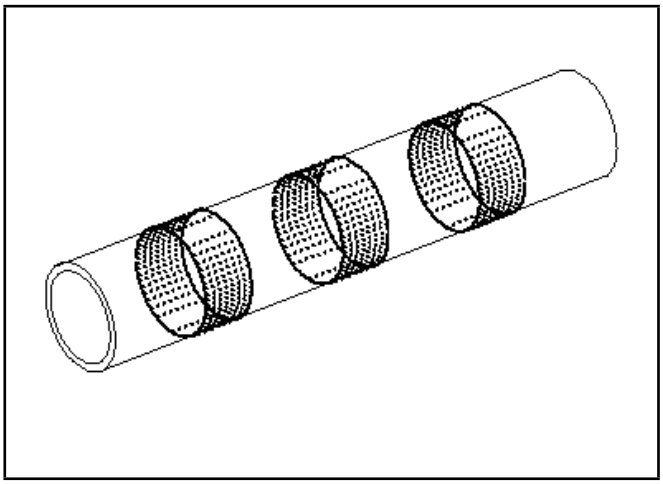

Figure 1. Isometric view of the cylinder with ring stiffeners.

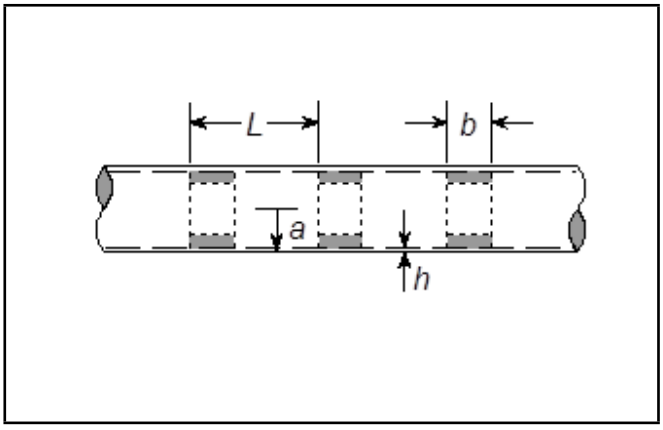

Figure 2. Side view of the cylinder with ring stiffeners.

2. SYSTEM MODEL AND DECOUPLED SOLUTION

The system model was that of a cylinder containing a radial stiffener of finite length, as shown in Figs. 1 and 2. This problem was analytically modeled by assuming the cylinder was governed with a dynamic formulation of Donnell shell equations and the stiffener was modeled as a spatially distributed translational spring in the longitudinal, circumferential, and radial directions. The model used the following assumptions: (1) the cylinder had infinite spatial extent in the axial direction, (2) the displacements in the cylinder were three-dimensional and linear, (3) the displacement field was constant across the thickness of the shell, (4) the stiffeners were periodic, and (5) the stiffener exerted forces in the longitudinal, circumferential, and radial directions on the cylinder that were proportional to the longitudinal, circumferential, and radial displacements of the cylinder, respectively.

The motion of the cylinder with ring stiffeners was governed by the equation of motion in the longitudinal direction written as:

$$\rho h\frac{\partial^2 u(z,\theta,t)}{\partial t^2} - \rho h c_p^2\frac{\partial^2 u(z,\theta,t)}{\partial z^2} - \frac{(1-\nu)\rho h c_p^2}{2a^2}\frac{\partial^2 u(z,\theta,t)}{\partial \theta^2} - \frac{(1+\nu)\rho h c_p^2}{2a}\frac{\partial^2 v(z,\theta,t)}{\partial z\partial\theta} - \frac{\nu\rho h c_p^2}{a}\frac{\partial w(z,\theta,t)}{\partial z} = \frac{K_z}{ab}u(z,\theta,t)\sum_{n=-\infty}^{n=+\infty}\left[\mathrm{H}(z-nL)-\mathrm{H}(z-b-nL)\right]; \quad (1)$$

in the tangential direction written as:

$$-\frac{(1+\nu)\rho h c_p^2}{2a}\frac{\partial^2 u(z,\theta,t)}{\partial z\partial\theta} - \frac{(1-\nu)\rho h c_p^2}{2}\frac{\partial^2 v(z,\theta,t)}{\partial z^2} - \frac{\rho h c_p^2}{a^2}\frac{\partial^2 v(z,\theta,t)}{\partial\theta^2} + \rho h\frac{\partial^2 v(z,\theta,t)}{\partial t^2} - \frac{\rho h c_p^2}{a^2}\frac{\partial w(z,\theta,t)}{\partial\theta} = \frac{K_t}{ab}v(z,\theta,t)\sum_{n=-\infty}^{n=+\infty}\left[\mathrm{H}(z-nL)-\mathrm{H}(z-b-nL)\right]; \quad (2)$$

and in the radial direction written as:

$$\frac{\nu\rho hc_p^2}{a}\frac{\partial u(z,\theta,t)}{\partial z}+\frac{\rho hc_p^2}{a^2}\frac{\partial v(z,\theta,t)}{\partial \theta}+\frac{\rho hc_p^2}{a^2}w(z,\theta,t)+\frac{\rho h^3c_p^2}{12}\frac{\partial^4 w(z,\theta,t)}{\partial z^4}+\frac{\rho h^3c_p^2}{6a^2}\frac{\partial^4 w(z,\theta,t)}{\partial z^2\partial\theta^2}+\frac{\rho h^3c_p^2}{12a^4}\frac{\partial^4 w(z,\theta,t)}{\partial\theta^4}+\rho h\frac{\partial^2 w(z,\theta,t)}{\partial t^2}=p_a(z,\theta,t)+\frac{K_r}{ab}w(z,\theta,t)\sum_{n=-\infty}^{n=+\infty}\left[\mathrm{H}(z-nL)-\mathrm{H}(z-b-nL)\right]; \quad (3)$$

where z was the axial direction, θ was the circumferential direction, t was time, $u(z,\theta,t)$ was the longitudinal displacement, $v(z,\theta,t)$ was the tangential displacement, $w(z,\theta,t)$ was the radial displacement, a was the radius of the shell, ν was Poisson's ratio of the shell, ρ was the density of the shell, h was the thickness of the shell, $p_a(z,\theta,t)$ was the external radial load on the shell, K_z as the longitudinal stiffness of the ring stiffener, K_t was the circumferential stiffness of the ring stiffener, K_r as the radial stiffness of the ring stiffener, b was the length of the ring stiffener, $\mathrm{H}(\cdot)$ was the Heaviside step function, and c_p was the plate wave speed, which was given by:

$$c_p=\sqrt{\frac{E}{\rho(1-\nu^2)}}. \quad (4)$$

The shell displacements were then written as double summations in the form:

$$u(z,\theta,t)=\sum_{m=-\infty}^{m=+\infty}\sum_{q=0}^{q=+\infty}U_{mq}\cos(q\theta)\exp(\mathrm{i}k_m z)\exp(-\mathrm{i}\omega t); \quad (5)$$

$$v(z,\theta,t)=\sum_{m=-\infty}^{m=+\infty}\sum_{q=0}^{q=+\infty}V_{mq}\sin(q\theta)\exp(\mathrm{i}k_m z)\exp(-\mathrm{i}\omega t); \quad (6)$$

and

$$w(z,\theta,t)=\sum_{m=-\infty}^{m=+\infty}\sum_{q=0}^{q=+\infty}W_{mq}\cos(q\theta)\exp(\mathrm{i}k_m z)\exp(-\mathrm{i}\omega t); \quad (7)$$

where i was the square root of -1, ω was the frequency, U_{mq} , V_{mq} , and W_{mq} were unknown longitudinal, tangential, and radial wave propagation coefficients respectively, whose solutions were sought, and k_m was the indexed longitudinal wavenumber, which was expressed as:

$$k_m=k+\frac{2\pi m}{L}; \quad (8)$$

where k was the wavenumber of excitation and L was the periodic spacing of the ring stiffeners. For the problems solved in this paper, the excitation was a ring load at definite wavenumber and frequency written as:

$$p_a(z,\theta,t)=P_a\exp(\mathrm{i}kz)\exp(-\mathrm{i}\omega t); \quad (9)$$

or a broad side plane wave at definite speed and frequency written as:

$$p_a(z,\theta,t)=P_a\left[\sum_{n=0}^{n=+\infty}\mathrm{i}^n\varepsilon_n\mathrm{J}_n\left(\frac{\omega a}{c}\right)\cos(n\theta)\right]\exp(-\mathrm{i}\omega t); \quad (10)$$

where P_a was the magnitude of the applied pressure excitation, ϵ_n was the Newmann factor ($\epsilon_n=1$ for $n=0$; $\epsilon_n=2$ for $n>0$), J was an ordinary nth order Bessel function of the first kind, and c was the propagation speed of the plane wave. At this point, the exponential with respect to time was suppressed in all of the equations. The insertion of Eqs. (5) to (9) into Eqs. (1) to (3) yielded:

$$\sum_{m=-\infty}^{m=+\infty}\sum_{q=0}^{q=+\infty}\left[\rho hc_p^2k_m^2+\frac{\rho hc_p^2(1-\nu)q^2}{2a^2}-\rho h\omega^2\right]\times U_{mq}\cos(q\theta)\exp(\mathrm{i}k_m z)+\sum_{m=-\infty}^{m=+\infty}\sum_{q=0}^{q=+\infty}\left[\frac{-\rho hc_p^2(1+\nu)\,\mathrm{i}\,k_m q}{2a}\right]\times V_{mq}\cos(q\theta)\exp(\mathrm{i}k_m z)+\sum_{m=-\infty}^{m=+\infty}\sum_{q=0}^{q=+\infty}\left[\frac{-\rho hc_p^2\nu\,\mathrm{i}\,k_m}{a}\right]W_{mq}\cos(q\theta)\exp(\mathrm{i}k_m z)=\frac{K_z}{ab}\sum_{m=-\infty}^{m=+\infty}\sum_{q=0}^{q=+\infty}U_{mq}\cos(q\theta)\exp(\mathrm{i}k_m z)\times\sum_{n=-\infty}^{n=+\infty}\left[\mathrm{H}(z-nL)-\mathrm{H}(z-b-nL)\right]; \quad (11)$$

$$\sum_{m=-\infty}^{m=+\infty}\sum_{q=0}^{q=+\infty}\left[\frac{\rho hc_p^2(1+\nu)\,\mathrm{i}\,k_m q}{2a}\right]\times U_{mq}\sin(q\theta)\exp(\mathrm{i}k_m z)+\sum_{m=-\infty}^{m=+\infty}\sum_{q=0}^{q=+\infty}\left[\frac{\rho hc_p^2(1-\nu)k_m^2}{2}+\frac{\rho hc_p^2q^2}{a^2}-\rho h\omega^2\right]\times V_{mq}\sin(q\theta)\exp(\mathrm{i}k_m z)+\sum_{m=-\infty}^{m=+\infty}\sum_{q=0}^{q=+\infty}\left[\frac{\rho hc_p^2\,q}{a^2}\right]W_{mq}\sin(q\theta)\exp(\mathrm{i}k_m z)=\frac{K_t}{ab}\sum_{m=-\infty}^{m=+\infty}\sum_{q=0}^{q=+\infty}V_{mq}\sin(q\theta)\exp(\mathrm{i}k_m z)\times\sum_{n=-\infty}^{n=+\infty}\left[\mathrm{H}(z-nL)-\mathrm{H}(z-b-nL)\right]; \quad (12)$$

and

$$\sum_{m=-\infty}^{m=+\infty}\sum_{q=0}^{q=+\infty}\left[\frac{\rho h c_p^2 \nu \,\mathrm{i}\, k_m}{a}\right] U_{mq}\cos(q\theta)\exp(\mathrm{i}k_m z)+ \sum_{m=-\infty}^{m=+\infty}\sum_{q=0}^{q=+\infty}\left[\frac{\rho h c_p^2\, q}{a^2}\right] V_{mq}\cos(q\theta)\exp(\mathrm{i}k_m z)+ \sum_{m=-\infty}^{m=+\infty}\sum_{q=0}^{q=+\infty}\left[\frac{\rho h c_p^2}{a^2}+\frac{\rho h^3 c_p^2 k_m^4}{12}+\frac{\rho h^3 c_p^2 k_m^2 q^2}{6a^2}+ \frac{\rho h^3 c_p^2 q^4}{12a^4}-\rho h\omega^2\right] W_{mq}\cos(q\theta)\exp(\mathrm{i}k_m z) = P_a\exp(\mathrm{i}kz)+\frac{K_r}{ab}\sum_{m=-\infty}^{m=+\infty}\sum_{q=0}^{q=+\infty} W_{mq}\cos(q\theta)\exp(\mathrm{i}k_m z)\times \sum_{n=-\infty}^{n=+\infty}\left[\mathrm{H}(z-nL)-\mathrm{H}(z-b-nL)\right]. \quad (13)$$

The Heaviside step function summation was then written using a Fourier series as:

$$\sum_{n=-\infty}^{n=+\infty}\left[\mathrm{H}(z-nL)-\mathrm{H}(z-b-nL)\right] = -\sum_{n=-\infty}^{n=+\infty} d_n\exp\left(\frac{\mathrm{i}2\pi n z}{L}\right); \quad (14)$$

where

$$d_n=\begin{cases}\frac{1-\exp(-\mathrm{i}2\pi n b/L)}{\mathrm{i}2\pi n} & n\neq 0\\ \frac{b}{L} & n=0.\end{cases} \quad (15)$$

Equation. (14) was inserted into Eqs. (11), (12), and (13), which yielded:

$$\sum_{m=-\infty}^{m=+\infty}\sum_{q=0}^{q=+\infty}\left[\rho h c_p^2 k_m^2+\frac{\rho h c_p^2(1-\nu)q^2}{2a^2}-\rho h\omega^2\right]\times U_{mq}\cos(q\theta)\exp(\mathrm{i}k_m z)+ \sum_{m=-\infty}^{m=+\infty}\sum_{q=0}^{q=+\infty}\left[\frac{-\rho h c_p^2(1+\nu)\,\mathrm{i}\,k_m q}{2a}\right]\times V_{mq}\cos(q\theta)\exp(\mathrm{i}k_m z)+ \sum_{m=-\infty}^{m=+\infty}\sum_{q=0}^{q=+\infty}\left[\frac{-\rho h c_p^2 \nu\,\mathrm{i}\,k_m}{a}\right] W_{mq}\cos(q\theta)\exp(\mathrm{i}k_m z) = \frac{-K_z}{ab}\sum_{m=-\infty}^{m=+\infty}\sum_{q=0}^{q=+\infty} U_{mq}\cos(q\theta)\exp(\mathrm{i}k_m z)\times \sum_{n=-\infty}^{n=+\infty} d_n\exp\left(\frac{\mathrm{i}2\pi n z}{L}\right); \quad (16)$$

$$\sum_{m=-\infty}^{m=+\infty}\sum_{q=0}^{q=+\infty}\left[\frac{\rho h c_p^2(1+\nu)\,\mathrm{i}\,k_m q}{2a}\right]\times U_{mq}\sin(q\theta)\exp(\mathrm{i}k_m z)+ \sum_{m=-\infty}^{m=+\infty}\sum_{q=0}^{q=+\infty}\left[\frac{\rho h c_p^2(1-\nu)k_m^2}{2}+\frac{\rho h c_p^2 q^2}{a^2}-\rho h\omega^2\right]\times V_{mq}\sin(q\theta)\exp(\mathrm{i}k_m z)+ \sum_{m=-\infty}^{m=+\infty}\sum_{q=0}^{q=+\infty}\left[\frac{\rho h c_p^2\, q}{a^2}\right] W_{mq}\sin(q\theta)\exp(\mathrm{i}k_m z) = \frac{-K_t}{ab}\sum_{m=-\infty}^{m=+\infty}\sum_{q=0}^{q=+\infty} V_{mq}\sin(q\theta)\exp(\mathrm{i}k_m z)\times \sum_{n=-\infty}^{n=+\infty} d_n\exp\left(\frac{\mathrm{i}2\pi n z}{L}\right); \quad (17)$$

and

$$\sum_{m=-\infty}^{m=+\infty}\sum_{q=0}^{q=+\infty}\left[\frac{\rho h c_p^2 \nu \,\mathrm{i}\, k_m}{a}\right] U_{mq}\cos(q\theta)\exp(\mathrm{i}k_m z)+ \sum_{m=-\infty}^{m=+\infty}\sum_{q=0}^{q=+\infty}\left[\frac{\rho h c_p^2\, q}{a^2}\right] V_{mq}\cos(q\theta)\exp(\mathrm{i}k_m z)+ \sum_{m=-\infty}^{m=+\infty}\sum_{q=0}^{q=+\infty}\left[\frac{\rho h c_p^2}{a^2}+\frac{\rho h^3 c_p^2 k_m^4}{12}+\frac{\rho h^3 c_p^2 k_m^2 q^2}{6a^2}+ \frac{\rho h^3 c_p^2 q^4}{12a^4}-\rho h\omega^2\right] W_{mq}\cos(q\theta)\exp(\mathrm{i}k_m z) = P_a\exp(\mathrm{i}kz)-\frac{K_r}{ab}\sum_{m=-\infty}^{m=+\infty}\sum_{q=0}^{q=+\infty} W_{mq}\cos(q\theta)\exp(\mathrm{i}k_m z)\times \sum_{n=-\infty}^{n=+\infty} d_n\exp\left(\frac{\mathrm{i}2\pi n z}{L}\right). \quad (18)$$

The last term in Eqs. (16), (17), and (18) were rewritten using the relationships:

$$\sum_{m=-\infty}^{m=+\infty}\sum_{q=0}^{q=+\infty} U_{mq}\cos(q\theta)\exp(\mathrm{i}k_m z)\times \sum_{n=-\infty}^{n=+\infty} d_n\exp\left(\frac{\mathrm{i}2\pi n z}{L}\right) = \sum_{q=0}^{q=+\infty}\left\{\sum_{n=-\infty}^{n=+\infty}\sum_{m=-\infty}^{m=+\infty} U_{nq} d_{m-n}\exp(\mathrm{i}k_m z)\right\}\cos(q\theta); \quad (19)$$

$$\sum_{m=-\infty}^{m=+\infty}\sum_{q=0}^{q=+\infty} V_{mq}\sin(q\theta)\exp(\mathrm{i}k_m z)\times \sum_{n=-\infty}^{n=+\infty} d_n \exp\left(\frac{\mathrm{i}2\pi n z}{L}\right) = \sum_{q=0}^{q=+\infty}\left\{\sum_{n=-\infty}^{n=+\infty}\sum_{m=-\infty}^{m=+\infty} V_{nq} d_{m-n}\exp(\mathrm{i}k_m z)\right\}\sin(q\theta)\ ; \tag{20}$$

and

$$\sum_{m=-\infty}^{m=+\infty}\sum_{q=0}^{q=+\infty} W_{mq}\cos(q\theta)\exp(\mathrm{i}k_m z)\times \sum_{n=-\infty}^{n=+\infty} d_n \exp\left(\frac{\mathrm{i}2\pi n z}{L}\right) = \sum_{q=0}^{q=+\infty}\left\{\sum_{n=-\infty}^{n=+\infty}\sum_{m=-\infty}^{m=+\infty} W_{nq} d_{m-n}\exp(\mathrm{i}k_m z)\right\}\cos(q\theta)\ . \tag{21}$$

Equations (16) and (18) were then multiplied by $\exp(-\mathrm{i}k_s z)\cos(t\theta)$, Eq. (17) was multiplied by $\exp(-\mathrm{i}k_s z)\sin(t\theta)$, and these resulting expressions were integrated on the intervals $[0, 2\pi]$ on θ and $[0, L]$ on z. Because these functions were orthogonal on their respective domains, the equations decouple into sets of st-indexed equations. Each one was individually written as:

$$\left[\rho h c_p^2 k_s^2 + \frac{\rho h c_p^2(1-\nu)t^2}{2a^2} - \rho h\omega^2\right] U_{st} + \left[\frac{-\rho h c_p^2(1+\nu)\,\mathrm{i}\,k_s t}{2a}\right] V_{st} + \left[\frac{-\rho h c_p^2 \nu\,\mathrm{i}\,k_s}{a}\right] W_{st} = \frac{-K_z}{ab}\sum_{n=-\infty}^{n=+\infty} d_{s-n} U_{nt}\ ; \tag{22}$$

$$\left[\frac{\rho h c_p^2(1+\nu)\mathrm{i}\,k_s t}{2a}\right] U_{st} + \left[\frac{\rho h c_p^2(1-\nu)k_s^2}{2} + \frac{\rho h c_p^2 t^2}{a^2} - \rho h\omega^2\right] V_{st} + \left[\frac{\rho h c_p^2 t}{a^2}\right] W_{st} = \frac{-K_t}{ab}\sum_{n=-\infty}^{n=+\infty} d_{s-n} V_{nt}\ ; \tag{23}$$

and

$$\left[\frac{\rho h c_p^2 \nu\,\mathrm{i}k_s}{a}\right] U_{st} + \left[\frac{\rho h c_p^2 t}{a^2}\right] V_{st} + \left[\frac{\rho h c_p^2}{a^2} + \frac{\rho h^3 c_p^2 k_s^4}{12} + \frac{\rho h^3 c_p^2 k_s^2 t^2}{6a^2} + \frac{\rho h^3 c_p^2 t^4}{12a^4} - \rho h\omega^2\right] W_{st} = \frac{-K_r}{ab}\sum_{n=-\infty}^{n=+\infty} d_{s-n} W_{nt} + \begin{cases} P_a & s=t=0 \\ 0 & \text{otherwise.}\end{cases} \tag{24}$$

This equation were written in matrix form as:

$$\mathbf{A}(s,t)\mathbf{x}_{st} = \frac{-K_z}{ab}\sum_{n=-\infty}^{n=+\infty}\mathbf{Z}_{s-n}\mathbf{x}_{nt} + \frac{-K_r}{ab}\sum_{n=-\infty}^{n=+\infty}\mathbf{T}_{s-n}\mathbf{x}_{nt} + \frac{-K_r}{ab}\sum_{n=-\infty}^{n=+\infty}\mathbf{R}_{s-n}\mathbf{x}_{nt} + \begin{cases}\mathbf{f} & s=t=0\\ \mathbf{0} & \text{otherwise.}\end{cases} \tag{25}$$

The entries of the matrices and vectors in Eq. (25) are listed in the Appendix. The left-hand side of this equation represents the dynamics of the shell and the right-hand side represents the dynamics of the ring stiffeners acting on the shell and the external load applied to the shell. At this point, all of the axial (s) and radial (t) modes could be combined into a single global matrix and a solution to the wave propagation coefficients could be calculated. However, because the radial modes individually decoupled, it was numerically more efficient to solve each radial mode equation separately and then combine their individual solutions using Eqs. (5), (6), and (7). Eqation (25) was written for all values of s and any single value of t and combined into the matrix equation:

$$\hat{\mathbf{A}}\,\hat{\mathbf{x}} = \frac{-K_z}{ab}\hat{\mathbf{Z}}\,\hat{\mathbf{x}} - \frac{K_t}{ab}\hat{\mathbf{T}}\,\hat{\mathbf{x}} - \frac{K_r}{ab}\hat{\mathbf{R}}\,\hat{\mathbf{x}} + \hat{\mathbf{f}}. \tag{26}$$

In Eq. (26), using five s terms ($-2 \le s \le 2$) and any single t term, $\hat{\mathbf{A}}$ was a block diagonal matrix that contained the dynamics of the tth radial mode of the shell and was written as:

$$\hat{\mathbf{A}} = \begin{bmatrix} \mathbf{A}(-2,t) & \mathbf{0} & \mathbf{0} & \mathbf{0} & \mathbf{0} \\ \mathbf{0} & \mathbf{A}(-1,t) & \mathbf{0} & \mathbf{0} & \mathbf{0} \\ \mathbf{0} & \mathbf{0} & \mathbf{A}(0,t) & \mathbf{0} & \mathbf{0} \\ \mathbf{0} & \mathbf{0} & \mathbf{0} & \mathbf{A}(1,t) & \mathbf{0} \\ \mathbf{0} & \mathbf{0} & \mathbf{0} & \mathbf{0} & \mathbf{A}(2,t) \end{bmatrix}; \tag{27}$$

$\hat{\mathbf{Z}}$ was a rank deficient block partitioned matrix that represented the stiffener forces acting in the longitudinal direction on the shell and was written as:

$$\hat{\mathbf{Z}} = \begin{bmatrix} \mathbf{Z}_0 & \mathbf{Z}_{-1} & \mathbf{Z}_{-2} & \mathbf{Z}_{-3} & \mathbf{Z}_{-4} \\ \mathbf{Z}_1 & \mathbf{Z}_0 & \mathbf{Z}_{-1} & \mathbf{Z}_{-2} & \mathbf{Z}_{-3} \\ \mathbf{Z}_2 & \mathbf{Z}_1 & \mathbf{Z}_0 & \mathbf{Z}_{-1} & \mathbf{Z}_{-2} \\ \mathbf{Z}_3 & \mathbf{Z}_2 & \mathbf{Z}_1 & \mathbf{Z}_0 & \mathbf{Z}_{-1} \\ \mathbf{Z}_4 & \mathbf{Z}_3 & \mathbf{Z}_2 & \mathbf{Z}_1 & \mathbf{Z}_0 \end{bmatrix}; \tag{28}$$

$\hat{\mathbf{T}}$ was a rank deficient block partitioned matrix that represented the stiffener forces acting in the tangential direction on the shell and was written as:

$$\hat{\mathbf{T}} = \begin{bmatrix} \mathbf{T}_0 & \mathbf{T}_{-1} & \mathbf{T}_{-2} & \mathbf{T}_{-3} & \mathbf{T}_{-4} \\ \mathbf{T}_1 & \mathbf{T}_0 & \mathbf{T}_{-1} & \mathbf{T}_{-2} & \mathbf{T}_{-3} \\ \mathbf{T}_2 & \mathbf{T}_1 & \mathbf{T}_0 & \mathbf{T}_{-1} & \mathbf{T}_{-2} \\ \mathbf{T}_3 & \mathbf{T}_2 & \mathbf{T}_1 & \mathbf{T}_0 & \mathbf{T}_{-1} \\ \mathbf{T}_4 & \mathbf{T}_3 & \mathbf{T}_2 & \mathbf{T}_1 & \mathbf{T}_0 \end{bmatrix}; \tag{29}$$

$\hat{\mathbf{R}}$ was a rank deficient block partitioned matrix that represented the stiffener forces acting in the radial direction on the shell and was written as:

$$\hat{\mathbf{R}} = \begin{bmatrix} \mathbf{R}_0 & \mathbf{R}_{-1} & \mathbf{R}_{-2} & \mathbf{R}_{-3} & \mathbf{R}_{-4} \\ \mathbf{R}_1 & \mathbf{R}_0 & \mathbf{R}_{-1} & \mathbf{R}_{-2} & \mathbf{R}_{-3} \\ \mathbf{R}_2 & \mathbf{R}_1 & \mathbf{R}_0 & \mathbf{R}_{-1} & \mathbf{R}_{-2} \\ \mathbf{R}_3 & \mathbf{R}_2 & \mathbf{R}_1 & \mathbf{R}_0 & \mathbf{R}_{-1} \\ \mathbf{R}_4 & \mathbf{R}_3 & \mathbf{R}_2 & \mathbf{R}_1 & \mathbf{R}_0 \end{bmatrix}; \quad (30)$$

$\hat{\mathbf{f}}$ was the vector for the ring load that contained the system excitation and was equal to:

$$\hat{\mathbf{f}} = \{ \ \mathbf{0}^{\mathrm{T}} \quad \mathbf{0}^{\mathrm{T}} \quad \mathbf{f}^{\mathrm{T}} \quad \mathbf{0}^{\mathrm{T}} \quad \mathbf{0}^{\mathrm{T}} \ \}^{\mathrm{T}}; \quad (31)$$

$\hat{\mathbf{x}}$ was the vector of unknown wave propagation coefficients and was written as:

$$\hat{\mathbf{x}} = \{ \ \mathbf{x}_{-2,t}^{\mathrm{T}} \quad \mathbf{x}_{-1,t}^{\mathrm{T}} \quad \mathbf{x}_{0,t}^{\mathrm{T}} \quad \mathbf{x}_{1,t}^{\mathrm{T}} \quad \mathbf{x}_{2,t}^{\mathrm{T}} \ \}^{\mathrm{T}}; \quad (32)$$

where,

$$\mathbf{x}_{st} = \{ \ U_{st} \quad V_{st} \quad W_{st} \ \}^{\mathrm{T}}. \quad (33)$$

The three stiffness matrices from the ring stiffener could be combined into a single matrix, however, they were kept separate to facilitate an understanding of the dynamics of the system. Note from Eq. (26) that the ring stiffener's forces coupled the axial modes of the shell together and did not respond independently, like they would have if the shell had been unstiffened. The solution to the t indexed wave propagation coefficients in Eq. (26) were found by:

$$\hat{\mathbf{x}} = \left[\hat{\mathbf{A}} + \frac{K_z}{ab}\hat{\mathbf{Z}} + \frac{K_t}{ab}\hat{\mathbf{T}} + \frac{K_r}{ab}\hat{\mathbf{R}} \right]^{-1} \hat{\mathbf{f}}. \quad (34)$$

These were then inserted back into Eqs. (5), (6), and (7) to yield the displacement field of the shell at any location. The dispersion curves of the system were calculated using:

$$\det \left[\hat{\mathbf{A}} + \frac{K_z}{ab}\hat{\mathbf{Z}} + \frac{K_t}{ab}\hat{\mathbf{T}} + \frac{K_r}{ab}\hat{\mathbf{R}} \right] = 0; \quad (35)$$

Although the curves generated in the wavenumber-frequency space were typically too modally dense to fully understand the behavior of the free waves.

3. MODEL VERIFICATION AND CONVERGENCE CRITERIA

The model that was developed in Sections 2 was validated by comparing it to finite element analysis. In this example problem, the following cylinder parameters were used: Young's modulus $E = 1 \times 10^7$ Nm^{-2}, Poisson's ratio $\nu = 0.48$, density $\rho = 1200$ kgm^{-3}, radius $a = 0.1$ m, and thickness $h = 0.001$ m. Additionally, the following stiffener properties were used: periodicity $L = 5$ m, length $b = 0.5$ m, axial spring constant $K_z = 1.59 \times 10^5$ Nm^{-1}, and radial spring constant $K_r = 1.59 \times 10^5$ Nm^{-1}. The following loading parameters were used: axial wavenumber $k = 0$ and the magnitude of the applied pressure $P_a = 1$ Nm^{-2}. Figures 3 and 4 were the radial displacement and the longitudinal displacement of the shell at (top) 30 Hz, (middle) 60 Hz, and (bottom) 90 Hz versus spatial position. In these plots, the solid line was the analytical model created using 201 axial terms (max $|n| = 100$) and one radial term ($q = 0$) and the circular markers were the finite element models that used discrete springs to model the stiffener forces. The finite element results were produced using the COMSOL Multiphysics finite element program. This model consisted of an axisymmetric shell with a set of linear translational springs attached to the area between $z = 0$ and $z = b = 0.5$ m to mimic the behavior of the stiffener. This approach reduced the number of necessary degrees of freedom and allowed for an examination of the effect of mismatch between the spring and shell stiffness without the inclusion of inertial effects of the stiffener. The finite element model consisted of 20001 nodes, 20000 elastic axisymmetric continuum elements, 2000 translational springs in the radial direction, and 2000 translational springs in the longitudinal direction. By enforcing user defined pointwise constraints, the model was nodally constrained so that the behavior would be periodic on the interval $[0, L]$. The constraint expression between the terminal $[0, L]$ nodes was one of Floquet type periodicity, wherein the wavenumber relating their translational degrees of freedom was that of the applied excitation. There was no rotational spring constant, as the model was axisymmetric and the displacements in the angular direction were zero. A single radial term was sufficient to model the dynamics for this case because the excitation was a ring load. The displacement differences between the two models were almost zero at all longitudinal locations.

Convergence of the summations listed in Eqs. (5) to (7) was an open issue, as the rate of convergence was dependent on many of the model parameters. However, for the modeled system presented in this paper, several generalized statements could be made. The number of terms needed for convergence was directly related to the mismatch between the stiffness of the shell and the stiffness of the stiffeners. If the stiffeners were not present, then only a single term (the $n = 0$ and $q = 0$ term) was needed for the series to converge to the proper solution (for a ring load). The influence of the mismatch between the cylinder stiffness and the stiffener stiffness could be studied with respect to the convergence of the solution. Figure 5 was a plot of the radial displacement convergence of the system versus number of terms and frequency for stiffener constants of (a) $K_z = K_r = 1 \times 10^4$ Nm^{-1}, (b) $K_z = K_r = 1 \times 10^5$ Nm^{-1}, and (c) $K_z = K_r = 1 \times 10^6$ Nm^{-1}. This convergence metric was calculated using the equation:

$$C(N, f) = 20 \log_{10} \left[\frac{1}{J} \sum_{j=1}^{J} \left| \frac{W^C(x_j) - W^N(x_j)}{W^C(x_j)} \right| \right]; \quad (36)$$

where $W^C(x_j)$ was the radial displacement calculated using 401 axial terms for each series (max $|n| = 200$) and a single radial term ($q = 0$), $W^N(x_j)$ was the radial displacement

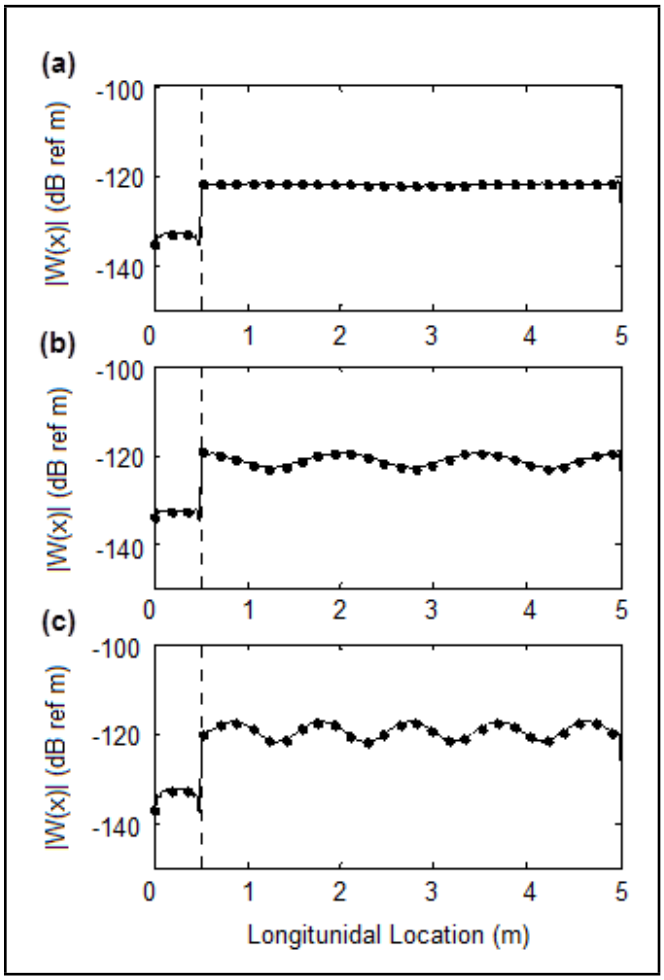

Figure 3. Radial displacement of the shell at (a) 30 Hz, (b) 60 Hz and (c) 90 Hz versus longitudinal location. The solid line is the analytical model and the circular markers are the finite element model with discrete springs modeling the stiffener. The dashed line $x = b = 0.5$ m denotes the location of the end of the stiffener.

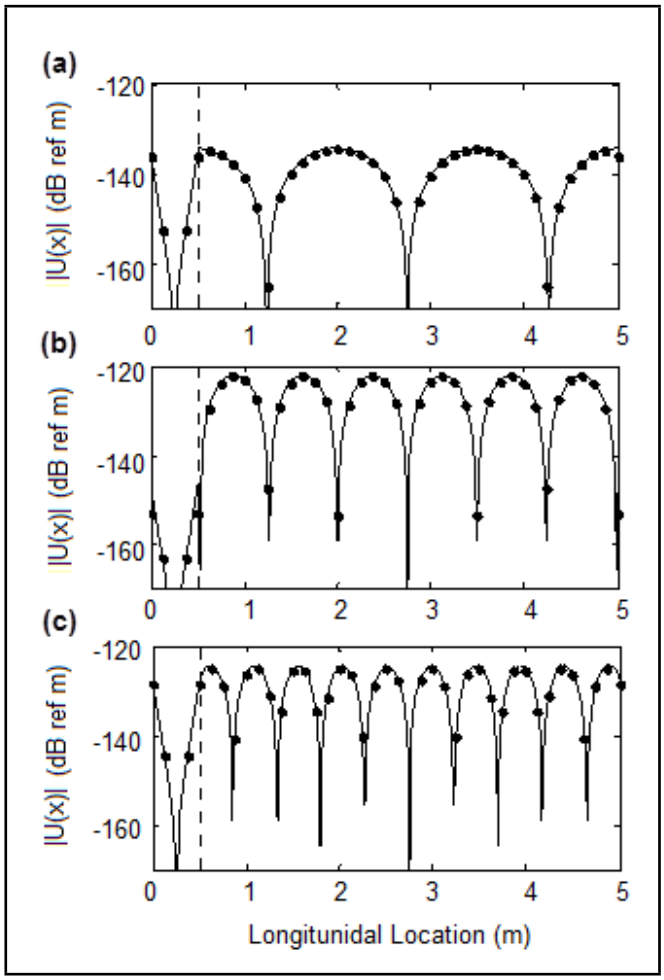

Figure 4. Longitudinal displacement of the shell at (a) 30 Hz, (b) 60 Hz and (c) 90 Hz versus longitudinal location. The solid line is the analytical model and the circular markers are the finite element model with discrete springs modeling the stiffener. The dashed line $x = b = 0.5$ m denotes the location of the end of the stiffener.

calculated using $2N + 1$ terms for each series, x_j was the location of the jth calculation, J was equal to 15, and the spatial locations were equally spaced from 0 to L. The region in white was -40 dB (or lower), which corresponded to a one percent (or less) normalized difference between the two solutions. As the ring stiffeners became stiffer, more terms were needed for the series to converge. It was useful to generate a plot similar to Fig. 5 in order to understand the decay of energy in the higher order terms and ensure convergence for any set of parameters that were to be modeled.

4. EXAMPLE PROBLEM USING AN INCIDENT PLANE WAVE LOAD

An example problem of system response to an incident plane wave load was then investigated. The cylinder parameters from Section 3 were used to calculate the displacement fields. For a plane wave load, the vector $\hat{\mathbf{f}}$ in Eq. (26) was equal to:

$$\hat{\mathbf{f}} = \{ \ \mathbf{0}^{\mathrm{T}} \quad \mathbf{0}^{\mathrm{T}} \quad \mathbf{f}_t^{\mathrm{T}} \quad \mathbf{0}^{\mathrm{T}} \quad \mathbf{0}^{\mathrm{T}} \ \}^{\mathrm{T}}; \tag{37}$$

The entries of the vector in Eq. (37) are listed in the Appendix. The wave speed of the plane wave load was 343 ms^{-1} and the frequency of excitation is 60 Hz. Fig. 6 is a plot of the cylinder displacement in the (a) longitudinal direction, (b) the tangential direction, and (c) the radial direction versus spatial location z and angle θ using stiffness constants of the spacer parameters in Section 3, as this corresponded to a relatively soft elastomeric stiffener. The scale of the plot was in dB ref m. Figure 7 is a plot of the cylinder displacement in the (a) longitudinal direction, (b) the tangential direction, and (c) the radial direction versus spatial location z and angle θ using stiffness constants of $K_z = 2.46 \times 10^5$ Nm^{-1}, $K_t = 4.33 \times 10^5$ Nm^{-1}, and $K_r = 6.28 \times 10^5$ Nm^{-1}, which were derived from spacer properties of $E_S = 1.00 \times 10^8$ Nm^{-2}, $G_S = 3.45 \times 10^7$ Nm^{-2}, and $a_S = 0.0980$ m, $A_S = 0.0012$ m^2, $I_\theta = 1.18 \times 10^{-5}$ m^4, and $I_Z = 5.91 \times 10^{-6}$ m^4, using the approximations:

$$K_z \approx \frac{A_s E_s}{b}; \tag{38}$$

$$K_t \approx \frac{G_s I_\theta}{a_s^3}; \tag{39}$$

and

$$K_r \approx \frac{E_s I_z}{a_s^3}. \tag{40}$$

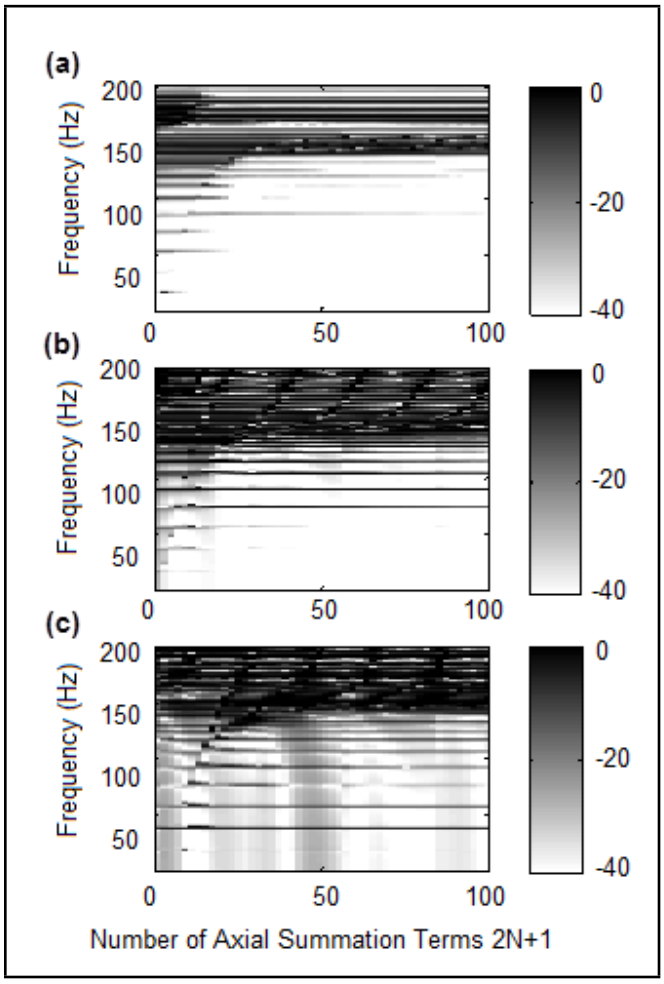

Figure 5. Convergence of the radial displacement versus total number of summation terms in each series and frequency for cylinder with periodic ring stiffeners expressed in a decibel scale. The stiffener constants used in the model were (a) $K_z = K_r = 1 \times 10^4$ Nm^{-1}, (b) $K_z = K_r = 1 \times 10^5$ Nm^{-1}, and (c) $K_z = K_r = 1 \times 10^6$ Nm^{-1}.

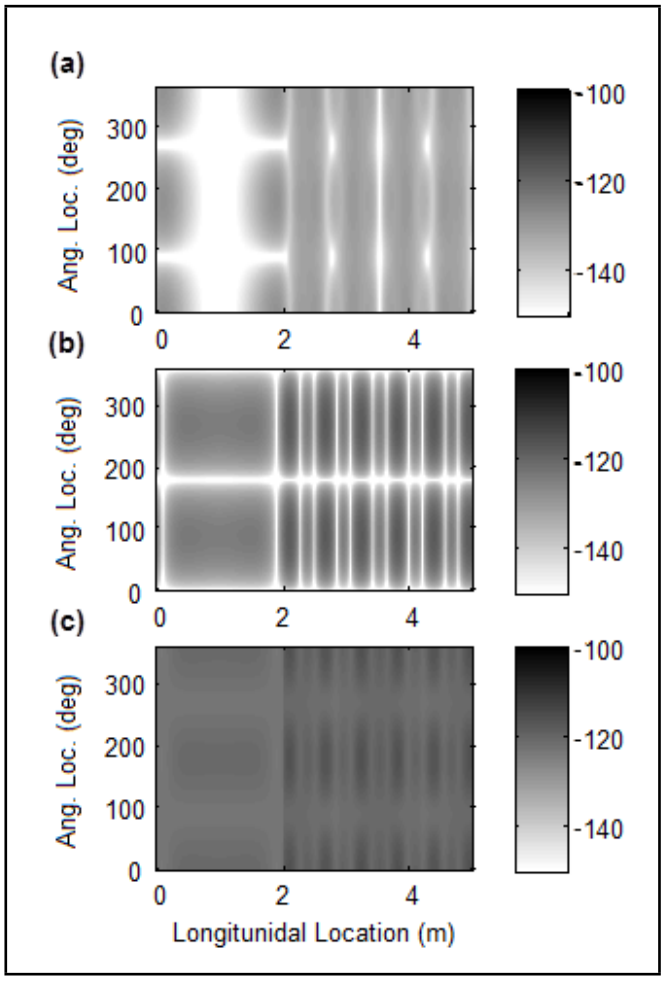

Figure 6. Displacement of the shell in the (a) longitudinal direction, (b) tangential direction and (c) radial direction modeled with a soft stiffener at 60 Hz versus longitudinal location and angular location. The scale of the plot is in dB ref m.

These values corresponded to a relatively hard elastomeric stiffener. The scale of the plot was in dB ref m. A comparison of Figs. 6 and 7 shows that as the stiffener value increased, the displacements had more spatial variation. Additionally, the effect of the hard stiffener was clearly discernable from 0 to 2.0 m in the displacement fields in Fig. 7, whereas it was less observable for the case of the soft stiffener. Figure 8 is a plot of the normalized magnitude of the (a) longitudinal coefficients, (b) tangential coefficients, and (c) radial coefficients versus longitudinal index s and tangential index t for the soft stiffener. Figure 9 is a plot of the normalized magnitude of the (a) longitudinal coefficients, (b) tangential coefficients, and (c) radial coefficients versus longitudinal index s and tangential index t for the hard stiffener. Because both of these plots were normalized, their scales were in dB. These plots were included so that the individual mode contributions could be discerned. Note that the higher order modes for the system with the hard stiffener had more energy than the system with the soft stiffener. Numerical simulations suggested that when the values of the higher order modes were approximately 80 dB below the value of the maximum mode, the displacement summations converged. One final note was that if the external load was some form other than a normal ring load or plane wave, then its analytical form had to be transformed into a series solution and inserted into the right hand side of Eq. (22) for longitudinal excitation, Eq. (23) for tangential excitation, and Eq. (24) for radial excitation.

5. CONCLUSIONS

This paper has derived a model of an infinite length cylindrical shell with finite length and periodically spaced ring stiffeners. Using a dynamic formulation of the Donnell shell equations, the stiffener effects are included as forces on the right hand side of the longitudinal, tangential, and radial equations of motion using Heaviside step functions. The displacements are then written as double summations with unknown coefficients multiplied by a tangential and a longitudinal function. These are inserted into the equations of motion and the Heaviside functions are replaced with their Fourier series representations. These equations are then orthogonalized on both the angular and longitudinal domains, resulting in sets of algebraic double indexed equations. These equations are assembled into a global matrix equation and the result is a solution to the displacement fields. Two example problems are included and dis-

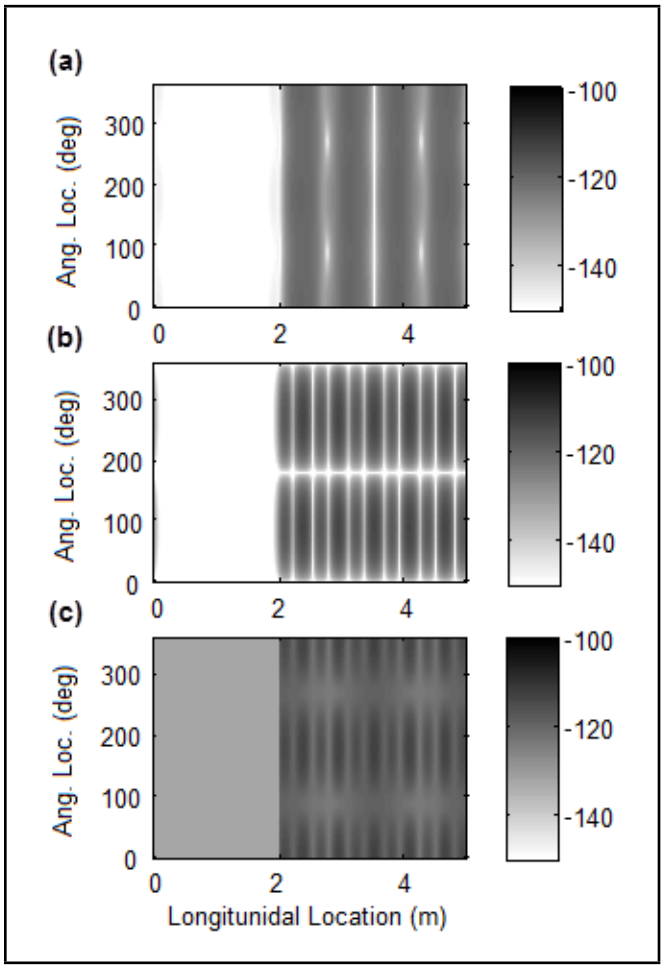

Figure 7. Displacement of the shell in the (a) longitudinal direction, (b) tangential direction and (c) radial direction modeled with a hard stiffener at 60 Hz versus longitudinal location and angular location. The scale of the plot is in dB ref m.

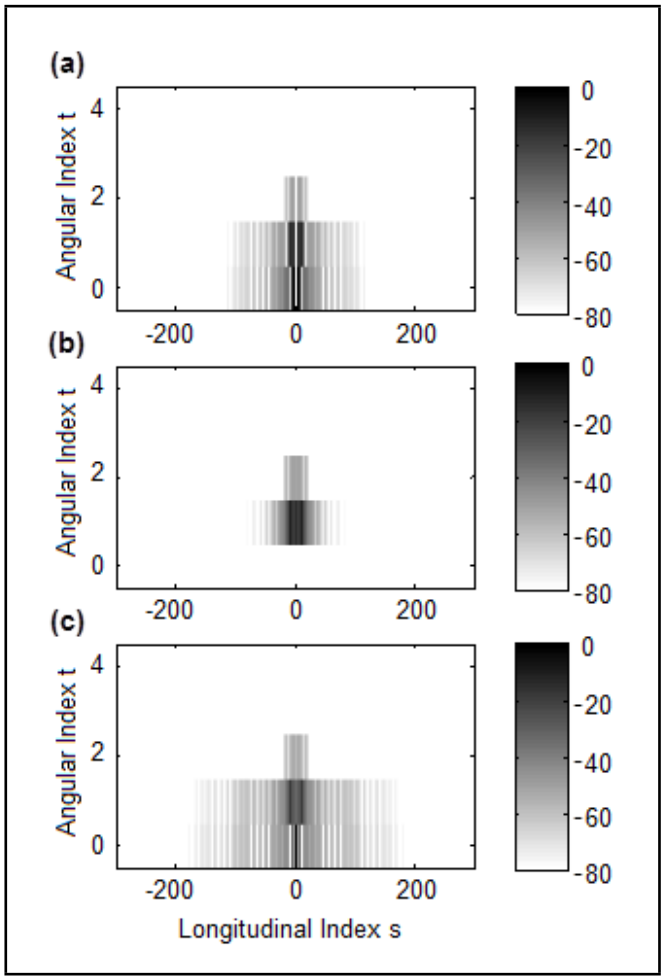

Figure 8. Normalized magnitude of the (a) longitudinal coefficients, (b) tangential coefficients and (c) radial coefficients versus longitudinal index and angular index for the soft stiffener. The scale of the plot is in dB.

cussed: the system subjected to a ring load and the system subjected to a plane wave. The ring load example is verified with finite element results. The problem of varying the stiffness of the stiffeners is studied and the corresponding changes in the shell displacements are examined. Finally, the modal distribution of the displacement field and convergence of the double summations is discussed.

ACKNOWLEDGEMENTS

This paper was funded by the Naval Undersea Warfare Center's In-House Laboratory Independent Research Program.

REFERENCES

[1] Graf, K. F. *Wave Motion in Elastic Solids,* Dover Publications, New York, New York (1975).

[2] Junger, M. C. and Feit, D. *Sound, Structures, and Their Interaction,* MIT Press, Cambridge, Massachusetts (1986).

[3] Gazis, D. C. Three-dimensional investigation of the propagation of waves in hollow circular cylinders. *I. Analytical foundation, J. Acoust. Soc. Am.,* **31** (5), 568–573, (1959). http://dx.doi.org/10.1121/1.1907753

[4] Ding, H., Chen, W., and Zhang, L. *Elasticity of Transversely Isotropic Materials,* Springer, Netherlands, (2006) http://dx.doi.org/10.1007/1-4020-4034-2

[5] Peloquin, M. S. Forced harmonic vibration of the generally orthotropic cylindrical shell with inner and outer fluid loading, Naval Undersea Warfare Center Technical Report 10,199, New London, Connecticut, (1992).

[6] Bennett, M. S. and Accorsi, M. L. Free wave propagation in periodically ring stiffened cylindrical shells, *Journal of Sound and Vibration,* **171** (1), 49–66, (1994). http://dx.doi.org/10.1006/jsvi.1994.1103

[7] Al-Najafi, A. M. J. and Warburton, G. B. Free vibration of ring-stiffened cylindrical shells, *J. Sound Vib.*, **13** (1), 9–25, (1970). http://dx.doi.org/10.1016/s0022-460x(70)80076-1

[8] Jafari, A. A. and Bagheri, M. Free vibration of non-uniformly ring stiffened cylindrical shells using analytical, experimental and numerical methods, *Thin-Walled Struct.*, **44** (1), 82–90, (2006). http://dx.doi.org/10.1016/j.tws.2005.08.008

[9] Beskos, D. E. and Oates, J. B. Dynamic analysis of ring-stiffened circular cylindrical shells, *J. Sound Vib.*,

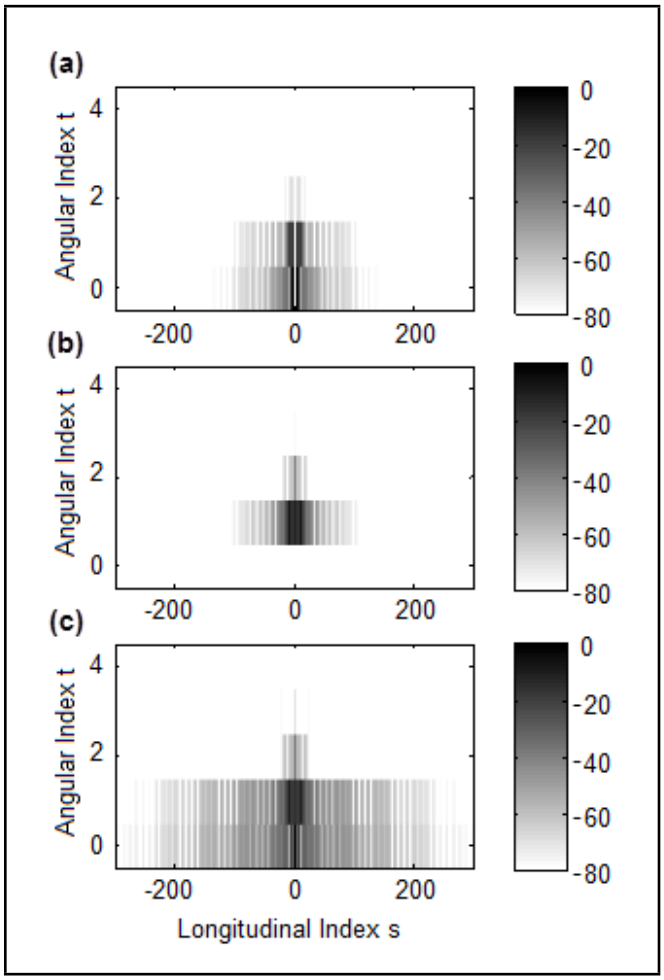

Figure 9. Normalized magnitude of the (a) longitudinal coefficients, (b) tangential coefficients and (c) radial coefficients versus longitudinal index and angular index for the hard stiffener. The scale of the plot is in dB.

75 (1), 1–15, (1981). http://dx.doi.org/10.1016/0022-460x(81)90232-7

[10] Burroughs, C. B. Acoustic radiation form fluid-loaded infinite circular cylinders with doubly periodic ring supports, *J. Acoust. Soc. Am.*, **75** (3), 715–722, (1984). http://dx.doi.org/10.1121/1.390582

[11] Hodges, C. H. Power, J. and Woodhouse, J. The low frequency vibration of a ribbed cylinder, Part 1: theory, *J. Sound Vib.*, **101** (2), 219–235, (1985). http://dx.doi.org/10.1016/s0022-460x(85)81217-7

[12] Mead, D. J. and Bardell, N. S. Free vibration of a thin cylindrical shell with periodic circumferential stiffeners, *J. Sound Vib.*, **115** (3), 499–520, (1987). http://dx.doi.org/10.1016/0022-460x(87)90293-8

[13] Gan, L., Li, X., and Zhang, Z. Free vibration analysis of ring-stiffened cylindrical shells using wave propagation approach, *J. Sound Vib.*, **326** (3–5), 633–646, (2009). http://dx.doi.org/10.1016/j.jsv.2009.05.001

[14] Pan, Z., Li, X., and Ma, J. A study on free vibration of a ring-stiffened thin circular cylindrical shell with arbitrary boundary conditions, *J. Sound Vib.*, **314** (1–2), 330–342, (2008). http://dx.doi.org/10.1016/j.jsv.2008.01.008

APPENDIX — MATRIX AND VECTOR ENTRIES

The entries of the matrices and vectors in the text are listed below. The entries of $\mathbf{A}(s,t)$ in Eq. (25) are

$$a_{1,1} = \rho h\omega^2 - \rho h c_p^2 k_s^2 - \frac{\rho h c_p^2 (1-\nu) t^2}{2a^2}; \tag{A.1}$$

$$a_{1,2} = \frac{-\rho h c_p^2 (1+\nu) k_s t}{2a}; \tag{A.2}$$

$$a_{1,3} = \frac{\rho h c_p^2 \nu \, \mathrm{i} k_s}{a}; \tag{A.3}$$

$$a_{2,1} = \frac{-\rho h c_p^2 (1+\nu) k_s t}{2a}; \tag{A.4}$$

$$a_{2,2} = \rho h\omega^2 - \frac{\rho h c_p^2 (1-\nu) k_s^2}{2} - \frac{\rho h c_p^2 t^2}{a^2}; \tag{A.5}$$

$$a_{2,3} = \frac{\rho h c_p^2 \, \mathrm{i} t}{a^2}; \tag{A.6}$$

$$a_{3,1} = \frac{\rho h c_p^2 \nu \, \mathrm{i} k_s}{a}; \tag{A.7}$$

$$a_{3,2} = \frac{\rho h c_p^2 \, \mathrm{i} t}{a^2}; \tag{A.8}$$

and

$$a_{3,3} = \frac{\rho h c_p^2}{a^2} + \frac{\rho h^3 c_p^2 k_s^4}{12} + \frac{\rho h^3 c_p^2 k_s^2 t^2}{6a^2} + \frac{\rho h^3 c_p^2 t^4}{12a^4} - \rho h\omega^2. \tag{A.9}$$

The non-zero entry of $\mathbf{Z}_m$ in Eq. (28) is

$$z_{1,1} = d_m. \tag{A.10}$$

The non-zero entry of $\mathbf{T}_m$ in Eq. (29) is

$$t_{2,2} = d_m. \tag{A.11}$$

The non-zero entry of $\mathbf{R}_m$ in Eq. (30) is

$$r_{3,3} = d_m. \tag{A.12}$$

The non-zero entry of $\mathbf{f}$ in Eq. (25) is

$$f_{3,1} = P_a. \tag{A.13}$$

The non-zero entry of $\mathbf{f}_t^T$ in Eq. (37) is

$$\mathbf{f}_t^{\mathrm{T}} = \left\{ \begin{array}{ccc} 0 & 0 & P_a \, \mathrm{i}^t \varepsilon_t \, \mathrm{J}_t \left(\frac{\omega c}{a}\right) \end{array} \right\}^{\mathrm{T}}. \tag{A.14}$$

Aeroelastic Analysis of Unrestrained Aircraft Wing with External Stores Under Roll Maneuver

Seyed Ahmad Fazelzadeh

Faculty of Mechanical Engineering, Shiraz University, Molla Sadra Ave, Shiraz, Iran. PO Box: 71345

Amir Hosein Ghasemi

Mechanical Engineering Department, Islamic Azad University, Shahr-Babak Branch, Daneshgah Ave, Shahr-Babak, Iran. PO Box: 18313

Abbas Mazidi

Mechanical Engineering Department, Yazd University, Daneshgah Ave, Yazd, Iran. PO Box: 47948

(Received 29 September 2014; accepted: 20 January 2015)

This paper discusses our study on the flutter of an unrestrained aircraft wing carrying a fuselage at its semispan and arbitrary placed external stores under roll maneuver. Maneuver terms are combined in the governing equations which are obtained using the Hamilton's principle. The wing is represented by a classical beam and incorporates bending-torsion flexibility. Theodorsen unsteady aerodynamic pressure loadings are considered to simulate the aeroelastic loads. The Galerkin method is subsequently applied to convert the partial differential equations into a set of ordinary differential equations. Numerical simulations are validated against several previous published results and good agreement is observed. In addition, simulation results are presented to show the effects of the roll angular velocity, fuselage mass, external stores mass, and their locations on the wing flutter of an aircraft in free-flight condition. Parametric studies show that the predicted flutter boundaries are very sensitive to the aircraft rigid body roll angular velocity, fuselage mass and external stores mass and locations.

NOMENCLATURE

b	Wing semi chord
e_F	Distance between the fuselage center of gravity and wing elastic axis
e_p	Distance between the store center of gravity and wing elastic axis
E	Young's modulus
G	Shear modulus
I	Wing cross-section moment of inertia
J	Wing cross-section polar moment of inertia
l	Wing length
L	Wing sectional lift
m	Mass of the wing per unit length
M	Aerodynamic moment
$\mathbf{R}_{w_i}$	Displacement vector of an arbitrary point of wings
T	Kinetic energy
U	Strain energy
v_f	Nondimensional flutter speed
w_i	Bending displacement
x_e, y_e, z_e	The external mass location in x, y and z directions, respectively
δ	Variational operator
ε_{ij}	Strain component
Λ	Sweep angle
θ_i	Twist angle
ρ	Density of the wing
ρ_∞	Air density
σ_{ij}	Stress component
ω_f	Flutter frequency
ω_θ	Torsional frequency
Ω	Roll angular velocity

1. INTRODUCTION

The flutter prediction of an unrestrained aircraft wing with stores is of paramount importance for the analysis and design of an aircraft. Clearly, estimating the aeroelastic instabilities of such aircraft with different wing configurations is critical to establish the flight envelope of newly designed aircrafts.

Many of the previous efforts made to simulate wing flutter have considered uniform straight wings with external stores. One of the first works devoted to the aeroelasticity of aircraft wings with external store is the paper by Goland and Luke on the determination of the flutter speed of a uniform cantilever wing with tip mass.[1] They verified the flutter speed by integration of the differential equations of the wing motion. Harry and Charles[2] analyzed the flutter of a uniform wing and made a comparison between the analytical and the experimental results. Lottati considered the aeroelastic stability of a swept wing with tip weights for an unrestrained vehicle.[3] In his work, a composite wing has been studied, and it was observed that flutter occurs at a lower speed as compared with a clean wing configuration. Gern and Librescu have made some efforts to show the effects of externally mounted masses on the static and dynamic aeroelasticity of advanced swept cantilevered wings.[4,5] The dynamic response of adaptive cantilevered beams carrying externally mounted stores and exposed to time-dependent external excitations has been con-

sidered by Na and Librescu.[6] Moreover, Librescu and Song[7] investigated the free vibration and dynamic response to external time-dependent loads of aircraft wings carrying eccentrically located heavy stores. They have modeled the wing as a thin-walled anisotropic composite beam. Also, Edwards and Wieseman[8] studied the flutter and divergence of three check cases that include unrestrained airfoils and wing models. The bending-torsional flutter characteristics of an aircraft wing containing an arbitrarily placed mass under a follower force have been studied by Fazelzadeh et al.[9] They showed the important influence of the location and magnitude of the store mass and the follower force on the flutter speed and frequency of the wing. Also, Mazidi and Fazelzadeh[10] investigated the flutter of an aircraft wing with a powered engine. They confirmed that the engine thrust and locations have a considerable effect on the wing aeroelastic stability region.

Although these works and several others addressed the problem of the wing-store aeroelasticity, the effect of the aircraft maneuvers on the unrestrained aircraft wing instability has not received much attention in the literature and only few works about the maneuver effects on the aeroelastic behavior of cantilever wing-stores configuration have been conducted.[11,12] The maneuver has a significant influence on the dynamic response and instability of the wing-store configuration, especially for unrestrained aircraft wing. Since rigid body rotations due to maneuver angular velocities, such as the one produced by a roll maneuver, can adversely affect the aircraft aeroelastic stability region, it is critical to include maneuvering angular velocities in aeroelastic analysis.

To add to the aforementioned bulk of literature in this field, the aeroelastic modeling and flutter study of an unrestrained aircraft under roll maneuver is considered in this study. The aircraft is modeled as a wing carrying a fuselage at its semispan and arbitrarily placed external stores.

2. GOVERNING EQUATIONS

An unrestrained aircraft with swept wings, shown in Fig. 1, is considered. As it can be seen in Fig. 1(b) the aircraft fuselage is modeled as a concentrated mass and inertia located at the center of the unrestrained swept wings. The structural flexibility as well as the roll angular velocity is taken into account when deriving the aeroelastic governing equations. The wing model is valid for long, straight, homogeneous beams and is derived based on the Goland wing model.

The equations of motion and boundary conditions are derived using Hamilton's variational principle that may be expressed as:[13]

$$\int_{t_1}^{t_2} \left[\delta U_T - \delta T_T - \delta W_T\right] dt = 0,$$
$$\delta w = \delta\theta = 0 \quad \text{at} \quad t = t_1 = t_2; \tag{1}$$

where U and T are strain energy and kinetic energy, and W is the work done by non-conservative forces. Also, the subscript 'T' means the total system. The use of Hamilton's principle is especially convenient in cases of unusual boundary conditions because the equation(s) of motion and boundary conditions are determined in a unified procedure. Therefore, the Hamilton's

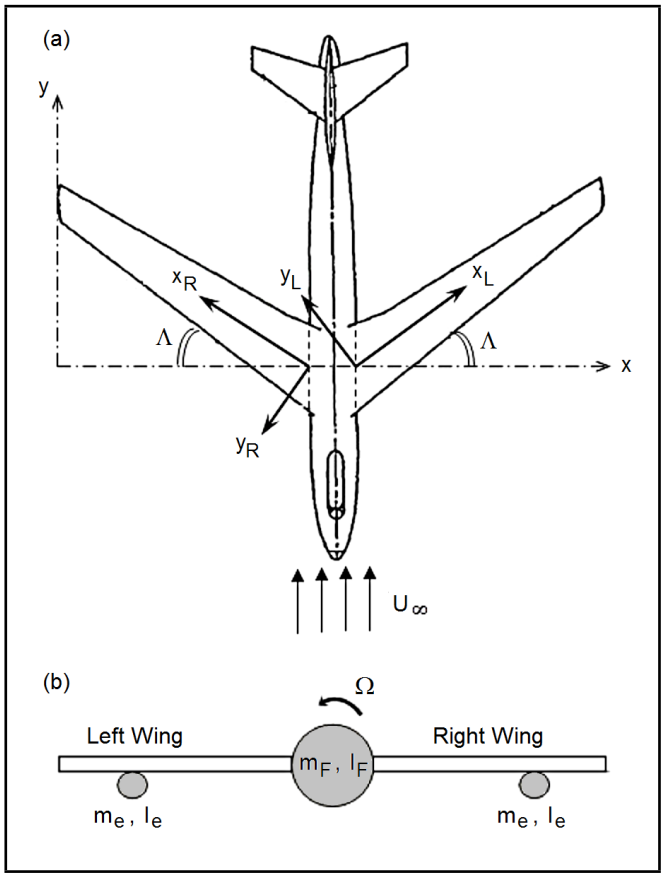

Figure 1. Schematic of an unrestrained aircraft wing under roll maneuver, (a) Top view; (b) Front view.

principle yields the equations of motion in the form of partial differential equations with accompanying boundary conditions.

The kinetic energy can be divided into three parts: wing, fuselage, and store, i.e. $T_T = T_w + T_e + T_F$. The subscripts w, e, and F identify the wing, externally mounted mass, and aircraft fuselage, respectively. The first variation of the wing kinetic energy is:

$$\delta T_w = \delta T_{w_1} + \delta T_{w_2}; \tag{2}$$

where δT_{w_1} and δT_{w_2} are the first variation of the right and left wing kinetic energy, respectively. Also,

$$\delta T_{w_1} = \int_0^l \iint_A \rho \dot{\mathbf{R}}_{w_1} \delta\dot{\mathbf{R}}_{w_1}\, dx\, dA;$$
$$\delta T_{w_2} = \int_0^l \iint_A \rho \dot{\mathbf{R}}_{w_2} \delta\dot{\mathbf{R}}_{w_2}\, dx\, dA. \tag{3}$$

$\mathbf{R}_w$'s are displacement vectors of arbitrary points of the right and left wings that are given by

$$\mathbf{R}_{w_1} = \mathbf{R}_{O_1} + \mathbf{r}_{w_1} = (R_X \cos\Lambda - R_Y \sin\Lambda)\mathbf{i}_1 + (R_X \sin\Lambda + R_Y \cos\Lambda)\mathbf{j}_1 + [w_1 + (y_1 - ab)\theta_1 - R_Z]\mathbf{k}_1;$$
$$\mathbf{R}_{w_2} = \mathbf{R}_{O_2} + \mathbf{r}_{w_2} = (R_X \cos\Lambda - R_Y \sin\Lambda)\mathbf{i}_2 + (-R_X \sin\Lambda - R_Y \cos\Lambda)\mathbf{j}_2 + [w_2 + (y_2 + ab)\theta_2 - R_Z]\mathbf{k}_2; \tag{4}$$

where $\mathbf{R}_O$'s are the wings root position vector with respect to airplane center of gravity, shown in Fig. 1 and $\mathbf{r}_w$'s are the

position vector of arbitrary points of the wings with respect to the wings root. The velocity vector of any points on the wing can be obtained through transport theorem as below:[14]

$$\dot{\mathbf{R}}_{w_i} = \frac{\partial \mathbf{R}_{w_i}}{\partial t} + (\mathbf{\Omega} \times \mathbf{R}_{w_i}) + \mathbf{V}_{\text{airplane}}. \tag{5}$$

In this equation, two first terms represent the velocity of the point and refer to the coordinate system located on the airplane center of gravity. The third term represents the velocity of the airplane and refers to the inertial reference coordinate system located on Earth:

$$\mathbf{V}_{\text{airplane}} = v_{xa}\hat{\mathbf{I}} + v_{ya}\hat{\mathbf{J}} + v_{za}\hat{\mathbf{K}}. \tag{6}$$

Here it is assumed that the airplane has roll maneuver, so the angular velocity equations of the airplane that refer to right and left wing coordinate systems are:

$$\begin{aligned} \mathbf{\Omega}_1 &= -\Omega \sin\Lambda\, \mathbf{i}_1 + \Omega \cos\Lambda\, \mathbf{j}_1; \\ \mathbf{\Omega}_2 &= -\Omega \sin\Lambda\, \mathbf{i}_2 + \Omega \cos\Lambda\, \mathbf{j}_2. \end{aligned} \tag{7}$$

By substitution of Eqs. (3)–(7) in Eq. (2), the first variation of the wing kinetic energy can be represented. Using the same kinematical procedure, the first variation of the engine kinetic energy can be derived as:

$$\begin{aligned} \delta T_e = {} & \sum_{i=1}^{N} m_e \delta_D(x - x_{ei}) \Big\{ \big[-\ddot{w}_1 - e_p \cos\Lambda \ddot{\theta}_1 - \ddot{H} + R_X \alpha + \\ & 2\alpha R_Y \sin\Lambda \cos\Lambda + \Omega^2 w_1 + \Omega^2 e_p \cos\Lambda \theta_1 - \Omega^2 R_Z \big] \delta w_1 + \\ & \big[-e_p \cos\Lambda \ddot{w}_1 - k_e^2 \cos^2\Lambda \ddot{\theta}_1 - e_p \cos\Lambda \ddot{H} + \\ & e_p \cos\Lambda R_X \alpha + 2\alpha R_Y e_p \sin\Lambda \cos^2\Lambda + e_p \cos\Lambda \Omega^2 w_1 + \\ & k_e^2 \cos^2\Lambda \Omega^2 \theta_1 - e_p \cos\Lambda \Omega^2 R_Z \big] \delta\theta_1 \Big\} + \\ & \sum_{i=1}^{N} m_e \delta_D(x - x_{ei}) \Big\{ \big[-\ddot{w}_2 - e_p \cos\Lambda \ddot{\theta}_2 - \ddot{H} - R_X \alpha + \\ & \Omega^2 w_2 + \Omega^2 e_p \cos\Lambda \theta_2 - \Omega^2 R_Z \big] \delta w_2 + \\ & \big[-e_p \cos\Lambda \ddot{w}_2 - k_e^2 \cos^2\Lambda \ddot{\theta}_2 - e_p \cos\Lambda \ddot{H} - \\ & e_p \cos\Lambda R_X \alpha + e_p \cos\Lambda \Omega^2 w_2 + k_e^2 \cos^2\Lambda \Omega^2 \theta_2 - \\ & e_p \cos\Lambda \Omega^2 R_Z \big] \delta\theta_2 \Big\}. \end{aligned} \tag{8}$$

In this equation, x_e denotes the store distance from the wing root, and e_p is the distance between the engine center of gravity and the wing elastic axis. Also, m_e and k_e are the store mass and radius of gyration, respectively. It should be noted that the velocity vector of any point on the engine, as before, is obtained through transport theorem. Also, the first variation of the fuselage kinetic energy can be derived as:

$$\begin{aligned} \delta T_F &= m_F \vec{V}_F \delta \vec{V}_F \\ &= \big[-m_F \ddot{w}_1 - e_F \ddot{\theta}_1 - \ddot{H} + \Omega^2 w_1 + \Omega^2 e_F \theta_1 \big] \delta w_1 \big|_{x=l} + \\ &\quad \big[-m_F e_F \ddot{w}_1 - m_F k_F^2 \ddot{\theta}_1 - m_F e_F \ddot{H} + m_F e_F \Omega^2 w_1 + \\ &\quad m_F k_F^2 \Omega^2 e_F \theta_1 \big] \delta\theta_1 \big|_{x=l}; \end{aligned} \tag{9}$$

where m_F and k_F are the fuselage mass and radius of gyration, respectively, and e_F is the distance between the fuselage center of gravity and the wing elastic axis.

The strain energy is considered next. The total strain energy, normally, consists of wing, fuselage, and store strain energy. Here, it is assumed that the fuselage and stores are rigid bodies. Consequently, the total strain energy is equal to the wing strain energy. The first variation of the strain energy is:[14]

$$\delta U = \int_V \left[\sigma_{xx} \delta\varepsilon_{xx} + \sigma_{x\eta} \delta\varepsilon_{x\eta} + \sigma_{x\xi} \delta\varepsilon_{x\xi} \right] dx\, dA; \tag{10}$$

where σ_{ij} and ε_{ij} are stress and strain components, respectively. η and ξ are the principal axes of the wing cross section that defines a local coordinate system on the shear center of the cross section.

The use of strain-displacement relations, together with the generalized Hooke's law, permits the strain energy to be expressed in terms of deformation quantities.[15] Using these expressions and integrating by parts, Eq. (10) recasts as:

$$\begin{aligned} \delta U_{w_1} = {} & \int_0^l \Big\{ \left[EI w_1'''' + abEI\theta_1'''' \right] \delta w_1 + \\ & \left[abEI w_1'''' + S\theta_1'''' - GJ\theta_1'' \right] \delta\theta_1 \Big\} dx; \\ \delta U_{w_2} = {} & \int_l^{2l} \Big\{ \left[EI w_2'''' + abEI\theta_2'''' \right] \delta w_2 + \\ & \left[abEI w_2'''' + S\theta_2'''' - GJ\theta_2'' \right] \delta\theta_2 \Big\} dx; \end{aligned} \tag{11}$$

where δU_{w_1} and δU_{w_2} are the right and left wing strain energy, respectively.

The virtual work of the aerodynamic forces acting on the wing may be expressed as:

$$\delta W_{nc} = \int_0^l \left(L_1 \delta w_1 + M_1 \delta\theta_1 \right) dx + \int_l^{2l} \left(L_2 \delta w_2 + M_2 \delta\theta_2 \right) dx; \tag{12}$$

where L and M are aerodynamic lift and moment, respectively. It should be noted here that the engine aerodynamic is not accounted for in governing equations. Aerodynamic lift and moment are derived from Theodorsen's unsteady thin-airfoil theory. These are:

$$\begin{aligned} L(x,t) = {} & -\pi \rho_\infty \omega^2 b^3 \Big[\frac{w}{b} L_{hh} + \frac{\partial w}{\partial x} L_{hh'} + \theta_{\mathit{eff}} L_{h\theta} + \\ & b \frac{\partial \theta_{\mathit{eff}}}{\partial x} L_{h\theta'} \Big]; \end{aligned} \tag{13}$$

$$\begin{aligned} M(x,t) = {} & \pi \rho_\infty \omega^2 b^4 \Big[\frac{w}{b} M_{\theta h} + \frac{\partial w}{\partial x} M_{\theta h'} + \theta_{\mathit{eff}} M_{\theta\theta} + \\ & b \frac{\partial \theta_{\mathit{eff}}}{\partial x} M_{\theta\theta'} \Big]; \end{aligned} \tag{14}$$

where $L_{hh}, L_{hh'}, \ldots, M_{\theta\theta'}$ are the aerodynamic coefficients.[16,17]

By substituting Eqs. (3)–(12) into Eq. (1), and noticing that for every admissible variation $(\delta w_1, \delta\theta_1, \delta w_2, \delta\theta_2)$ the coefficient of these variations must be zero, the aeroelastic governing

equations are obtained as:

$$-EIw_1''''+m\ddot{w}_1+mx_\theta\ddot{\theta}_1+m\ddot{H}-mR_X\alpha- 2mR_Y\alpha\sin\Lambda\cos\Lambda-m\Omega^2w_1-mx_\theta\Omega^2\theta_1+m\Omega^2R_Z+ m_F\big(\ddot{w}_1+e_F\ddot{\theta}_1+\ddot{H}-\Omega^2w_1-\Omega^2e_F\theta_1\big)|_{x=l}+ \sum_{i=1}^{N}m_e\delta_D(x_1-x_{ei})\big(\ddot{w}_1+e_p\cos\Lambda\ddot{\theta}_1+\ddot{H}-R_X\alpha- 2R_Y\alpha\sin\Lambda\cos\Lambda-\Omega^2w_1-\Omega^2e_p\cos\Lambda\theta_1+\Omega^2R_Z\big)- L_1=0; \quad (15)$$

$$-GJ\theta_1''+mx_\theta\ddot{w}_1+I_\theta\ddot{\theta}_1+mx_\theta\ddot{H}-mx_\theta R_X\alpha- 2mx_\theta R_Y\alpha\sin\Lambda\cos\Lambda-mx_\theta\Omega^2w_1-I_\theta\Omega^2\theta_1+mx_\theta\Omega^2R_Z+ \sum_{i=1}^{N}m_e\delta_D(x_1-x_{ei})\big(e_p\cos\Lambda\ddot{w}_1+k_e^2\cos^2\Lambda\ddot{\theta}_1+e_p\cos\Lambda\ddot{H}- e_p\cos\Lambda R_X\alpha-2e_pR_Y\alpha\sin\Lambda\cos^2\Lambda-e_p\cos\Lambda\Omega^2w_1- k_e^2\cos^2\Lambda\Omega^2\theta_1+e_p\cos\Lambda\Omega^2R_Z\big)-M_1=0; \quad (16)$$

$$-EIw_2''''+m\ddot{w}_2+mx_\theta\ddot{\theta}_2+m\ddot{H}-mR_X\alpha- m\Omega^2w_2-mx_\theta\Omega^2\theta_2+m\Omega^2R_Z+ \sum_{i=1}^{N}m_e\delta_D(x_2-x_{ei})\big(\ddot{w}_2+e_p\cos\Lambda\ddot{\theta}_2+\ddot{H}+R_X\alpha-\Omega^2w_2- \Omega^2e_p\cos\Lambda\theta_2+\Omega^2R_Z\big)-L_2=0; \quad (17)$$

$$-GJ\theta_2''+mx_\theta\ddot{w}_2+I_\theta\ddot{\theta}_2+mx_\theta\ddot{H}-mx_\theta R_X\alpha- mx_\theta\Omega^2w_2-I_\theta\Omega^2\theta_2+mx_\theta\Omega^2R_Z+ \sum_{i=1}^{N}m_e\delta_D(x_2-x_{ei})\big(e_p\cos\Lambda\ddot{w}_2+k_e^2\cos^2\Lambda\ddot{\theta}_2+e_p\cos\Lambda\ddot{H}+ e_p\cos\Lambda R_X\alpha-e_p\cos\Lambda\Omega^2w_2-k_e^2\cos^2\Lambda\Omega^2\theta_2+ e_p\cos\Lambda\Omega^2R_Z\big)-M_2=0. \quad (18)$$

3. SOLUTION METHODOLOGY

Due to intricacy of aeroelastic governing equations, it is difficult to get the exact solution. Therefore, in order to solve the aeroelastic governing equations in a general way, the Galerkin's method is used.[18] To this end, w_i, θ_i (bending and torsion generalized coordinates) are represented by means of series of trial functions, φ_{j_i}, that should satisfy the boundary conditions, multiplied by time dependent generalized coordinates, $\mathbf{q}_{j_i}$:

$$w_i=\varphi_{1_i}^T\mathbf{q}_{1_i}; \qquad \theta_i=\varphi_{2_i}^T\mathbf{q}_{2_i}. \quad (19)$$

The following family of orthogonal functions for w and θ is used here:[16]

$$\varphi_{1_i}=\frac{(x/l)^{1+i}\{6+i^2(1-x/l)^2+i[5-6x/l+(x/l)^2]\}}{i(1+i)(2+i)(3+i)};$$
$$\varphi_{2_i}=\sin\Big(\frac{i\pi x}{l}\Big). \quad (20)$$

Table 1. Validation of the flutter speed and frequency for a wing in free flight condition.

Method	Flutter Speed (m/s)	Error (%)	Flutter Frequency (rad/s)	Error (%)
Exact (Goland & Luke[1])	292.72	—	19.17	—
Lottati[3]	289.68	1.04	19.42	1.3
Gern & Librescu[5]	293.61	0.31	21.68	13.09
Present	308.72	5.46	18.30	4.53

Two bending modes and two torsion modes are considered for each wing. By applying the Galerkin procedure on governing equations and using orthogonal properties in the required integrations, the following set of ordinary differential equations are obtained:

$$\mathbf{M}\ddot{\mathbf{q}}+\mathbf{C}\dot{\mathbf{q}}+\mathbf{K}\mathbf{q}=0. \quad (21)$$

Herein, $\mathbf{M}$, $\mathbf{C}$, and $\mathbf{K}$ denote the mass matrix, the damping matrix and the stiffness matrix, respectively, while $\mathbf{q}$ is the overall vector of generalized coordinates. Finally, Eq. (21) converts to

$$\dot{\mathbf{Z}}=[\mathbf{A}]\mathbf{Z}; \quad (22)$$

where the state vector $\mathbf{Z}$ is defined as

$$\mathbf{Z}=\begin{Bmatrix}\mathbf{q}^T & \dot{\mathbf{q}}^T\end{Bmatrix}^T; \quad (23)$$

and the system matrix $[\mathbf{A}]$ has the form

$$[\mathbf{A}]=\begin{bmatrix}[\mathbf{0}] & [\mathbf{I}]\\ -[\mathbf{M}]^{-1}[\mathbf{K}] & -[\mathbf{M}]^{-1}[\mathbf{C}]\end{bmatrix}. \quad (24)$$

The problem is now reduced to that of finding out the eigenvalues of matrix $[\mathbf{A}]$ for given values of the air speed parameter U_∞. The eigenvalue ω is a continuous function of the air speed U_∞. For $U_\infty\neq 0$, ω is in general complex, $\omega=\mathrm{Re}(\omega)+i\mathrm{Im}(\omega)$. When $\mathrm{Re}(\omega)=0$ and $\mathrm{Im}(\omega)\neq 0$, the wing is said to be in critical flutter condition. At some point, as U_∞ increases, $\mathrm{Re}(\omega)$ turns from negative to positive so that the motion turns from asymptotically stable to unstable.

4. RESULTS

As stated in the previous section, the solution to this aeroelastic problem through the extended Galerkin method is sought by using a numerical integration scheme. Two bending modes and two torsion modes for each wing are considered in the solution procedure to this end. The effects of the external mass value and location and the roll angular velocity on the flutter speed of unrestrained wings are simulated. Relevant data for the particular wing-weight combination used here are the same as those utilized in the work of Goland and Luke.[1] Also, dimensionless parameters used in the numerical simulation are

$$v_f=\frac{U_f}{b\omega_\theta};\ \ \omega_f=\frac{\overline{\omega}_f}{\omega_\theta};\ \ X_e=\frac{x_e}{l};\ \ \eta_F=\frac{m_F}{ml};\ \ \eta_e=\frac{m_e}{ml}; \quad (25)$$

where U_f and $\overline{\omega}_f$ are the flutter speed and frequency, respectively.

Our results, without the angular roll velocity, are in good agreement and have been obtained with results from previously published papers, as shown in Table 1.

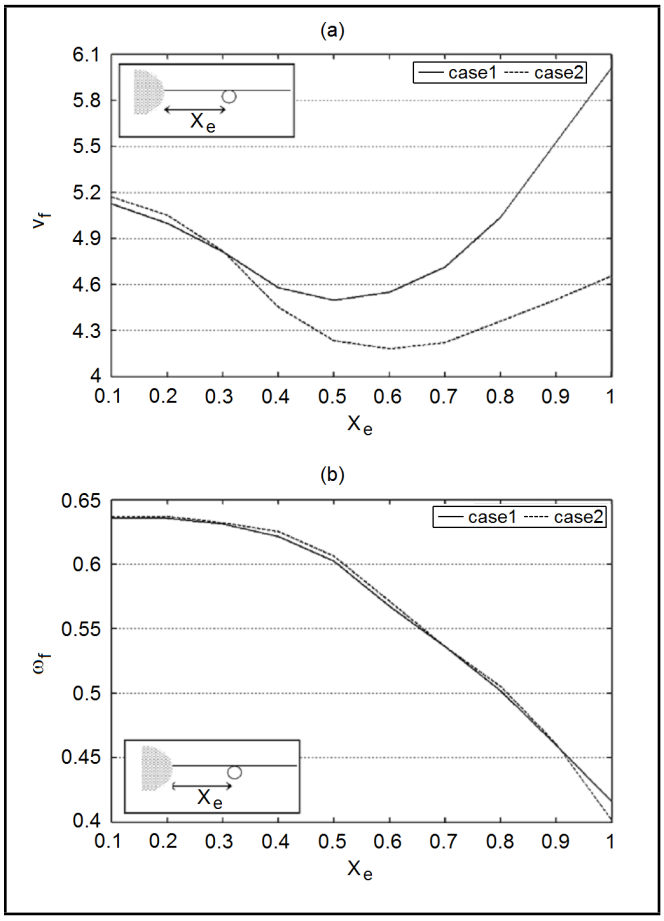

Figure 2. Effects of the spanwise position of the external mass on the aircraft flutter boundary for case1 ($e_p = 0$) and case2 ($e_p = 0.63$). (a) Flutter speed; (b) Flutter frequencies.

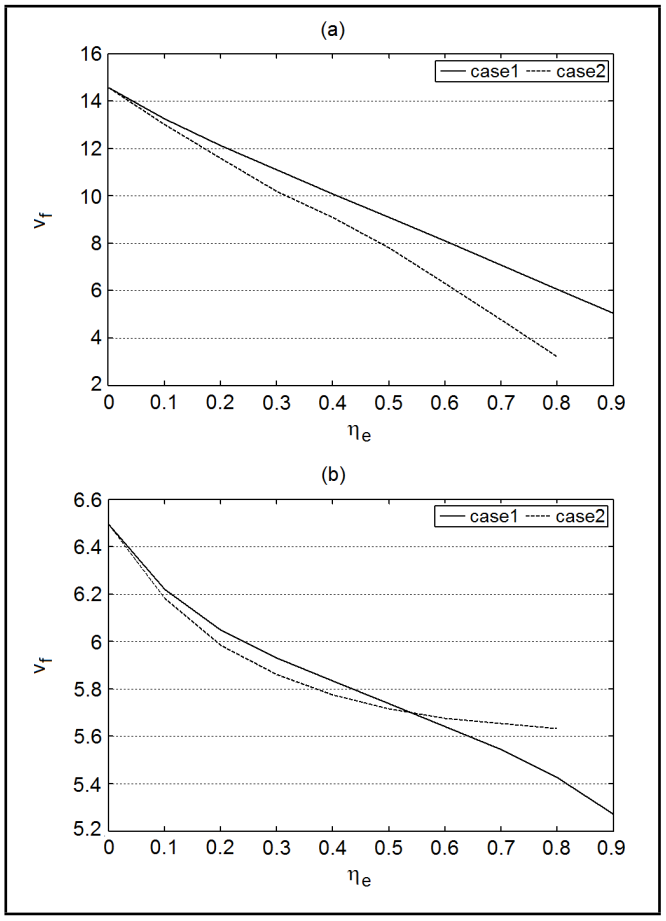

Figure 3. Effects of the store mass on the aircraft flutter boundary for case1 ($e_p = 0$) and case2 ($e_p = 0.63$). (a) Flutter speed; (b) Flutter frequencies.

4.1. Non-Maneuver Aircraft

First, the flutter results of the non-maneuvering unrestrained aircraft are considered. Figure 2 shows a parametric study investigating the effect of the store spanwise location on the flutter speed and frequency for two selected values of e_p. The store mass is assumed to be $\eta_e = 0.5$, and the fuselage mass is $\eta_F = 0.5$. The lowest value of the flutter speed takes place around $X_e = 0.6$. So, one can say that this point is the critical location for store mounting for this wing characteristic.

This behavior is the same as those reported in previous published papers.[5,10] Also, it can be seen in this figure that increasing the distance of the engine center of gravity from the wing elastic axis will decrease the flutter speed. Figure 2(b) also reveals that the flutter frequency drops in the usual way by moving the external mass towards the wing tip.

The effect of the store mass on the flutter boundary and corresponding flutter frequency of the unrestrained wing is illustrated in Fig. 3 for two selected values of e_p. The store is assumed to be placed at the middle of the wing span and the fuselage mass is $\eta_F = 0.5$. Figure 3(a) shows that increasing the store mass restricts the stability region. Also, effects of the store distance from the wing elastic axis on the wing flutter are clear in this figure. Figure 3(b) illustrates that increasing the engine mass value will decrease the flutter frequency, noticeably.

Figure 4 shows the variation of the flutter speed and frequency of the wing due to variations in the aircraft fuselage mass for selected values of e_p. The results show that an increase of fuselage mass can induce a higher flutter speed. Also, the effect of the store distance from the wing elastic axis on the flutter speed and frequency is clearly highlighted.

4.2. Rolling Maneuver Aircraft

This subsection focuses on the flutter simulations of the unrestrained aircraft under roll maneuver. The effect of the store mass on the flutter boundary and corresponding flutter frequency is illustrated in Fig. 5 for different values of the roll angular velocity.

The stores are assumed to be placed at the middle of the wings span and the nondimensional fuselage mass is $\eta_F = 1$. Figure 5(a) shows that the stability region is limited when the larger external mass is attached to the wing. This is almost independent of the roll angular velocity. Also, effects of the roll maneuver angular velocity on postponing the wing flutter are clear in this figure. Figure 5(b) illustrates that increasing the store mass value will decrease the flutter frequency, noticeably, for all values of the aircraft roll angular velocity.

The influence of the spanwise location of the store on the flutter speed and frequency of the unrestrained wing for selected values of the roll angular velocity is shown in Fig. 6. In this case, the store and fuselage mass ratio is $\eta_e = \eta_F = 1$ and the store is assumed to be located at the wing elastic axis. It can be seen in Fig. 6(a) that increasing the distance of the stores from the wing root, in this case, increases the flutter speed. Also, it can be seen that increasing the roll angular ve-

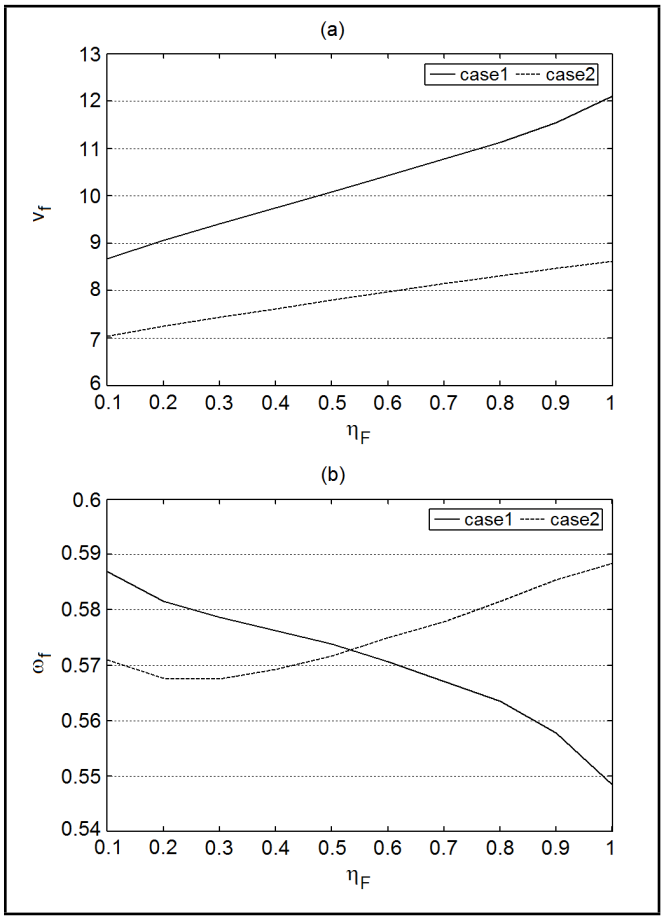

Figure 4. Effects of the fuselage mass on the aircraft flutter boundary for case1 ($e_p = 0$) and case2 ($e_p = 0.63$). (a) Flutter speed; (b) Flutter frequencies.

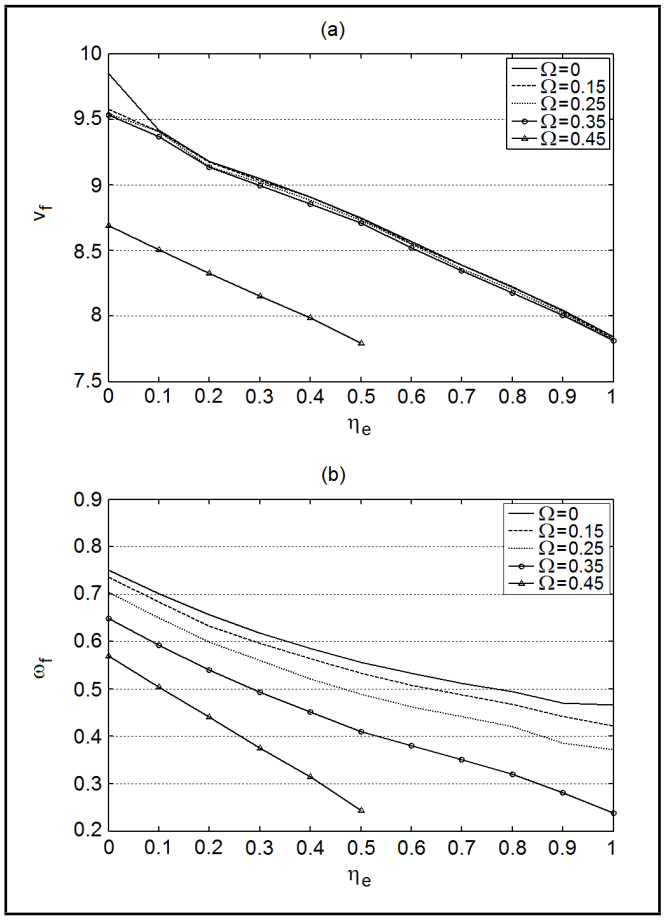

Figure 5. Effects of the store mass on the aircraft flutter boundary for $\eta_F = 1$. (a) Flutter speed; (b) Flutter frequencies.

locity will decrease the flutter speed, noticeably. Figure 6(b) also reveals that the flutter frequency drops in the usual way by moving the stores towards the wings tip. Moreover, the magnitude of the roll angular velocity has noticeable influence on the flutter frequency.

Figure 7 demonstrates the effect of the spanwise location of the stores on the flutter speed and frequency of the unrestrained aircraft with four stores for the selected values of the roll angular velocities. For every wing, the first store is assumed to be placed at the $X_{e_1} = 0.3$, and only the second store slides from the middle of the wing to the wing tip. Both stores and fuselage have equal mass ratio of $\eta_{e_1} = \eta_{e_2} = \eta_F = 1$. It is clear from Fig. 6(a) that increasing the distance of the second engine from the wing root, in this case, will increase the flutter speed. Influence of the second engine spanwise location on the flutter frequency is shown in Fig. 6(b). It can be seen that sliding the engine toward the wing tip will decrease the flutter frequency for all values of the roll angular velocity.

5. CONCLUSIONS

In this study, the aircraft is considered as an unrestrained wing carrying fuselage at its semi span and some arbitrarily placed stores. The effect of the roll maneuver, one of the most popular flight maneuvers, on flutter of the unrestrained wing is considered. To this end, the complete aeroelastic equations for an isotropic, unrestrained Goland wing under roll maneuver are formulated. The equations include effects of both maneuver induced and flow induced forces.

Results show the influence of the roll angular velocity, fuselage mass, and the stores mass and locations on the flutter speed of the wing. The rolling maneuver restricts the wing dynamic stability region in most of cases. Also, it is found that the flutter speed in the case of heavy stores is lower than those obtained for light ones, independent of the maneuver conditions.

REFERENCES

[1] Goland, M. and Luke, Y. L. The flutter of a uniform wing with tip weights, *Journal of Applied Mechanics*, **15**, 13–20, (1948).

[2] Harry, L. R. and Charles, E. W. Flutter of a uniform wing with an arbitrarily placed mass according to a differential equation analysis and a comparison with experiment, NASA Technical Report, NACA TN-1848, (1949).

[3] Lottati, T. A. Aeroelastic stability characteristics of a composite swept wing with tip weight for an unrestrained vehicle, *Journal of Aircraft*, **24** (11), 793–802, (1987). http://dx.doi.org/10.2514/3.45523

[4] Gern, F. H. and Librescu, L. Static and dynamic aeroelasticity of advanced aircraft wings carrying external stores, *AIAA Journal*, **36**, 1121–1129, (1998). http://dx.doi.org/10.2514/3.13944

[5] Gern, H. and Librescu, L. Effect of externally mounted stores on aeroelasticity of advanced aircraft wings,

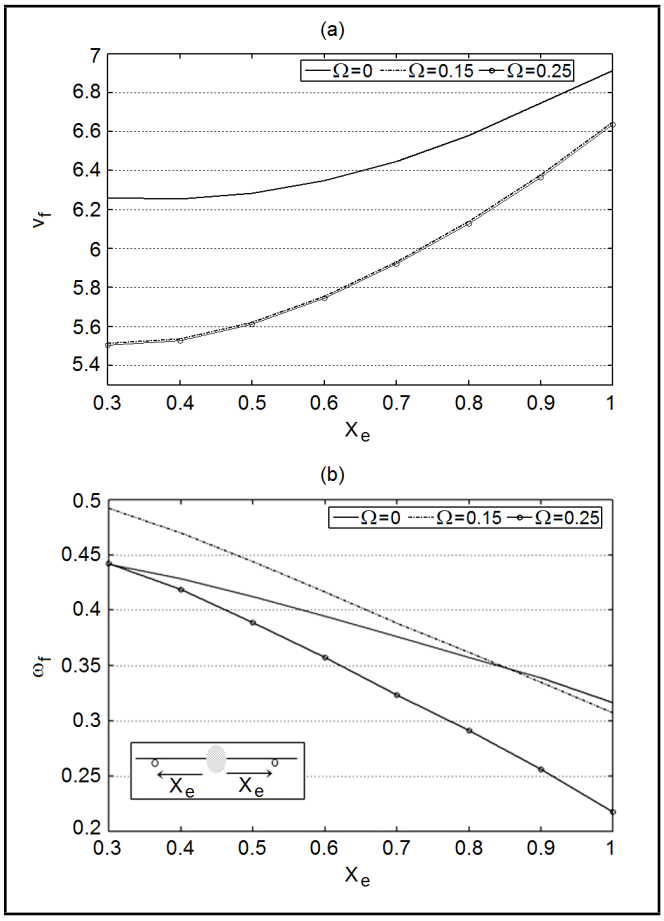

Figure 6. Effects of the spanwise position of the store on the aircraft flutter boundary for $\eta_e = \eta_F = 1$. (a) Flutter speed; (b) Flutter frequencies.

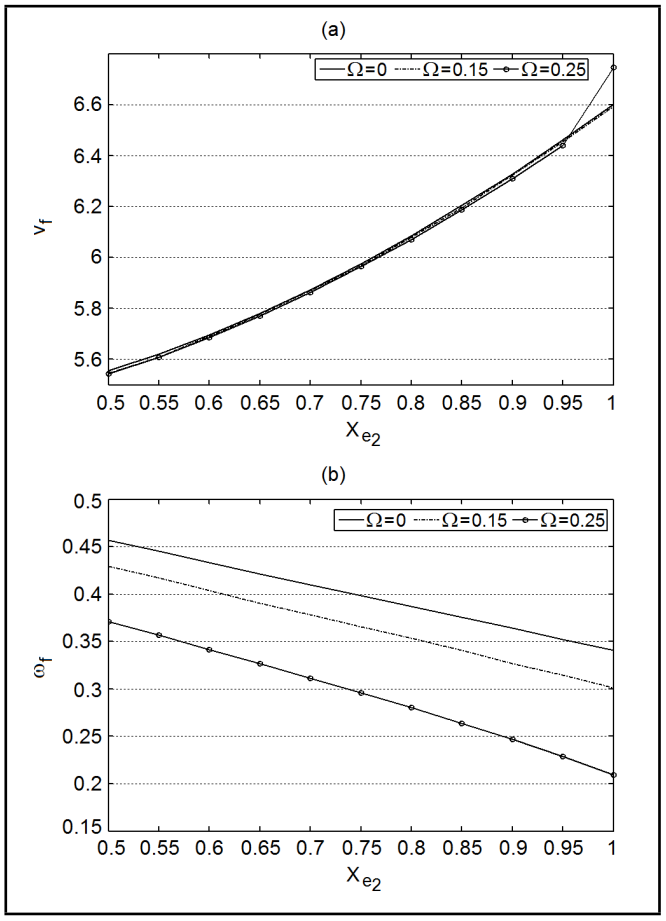

Figure 7. Effects of the spanwise position of the second engine on (a) the flutter speed and (b) the flutter frequency for $X_{e_1} = 0.3$ and $\eta_{e_1} = \eta_{e_2} = \eta_F = 1$.

Aerospace Science and Technology, **2** (5), 321–333, (1998). http://dx.doi.org/10.1016/s1270-9638(98)80008-4

[6] Na, S. and Librescu, L. Dynamic response of adaptive cantilevers carrying external stores and subjected to blast loading, *Journal of Sound and Vibration*, **231**, 1039–1055, (2000). http://dx.doi.org/10.1006/jsvi.1999.2627

[7] Librescu, L. and Song, O. Dynamics of composite aircraft wings carrying external stores, *AIAA Journal*, **46**, 568–572, (2008). http://dx.doi.org/10.2514/1.25541

[8] Edwards, J. W. and Wieseman, C. D. Flutter and divergence analysis using the generalized aeroelastic analysis method, *Journal of Aircraft*, **45** (3), 906–915, (2008). http://dx.doi.org/10.2514/1.30078

[9] Fazelzadeh, S. A., Mazidi, A., and Kalantari, H. Bending-torsional flutter of wings with an attached mass subjected to a follower force, *Journal of Sound and Vibration*, **323**, 148–162, (2009). http://dx.doi.org/10.1016/j.jsv.2009.01.002

[10] Mazidi, A. and Fazelzadeh, S. A. The flutter of a swept aircraft wing with a powered-engine, *Journal of Aerospace Engineering*, **23**, 243–250, (2010). http://dx.doi.org/10.1061/(asce)as.1943-5525.0000037

[11] Fazelzadeh, S. A., Marzocca, P. A., Rashidi, E., and Mazidi, A. Effects of rolling maneuver on divergence and flutter of aircraft wing store, *Journal of Aircraft*, **47** (1), 64–70, (2010). http://dx.doi.org/10.2514/1.40463

[12] Mazidi, A., Fazelzadeh, S. A., and Marzocca, P. A. Flutter of aircraft wings carrying a powered engine under roll maneuver, *Journal of Aircraft*, **48**, 874–884, (2011). http://dx.doi.org/10.2514/1.c031080

[13] Baruh, H. *Analytical Dynamics*, McGraw-Hill, Boston, (1999).

[14] Hodges, D. H. and Dowell, E. H. Nonlinear equations of motion for the elastic bending and torsion of twisted nonuniform rotor blades, NASA Technical Report, NASA TN D-7818, (1974).

[15] Behera, R. K. and Parhi, R. K. Dynamic characteristics of a cantilever beam with transverse cracks, *International Journal of Acoustics and Vibration*, **11** (1), 3–18, (2006).

[16] Hodges, D. H. and Pierce, G. A. *Introduction to Structural Dynamics and Aeroelasticity*, Cambridge University Press, Cambridge, (2002). http://dx.doi.org/10.1017/cbo9780511997112.002

[17] Dowell, E. H., Crawley, E. F., Curtiss, H. C., Peters, D. A., Scanlan, R. H., and Sisto, F. A. *Modern Course in Aeroelasticity*, Kluwer Academic, Dordrecht, (1995).

[18] Fletcher, C. A. J. *Computational Galerkin Methods*, Springer-Verlag, New York, (1984). http://dx.doi.org/10.1007/978-3-642-85949-6_2

Research on Fault Feature Extraction of Rubbing Rotor Based on Vector-Bispectrum Energy

Zhang Chao

Department of Mechanical Engineering, North China Electric Power University (071003), Baoding, China

(Received 11 December 2014; accepted 10 June 2016)

Signals collected from dual-channel sensors contain abundant fault characteristic information when the rub-impact fault occurs in a rotor system. As a combination of bispectrum and vector-spectrum analisys, vector-bispectrum analysis can achieve an effective elimination of Gaussian noise and accurate analysis on quadratic phase coupling in signals by combining dual-channel information. However, it has been found in the slight rubbing experiment that part of the fault information is lost by simply using the bispectrum or vector-bispectrum method. In order to resolve this problem, a new fault feature extraction approach for the rubbing rotor based on the energy index of vector-bispectrum is proposed and used in the experimental test to obtain typical characteristics of the full annular rub-impact fault. It is shown that this novel method of feature extraction inherits the advantages of vector-spectrum analysis. The features of the rub-impact fault based on the energy index of vector-bispectrum has been extracted successfully, and the result of classification through SVM illustrates that the extracted features are very noticeable, and the proposed method can comprehensively reflect nonlinear information of the rubbing rotor.

1. INTRODUCTION

In a theoretical sense, the rotor of rotating machinery is a complicated nonlinear system. The occurrence of the rub-impact faults in a rotor system may result in irregular and unstable shafting vibrations containing nonlinear phase coupling, which was harmful to the unit. Typically, conventional methods for fault detection use the power spectrum analysis based on Fourier transformation, which was built on the assumption of stable and Gaussian signals. Spectrum analysis could be used to characterize the Gaussian process, but it was not suitable for processing non-minimum phase systems or non-Gaussian signals due to its incapability of reflecting Gaussian skewness and nonlinear characteristics of signals.[1] Consequently, developing better ways to analyze the fault of the rubbing rotor has attracted much attention in the field of fault diagnosis of rotating machinery.

High order statistics analysis, in contrast with power spectrum analysis, could suppress Gauss noise completely in theory, and meanwhile effectively reveal the nonlinear information of the signal. As the simplest and lowest-order means in the high order statistics, bispectrum was the most commonly used high-order spectrum, and can be applied to deal with nonlinear phase coupling existing in nonlinear vibration signals. In the current study, bispectrum was generally used in the extraction of fault features in double frequency domain for rotating elements, such as gears and bearings.[2–6] Shen et al. applied bispectrum to extract the features of the rub-impact fault, and the results indicated the obvious existence of differences in bispectrum between the X-direction and the Y- direction signals.[7] However, why only the Y-direction signals were not selected for analysis was not explained. Yan et al. adopted the method of diagonal slice of bispectrum to analyze nonlinear coupling of harmonics occurred in steam turbines, but the results showed that the difference between the stable and the unstable vibrations was not notable in the figure of diagonal slice of bispectrum.[8] Generally, fault diagnostics based on bispectrum used the method of the statistical change detection, which was not ideal to distinguish the fault degree.[9] Therefore bispectrum coupled with other methods such as HHT or LMD, were suggested, but the complexity of the algorithm would increased.[10–13]

In general, the monitoring system of a rotor had a couple of sensors at each measuring point. The aforementioned studies mostly computed bispectrum of signal per channel respectively and selected the most obvious difference as the fault features by intercomparison. In fact, the signals of different directions were not identical due to the anisotropy of rotor systems. Hence, single channel based bispectrum analysis was not enough to comprehensively and exactly reflect the fault features because the insufficient signal combination would lead to the fault information missing. Based on the research of vector spectrum,[14] a new method of vector-spectrum integrating dual-channel signals was discussed and used to extract the feature of fault signals.[15] However, applications of this method carried out by the author of this paper for the fault signals of the rubbing rotor showed that the fault features reflected by vector-bispectrum were not obvious enough to identify the rubbing rotor.

In short, a new method of feature extraction based on the energy index of vector-spectrum was proposed for the rubbing rotor in this paper. The experiment results show that the energy index of vector-spectrum obtains bispectral characteristics of the full annular rub-impact fault, and a reasonable explanation is given. Finally, a SVM classifier is developed to validate the effectiveness of this method.

2. PRINCIPLE OF VECTOR-SPECTRUM

Assume that X- and Y- are the two orthogonal directions at a measuring point in a rotor system, and x_k, y_k are the discrete time series of X- and Y-direction respectively. X_k and Y_k are defined as the Fourier transforms of x_k and y_k. Let R_{xk}, I_{xk}, R_{yk}, I yk as the real and the imaginary parts of X_k and Y_k, respectively. The amplitude and phase of harmonics included in x_k and y_k are defined by:

$$\begin{cases} A_{xk} = \sqrt{R_{xk}^2 + I_{xk}^2} \\ \varphi_{xk} = \arctan\left(I_{xk}/R_{xk}\right) \\ A_{yk} = \sqrt{R_{yk}^2 + I_{yk}^2} \\ \varphi_{yk} = \arctan\left(I_{yk}/R_{yk}\right) \end{cases}; \tag{1}$$

where A_{xk}, A_{yk} are the amplitudes, and φ_{xk}, φ_{yk} are the phases of k-th harmonic in the X- and Y-direction, respectively. Note that the value range of φ_{xk} or φ_{yk} should be $[-\pi, +\pi]$ in Eq. (1), according to the positive and negative of I_k or R_k instead of limited in a single monotonous zone $(-\pi/2, +\pi/2)$ of arctan function.

According to the function:

$$A_k = \sqrt{A_{xk}^2 + A_{yk}^2}. \tag{2}$$

In the method of harmonic fusion described by Li, et al.,[14] the signals fusing the X- and Y-directions are constructed as follows:

$$\begin{aligned} X'_k &= A_k \left(\cos\varphi_{xk} + j\sin\varphi_{xk}\right) \\ Y'_k &= A_k \left(\cos\varphi_{yk} + j\sin\varphi_{yk}\right); \end{aligned} \tag{3}$$

where A_k is the amplitude of harmonic fusion and X'_k, Y'_k are the fusion signals in the X- and Y-direction, respectively.

New discrete time series x'_k and y'_k were computed by the inverse Fourier transforms of X'_k and Y'_k. The new time series reflected nonlinear characteristic information in the original signals by fusing the dual-channels data.[14] The third-order cumulant functions of x'_k and y'_k were written as follows:

$$\begin{cases} C'_{3x}(\tau_1, \tau_2) = E\left[x'(k) \cdot x'(k+\tau_1) \cdot x'(k+\tau_2)\right] \\ C'_{3y}(\tau_1, \tau_2) = E\left[y'(k) \cdot y'(k+\tau_1) \cdot y'(k+\tau_2)\right] \end{cases}; \tag{4}$$

where $C'_{3x}(\tau_1, \tau_2)$ and $C'_{3y}(\tau_1, \tau_2)$ are the third-order cumulant functions of x'_k and y'_k, and E is the mathematical expectation function.

Then, the two-dimensional Fourier transform of C'_{3x} and C'_{3y} can be computed by:

$$\begin{cases} B'_x(\omega_1, \omega_2) = \sum\limits_{\tau_1}\sum\limits_{\tau_2} C'_{3x}(\tau_1, \tau_2) e^{-j(\omega_1\tau_1 + \omega_2\tau_2)} \\ B'_y(\omega_1, \omega_2) = \sum\limits_{\tau_1}\sum\limits_{\tau_2} C'_{3y}(\tau_1, \tau_2) e^{-j(\omega_1\tau_1 + \omega_2\tau_2)} \end{cases}; \tag{5}$$

where $B'_x(\omega_1, \omega_2)$ and $B'_y(\omega_1, \omega_2)$ are the vector-bispectrums of the original signals x_k and y_k. They provided an integration of amplitude information from dual channels maintaining phase information of original signals unchanged. Vector-spectrum inherited the advantages of bispectrum, so it could also remove the Gaussian noise from the original signal to identify the components of the quadratic phase coupling, then the nonlinear information in signals would be indicated.

Since vector-bispectrum is a two-dimensional function with extensive computational efforts, the method of diagonal slice of vector-bispectrum was suggested in practical use to speed up the calculation. Considering a simplified case where $\tau_1 = \tau_2$ in Eq. (5), a one-dimensional function as follows can be obtained.

$$\begin{cases} C'_{3x}(\tau) = E\left[x'(k) \cdot x'(k+\tau) \cdot x'(k+\tau)\right] \\ C'_{3y}(\tau) = E\left[y'(k) \cdot y'(k+\tau) \cdot y'(k+\tau)\right] \end{cases}; \tag{6}$$

where $C'_{3x}(\tau)$ and $C'_{3y}(\tau)$ are the diagonal slices of the third-order cumulant functions of x'_k and y'_k.

The diagonal slice for vector-bispectrum can be obtained by one-dimensional Fourier transform of Eq. (6) as:

$$\begin{cases} B'_x(\omega) = \sum\limits_{\tau_1} C'_{3x}(\tau) e^{-j\omega\tau} \\ B'_y(\omega) = \sum\limits_{\tau_1} C'_{3y}(\tau) e^{-j\omega\tau} \end{cases}. \tag{7}$$

It should be noted that the diagonal slice of bispectrum preserves the information of high order statistic and quadratic phase coupling with low computational complexity, and was frequently used to extract fault features.[8,12]

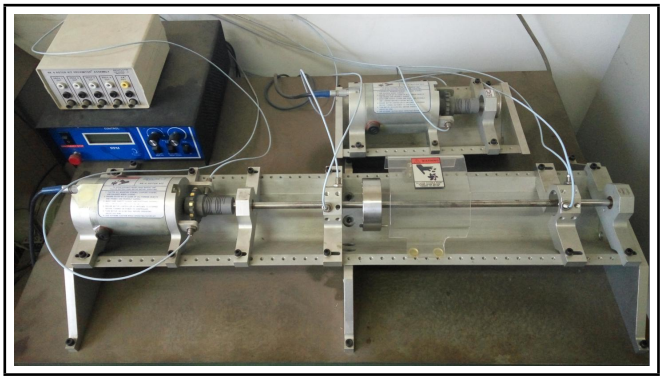

Figure 1. Test apparatus.

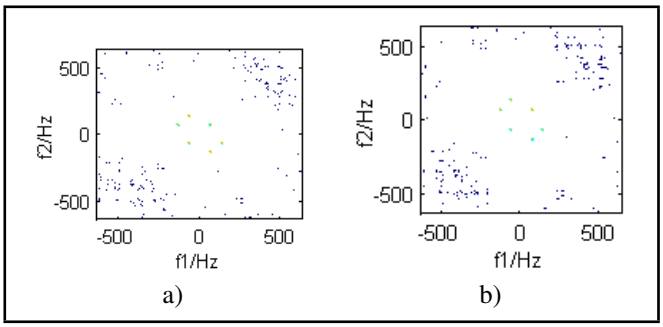

Figure 2. Bispectrum contour of normal rotor.

3. FEATURE EXTRACTION BASED ON VECTOR-BISPECTRUM ENERGY

For practical bearings in rotor systems, the stiffness, the damping, and the equivalent of bearings are not the same in different directions. In addition, there are also coupling effects between different coordinates. In other words, the support of a rotor system is anisotropic. When rub-impact faults occur, the characteristic information of the rubbing rotor does not necessarily appear in the diagonal frequencies due to the influence of the anisotropy of bearings. Therefore, it is possible that the diagonal slice cannot exactly extract the fault features of the rub-impact rotor.

In order to verify the statement above, we took an experimental test to simulate the rub-impact fault in the BENTLY NEVADA RK-4 ROTOR KIT, as shown in Fig. 1. Two bearings were installed on a shaft with a single rotor, and an AC motor was coupled to the shaft to drive the shaft. Two measuring points, each of which was with two eddy current sensors in the orthogonal directions, were set up on both sides of the rotor to collect the radial vibration data. Beside it, we placed another eddy current sensor close to driver to measure the actual rotational speed of the shaft. A plastic rod with adjustable distance was fixed to generate full annular rub to the rotor. The test was conducted repeatedly at different rotational speeds to ensure statistical consistency. We selected the data collected under a constant rotational speed of 4035 RPM (the fundamental frequency $f_r = 67.25$ Hz) including 14, 336 samples with a sampling frequency of 1280 Hz. The data length for analysis was 8,192 divided into 16 segments, and the data overlap rate was set to 50%. The bispectrum of selected signals are shown in Figs. 1 and 3.

As seen in Figs. 2 and 3, there are a few differences in bispectrums of the Y- direction between the normal and the rubbing rotor in high frequencies. This illustrates that the bispectrum contains some information of rub-impact faults. Also, it

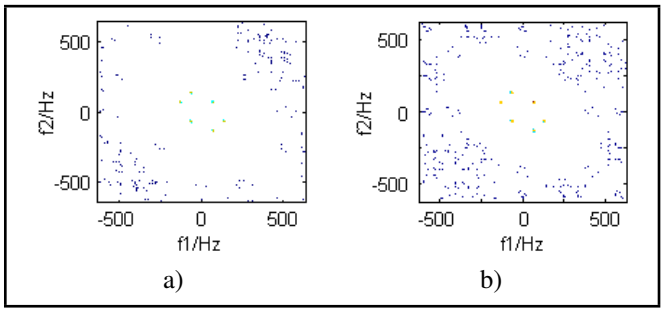

Figure 3. Bispectrum contour of rubbing rotor.

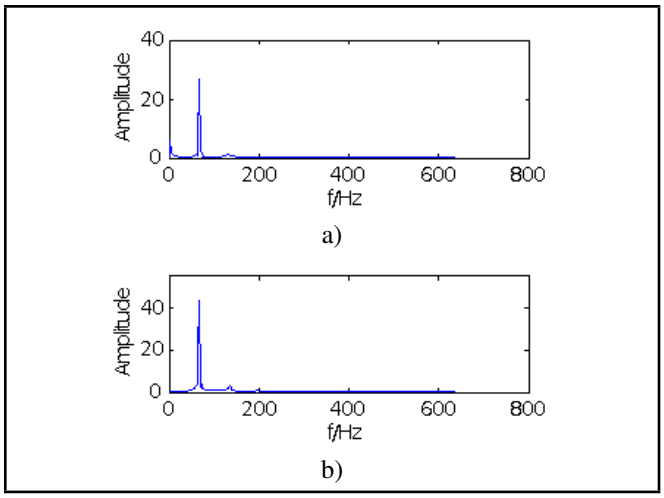

Figure 4. Bispectrum diagonal slice of normal rotor and rubbing rotor.

should be noted that we cannot distinguish the normal rotor from the rubbing rotor via bispectrum of the X-direction.

In the above test, we used a plastic rod with an adjustable distance to the rotor in order to simulate the stator and gradually decreased the distance until the plastic rod touched the outer edge of the rotor, and meanwhile maintained a certain force to produce the rub-impact fault. The material of the plastic rod was soft and had a globular head, which would not do any harm to the rotor. In order to simplify the analysis of two-dimensional spectrum a diagonal slice of the bispectrum was used to obtain the fault information as shown in Fig. 4. It can be observed in Fig. 4 that the amplitude of bispectrum of the rubbing rotor did not grow much compared with the normal rotor. Therefore, we think that the degree of the rub-impact fault in our experiments would be slight. Note that Fig. 4 has little difference in bispectrum diagonal slices between the normal rotor and the rubbing rotor, which shows that the bispectrum diagonal slice of bispectrum was not capable of reflecting slight rub-impact faults in this case.

Based on the considerations above, we proposed a new method based on vector-bispectrum energy to extract features of the rub-impact faults. According to the method of energy spectrum,[16] we put forward an extra parameter named index of vector-bisepctrum energy defined by:

$$G_z = \frac{|B'_x|^2 + |B'_y|^2}{2}; \tag{8}$$

where G_z is called the energy index of vector-bisepctrum.

The energy spectrum based on the signal intensity can intuitively reflect the direction of the maximum energy of the rotor in the rotating process with a simple algorithm. This method expands the characteristic frequency information in the diagonal slice of the vector-bispectrum and is capable of analyzing the characteristic frequency information directly in the frequency plane of the vector- bispectrum, which may dig out the fault information as much as possible.

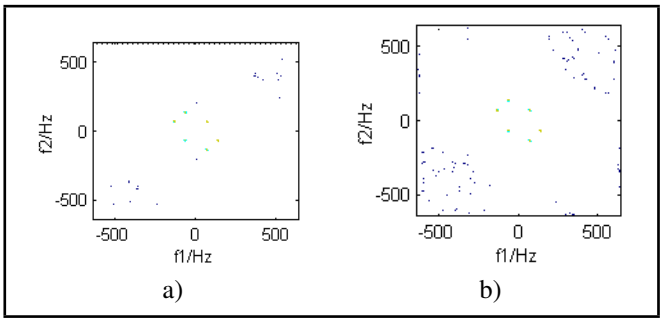

Figure 5. Vector-bispectrum energy contour of normal rotor.

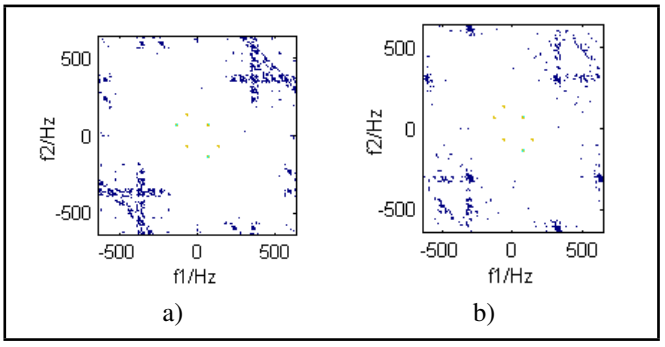

Figure 6. Bispectrum and vector-bispectrum contour of rubbing rotor in Y-direction.

4. VECTOR-BISPECTRUM ENERGY INDEX BASED TEST

According to the construction of the vector-bispectrum, we computed the bispectrum and the vector-bispectrum of the vibration signals at two measuring points respectively, and the results are shown in Figs. 5 and 6.

As indicated in Fig. 5, the scattering pattern of the bispectrum and the vector-bispectrum are similar under the state of the slight full annular rub-impact fault. A further comparison of the vector- bispectrum in the Y-direction between Figs. 5 and 6 show that the vector-spectrum implies the existence of faults. It follows that the vector-bispectrum contains more fault information than the bispectrum due to the effective combination of the dual-channel signals, and was able to suppress the Gaussian noise in signals to analyze the characteristics of nonlinear systems superior to the single- channel analysis.

It should be noted that the vibration signals emitted by the rub-impact faults generally contained subharmonic components with appearances of low-frequency couplings. However, we could not find enough subharmonic information as expected in the results produced by the vector-bispectrum and the bispectrum in Figs. 4 and 5, respectively. In order to solve this problem, we used the energy index of vector-bispectrum to reconstitute the contour of vector-bispectrum above. The results are shown in Fig. 7.

In Fig. 7, the subharmonic components of signals are revealed, it illustrates the occurrences of the quadratic phase coupling in the low frequency stage. Comparing Figs. 7a with 7b, the quadratic phase coupling mainly appears in the low frequency stages during the normal operation of the rotor. In contrast, when the rub-impact fault occurs, the high frequency

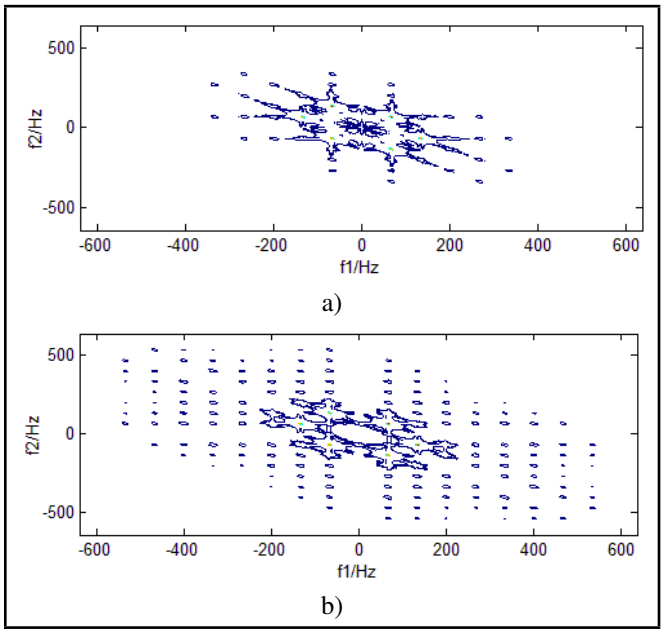

Figure 7. Vector-bispectrum energy contour.

Table 1. Fault recognition ratio with different methods.

Methods	Recognition ratio	
	Normal	Rubbing
Vector-bispectrum	82%	76%
Vector-bispectrum energy index	96%	100%

coupling begins to take place in the vibration signals and will expand to the high frequency stages. However, the components of low frequencies were still in the dominant position. Besides, in Fig. 7b, it can be observed that there are harmonic components that match the fault feature of the rubbing rotor extracted by the conventional method of Fourier transformation.

The diagonal slices for the energy of vector-bispectrum were computed and shown in Fig. 8. Comparing Figs. 8a with 8b, the diagonal slice of the normal rotor is different from the rubbing rotor in frequency distribution. Several harmonic frequencies in the diagonal slice of the rubbing rotor can be observed in Fig. 8b. This indicates that the diagonal slice of the vector-bispectrum energy index contains more fault information than the vector-bispectrum. From the perspective of energy distribution of vector-bispectrum, the energy of the vector-bispectrum mainly centralized in the frequency region below the 2nd harmonic frequency and the largest proportion of the fundamental frequency component indicated the main problem of rotor unbalance. The vector- bispectrum energy of the rubbing rotor is dispersive in the frequency axis with fewer components below the half-frequency. The most concentrated location of energy was in the region between the fundamental frequency and the 4th harmonic frequency, where the quadratic phase coupling came up with the maximum probability.

In order to validate the effectiveness of the fault feature extraction method based on the vector- bispectrum energy index, we applied Support Vector Machine (SVM) as a classifier to distinguish the normal state from the faulty state. In the SVM arithmetic, we used a RBF kernel function, $K(x_i, x_j) = exp(-|x_i - x_j|^2/\sigma^2)$, $\sigma = 0.5$, and selected the amplitude of the bispectrum in $0.5f_r$, f_r, $2f_r$, $3f_r$, $4f_r$, $5f_r$, $6f_r$, and $7f_r$ as the input vectors of SVM. There were 30 samples used to train the SVM classifier and 50 samples for the test. Table 1 illustrates the result of the fault recognition with different methods.

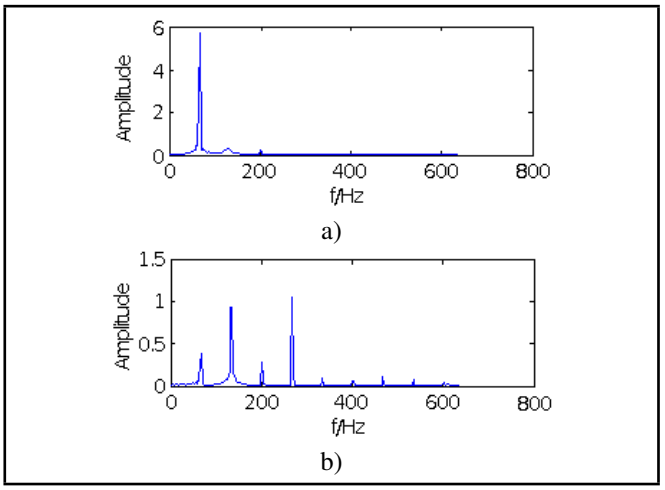

Figure 8. Diagonal slice of Vector-bispectrum energy index.

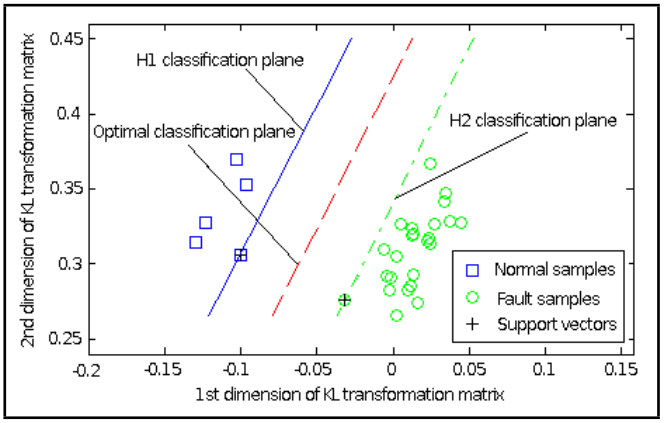

Figure 9. Classification result of SVM after K-L transformation.

Table 1 suggests that the method of vector-bispectrum energy index obtains perfect results of recognition for the rubbing fault, and most normal samples are classified correctly. In order to obtain the visual diagrams of classification, we introduced Karhunen-Loeve transform to compress the eight-dimensional input of SVM. Karhunen-Loeve transform is a normalized orthogonal transformation, which can retain main information of the original data. The test data contains 25 samples of the rubbing state and five samples of normal state, and the classification results based on Karhunen-Loeve transform are shown in Fig. 9. As indicated in Fig. 9, it is shown that that all samples are classified correctly.

5. CONCLUSIONS

The rubbing rotor is a theoretically nonlinear system. The vibration signals of the rotor are unstable when the quadratic phase coupling happens. To solve this problem, we proposed a novel energy index based on the vector-bispectrum method for feature extraction of rubbing rotors. An experimental test was conducted, where the rub-impact fault features were extracted by the proposed method. The primary conclusions drawn from the study are as follows:

1. The bispectrum can restrain the Gaussian noise and analyze the components of the quadratic phase coupling in the original signals. However, it is found that the bispectrum based feature extraction method does not have any advantages for slight rubbing faults and its diagonal slice may lose fault features.

2. The vector-bispectrum inherits excellent properties of the bispectrum and meanwhile is more comprehensive than the bispectrum in reflecting the fault information due its information combination of dual-channels. Like the bispectrum, the vector- bispectrum has the probability of losing part of subharmonic components in the slight rubbing fault. The main reason is that the high frequency nonlinear components in vibration signals are in the dominant position, and the subharmonic components do not appear in the resulting figures because they are concealed by high frequency components.

3. The method of vector-bispectrum energy index proposed in this paper is able to distinguish the normal rotor from the rubbing rotor, and the diagonal slice of the vector-bispectrum energy index contains more fault information than the bispectrum to extract fault features from the full annular rub-impact fault rotor. The results of this study indicate that there are components of quadratic phase coupling below the 2nd harmonic frequency during normal operation of rotor. When the rub-impact fault occurs, the components of the quadratic phase coupling will expend to high frequency stages, and the components below the 4th harmonic frequency are in the dominant position.

ACKNOWLEDGEMENT

This work is in part supported by National Natural Science Foundation of China (No. 51307058), Natural Science Foundation of Hebei Province, China (No. E2014502052 and No. E2015502013), and Chinese Fundamental Research Funds for the Central Universities (No. 2015ZD27).

REFERENCES

[1] Zheng, H.-B., Chen, X. Z., and Li, Z. Y. Bispectrum based gear fault feature extraction and diagnosis, *Journal of Vibration Engineering*, **15** (3), 354–358, (2002). http://dx.doi.org/10.3969/j.issn.1004-4523.2002.03.022

[2] Shen, G. J., Stephen, M. L., and Xu, Y. C., et al. Theoretical and experimental analysis of bispectrum of vibration signals for fault diagnosis of gears, *Mechanical Systems and Signal Processing*, **43** (1-2), 76–89, (2014). http://dx.doi.org/10.1016/j.ymssp.2013.08.023

[3] Li, X. J, Jiang, L. L., and Yang, D. L., et al. Cluster analysis and fault diagnosis for gear based on bispectrum distribution, *Journal of Vibration Engineering*, **24** (3), 304–308, (2011). http://dx.doi.org/10.3969/j.issn.1004-4523.2011.03.014

[4] Fidel, E. H. M. and Oscar, C. M. The application of bispectrum on diagnosis of rolling element bearings: A theoretical approach, *Mechanical Systems and Signal Processing*, **22** (3), 588–596, (2008). http://dx.doi.org/10.1016/j.ymssp.2007.09.003

[5] Li, H., Zheng, H. Q., and Tang, L. W. Gear fault diagnosis based on order bispectrum analysis, *Journal of Basic Science and Engineering*, **15** (3), 351–356, (2007). http://dx.doi.org/10.3969/j.issn.1005-0930.2007.03.009

[6] Zhang, R. G. and Tan, Y. H. Intelligent fault diagnosis of rolling element bearings based on bispectrum principal components analysis, *Journal of Vibration Engineering*, **27** (5), 763–769, (2014). http://dx.doi.org/10.3969/j.issn.1004-4523.2014.05.017

[7] Wang, L. P., Ye, P. Q., and Wang, J.-S., et al. Bispectrum characteristics of the faults of rubbing rotor system based on experimental study, *Journal of Vibration Engineering*, **15** (1), 62–67, (2002). http://dx.doi.org/10.3969/j.issn.1004-4523.2002.01.012

[8] Yan, K. G., Liu, Y. B., and Xu, H., et al. Fault feature extraction of large steam turbine based on bispectra analysis of vibration signal, *Proceedings of the Chinese Society of Electrical Engineering*, **30** (2), 98–103, (2010). http://dx.doi.org/10.13334/j.0258-8013.pcsee.2010.02.011

[9] Liu, X. L., Xu, X. L., and Jiang, Z. L., et al. Application of the state deterioration evolution based on bi-spectrum entropy and HMM in wind turbine, *Chaos Solitons and Fractals*, **89**, 160–168, (2016). http://dx.doi.org/10.1016/j.chaos.2015.10.018

[10] Lotfi S., Jaouher, B. A., and Farhat, F. Bi-spectrum based-EMD applied to the non-stationary vibration signals for bearing faults diagnosis, *ISA Transactions*, **53** (5), 1650-1660, (2014). http://dx.doi.org/10.1109/socpar.2014.7007976

[11] Zheng, H., Zhou, L., and Yang, H. Rolling element bearing fault diagnosis based on spectral kurtosis and bi-spectrum, *Journal of Beijing University of Aeronautics and Astronautics*, **40** (9), 1176–1182, (2014). http://dx.doi.org/10.13700/j.bh.1001-5965.2013.0628

[12] Tang, G. J. and Wang, X. L. Fault diagnosis of roller bearings based on local mean decomposition and slice bispectrum, *Journal of Vibration and Shock*, **32** (24), 83–88, (2013). http://dx.doi.org/10.3969/j.issn.1000-3835.2013.24.015

[13] Yang, J. T. and Zhao, M. Y. Fault diagnosis of traction motor bearings using modified bispectrum and empirical mode decomposition, *Proceedings of the Chinese Society of Electrical Engineering*, **32** (18), 116–122, (2012). http://dx.doi.org/10.13334/j.0258-8013.pcsee.2012.18.003

[14] Li, L. J., Han, J., and Li, P. Y., et al. Vector-bispectrum analysis and its application in machinery fault diagnosis, *Journal of Mechanical Engineering*, **47** (17), 50–54, (2011). http://dx.doi.org/10.3901/jme.2011.17.050

[15] Li, L. J., Han, J., and Li, P.-Y., et al. Intelligent fault diagnosis method based on vector-bispectrum, *Journal of Mechanical Engineering*, **47** (11), 64–68, (2011). http://dx.doi.org/10.3901/jme.2011.11.064

[16] Cheng, J. S., Yang, Y., and Zhang, K., et al. Application of cycle frequency and energy spectrum based on local mean decomposition to gear fault diagnosis, *Journal of Vibration Engineering*, **24** (1), 78–82, (2011). http://dx.doi.org/10.16385/j.cnki.issn.1004-4523.2011.01.017

Performance of Sound Insulation in Buildings — A Case Study

Marcus Vinícius Manfrin de Oliveira Filho and Paulo Henrique Trombetta Zannin

Federal University of Paraná, Brazil

(Received 6 February 2015; accepted 3 May 2016)

The purpose of this study is to recognize usual facade sound insulation problems that affect a construction's acoustical quality by measuring the facade's sound insulation. Thirteen different situations were evaluated through in situ measurements in Curitiba, Brazil. By measuring buildings in different locations with constructive materials and different designs, this research found that the performance of the majority of evaluated facades did not reach the minimum proposed by both Brazilian and Portuguese standards. These results indicate that the sound insulation quality in Brazilian buildings is low and is mainly due to constructive imperfections and the use of materials with unfavorable acoustical properties.

1. INTRODUCTION

Recent studies have found that, like other Brazilian metropolises, Curitiba is acoustically polluted.[1–7]The solution to this environmental problem involves control by means of technical, political, and educational actions. One of the main tools available to ensure adequate sound pressure levels inside buildings is the sound insulation of their facades. Like so many other branches of engineering, sound insulation design requires dedicated study to reach established goals and to correct nonconforming situations by taking into account the management of various resources (e.g. financial, time, labor, materials, etc.).

Previous studies suggest builders were negligent with the acoustical quality of Brazil's building facades. Based on statistical surveys, Jobim claimed that the lack of acoustic comfort is a major source of dissatisfaction among home owners.[8] According to Queiroz and Viveiros, the quality of sound insulation of frontal facades in Brazil declined significantly between 1968 and 2005.[9] All the homes assessed by Ferreira and Zannin in Curitiba presented sound insulation values that did not meet the German standard DIN 4.109 "Schallschutz im Hochbau".[10,11]

Thirteen different situations of facades were evaluated in situ in Curitiba, state of Paraná, according to the parameter of weighted standardized level difference — $D_{2m,nT,w}$. The results were compared with the Brazilian standard NBR 15.575 "Edificações habitacionais Desempenho" and Portugal's Building Acoustics Regulations — RRAE "Regulamento de Requisitos Acústicos de Edificações".[12,13] Gaps of approximately 0.5 cm in length were left deliberately in three facades in order to study their effect on the sound insulation of the buildings.

2. METHODOLOGY

Sound insulation measurements were taken in thirteen situations at different building facades (e.g. apartments, homes and classrooms) in various parts of Curitiba. Several situations were addressed and took different building materials into account.

The measurements were taken according to the global method described in the standard ISO 140-5 "Acoustics Measurement of sound insulation in buildings and of building elements".[14] The loudspeaker and traffic noise methods were used according to the most suitable one for each situation. Internal sound sources (e.g. neighbors and household appliances)were not considered, since measurements were taken in quiet conditions. The measured parameter was the standardized level difference $D_{2m,nT}$, in the 100 to 3150 Hz frequency range. Then, the procedure described in the standard ISO 717-1 "Acoustic Rating of sound insulation in buildings and of building elements Part 1: Airborne sound insulation" was used, which allowed the team to obtain a single value for sound insulation performance (i.e. the weighted standardized level difference), $D_{2m,nT,w}$.[15]

This single value represents the result of the measurement of acoustic parameters taken in octave or one-third octave frequency bands. This value was used as the criterion to compare the measured values and those established by Brazilian and Portuguese standards (NBR 15.575 and RRAE, respectively).

The standardized level difference, $D_{2m,nT}$, is given by:[14]

$$D_{2m,nT} = L_{1,2m} - L_2 + 10\log\left(\frac{T}{T_o}\right); \qquad (1)$$

where:

$D_{2m,nT}$ – standardized level difference measured 2 m away from the facade, dB;

$L_{1,2m}$ – external sound pressure level 2 m away from the facade, dB;

L_2 – indoor average sound pressure level, dB;

T – indoor average reverberation time, s;

T_o – indoor reference reverberation time value, = 0,5 s, s.;

The parameters $L_{1,2m}$ and L_2 were measured simultaneously by using two microphones, a dual channel adapter, and a flat cable. This flat cable could be passed through an element that separates the facade (door or window) even when it was closed. This was necessary because if a cylindrical cable was used, a crack would have had to be left open in the separating element, which would have impair the accuracy of the measurement of the sound insulation, thus underestimating its levels.[14] All data was collected in the afternoon over the course of several days and, although the equipment set up time was long, each measurement lasted for only a few seconds.

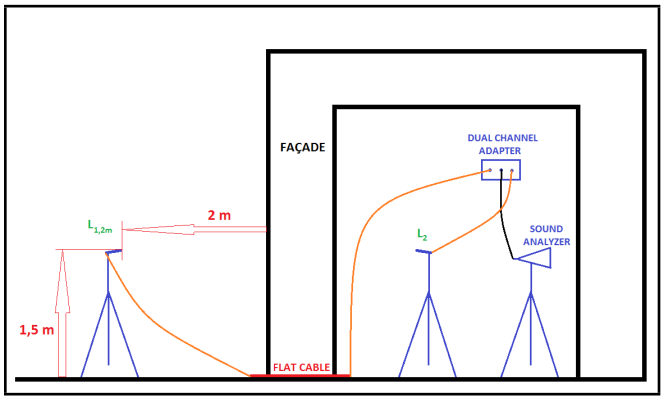

Figure 1. The measurement scheme.

Figure 2. Flat cable through a window.

Reverberation time, a parameter required for the calculation of the weighted standardized level difference, was measured as specified by ISO 354 "Measurement of sound absorption in a reverberation room".[16] This standard regulated all of the procedures needed for the determination of this parameter by the interrupted noise method.

All measurements were taken with Class 1 *Brüel & Kjaer* equipment, which included microphones, cables, and a sound analyzer. The microphones were externally calibrated with a caliper before each measurement, as was recommended in the user manual.[17]

2.1. Regulatory Aspects

The Brazilian standard NBR 15.575-4 provided methods and values for the performance of buildings in various branches.[12] With regard to acoustic performance, the Brazilian standard NBR 15.575-4 presented a table containing the minimum allowable values for the sound insulation of facades, depending on the location of the home.

The RRAE (Portugal's Building Acoustics Regulations) established minimum values for the weighted standardized level difference, which were reached according to the type and zoning of buildings.13 The General Regulation on Noise (RGR) was consulted to determine the zoning of each building. This law established the zoning of urban areas according to land use.[18]

Note that foreign standards had to be used to assess the acoustic quality of buildings in Brazil, since the Brazilian standard NBR 15.575 covers only acoustic requirements for bedrooms. Brazil has no valid regulation on sound insulation requirements for hospitals, classrooms, offices, churches, or other types of buildings.

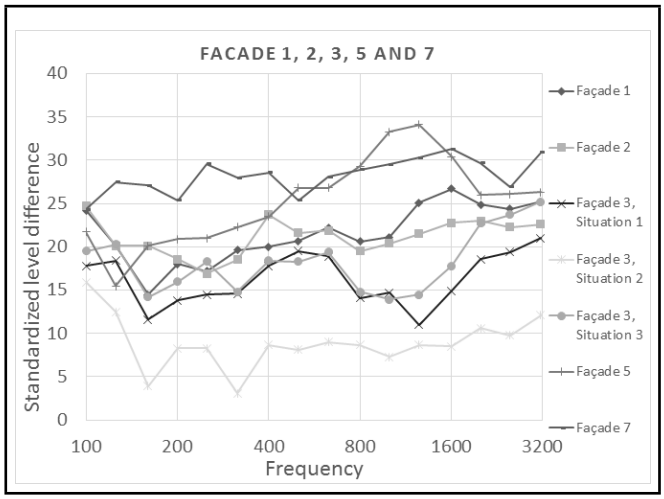

Figure 3. Standardized level difference for facades 1, 2, 3, 5 and 7.

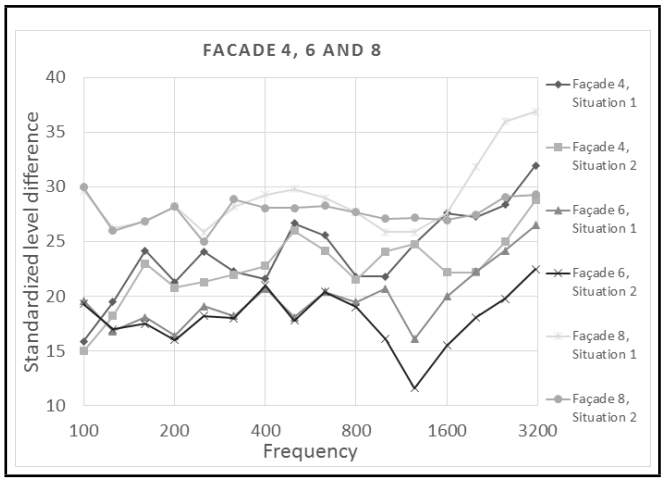

Figure 4. Standardized level difference for facades 4, 6 and 8.

The Portuguese regulation was chosen because it uses the same parameter of comparison for the sound insulation of facades as that of the NBR 15.575-4 standard — the weighted standardized level difference, $D_{2m,nT,w}$. According to both the Brazilian and the Portuguese standards, this parameter established minimum values for each case are shown in section 3.7.

3. RESULTS AND DISCUSSION

Table 1 shows the room types, location, and building aspects of the eight studied facades. Figures 3 and 4 show the measured standardized level difference curve for all the situations presented in this study. Other measurement relevant descriptions — measured values, photographs, and pertinent comments — are given in the following sections. The global loudspeaker method was used in Facades 1 to 7. Measurements on Facade 8 were taken considering the road traffic noise (other noise sources were negligible in the area) by using the global traffic noise method.[14]

Table 1. The facades aspects.

Facade	Room type	Location (neighborhood)	Facade constitution	Materials thickness
1	bedroom	Cristo Rei	masonry walls - 11.68 m^2 plain glass sliding windows - 5.6 m^2 total - 17.28 m^2	walls - 12.5 cm plain glass - 6 mm
2	bedroom	Cristo Rei	masonry walls - 6.89 m^2 plain glass sliding windows - 2.8 m^2 total - 9.69 m^2	walls - 12.5 cm plain glass - 6 mm
3	bedroom	Uberaba	masonry walls - 5.07 m^2 plain glass / light metal shutter sliding door - 3.18 m^2 total - 8.25 m^2	walls - 12.5 cm plain glass - 6 mm light metal shutter - 3 mm
4	living room	Uberaba	masonry walls - 5.32 m^2 sliding glass door - 4.91 m^2 total - 10.23 m^2	walls - 12.5 cm plain glass - 6 mm
5	classroom	Jardim das Américas	masonry walls - 17.36 m^2 plain glass windows - 20.5 m^2 total - 37.86 m^2	walls - 25 cm plain glass - 8 mm
6	2nd floor bedroom	Uberaba	masonry walls - 5.95 m^2 plain glass sliding door - 3.18 m^2 total - 9.13 m^2	walls - 12.5 cm plain glass - 6 mm
7	living room	Uberaba	brick walls - 4.05 m^2 stained glass extending to the second floor 2.06 m^2 heavy wooden door 2.09 m^2	brick walls - 12.5 cm wooden door - 3.2 cm
8	6th floor bedroom	Downtown	total 8.20 m^2 masonry walls - 8.22 m^2 double glazed acoustic window - 2.7 m^2 total - 10.92 m^2	stained glass - 8 mm walls - 12.5 cm two 4 mm thick glass layers

SOURCE: The authors (2013).

3.1. Facade 1

A value of 23 dB for the weighted standardized level difference was determined from this measurement, thus indicating that Facade 1 did not meet the minimum 25 dB requirement stipulated by the Brazilian standard NBR 15.575-4 for this case.

Because the facade area was made of single-layered plain glasses, the levels of sound insulation were decreased in the 500 to 1500 Hz frequency range approximately, when compared to the shifted reference values curve utilized to calculate the weighted standardized level difference.[15, 19] In addition, the sliding window did not have an appropriate sealing, leaving gaps between the metal structures that sustained the glasses. These constructive imperfections were caused due to the lack of the window maintenance and to the use of non-standard materials.

3.2. Facade 2

The sliding windows of Facade 2 showed gaps between the wooden window frames and the glass panes, as illustrated in Fig. 5. This type of crack was quite common and often found in Brazilian buildings. A value of 22 dB for the weighted standardized level difference was determined from this measurement, thus indicating that Facade 2 does not meet the minimum 25 dB requirement stipulated by the Brazilian standard for this case.

Facade 2 presented a poor sound insulation performance in the higher frequencies when compared to the shifted reference curve. The same behavior was found in Facades 4, 6, and 8, in which openings of 0.5 cm were intentionally left, as shown in section 3.4. This suggests that gaps of this magnitude affect the facade sound insulation levels, especially in this frequency range. The cracks found in Facade 2 were consequences of the use of non-standardized materials, which had unfavorable acoustic properties.

Figure 5. Gaps in the window frames of facade 2.

3.3. Facade 3

Facade 3 was evaluated in three different situations:

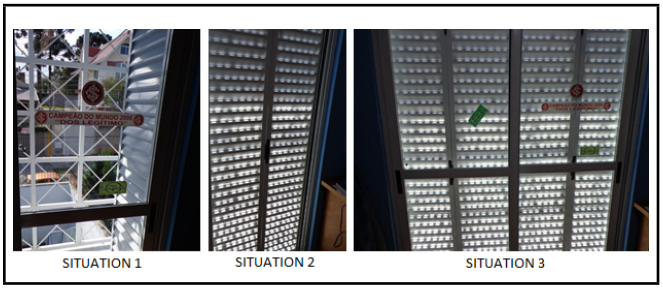

Figure 6. Facade 3 in the three different situations.

Table 2. The measurements of facade 3.

Situation	$D_{ls,2m,nT,w}$ [dB]
1	17
2	9
3	19

SOURCE: The authors (2013).

1. Situation 1 — Only the glass door closed (metal shutters open);
2. Situation 2 — Only the metal shutters closed (glass door open);
3. Situation 2 — Metal shutters and glass door both closed.

Fig. 6 illustrates the evaluated situations.

The results of the measurements of Facade 3 are listed in Table 2.

As can be seen, Facade 3 does not meet the minimum 25 dB requirement set by the Brazilian standard in any of the three measured situations. The contribution of the metal shutters to the sound insulation combined with that of the glass door is 2 dB for the weighted standardized level difference (from 17 to 19 dB).

Since there are no gaps in Facade 3, the results under the minimum value established by the Brazilian Standard are due to the use of materials with unfavorable acoustic properties, such as light metals and a single layered plain glass door. Similarly to Facade 1, Facade 3 presents low sound insulation levels in the 500 to 1500 Hz frequency range approximately, when compared to those found in the shifted reference values curve described in ISO 717.[15] These weak points were caused by the use of single-layered plain glasses that have had a worse performance than the 10 cm thick masonry walls.[19]

3.4. Facade 4, 6, 8

Facades 4, 6, and 8 were evaluated in two different situations:

1. Situation 1 — Glass door / window completely closed;
2. Situation 2 — Glass door / window open 0.5 cm; the opening was left intentionally to simulate gaps in the order of magnitude commonly found in Brazilian buildings.

Figure 7 illustrates Situations 1 and 2.

The values determined for the weighted standardized level difference of Facades 4, 6, and 8 in Situations 1 and 2 are shown in Table 3.

Facade 4 sound insulation levels are below the 28 dB minimum value recommended by Portuguese standards. The Brazilian standard does not provide for sound insulation levels for rooms other than bedrooms. There were difficulties on opening and closing the door of this facade due to the friction between the lower part of the door and the metal sliding guide. This constructive imperfection, which could also cre-

Figure 7. Facade 4 sliding glass door closed, and with an 0.5 cm opening situations 1 and 2.

Table 3. Depth of crack for different crack widths and aspect ratios.

		Measured $D_{2m,nT,w}$ * [dB]	Minimum $D_{2m,nT,w}$ according to NBR 15.575-4 [dB]	Minimum $D_{2m,nT,w}$ according to Portugal's RRAE [dB]
Facade 4 (living room)	Situation 1 Situation 2	26 24	not specified	28
Facade 6 (bedroom)	Situation 1 Situation 2	21 18	25	28
Facade 8 (bedroom)	Situation 1 Situation 2	30 28	30	33

SOURCE: The authors (2013).

ate gaps, was explained by the low-quality workmanship and a lack of maintenance. Additionally, the constructive material, which was a single layered pain glass sliding door, did not offer a high performance sound insulation, which explained the results under the minimum established by the Portuguese standard.[19]

The values determined for the weighted standardized level difference of Facade 6 were below the minimum values recommended by both the Brazilian and the Portuguese standards. There were found no gaps during the measurements of this facade. The results under the minimum established by the standards were due to the use of materials with unfavorable acoustic properties, such as light metals and a single layered plain glass door.

The value determined for the weighted standardized level difference for Facade 8 in situation 1 was $D_{tr,2m,nT,w} = 30$ dB. Thus, this value lies within the permissible minimum threshold according to the Brazilian standard, but did not attend the Portuguese standard requirements. The double layered glass acoustic window showed a remarkably determining performance in this case. Without it (or with the window open), the sensation of acoustic discomfort in the bedroom was heightened due to the heavy vehicle traffic, disturbing simple daily activities, such as sleeping or reading.

Since Facade 8 was from a bedroom located on the 6th floor of an apartment building, the measurement of the $L_{1,2m}$ level was taken with the external microphone attached to a fishing rod suspended on the balcony of an adjoining room. The procedure, illustrated in Fig. 8, allowed the microphone to be held 2 m away from the facade.[14,20]

In Table 3, Facades 4 and 8 present a decrease of 2 dB and Facade 6 presents a decrease of 3 dB over the weighted standardized level difference between situations 1 and 2, when a gap of 0.5 cm was left open deliberately. The test with the open gap confirmed the effect perceived subjectively: the lack of sealing in an element separating two environments deteriorates the quality of sound insulation between them.

In addition, it was noted that the gaps affected the standardized level difference curve in a similar way for Facades 4, 6, and 8. Sound insulation level curves suffered a significant decrease in high frequencies. Facade 4, for example, had a decrease of 5.4 dB in the 1600 Hz frequency band when compared to Situations 1 and 2; Facade 6 had a 4.6 dB decrease in the 1000 Hz frequency band; and Facade 8 had a 6.9 dB decrease in the 2500 Hz frequency band. The levels in frequencies lower than 1000 Hz remained close in both Situations 1 and 2, as shown in Fig. 4.

3.5. Facade 5

Facade 5 was from classroom PG-06 located on the campus of the Polytechnic Center of the Federal University of Paraná UFPR. The measurement was taken while the classroom was unoccupied. The measurements showed that Facade 5 provides acoustic insulation of $D_{ls,2m,nT,w} = 28$ dB, indicating that

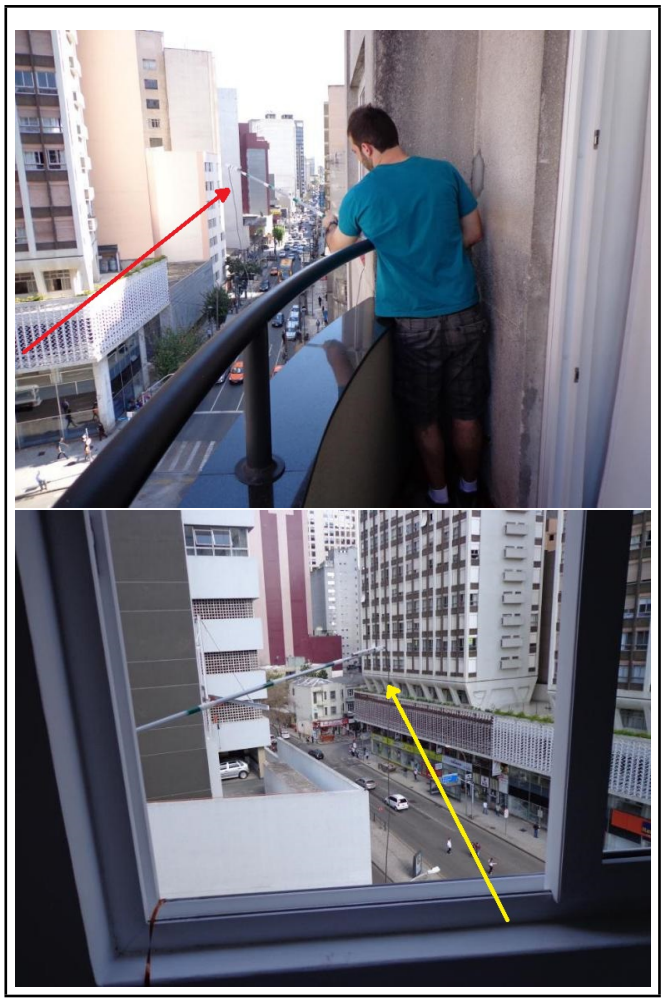

Figure 8. Use of a fishing rod to support the microphone during the measurements of facade 8 — external and internal views of the bedroom

classroom PG-06 was in compliance with the minimum acceptable limit recommended by the Portuguese standard (Brazilian standard cannot be used in this situation, since it covers exclusively bedrooms).

Although there were found small gaps between the glass panels, the classroom ha thick masonry walls (25 cm thick) covered by a layer of a tile wall and thicker glasses than the situations shown before. This combination warranted higher sound insulation levels.

3.6. Facade 7

A weighted standardized level difference of $D_{ls,2m,nT,w} = 29$ dB was determined from this measurement. Thus, Facade 7 fell within the acceptable limit of 28 dB recommended by the European standard.[13,18]

The value of $D_{ls,2m,nT,w} = 29$ dB is attributed to good insulation presented by Facade 7. The stained glass panel was sealed hermetically against the masonry walls. The wooden

door has a rubber bottom door seal that pressed against the floor of the foyer, providing water-tight acoustic and thermal insulation. In fact, it was difficult to pass the flat cable through the door to take this measurement. The door also had tetra key locks, which mitigated the effects of loss of sound insulation, since the two adjacent rooms were not exposed to direct openings, such as ordinary door locks.

3.7. Table of Results

Table 4 lists the values of weighted standardized level difference measured in each situation and compares them to the values stipulated by the Brazilian and Portuguese standards NBR 15.575-4 and RRAE, respectively.

Considering all the measurements and analyzing the data given in Table 4, one can see that the sound insulation of the facades of Brazilian buildings is not ideal. Approximately 77% of the studied cases (10 out of 13) failed to meet the minimum requirements established by the standards. The average value of the measured weighted standardized level difference was 22 dB, which is lower than the minimum stablished by Portuguese and Brazilian standards for urban environments.

An analysis of the effects of the gaps left open intentionally proves that they could be perceived subjectively (i.e. there is a deterioration in the quality of sound insulation). Facades 4, 6, and 8 showed sound insulation losses of 2 to 3 dB according to the parameter $D_{2m,nT,w}$, when openings were inserted. Facade 8, which was in compliance with NBR 15.575-4, became noncompliant with the minimum value when the acoustic window was not completely closed. In addition, the gaps affected more the sound insulation levels on high frequencies (1000 to 3150 Hz), rather than on low frequencies. This suggested that sound insulation levels in this frequency range are especially sensitive to gaps of 0.5 cm order of magnitude.

Differences were found between the Brazilian construction model and that of developed countries. The latter used lighter materials in large-scale construction of walls and ceilings, and windows and doors that provide afford acoustic and thermal insulation.[21–23]

This finding points to systemic problems in Brazilian civil construction: the low quality of labor, the use of non-standard materials, the use of materials with unfavorable acoustic properties, the lack of maintenance and the unfamiliarity about the subject, which result in low quality buildings. Single layered glass windows are problematic for sound insulation, since glasses present a lower performance than brick walls, especially in the 500 to 1500 Hz frequency range.[19] While masonry walls were built by an almost artisanal process (brick by brick), ensuring heavy buildings with high values of Rw, doors and windows were the weak link in the acoustic insulation of Brazilian buildings.[23,24]

4. CONCLUSIONS

The problem of environmental noise that affects Curitiba and other metropolises (not just in Brazil) has no single solution, but requires joint measures by society, scientists, and authorities. Noise emission levels must be reduced because imission levels (i.e., those that reach the receivers) must also be attenuated. In this context, the sound insulation of facades is an important measure to control noise pollution particularly in urban areas where traffic noise is responsible for environmental damage that deteriorates the quality of life.

Thirteen facades of different buildings in Curitiba were evaluated to determine their levels of sound insulation. The results of the measurements revealed that 77% of the analyzed facades are noncompliant with the Brazilian and Portuguese standards.

Openings of approximately 0.5 cm were left intentionally in two windows and a door to simulate the effect of gaps commonly found in Brazilian buildings. In the three situations, there was a decrease of 2 to 3 dB in the value of the parameter weighted standardized level difference — $D_{2m,nT,w}$. The gap's effects on sound insulation levels in the 1000 to 3150 Hz frequency range is more significant than in the 100 to 1000 Hz frequency range.

The findings of this study are consistent with those of other researchers: Brazil has a systemic problem in the acoustic quality of its buildings. The main reasons are: imperfections in the finishing due to a poorly qualified workforce, lack of standardization of materials, lack of maintenance, and negligence or ignorance during the construction phase. Doors and windows are the weak link in the sound insulation of most buildings in Brazil.

There is no single action solution for this verified low sound insulation problem. The use of materials with higher acoustic performance, the training of qualified workforce, continuous maintenance, and the creation of awareness campaigns about noise directed to population are suggested as mitigation actions for this architectural and environmental issue.

REFERENCES

[1] Pinto, F. A. C., Mardones, M. D. M. Noise mapping of densely populated neighborhoods example of Copacabana Rio de Janeiro Brazil. *Environmental Monitoring Assessment*, **155**, 309–318, (2009). http://dx.doi.org/10.1007/s10661-008-0437-9

[2] Bunn, F. *Impacto ambiental sonoro no trecho Sul da Linha Verde na cidade de Curitiba (Environmental noise impact in the South segment of the Green Line in Curitiba), Graduate assignment in Environmental Engineering,* Federal University of Paraná, Brazil, (2010).

[3] Guedes, I. C. M.. Bertoli, S. R., and Zannin, P. H. T. Influence of urban shapes on environmental noise: a case study in Aracaju Brazil. *Science of the Total Environment*, **412**, 66–76, (2011). http://dx.doi.org/10.1016/j.scitotenv.2011.10.018

[4] Engel, M. S. *Caracterização da poluição sonora, através de medições e mapeamentos sonoros e entrevistas de percepção sonora na Linha Verde em Curitiba (Characterization of noise pollution based on measurements, noise mapping, and interviews on noise perception on the Green Line in Curitiba). Dissertation (Master's in Water Resources and Environmental Engineering),* Federal University of Paraná, Brazil, (2012).

[5] Zannin, P. H. T., Engel, M. S., Fiedler P. E. K., and Bunn F. Characterization of environmental noise based on noise measurements, noise mapping and interviews: A case study at a university campus in Brazil, *Cities*, **31**, 317–327, (2012). http://dx.doi.org/10.1016/j.cities.2012.09.008

[6] Bunn, F. *Avaliação da Poluição Sonora Gerada Pelo Tráfego Ferroviário na Cidade de Curitiba (Assessment of Noise Pollution Generated By Rail Traffic in Curitiba). Dissertation (Master's in Water Resources and Environmental Engineering),* Federal University of Paraná, Brazil, (2013).

Table 4. Measured $D_{2m,nT,w}$ values compared to the standards.

CASE	FACADE	TYPE	Measured $D_{2m,nT,w}$ * [dB]	Minimum $D_{2m,nT,w}$ according to NBR 15.575-4[dB]	Minimum $D_{2m,nT,w}$ according to Portugal's RRAE [dB]
1	1	bedroom	23 I	25	28
2	2	bedroom	22 I	25	28
3	3 Situation 1	bedroom	17 I	25	28
4	3 Situation 2	bedroom	9 I	25	28
5	3 Situation 3	bedroom	19 I	25	28
6	4 Situation 1	living room	26 I	not specified	28
7	4 Situation 2	living room	24 I	not specified	28
8	5	classroom	28 S	not specified	28
9	6 Situation 1	bedroom	21 I	25	28
10	6 Situation 2	bedroom	18 I	25	28
11	7	living room	29 S	not specified	28
12	8 Situation 1	bedroom	30**	30	33
13	8 Situation 2	bedroom	28 I	30	33

SOURCES: Portugal (2008); ABNT (2013); the authors (2013)
*Values followed with the letter S are satisfactory; they meet the minimum requirements of the standards;
* Values followed with the letter I are insufficient; they do not meet the established requirements;
**Case 12 meets the Brazilian standard, but is noncompliant with the Portuguese standard.

[7] Fiedler, P. E. K. *Poluição sonora nos eixos estruturais de transporte da cidade de Curitiba PR (Noise pollution in the structural transport hubs of Curitiba, PR). Dissertation (Master's in Water Resources and Environmental Engineering),* Federal University of Paraná, Brazil, (2013).

[8] Jobim, M. S. S. *Método de avaliação do nvel de satisfação dos clientes de imóveis residenciais (Method for assessing the level of satisfaction of residential real estate clients). Dissertation (Master's in Civil Engineering),* Federal University of Rio Grande do Sul, Brazil, (1997).

[9] Queiroz, C. S. and Viveiros, E. B. Simulação do desempenho do isolamento acústico de fachadas de edificações residenciais multifamiliares de diferentes perodos arquitetonicos (Simulation of the performance of sound insulation of façades of multifamily apartment buildings of different architectural periods). *VI Congresso Iberoamericano de Acústica* FIA 2008, Buenos Aires, Argentine, (2008).

[10] Ferreira, J. A. C. and Zannin, P. H. T. *Determinação de coeficientes de isolamento acústico: medições in situ e simulação computacional.* Revista Ambiente Construdo, Porto Alegre, (2007).

[11] Deutsches Institut f ur Normung. DIN 4.109: Schallschutz im Hochbau. Germany, (1989).

[12] Associação Brasileira de Normas Técnicas (ABNT). (Brazilian Association of Technical Standards). NBR 15.575-4: Edificações habitacionais Desempenho Parte 4: Requisitos para os sistemas de vedações verticais internas e externas SVVIE [Residential Buildings Performance Part 4: Requirements for internal and external partition wall systems SVVIE]. Rio de Janeiro, (2013).

[13] Portugal Presidência da República. Decreto do Presidente da República n.º 34/2008. Diário da República, 1.ª Série N.º 110–09 de junho de 2008.

[14] International Standard ISO 140-5 *Acoustics Measurement of sound insulation in buildings and of building elements Part 5: Field measurements of airborne sound insulation of façade elements and façades.* 2nd Edition, (1998).

[15] International Standard ISO 717-1 *Acoustic Rating of sound insulation in buildings and of building elements Part 1: Airborne sound insulation.* Geneva, (1996).

[16] International Standard ISO 354 Measurement of sound absorption in a reverberation room. Geneva, (2003).

[17] Brüel and Kjaer. *Technical Documentation. Building Acoustics System. For Modular Precision Sound Analyzer Type 2260,* (1996).

[18] Portugal Ministério do Ambiente, do Ordenamento do Território e do Desenvolvimento Regional. Decreto Lei n.º 9/2007. Diário da República, 1.ª Série N.º 12–17 de janeiro de 2007.

[19] Bistafa, S. R. *Acústica Aplicada ao Controle de Rudos [Acoustics Applied to Noise Control].* Ed. Edgard Blcher. São Paulo, (2006).

[20] Ferreira, J. A. C. *Avaliação Acústica de Residłncias: Resultados Medidos e Simulados (Acoustic Assessment of Residences: Measured and Simulated Results).* Dissertation (Master's in Mechanical Engineering), Federal University of Paraná, Brazil, 2004.

[21] Bordeau, L. Sustainable development and the future of construction: a comparison of visions from various countries. *Building Research & Information*, **27**, 354–366, (1999). http://dx.doi.org/10.1080/096132199369183

[22] Abiko, A. K., Gonçalves, O. M., and Cardoso, L. R. A. *O futuro da construção civil no Brasil Resultados de um estudo de prospecção tecnológica da cadeia produtiva da construção habitacional (The Future of Construction in Brazil - Results of a technological study on the production chain of housing construction).* São Paulo, (2003).

[23] Zannin, P. H. T. and Ferreira, J. A. C. In situ performance of materials used in Brazilian building construction. *Construction and Building Materials*, **21**, 1820–1824, (2007). http://dx.doi.org/10.1016/j.conbuildmat.2006.05.015

[24] Polli, T. O. *isolamento acústico comparado aos investimentos financeiros em edifcios multifamiliares de Florianópolis (Acoustic insulation compared to financial investments in multifamily buildings in Florianopolis). Dissertation (Master's in Architecture and Urbanism)* Federal University of Santa Catarina, Brazil, (2007).

Dynamic Feature Extraction for Speech Signal Based On MUSIC and Modulation Spectrum

Han Zhiyan and Wang Jian

College of Engineering, Bohai University, No. 19, Sci-tech Road, High & New Technological and Industrial Development District, Jinzhou, China, 121000

(Received 19 August 2015; accepted 30 June 2016)

A novel dynamic feature extraction algorithm is proposed to help improve speech recognition robustness in noise environmental conditions. Owing to the modulation spectrum having time-frequency agglomeration performance, according to different reflections in the modulation spectrum for interference and speech signals, we first calculate the Multiple Signal Classification (MUSIC) spectrum and then get the modulation spectrum. We then filter the modulation spectrum signal. For the filter signal, use a 32 frames signal is used as a processing unit to get the modulation spectrum energy vector. This reveals the close correlation between the speech signal frames and can well reflect speech dynamic characteristics. Finally, the cepstrum coefficients are extracted as the feature parameter. It not only adequately reflects speech dynamic characteristics, but also has lower sensitivity for the speech environment. The effectiveness of the feature is discussed in view of the class separability and speaker variability properties. We evaluated the feature under different kinds of noise (white noise, pink noise, street noise, and panzer noise) and different signal-to-noise ratios (-5 dB, 0 dB, 5 dB, 10 dB, and 15 dB). The experimental results show that the novel feature has good robustness and computational efficiency under low signal-to-noise ratios and plays a very good foreshadowing role in latter speech research.

NOMENCLATURE

MFCC:	Mel Frequency Cepstral Coefficient
MUSIC:	Modulation Spectrum; Multiple Signal Classification
LPC:	Linear Prediction Coefficients
LSP:	Linear Spectrum Pair
FFT:	Fast Fourier Transform
LDA:	Linear Discriminant Analysis
DM:	Determinant Measure
HMM:	Hidden Markov Model
BPNN:	Back-Propagation Neural Networks
SNR:	Signal-to-Noise Ratio

1. INTRODUCTION

Research on the robustness of speech recognition was still a challenging task, especially in the development of core speech processing algorithms. One example was feature extraction from speech signals. Namely, extracting features that could reflect speech characteristics from the speech waveforms. It not only could reduce the number of calculations and storage, but could also filter out useless and redundant information and was one of the most fundamental and important aspects of speech recognition. Some time domain features, such as amplitude feature, short-time frame average energy, short-time frame zero crossing rate, short-time autocorrelation coefficient, et cetera appeared. With the development of recognition technology, we found that the stability and separating capacity for the time domain features were not good, so we began using the frequency domain feature as a speech feature, such as pitch period, formant frequency, linear prediction coefficients (LPC), linear spectrum pair (LSP), cepstrum coefficient, and so on. Among them, the MFCC, which was based on the auditory model, was a widely-applied feature at present. However, once these features were used in the noise environment, their performance droped sharply.[1–4]

The features mentioned above reflect the static feature of speech signal, while a dynamic feature was part of speech diversity, which was different from a stationary random process. It had time correlation, and revealed the close relationship between speech signal (pre and post). We could get the dynamic feature by differential parameters and acceleration parameters for the static feature. However, differential parameters and acceleration parameters could not fully dig out dynamic information. Therefore, studying the dynamic feature of the speech signal was an inevitable trend to improve the performance of speech recognition.

Estimating the time-varying spectrum was a key first step in the speech feature extraction.[5–10] MFCC was computed by applying a Mel-scaled filter bank either to the short-time Fast Fourier Transform (FFT) magnitude spectrum or to the short-term LPC-based spectrum. However, both FFT and LPC-based spectrum were very sensitive to noise contamination. Eigenvector-based methods, such as MUSIC, were popular in sinusoidal frequency estimation due to their high resolution and less prior information. Moreover, MUSIC algorithm had well noise restraining ability. We adopted the MUSIC spectrum instead of the traditional method.

Owing to the modulation spectrum having time-frequency agglomeration performance, it not only adequately reflected speech dynamic characteristics, but also had lower sensitivity for the speech environment. In the modulation spectrum, the interference component produced by additive noise and channel distortion eased to separate from speech signal. Which is why we used modulation spectrum technology in this study to extract feature, which will be better.

2. ALGORITHM DESCRIPTION

2.1. MUSIC Algorithm

According to matrix theory, linear space $\mathbf{v}_1, \mathbf{v}_2 \ldots \mathbf{v}_N$, could decompose into a direct sum of two subspaces $\mathbf{V}_1$ and $\mathbf{V}_2$, that is:[11–13]

$$\mathbf{V}_1 = [\mathbf{v}_1, \mathbf{v}_2, \ldots \mathbf{v}_p]; \tag{1}$$

$$\mathbf{V}_2 = [\mathbf{v}_{p+1}, \mathbf{v}_{p+2}, \ldots \mathbf{v}_N]; \tag{2}$$

then:

$$\mathbf{V} = [\mathbf{V}_1 \ \mathbf{V}_2]. \tag{3}$$

For the signal consisting of p sinusoidal components, the complex amplitudes and frequencies were $g_k, \omega_k, k = 1, 2, \ldots p$ respectively, then the signal could be expressed as:

$$\mathbf{X} = \mathbf{S}\mathbf{g} + \mathbf{W}; \tag{4}$$

where $\mathbf{W}$ was white noise with a zero mean and a variance σ^2, $\mathbf{X}^T = [\mathbf{X}_1, \mathbf{X}_2, \ldots \mathbf{X}_N]$, $\mathbf{S} = [e(\omega_1), e(\omega_2), \ldots e(\omega_p)]$, $\mathbf{e}^T(\omega_k) = \left[1, e^{j\omega_k}, \ldots e^{j(N-1)\omega_k}\right]$, $\mathbf{g}^T = [g_1, g_2, \ldots g_p]$, $\mathbf{W}^T = [w_1, w_2, \ldots w_N]$.

The autocorrelation matrix for signal $\mathbf{X}_n, n = 1, 2, \ldots N$ can be shown as:

$$\mathbf{R}_{XX} = E\left[\mathbf{X}\mathbf{X}^H\right] = \mathbf{S}\mathbf{G}\mathbf{S}^H + \sigma^2\mathbf{I}; \tag{5}$$

where $\mathbf{G}$ was the autocorrelation matrix with p sinusoidal components.

According to the matrix theory, eigenvalue decomposition for Eq. (5) was:

$$\mathbf{R}_{XX} = \mathbf{V}\mathbf{\Lambda}\mathbf{V}^H = \sum_{i=1}^{N} \lambda_i \mathbf{v}_i \mathbf{v}_i^H; \tag{6}$$

where $\mathbf{V} = [\mathbf{v}_1, \mathbf{v}_2, \ldots \mathbf{v}_N]$, $\mathbf{\Lambda} = \text{diag}\,[\lambda_1, \lambda_2, \ldots \lambda_N]$.

MUSIC algorithm was a noise subspace frequency estimator; the weighted spectrum estimation is as follows:

$$P(\omega) = \sum_{i=p+1}^{N} \mathbf{u}_k \left|\mathbf{e}^H(\omega)\mathbf{v}_i\right|^2; \tag{7}$$

where $\mathbf{v}_i, i = p+1, p+2, \ldots N$ was the eigenvector corresponding to noise subspace and u_k was a group of positive weights, $\mathbf{e}^H = \left[1, e^{j\omega}, \ldots e^{j(N-1)\omega}\right]$. Notice here, when $\omega = \omega_i$, $P(\omega_i) = 0, i = 1, 2, \ldots p$, the reciprocal of $P(\omega)$ was the peak function in the frequency domain. This provided a method for sinusoidal component frequency estimation. So the power spectrum function was as follows:

$$P_{MUSIC}(\omega) = \frac{1}{\sum\limits_{i=p+1}^{N} \left|\mathbf{e}^H(\omega)\mathbf{v}_i\right|^2}. \tag{8}$$

According to the process of the MUSIC algorithm, we could see that the mathematical principle of this algorithm was through singular value decomposition for the signal autocorrelation matrix. The signal eigenspace was decomposed into signal subspace relative to the signal component and noise subspace orthogonal to the signal component, and then estimated signal frequencies using the orthogonality of the two spaces. So, in theory, this method had the advantages that FFT could not substitute. Therefore, it was called the super-resolution frequency estimation algorithm.

2.2. Modulation Spectrum Principle

The definition of speech modulation spectrum is as follows:

$$M(\omega, \eta) = \frac{1}{2\pi} \int_{-\infty}^{\infty} \int_{-\infty}^{\infty} x(t + \frac{\tau}{2}) x^*(t - \frac{\tau}{2}) e^{-j\omega\tau} e^{-j\eta\tau} d\tau dt = X^*(\omega - \frac{\eta}{2}) X(\omega + \frac{\eta}{2}); \tag{9}$$

where τ is delay time, ω and η are speech frequency and modulation spectrum respectively.

$M(\omega, \eta)$ could be considered as the two dimensional transform of the autocorrelation function $x(t)$ or as the autocorrelation function for $X(\omega)$. However, there was also some unwanted coherent term. So we had to smooth process on the modulation spectrum $M(\omega, \eta)$ via short window. We usually choose a Hamming window as the window function. After smoothing, the modulation spectrum is as follows:

$$M^{sp}(\omega, \eta) = M_W(\omega, \eta) * M_x(\omega, \eta); \tag{10}$$

where $M_W(\omega, \eta)$ is the modulation spectrum for window function $W(t)$.

Figure 1 and Fig. 2 show the improvements of clean speech recognition rate and noise speech recognition rate on different modulation spectrum frequency bands respectively.[14–16]

The figures, from the first section to the thirteenth section express the frequency in the range of 0–0.5 Hz, 0.5–1 Hz, 1–1.4 Hz, 1.4–2 Hz, 2–2.8 Hz, 2.8–4 Hz, 4–5.7 Hz, 5.7–8 Hz, 8–11.3 Hz, 11.3–16 Hz, 16–22.6 Hz, 22.6–32 Hz, and 32–40 Hz respectively.

From Figs. 1 and 2, we can see that almost all the useful features for speech recognition were concentrated on 1–13 Hz. Among them, the characteristics around 4 Hz were the most important. We could also see that all of the modulation components were useful in a clean speech environment, but in a noise speech environment, the modulation components under

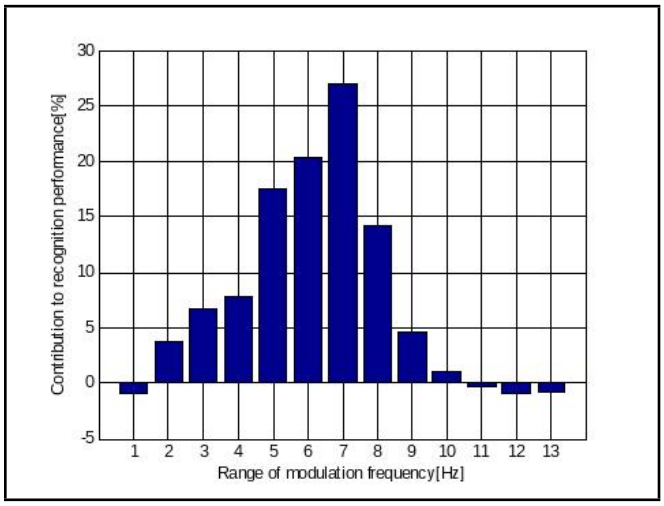

Figure 1. The improvement of recognition accuracy by including the modulation frequency for clean speech.

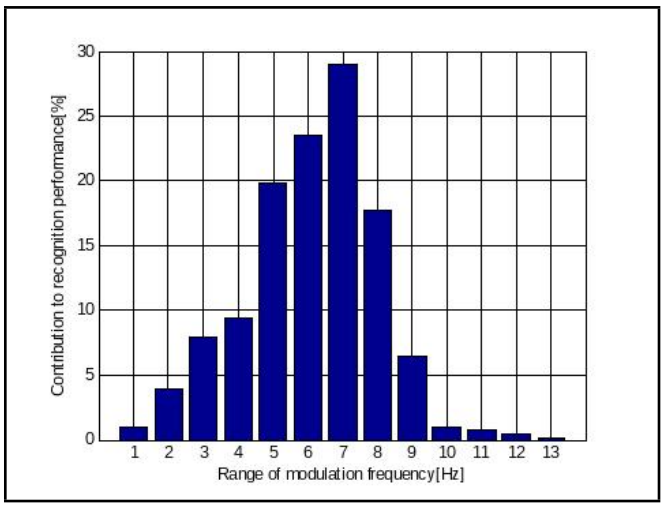

Figure 2. The improvement of recognition accuracy by including the modulation frequency for noise speech.

0.5 Hz and over 16 Hz did not affect the recognition rate; if we had used them, the recognition rate would have decreased.

According to the characteristics of the modulation spectrum, we designed a band-pass filter to suppress interfering components with passband of 1–13 Hz. The transfer function was as follows:

$$H(z) = 0.1z^4 \frac{2 + z^{-1} + z^{-3} - 2z^{-4}}{1 - 0.98z^{-1}}. \tag{11}$$

The frequency response is shown in Fig. 3.

3. DF-MMS FEATURE EXTRACTION

The new feature was called DF-MMS. Figure 4 shows a schematic diagram of the DF-MMS.

We assumed that $x(n)$ denoted an input speech signal the proposed DF-MMS algorithm could be summarized as follows:

Step 1: Speech signal $x(n)$ underwent a series of preprocessing, which included preemphasis, frame, window interception and endpoint detection.

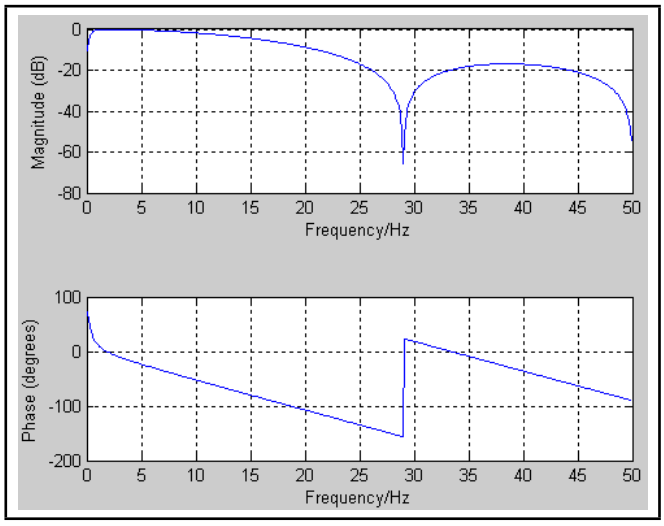

Figure 3. The frequency response for filter.

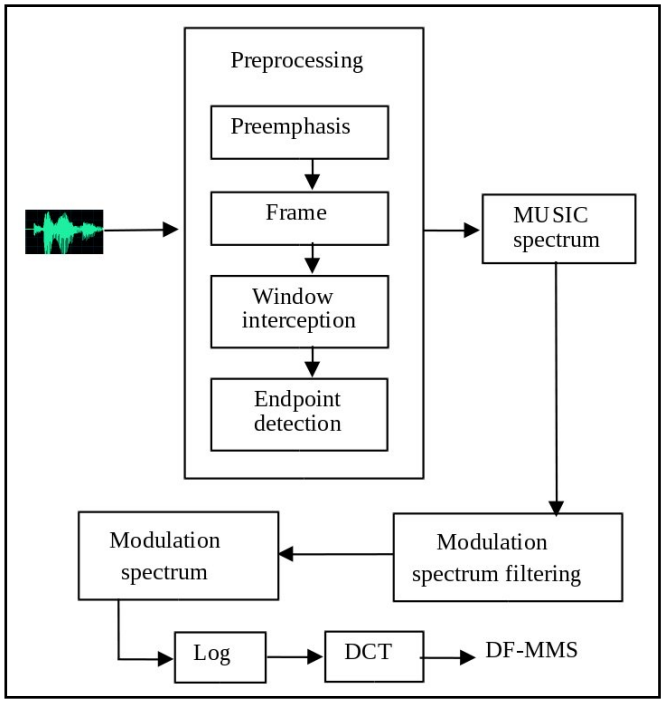

Figure 4. A schematic diagram of the DF-MMS.

Step 2: Calculated the MUSIC spectrum using Eq. (8).

$$P_{MUSIC}(\omega) = \frac{1}{\sum_{i=p+1}^{N} |\mathbf{e}^H(\omega)\mathbf{v}_i|^2}. \tag{12}$$

Step 3: Let speech MUSIC spectrum at the time t be $P_{MUSIC}(t, \omega)$, then the modulation spectrum will be:

$$M^{sp}(\omega, \eta) = \int P_{MUSIC}(t, \omega) W(t) e^{-j\eta t} dt. \tag{13}$$

The filter of Eq. (11) was then used to suppress interfering components for the modulation spectrum and get the signal spectrum $F(\omega, \eta)$.

Step 4: For the molulation spectrum filtering signal $F(\omega, \eta)$, 32 frames signal was used as a processing unit to get a $F \times 32$ matrix. The sum of squares of the same row data were

then calculated. We could get a vector, that is, the modulation spectrum energy vector $t(i), 0 \leq i \leq F$, F was frame size.

Step 5: Calculated the Log for the front $F/2+1$ features.

$$\mathbf{u}(i) = \log(\mathbf{t}(i)), \quad i = 0, 1, \ldots F/2. \tag{14}$$

Step 6: Took the DCT.

$$\mathbf{c}[n] = \cos[n \cdot (i+0.5) \cdot \frac{\pi}{F/2+1}] * \mathbf{u}(i); \tag{15}$$

where $i = 0, 1, \ldots F/2$, $1 \leq n \leq L$; L was the desired order of DF-MMS.

4. EXPERIMENT AND RESULT ANALYSIS

4.1. Class Separability and Interspeaker Variability

The effectiveness of a feature extraction scheme depended mainly on how well separated the different speech classes and suppress speaker dependent information were. We described a measure based on the linear discriminant analysis (LDA) technique in order to analyze class separability and interspeaker variability .

4.1.1. Class separability analysis

Class separability could be measured by using Fishers LDA.[17] The class mean $\mathbf{m}_c$ and global mean $\mathbf{m}$ were computed as:

$$\mathbf{m}_c = \frac{1}{N_c} \sum_{i=1}^{N_c} \mathbf{x}_{c,i}; \tag{16}$$

$$\mathbf{m} = \frac{1}{N} \sum_{c=1}^{C} \sum_{i=1}^{N_c} \mathbf{x}_{c,i}; \tag{17}$$

where $\mathbf{x}_{c,i}, c = 1, 2, \ldots C, i = 1, 2, \ldots N_c$ was D dimensional feature vectors for speech class c. $N = \sum_{c=1}^{C}$ stood for the total sample numbers.

The within-class scatter matrices $\mathbf{S}_W$ and the between-class scatter matrices $\mathbf{S}_B$ were computed as:

$$\mathbf{S}_W = \frac{1}{N} \sum_{c=1}^{C} \sum_{i=1}^{N_c} (\mathbf{x}_{c,i} - \mathbf{m}_c)(\mathbf{x}_{c,i} - \mathbf{m}_c)^T \mathbf{x}_{c,i}; \tag{18}$$

$$\mathbf{S}_B = \frac{1}{N} \sum_{c=1}^{C} N_c (\mathbf{m}_c - \mathbf{m})(\mathbf{m}_c - \mathbf{m})^T. \tag{19}$$

We considered a linear projection of the feature vectors onto a d dimensional subspace, where $d \ll D$. The projection matrix $\mathbf{A}$ was chosen so that the projected feature vectors belonged to one class. This was achieved by computing a projection that maximized the objective function of the ratio between the within-class variance and the between-class variance in the projected space:

$$\mathbf{A} = \underset{L}{\operatorname{argmax}} \frac{\left|\mathbf{L}\mathbf{S}_B\mathbf{L}^T\right|}{\left|\mathbf{L}\mathbf{S}_W\mathbf{L}^T\right|}. \tag{20}$$

The columns of $\mathbf{A}$ were the eigenvectors corresponding to the largest eigenvalues of $\mathbf{S}_W^{-1}\mathbf{S}_B$. The optimum value of objective function was the product of the d largest eigenvalues. We used the logarithm of product as the Determinant Measure (DM):

$$DM = \log\left(\prod_{i=1}^{d} \lambda_i\right). \tag{21}$$

We used the Hidden Markov Model (HMM) stated as the speech classes. For all the features, we generated $D = 96$ dimensional feature vectors by splicing eight consecutive frames. These feature vectors were then projected onto a $d = 30$-dimensional subspace using LDA. The DM values for DF-MMS and differential parameter for MFCC were -70.42 and -83.06 respectively. The results indicated that DF-MMS achieved the best class separability among all schemes considered.

4.1.2. Interspeaker variability analysis

We used a simple modification of the LDA method to evaluate the robustness of speaker variability.[17] The following equation was used to define the mean of class c for speaker s:

$$\mathbf{m}_{c,s} = \frac{1}{N_{c,s}} \sum_{i=1}^{N_{c,s}} \mathbf{x}_{c,s,i}; \tag{22}$$

where $\mathbf{x}_{c,s,i}, c = 1, 2, \ldots C, s = 1, 2, \ldots S, i = 1, 2, \ldots N_{c,s}$ was D dimensional feature vector for speech class c and speaker s. Let M_c denote the total number of speakers that had samples in class c, $N_{c,s} \neq 0$. For the large databases, all the speakers had samples from all classes. Hence, M_c will equal to S. We can now compute the class means as:

$$\mathbf{m}_c = \frac{1}{M_c} \sum_{s} \mathbf{m}_{c,s}. \tag{23}$$

The global mean for the entire database was computed as:

$$\mathbf{m} = \frac{1}{M} \sum_{c=1}^{C} M_c \mathbf{m}_c; \tag{24}$$

where M was the total number of such means.

The between-class $\mathbf{S}_B$ and the within-class $\mathbf{S}_W$ scatter matrices were computed as:

$$\mathbf{S}_W = \frac{1}{M} \sum_{c=1}^{C} \sum_{s} (\mathbf{m}_{c,s} - \mathbf{m})(\mathbf{m}_{c,s} - \mathbf{m})^T; \tag{25}$$

$$\mathbf{S}_B = \frac{1}{M} \sum_{c=1}^{C} M_c (\mathbf{m}_c - \mathbf{m})(\mathbf{m}_c - \mathbf{m})^T. \tag{26}$$

Using the above expressions for $\mathbf{S}_B$ and $\mathbf{S}_W$, the DM values for DF-MMS and differential parameter for MFCC were -63.85 and -80.94 respectively. The results indicated that DF-MMS had the largest DM.

4.2. Recognition Efficiency

Some experiments were conducted to evaluate the proposed feature for speech recognition system performance. They could be considered in two aspects: recognition rate and computational consideration. The recognition rate was evaluated under different noises (white noise, pink noise, street noise, and panzer noise) and different SNR (-5 dB, 0 dB, 5 dB, 10 dB, and 15 dB). The data was recorded at 11.025 kHz sampling rate and coded into 256 sampling points with a frame shift of 80 sampling points, where each frame was represented by a 13 dimension vector. We used improved Back-Propagation Neural Networks (BPNN) as the classifier and binary coding output to improve the real-time performance.[18]

The noisy speech data was derived by adding noisy data into the clean speech signal. Because the noise could be divided into additive noise and multiplicative noise, the multiplicative noise could be transformed to additive noise through homomorphic transform. Therefore, discussing additive noise had representative. In this paper, we used global SNR as follows:

$$SNR = 10 \log \frac{\sum_{k=0}^{N-1} s^2(k)}{\sum_{k=0}^{N-1} n^2(k)}; \tag{27}$$

where $s(k)$ was the clean speech signal through the endpoint detector, and was $n(k)$ was the noisy speech signal.

Figures 5(a)–(d) show the recognition performance curves of using DF-MMS and differential parameter for MFCC under white noise, pink noise, street noise, and panzer noise respectively.

From Figs. 5(a)–(d), we can see that the feature DF-MMS improved the recognition rate and robust performance compared with a differential parameter for MFCC under low SNR. This was because we used MUSIC spectrum and the modulation spectrum. In particular, the use of the modulation spectrum not only reflected speech dynamic characteristics, but also had lower sensitivity for the speech environment. And we used a 32 frames signal as a processing unit to get the modulation spectrum energy vector, which revealed the close correlation between the speech signal frames could well reflect speech dynamic characteristics.

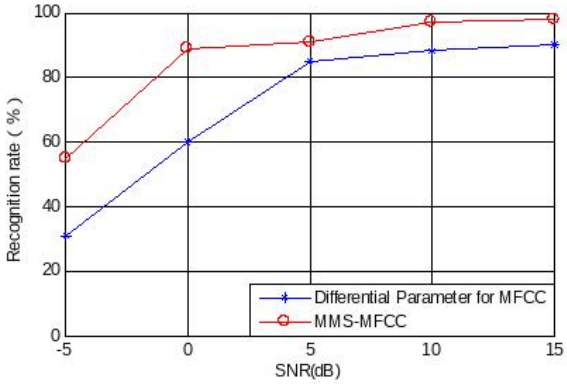

(a) The recognition curve under white noise.

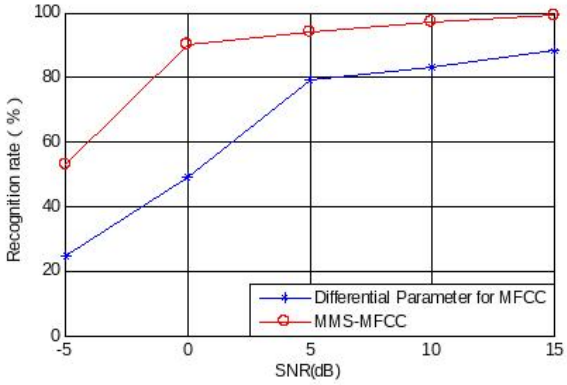

(b) The recognition curve under pink noise.

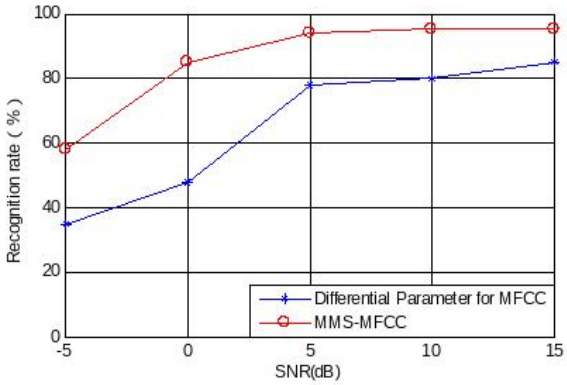

(c) The recognition curve under street noise.

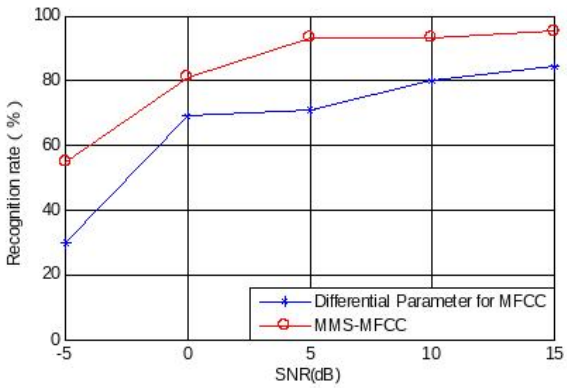

(d) The recognition curve under panzer noise.

Figure 5. The recognition performance curve under different SNR.

5. CONCLUSIONS

In this paper, we proposed a robust speech feature extraction method based on MUSIC and the modulation spectrum. The results show that significant advances have been achieved in this area. Although feature DF-MMS can be seen to be modest increase over the differential parameter for MFCC, it compensates for the loss in the search and its kernel algorithm has been used in the voice controlled system of a company.

ACKNOWLEDGMENTS

This work was supported by a grant from the National Natural Science Foundation of China (No. 61403042, No.

61503038) and a grant from Education Department of Liaoning Province of China (No. L2013423).

REFERENCES

[1] Jo, J., Yoo, H., and Park, I. C. Energy-Efficient floating-point MFCC extraction architecture for speech recognition systems, *IEEE Trans. on Very Large Scale Integration Systems*, **24**(2), 754–758, (2016). http://dx.doi.org/tvlsi.2015.2413454

[2] Jang, G. J., and Cho, H. Y. Efficient spectrum estimation of noise using line spectral pairs for robust speech recognition, *Electronics Letters*, **47**(25), 1399–1401, (2011). http://dx.doi.org/10.1049/el.2011.2830

[3] Taabish, G., Anand, S., and Sandeep, S. Comparative analysis of LPCC, MFCC and BFCC for the recognition of Hindi words using artificial neural networks, *International Journal of Computer Applications*, **101**(12), 22–27, (2014). http://dx.doi.org/10.5120/17740-8271

[4] Murty, K. S. R. and Yegnanarayana, B. Combining evidence from residual phase and MFCC features for speaker recognition, *IEEE Trans. on Acoustics, Speech and Signal Processing*, **13**(1), 52–55, (2006). http://dx.doi.org/10.1109/lsp.2005.860538

[5] Yang, L. D., Wang, J., Xie, X., and Kuang, J. M. Application of tucker decomposition in speech signal feature extraction, *2013 International Conference on Asian Language Processing*, Urumqi, (2013). http://dx.doi.org/10.1109/ialp.2013.50

[6] Wu, Q., Zhang, L. Q., and Shi, G. C. Robust multifactor speech feature extraction based on gabor analysis, *IEEE Trans. on Audio, speech, and Language Processing*, **19**(4), 927–936, (2011). http://dx.doi.org/10.1109/tasl.2010.2070495

[7] Zou, X. Y., Zheng, W. Q., Wei, S., and Hong, L. Improved voice activity detection based on support vector machine with high separable speech feature vectors, *The 19th international Conference on Digital Signal Processing*, Hong Kong, (2014). http://dx.doi.org/10.1109/icdsp.2014.6900767

[8] Deng, J. P., Bouchhard, M., and Yeap, T. H. Feature enhancement for noisy speech recognition with a time-variant linear predictive HMM structure, *IEEE Trans. on Audio, speech, and Language Processing*, **16**(5), 891–899, (2008). http://dx.doi.org/10.1109/tasl.2004.924593

[9] Ludovic, T., Philippe, G., and Brahim, C. D. Feature selection for robust automatic speech recognition: a temporal offset approach, *International Journal of Speech Technology*, **18**(3), 395–404, (2015). http://dx.doi.org/10.1007/s10772-015-9276-6

[10] Sharma, U., Maheshkar, S., and Mishra, A. N. Study of robust feature extraction techniques for speech recognition system, *The International Conference on Futuristic Trends on Computational Analysis and Knowledge Management*, Noida, (2015). http://dx.doi.org/10.1109/ablaze.2015.7154944

[11] Rieken, D. W. and Fuhrmann, D. R. Generalizing MUSIC and MVDR for multiple noncoherent arrays, *IEEE Trans. on Signal Processing*, **52**(9), 2396–2406, (2004). http://dx.doi.org/10.1109/tsp.2004.832153

[12] Kaushik, M. Spectrum estimation, notch filters, and MUSIC, *IEEE Trans. on Signal Processing*, **53**(10), 3727–3737, (2005). http://dx.doi.org/10.1109/tsp.2005.855395

[13] Chen, X. D. and Agarwal, K. MUSIC algorithm for two-dimensional inverse problems with special characteristic of cylinders, *IEEE Trans. on Antennas and Propagation*, **56**(6), 1808–1812, (2008). http://dx.doi.org/10.1109/tap.2008.923333

[14] Smith, C. L., Browman, C. P., Mcgowan, R. S., and Kay, B. Extracting dynamic parameters from speech movement data, *J. Acoust. Soc. Am.*, **93**(3), 1580–1588, (1993). http://dx.doi.org/10.1121/1.406817

[15] Yousefi, M. T. and Kschischang, F. R. Information transmission using the nonlinear fourier transform, part III: spectrum modulation, *IEEE Trans. on Information Theory*, **60**(7), 4346–4369, (2014). http://dx.doi.org/10.1109/tit.2014.2321155

[16] Sridhar, K. N., Kailash, P., and Mounya, E. A multistream feature framework based on bandpass modulation filtering for robust speech recognition, *IEEE Trans. on Audio, Speech, and Language Processing*, **21**(2), 416–426, (2013). http://dx.doi.org/10.1109/tit.2014.2321155

[17] Dharanipragada, S., Yapanel, U. H., and Rao, B. D. Robust feature extraction for continuous speech recognition using the MVDR spectrum estimation method, *IEEE Trans. on Audio, speech, and Language Processing*, **15**(1), 224–234, (2007). http://dx.doi.org/10.1109/tasl.2006.876776

[18] Yang, S. S., Ho, C. L. and Lee, C. M. HBP improvement in BP algorithm for an adaptive MLP decision feedback equalizer, *IEEE Trans. on Circuits and Systems*, **53**(3), 240–244, (2006). http://dx.doi.org/10.1109/tcsii.2005.858494

About the Authors

Alessandro Anobile received his MS degree in aeronautical engineering from Roma TRE University in 2009 with a dissertation on higher-harmonic control systems for reducing noise emitted by helicopters in descending flight. Currently, he is a PhD student of the doctoral mechanical engineering program at Roma Tre University in Rome, Italy, where he has been awarded a fellowship for 2012-2014 for studies concerning development of design computational tools for rotorcraft. Specifically, his research interests include the study of efficient procedures and formulations suitable for aeroelastic and aeroacoustic analyses in rotorcraft preliminary design and optimization. He has presented several papers at international conferences dealing with the numerical application of developed active and passive approaches aimed at reducing noise and vibrations in helicopters.

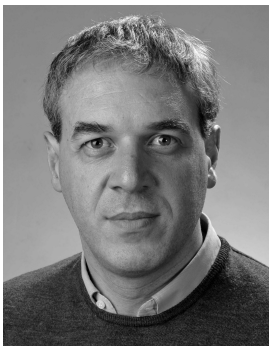

Giovanni Bernardini received his MS degree in aeronautical engineering from the University of Rome La Sapienza in 1996 and his PhD in aerospace engineering from Politecnico di Milano in 2000. From 2000 to 2010, he worked as a research associate for the Department of Mechanical and Industrial Engineering at Roma TRE University, also teaching courses concerning the design of aeronautical structures. In this period, he served as a lecturer of fluid mechanics in the Department of Environmental Sciences at the University of Pisa. He is currently an assistant professor in the Department of Engineering of Roma TRE University in Rome, Italy, teaching courses concerning aircraft structures design and aeronautical structures. His present research interests include unsteady aerodynamics, structural dynamics, aeroelasticity, and aeroacoustics of rotorcraft, as well as multi-disciplinary optimization for the conceptual/preliminary design of conventional and innovative aircraft/rotorcraft configurations.

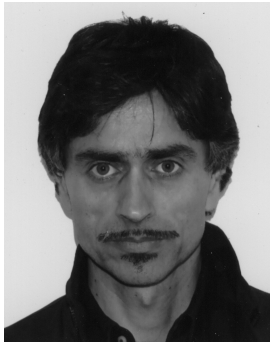

Massimo Gennaretti received his MS degree in aeronautical engineering in 1989 and his PhD in theoretical and applied mechanics in 1992 from the University of Rome La Sapienza. In 1994, he joined Roma TRE University as an assistant professor of flight mechanics. He is currently a professor of aeronautical structures at Roma TRE University in Rome, Italy, where he teaches the courses in aeroelasticity and mathematical modeling for aeronautics within the aeronautical engineering master's degree program. His present research interests include unsteady aerodynamics, aeroelasticity and aeroacoustics of rotorcraft, as well as interior and exterior acoustics concerning aeronautical applications. He has been involved as team leader in several research projects funded by EU.

Xiaojun Wang is a professor in the Institute of Solid Mechanics at Beihang University. He graduated with a degree in theoretical and applied mechanics from Hebei University, China, in 2001 and received his PhD from Beihang University, China, in 2006. He has been working at the Institute of Solid Mechanics, Beihang University, as a professor in uncertain structural mechanics since 2013. His main research areas include computational solid mechanics, structural dynamics, structural reliability, structural damage identification and health monitoring, structural dynamic load identification, and aero-elasticity. He has authored and co-authored five books, more than 100 technical papers and holds more than five patents on uncertain analysis.

Yunlong Li is a sixth year PhD candidate at the Institute of Solid Mechanics at Beihang University. He received his BS from Shandong University of Science and Technology, China, 2010. His main research areas include active control of vibration and noise, structural reliability analysis, uncertain optimization, computational solid mechanics and structural dynamics. He has authored and co-authored more than 15 technical papers and holds more than three patents on design of active control system.

Zhiliang Ma is a Master's candidate in the Institute of Solid Mechanics at Beihang University. His main research areas include acoustic analysis, design optimization of vibro-acoustic system, reliability optimization and robust optimization of vibro-acoustic system.

Zhiping Qiu is a professor emeritus at the Institute of Solid Mechanics at Beihang University. He studied applied mechanics at Jilin University, China, in 1984 and received his PhD from Jilin University, China, in 1994. He has been working at the Institute of Solid Mechanics, Beihang University, as a professor in uncertain structural mechanics since 1996. He visited Germany as a Humboldt Research Fellow 19992000. His main research areas include structural dynamics, calculation and analysis of solid mechanics, structural strength, structural reliability, fatigue, damage limits and durable design, structural optimization design, random vibration, mechanics of composite materials, smart materials and structures, pneumatic elasticity mechanics, thermodynamics, mechanics of nonlinear asked questions. He has authored and co-authored six books, more than 150 technical papers and holds more than 15 patents on uncertain analysis.

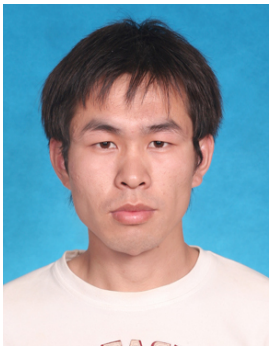

Xie Yong was born in 1987. He is a PhD candidate at Shanghai Jiao Tong University, China. His major is in engineering mechanics. His current research interests focus on spacecraft dynamics and control.

Liu Pan was born in 1986. He is a PhD candidate at Shanghai Jiaotong University, China. His major is in engineering mechanics. His current research interests focus on spacecraft dynamics and control.

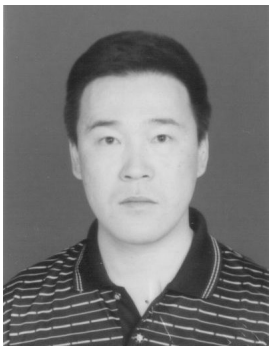

Cai Guo-Ping is a professor in the Department of Engineering Mechanics atShanghai Jiaotong University, China. He received his PhD in engineering mechanics from Xi'an Jiaotong University in 2000. His current research interests focus on structural dynamics and control, delayed system dynamics and control, and coupled system dynamics and control.

About the Authors

Ibrahim Abbas was born on November 20, 1971 in Sohag Egypt. In 2004, he received his PhD in mathematics at South Valley University, Egypt. He is a member of the Egyptian Mathematical Society and is a professor at Sohag University, Egypt. As a professor at Sohag University, his research focuses on the theory of thermoelasticity and fluid mechanics using the finite element method and eigenvalue approach. He has published 150 papers in international journals and 8 conference papers. His more detailed CV can be found in "Who's Who in Science and Engineering."

Sadettin Orhan received his PhD at Krkkale University and his undergraduate studies at Seluk University. He is an associate professor in the Department of Mechanical Engineering at Yldrm Beyazt University, where he has been a faculty member since 2011. His research interests include mechanical vibration, structural health monitoring, and predictive maintenance. He has also interested in tool wear detection as a collaborative study, as well as manufacturing, ranging from theory to design to implementation, with a focus on improving machine quality. In recent years, he has focused on vibration-based energy harvesting and MEMS with researchers in disciplines of electronics engineering. He has taught on discrete and continuous vibrations, dynamics of machinery, mechanisms, and predictive maintenance.

Murat Lüy completed his PhD at Krkkale University and his undergraduate studies in the Department of Electrical and Electronics Engineering at Seluk University. He is an assistant professor in the Department of Electrical and Electronics Engineering at Krkkale University, where he has been a faculty member since 2009. His research interests include renewable energy sources, power plants, and artificial neural networks. In recent years, he has focused on pitch control in wind turbine and wind forecasts. He has taught on electronics, digital electronics, basic computer science, and interior installation and illumination project. In his spare time, he enjoys watching football and taking nature trips. For additional information see http://www.muratluy.com.

M. Husnu Dirikolu completed his PhD degree at the University of Leeds and his undergraduate studies at Middle East Technical University. He is a professor in the Department of Mechanical Engineering at Istanbul University, where he has been a faculty member since 2011. completed his Ph.D. at the University of Leeds and his undergraduate studies at Middle East Technical University. His research interests lie in the area of engineering materials and manufacturing, ranging from theory to design to implementation, with a focus on improving machine quality. In recent years, he has focused on structural weight reduction using polymeric composites. He has collaborated actively with researchers in several other disciplines of medicine and dentistry. He has taught on engineering materials, smart materials, and deformation and failure of materials. In his spare time, he enjoys good food, watching live football, and hiking.For additional information see http://aves.istanbul.edu.tr/dirikolumh/.

Gazi Mustafa Zorlu completed his undergraduate and graduate studies at Krkkale University. He is currently pursuing his PhD degree at Gazi University. His PhD thesis is titled "Elimination and Modelling of Delamination Problems Encountered During Machining of Fiber — Reinforced Polimer Composite Materials." He has been working as a mechanical engineer in Turkish State Railway (TCDD) since 2010. In his spare time, he enjoys watching live football, swimming, traveling, fitness, and body building.

Emrah Kurt received a BS in mechanical engineering from stanbul University in 2007 and MS in mechanical engineering from Erciyes University in 2012. He still works for Afsin-Elbistan Thermal Reactor as a mechanical engineer at Kahramanmaras, Turkey.

Hamdi Taplak received a BS in mechanical engineering from Erciyes University in 1993, MS in mechanical engineering from Erciyes University in 1996, and a PhD in mechanical engineering from Erciyes University in 2002. He is currently an associate professor in the Department of Mechanical Engineering at Erciyes University in Kayseri, Turkey. His research interests include predictive maintenance, rotordynamics, dynamics of machinery, and mechanical vibration.

Mehmet Parlak received a BS in mechanical engineering from Erciyes University in 2008, MS degree in mechatronic engineering from Erciyes University in 2010 on topic about computer aided modelling the rotors and dynamic analysis of them. He worked for Siterm Heat Systems about one year. He has been working on a PhD at Erciyes University as a research assistant in Kayseri, Turkey. His research interests include rotordynamics, dynamics of mechanical systems, and biomechanics.

Sachin S. Harak completed his Graduation in mechanical engineering and Post-Graduation in design engineering from the University of Pune, Pune. He completed his doctoral studies from the Indian Institute of Technology Roorkee and is currently working as an associate professor in the Department of Mechanical Engineering at Late G. N. Sapkal College of Engineering Nashik. His research interests include vibration and control. He has completed a number of research and consultancy projects under the guidance of S. P. Harsha and Satish C. Sharma.

Satish C. Sharma completed his graduation, post-graduation, and doctoral studies from the University of Roorkee, now Indian Institute of Technology Roorkee. He currently works as a professor in the Mechanical and Industrial Engineering Department (MIED) at IIT Roorkee. He is also the Indian Railway Chair Professor (Vehicle Dynamics) and Coordinator for the Centre for Railway Engineering at IIT Roorkee. His research areas include machine design, tribology, hydrodynamic/hydrostatic lubrication, andCoriolis mass flow measuring techniques. He has guided more than 15 research scholars and published more than 100 research papers in peer review journals. He has also completed numerous research and consultancy projects funded by the Government of India.

About the Authors

S. P. Harsha completed his graduation in mechanical engineering & post Graduation in thermal engineering from MBM Engineering College in Jodhpur and his PhD from BITS, Pilani. He currently works as an associate professor in the Mechanical and Industrial Engineering Department (MIED) at IIT Roorkee. He previously worked as a post-doctoral research fellow for a NASA/ONR sponsored project in Philadelphia, USA for one and half years. He also served as an assistant professor in the Mechanical Department at BITS, Pilani. His research areas include vibration and control, nonlinear dynamics and chaos, fault diagnosis and prognosis of high speed machinery, CNT and BNNT based mass sensors, and human vibration. He has published more than 100 research papers in peer reviewed journals and has guided more than 15 research scholars. He has also completed many research and consultancy projects funded by the Government of India.

Ali Belhocine received his master's degree in mechanical engineering in 2006 from Mascara University in Mascara, Algeria. Afterwards, he was a PhD student at the University of Science and the Technology of Oran (USTO Oran) in Algeria. He recently obtained his PhD in mechanical engineering at the same university. His research interests include automotive braking systems, finite element method (FEM), ANSYS simulation, CFD Analysis, heat transfer, thermal-structural analysis, tribology, and contact mechanic.

Nouby Mahdy Ghazaly is an assistant professor in the Department of Mechanical Engineering at South Valley University, Egypt. He received his BS and MS from the Department of Automotive and Tractor Engineering at Minia University, Egypt in 1999 and 2003, respectively. He obtained his PhD from AU-FRG Institute for CAD/CAM, Faculty of Mechanical engineering from Anna University, India in 2011. He has published a book and more than 50 research papers in refereed journals and international conferences in the areas of vehicle dynamics, noise and vibrations and ComputerAidedDesign. He is a member of Editorial Board and a Reviewer of several international journals and conferences. He is currently serving as a consulting engineer of ATALON for testing and consulting engineers in India since 2010.

Luyun Chen was born in September 1975. He received his PhD in design and manufacture of naval architecture and ocean structure from Shanghai Jiaotong University in 2008. He is currently a lecturer in the State Key Laboratory of Ocean Engineering of Shanghai Jiaotong University. His current research includes structure vibration control and structural-acoustic optimization. He is the corresponding author of this article, and his email is *cluyun@sjtu.edu.cn*.

Yong Liu was born in March 1981. He received his PhD in design and manufacture of naval architecture and ocean structure from Shanghai Jiaotong University in 2014. He is currently an engineer in China Ship Scientific Research Center, Shanghai branch. His current research includes ship and offshore structure fatigue reliability analysis, vibration, and acoustic radiation. His email is *flydark@126.com*.

Seyedeh Elnaz Naghibi was born in 1987 in Tehran, Iran. She received her BS in solid mechanics in 2009 and her MS in applied design in 2011, both from the School of Mechanical Engineering at Shiraz University, Shiraz, Iran. She is currently working toward her PhD in applied design in Sharif University of Technology, Tehran, Iran, and since April 2014, she has been a visiting research associate at Queen Mary, University of London, United Kingdom, investigating the interactions of the earth's Chandler wobble and large-scale oceanic currents through modification and numerical validation of a semi-analytical approach devised in her PhD thesis. Mrs. Naghibi was awarded the POGO-SCOR visiting fellowship for her current visit in 2014.

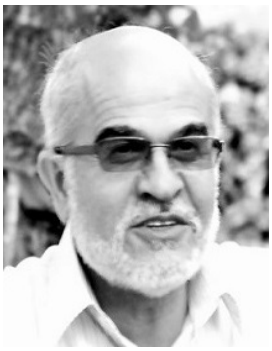

Mojtaba Mahzoon was born in 1960 in Shiraz, Iran. He received his BS in mechanical engineering from Abadan Institute of Technology, Abadan, Iran, in 1973 and his PhD from the University of California at Berkeley, Berkeley, California, United States, in 1984. He is currently an associate professor in the School of Mechanical Engineering, Shiraz University, Shiraz, Iran. His research interests include dynamic modelling, vibrations and control of mechanical systems using advanced continuum mechanics and mathematics. Dr. Mahzoon has more than 41 published journal papers and 24 national and international conference papers and has supervised over 53 students in their MS and PhD research during his 30 years of being a faculty member in Shiraz University and Isfahan University of Technology.

Andrew J. Hull received his BS in 1983, MS in 1985, and PhD in 1990, all in mechanical engineering from Michigan State University, East Lansing, Michigan, USA. He currently works as a mechanical engineer at the Undersea Warfare Weapons, Vehicles and Defensive Systems Department at the Naval Undersea Warfare Center in Newport, Rhode Island, USA. His research interests are in the areas of mechanical vibrations, acoustics, and boundary value problems. He is a member of the International Institute of Acoustics and Vibrations and a fellow of the Acoustical Society of America.

Geoffrey R. Moss holds a BS (2006) and MS (2009) in mechanical engineering from the University of Massachusetts at Amherst. He also holds an MS (2016) in engineering acoustics from the Naval Postgraduate School in Monterey, CA. He currently serves as the Science Advisor to the Commander of Submarine Forces, Pacific Fleet at Pearl Harbor, HI. In addition to his duties as the senior scientific and technical advisor on staff, his research interests include forced vibration problems and numerical approaches to acoustic-structural interaction. He is a member of the Acoustical Society of America.

About the Authors

S. Ahmad Fazelzadeh received his BS and MS degrees in Mechanical Engineering from Shiraz University and Sharif University of Technology in 1992 and 1994, respectively. He received his PhD degrees in Aerospace Engineering from the Sharif University of Technology in 2002. Dr. Fazelzadeh is currently a professor at the School of Mechanical Engineering, Shiraz University. His research interests focus on aeroelasticity, smart materials and

Amir Hossein Ghasemi obtained a MS from the Department of Mechanical Engineering at Shiraz University and BS from the faculty of Engineering at Sistan & Balouchestan University (USB). His master's work dealt with the analysis of flutter of aeroelastic aircraft wings. His present research interests lie in high tonnage centrifugal cooled-water chillers and engineering survey in which he has acquired expertise while working with Ofogh Consultant Engineering (OCE) Company.

Abbas Mazidi received his PhD degree in mechanical engineering from the Shiraz University in 2011. Presently, he is an assistant professor in the Mechanical Engineering Department of the Yazd University. His research interests include aeroelasticity, dynamics of flexible structures, and dynamical systems.

Zhang Chao received his BS and MS in mechanical engineering from North China Electric Power University in Baoding City, China in 2000 and 2003 respectively. He received his PhD in thermal engineering from North China Electric Power University in Baoding, China in 2009. He is currently a lecturer in the Department of Mechanical Engineering at North China Electric Power University. His main research interest is rotary machine condition monitoring and fault diagnosis.

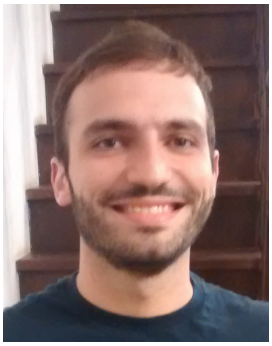

Marcus Vinícius Manfrin de Oliveira Filho earned his BS in mechanical engineering from the Federal University of Paran inUFPR, Brazil in 2011. He earned his MS in hydric resources and environmental engineering with a concentration in environmental engineering from the same university in 2014 under the guidance of Professor Paulo Zannin, PhD. He is an assistant professor at Positivo University in Paran, Brazil and a PhD student in mechanical engineering with a concentration in solids and vibration at the Federal University of Paran under the guidance of Professor Carlos Bavastri, PhD. He is the author of three scientific articles in the field of environmental noise and architectural acoustics, all which have been published in international journals. He has also published two book chapters in the area of acoustics and noise mapping.

Paulo Henrique Trombetta Zannin earned his BS in mechanical engineering from the Federal University of Santa Catarina inUFSC, Brazil in 1985 and his MS in mechanical engineering with a concentration in acoustics and vibrations from the same university in 1991 under the guidance of Professor Samir N. Y. Gerges, PhD. He earned his PhD from the Technische Universitt Berlin — Institut fr Technische Akustik, Germany in 1996, under the guidance of Dr. Manfred Heckl. He is a professor at the Federal University of Paran, Brazil and the Coordinator of the Laboratory of Environmental and Industrial Acoustics and Acoustic Comfort. He is the editor of two books: Noise and Ergonomics in the Workplace and Noise Pollution in Urban and Industrial Environments — Measurements and Noise Mapping, as well as the author of 90 scientific articles. He has also published 17 book chapters in the area of acoustics. Dr. Zannin has supervised 27 master's theses and six doctoral theses. He is a member of the European Acoustic Association (EEA) and of the German Acoustical Society (DEGA). He is also a level 1"B" researcher ofNational Council for Scientific and Technological Development (CNPq), a branch of Brazil's Ministry of Science and Technology.

Han Zhiyan was born in Chifeng, which is in inner Mongolia, on March 1982. She graduated from in 2009 Northeastern University with a PhD , and is currently an associate professor at Bohai University. Her research interests mainly include speech signal processing, emotion recognition, and fault diagnosis. She has published papers in *International Journal of Circuits, Systems and ComputersInternational Journal of Modelling, Identification and ControlChinese Journal of ElectronicsJournal of Northeastern UniversityComputer Science,* and many more.

Wang Jian was born in Dalian of Liaoning Province on February 1982. He graduated in 2015 from Northeastern University with a PhD and is currently an associate professor at Bohai University. His research interests mainly include signal processing, fault diagnosis, and fuzzy control theory. He has published papers in *IEEE Transactions on Automation Science and Engineering,International Journal of Circuits, Systems and Computers,Control and Decision,Journal of Northeastern University* and many more.